People's Democratic Republic of Algeria
Ministry of Higher Education and Scientific Research
Abderrahmane Mira University of Bejaia

جامعة بجاية
Tasdawit n Bgayet
Université de Béjaïa

Faculty of Technology
Electrical Engineering Departement
Laboratoire de Technologie Industrielle et de l'Information

PhD Dissertation

In Partial Fulfillment of the Requirement for the Degree of

DOCTORATE

Domain: Science and Technology   **Field: Electrotechnic**
Option: Control and energy conversion

Presented by
Adel OUBELAID

Title

Contribution to the optimization of hybrid electric vehicle actuators' control

---

Defended on: November 5th 2022   **In front of the Jury composed of:**

First last names   **Grade**

Mr Farid HAMOUDI	Professor	Univ. of Bejaïa	President
Mr Nabil TAIB	Professor	Univ. of Bejaïa	Thesis director
Mr Toufik REKIOUA	Professor	Univ. of Bejaïa	Thesis co-director
Mr Aissa KHELDOUN	Professor	Univ. of Boumerdes	Examiner
Mr Abdelmadjid RECIOUI	Professor	Univ. of Boumerdes	Examiner

Academic year: 2021/2022

République Algérienne Démocratique et Populaire
Ministère de l'Enseignement Supérieur et de la Recherche Scientifique
Université A.MIRA-BEJAIA

Tasdawit n Bgayet
Université de Béjaïa

Faculté de Technologie
Département de Génie Electrique
Laboratoire de Technologie Industrielle et de l'Information

THÈSE

EN VUE DE L'OBTENTION DU DIPLOME DE DOCTORAT

Domaine : Sciences et Technologies   Filière : Electrotechnique
Spécialité : Commande et Conversion d'Energie

Présentée par
Adel OUBELAID

Thème

Contribution à l'optimisation de la commande des actionneurs des véhicules électriques hybrides

Soutenue le : 5 novembre 2022   **Devant le Jury composé de :**

Nom et Prénom	Grade		
Mr Farid HAMOUDI	Professeur	Univ. de Bejaïa	Président
Mr Nabil TAIB	Professeur	Univ. de Bejaïa	Rapporteur
Mr Toufik REKIOUA	Professeur	Univ. de Bejaïa	Co-rapporteur
Mr Aissa KHELDOUN	Professeur	Univ. de Boumerdes	Univ.de Boumerdes
Mr Abdelmadjid RECIOUI	Professeur	Univ. de Boumerdes	Univ.de Boumerdes

Année Universitaire : 2021/2022

Dedication

To my parents

To my brothers and sisters

To my friends

To all people that helped me

Acknowledgement

I thank God for helping me reaching this step. I dedicate this work to my family without which i would never have had the courage to continue to work and to resist the various difficulties encountered throughout my thesis.

I would like to thank Professor Nabil TAIB and Professor Toufik REKIOUA for their assistance, their availability and their support throughout my thesis years. I would like also to thank professor Abdelmadjid RECIOUI, professor Aissa KHELDOUN and professor Farid HAMOUDI for accepting to examine and evaluate my thesis manuscript.

Finally, I would like to thank all my friends and the research laboratory members for their help, support and precious advices during my thesis period.

Adel OUBELAID

Table of content

List of figures

vii

List of tables

List of abbreviations and symbols

Abbreviations

BAT	Battery
DTC	Direct Torque Control
DC	Direct Current
EV	Electric Vehicle
FLC	Fuzzy Logic Control
FCHEV	Fuel Cell Hybrid Electric Vehicle
FC	Fuel Cell
GA	Genetic Algorithm
HEV	Hybrid Electric Vehicle
ICE	Internal Combustion Engine
Li-Io	Lithium- Ion
PEMFC	Proton Exchange Membrane Fuel Cell
PMSM	Permanent Magnet Synchronous Machine
RT	Real Time
TDS	Torque Distribution Strategy
SVM	Space Vector Modulation
SC	Supercapacitor
SOC	State Of Charge

Symbols

C	Capacitance between FC anode and cathode [F]
C_{FC}	Fuel cell contribution factor
C_{SC}	Supercapacitor contribution factor
C_{BAT}	Battery contribution factor
C_p	Parallel branch capacitance [F]
C_{BUS}	Bus capacitance [F]
d	Duty cycle
E_{Nernst}	Nernst potential [V]
F	Faraday's constant [C. mol^{-1}]

g_{BAT}	Battery gate signal
g_{FC}	Fuel cell gate signal
g_{SC}	Supercapacitor gate signal
i_L	Limit current [A]
i_{FC}	Fuel cell current [A]
i_{BAT}	Battery current [A]
i_{SC}	Supercapacitor current [A]
N_{bs}	Number of series battery cells
n	Number of electrons in the FC reaction
i_0	Exchange current [A]
P_{FC}	Fuel cell power [W]
P_{BAT}	Battery power [W]
P_{SC}	Supercapacitor power [W]
P_{HEV}	Vehicle power [W]
Q_{init}	Initial supercapacitor charge [C]
Q_T	Instantaneous supercapacitor charge [C]
R_{act}	Resistance due to activation polarization [Ω]
R_{con}	Resistance due to conduction polarization [Ω]
R_{ohm}	Resistance due to ohmic polarization [Ω]
R_p	Parallel branch resistance [Ω]
R_{SC}	Supercapacitor equivalent series resistance [Ω]
R_i	Battery internal resistance [Ω]
R_L	Load resistance [Ω]
R	Gas constant [Jmol^{-1}K^{-1}]
T	Fuel cell temperature [K]
t_i	Transference number
T_S	Sampling time [s]
t_{trig}	Triggering instant [s]
U_{act}	Activation polarization [V]
U_{con}	Concentration polarization [V]
U_{ohm}	Ohmic polarization [V]
$V_{FC,CELL}$	Fuel cell voltage [V]
$V_{BAT,CELL}$	Battery cell voltage [V]

$V_{BAT,TOT}$	Total battery voltage [V]
V_{OC}	Open circuit voltage [V]
V_{DC}	DC bus voltage [V]
V_{NL}	No load voltage [V]
V_{FL}	Full load voltage [V]
V_{SC}	Supercapacitor voltage [V]
V_C	Capacitor voltage [V]
z	Activity coefficient
F_{ext}	External force [N]
F_r	Resistive force [N]
F_t	Tractive force [N]
F_{aero}	Aerodynamic force [N]
F_g	Gravitational force [N]
F_{tire}	Tire force [N]
F_{acc}	Acceleration force [N]
m	Vehicle mass [kg]
a	Vehicle acceleration [m/s^2]
A	Vehicle front area [m^2]
C_d	Aerodynamic coefficient []
V_{wheel}	Wheel speed [m/s]
V_{wind}	Wind speed [m/s]
ρ	Air density [kg/m^3]
t_a	Vehicle time constant [s]
α	Road slope angle
Φ_d	Direct axis flux [Wb]
Φ_q	Quadratic axis flux [Wb]
Φ_{PM}	Permanent magnet flux [Wb]
L_d	Direct axis inductance [H]
L_q	Quadratic axis inductance [H]
i_d	Direct axis current [A]
i_q	Quadratic axis current [A]
T_e	Electromagnetic torque [$N.m$]
Θs	Stator flux angle [°]

V_{DC}	DC bus voltage [V]
$[S_a\ S_b\ S_c]^T$	Inverter switching state vector
τ_1	Charging battery time constant, [s]
τ_2	Discharging battery time constant [s]
τ_{FC}^{NL}	No load FC time constant [s]
τ_{FC}^{FL}	Full load FC time constant [s]
σ	Equivalent conductance, [$m^2\Omega^{-1}$]
α, β, γ	Weighting factors

List of scientific contributions

Journal papers

1. A. Oubelaid, N. Taib, T. Rekioua, (May 2022). Novel coordinated power sources switching strategy for transient performance enhancement of hybrid electric vehicles. COMPEL-The international journal for computation and mathematics in electrical and electronic engineering, Vol. 41 No. 5. pp.1880-1919; DOI: 10.1108/COMPEL-10-2021-0399

2. A. Oubelaid, F. Albalawi, T. Rekioua, S. S. M. Ghoneim, N. Taib and S. A. Mohamed Abdelwahab, (June 2022). "Intelligent Torque Allocation Based Coordinated Switching Strategy for Comfort Enhancement of Hybrid Electric Vehicles" *IEEE Access*, Vol. 10, pp. 58097-58115; DOI: 10.1109/ACCESS.2022.3178956

3. A. Oubelaid, N. Taib, S. Nikolovski, T.E.A. Alharbi, T. Rekioua, A. Flah, S. S. M. Ghoneim, (June 2022). Intelligent Speed Control and Performance Investigation of a Vector Controlled Electric Vehicle Considering Driving Cycles. *Electronics*, Vol. *11, No. 13. 1925;* DOI: https://doi.org/10.3390/electronics11131925

4. A. Oubelaid; H. Alharbi ;A.S.B Humayd; N. Taib; T. Rekioua; S.S.M. Ghoneim. Fuzzy-Energy-Management-Based Intelligent Direct Torque Control for a Battery—Supercapacitor Electric Vehicle. Sustainability (2022), Vol. 14, 8407. DOI: https://doi.org/10.3390/su14148407

5. A. Oubelaid, N. Taib, T. Rekioua, M. Bajaj, A. Yadav, M. Shouran, S. Kamel, Secure Power Management Strategy for Direct Torque Controlled Fuel cell/Supercapacitor Electric Vehicles. Frontiers in Energy Research, 1425. DOI: 10.3389/fenrg.2022.971357

6. A. Oubelaid, Taib, N.; Rekioua, T.; Bajaj, M.; Blazek, V.; Prokop, L.; Misak, S.; Ghoneim, S.S.M. Multi Source Electric Vehicles: Smooth Transition Algorithm for Transient Ripple Minimization. *Sensors* 2022, *22*, 6772. DOI: https://doi.org/10.3390/s22186772

7. S. Belaid, D. Rekioua, **A. Oubelaid**, D. Ziane, T. Rekioua, (2022). A power management control and optimization of a wind turbine with battery storage system. Journal of Energy Storage, 45, 103613. DOI: https://doi.org/10.1016/j.est.2021.103613

8. S. Belaid, D. Rekioua, **A. Oubelaid**, D. Ziane, T. Rekioua, (2022). Proposed Hybrid Power Optimization for Wind Turbine/Battery System. Periodica Polytechnica Electrical Engineering and Computer Science, 66(1), 60-71. DOI:https://doi.org/10.3311/PPee.18758

9. K.Kakouche; T. Rekioua; S. Mezani; **A. Oubelaid**; D. Rekioua; V. Blazek; L. Prokop; S. Misak; M. Bajaj; S. S. M. Ghoneim. Model Predictive Direct Torque Control and Fuzzy Logic Energy Management for Multi Power Source Electric Vehicles. *Sensors* **2022***, 22*, 5669. DOI: https://doi.org/10.3390/s22155669

10. D. Ziane, A. Azib, A. Oubelaid, N. Taib, T. Rekioua, D. Rekioua, "Proposed Power Factor Correction Circuit Based on the Single-Ended Primary Inductor Converter Controlled by Sliding Mode Control Strategy Used in an Electric Vehicle Charging Station", Rev. Roum. Sci. Techn.–Électrotechn. et Énerg.Vol.67, 3, pp. 241–245, Bucarest, 2022.

Chapters

M. Ahmed, B. Khadidja, R. Djamila, **A. Oubelaid**, M. Nasser Eddine, 'Enhancement of Extracted Photovoltaic Power Using Artificial Neural Networks MPPT Controller' , (2021), In book: Advances in Green Energies and Materials Technology.

Conference papers

1. A. Oubelaid, N. Taib, and T. Rekioua: Performance assessment of a direct torque controlled electric vehicle considering driving cycles and real load conditions, International Conference on Advanced Electrical Engineering (ICAEE 2019), November 2019, Algiers, Algeria.

2. A. Oubelaid, N. Taib, and T. Rekioua: Design and voltage control of an automatic voltage regulator using particle swarm optimization, Electrical Engineering International Conference (EEIC'19), December 2019, Bejaia, Algeria

3. A. Oubelaid, N. Taib, and T. Rekioua, A. Zouagui: Proposed cost function for speed control of PMSM using particle swarm optimization, International Conference on Electronics and Electrical Engineering (IC3E'18), November 2018, Bouira, Algeria.

4. A. Oubelaid, Y. Berkani, N. Taib, T. Rekioua, «Speed Control and Performance Analysis of PMSM using Particle Swarm Optimization » The 2nd International Conference on Applied Automation and Industrial Diagnostics 2017, (ICAAID 2017), September2017, Djelfa

5. Y. Berkani, **A. Oubelaid**, N. Taib: Cyclic Venturini modulation for matrix converter fed vector controlled five-phase PMSM, The 3th International Conference on Power Electronics and their Applications 2017 (*ICPEA*'17) 2016-2017 September, Djelfa, Algeria

6. A. Kheldoun, M. Brahim, **A. Oubelaid**, M. Djamel, "Optimal adjustment of PID parameters using population based-optimization algorithms for an Automatic Voltage Regulator",(2016), Séminaire national sur les procédés industriels et l'économie des énergies, SNPIEE'16, University of EL Oued, Algeria

7. Mouhamedi, D. Rekioua, T. Rekioua, N. Mebarki, **A. Oubelaid**: New photovoltaique pumping system with direct torque control, The 1st International Conference on sustainable renewable energy systems, (ICSRESA'19), Tebessa, Algeria.

General introduction

Nowadays trend in the field of electrical engineering is the integration of renewable energy sources in almost all industrial disciplines. For instance, wind, solar and tidal energies- which are clean and everlasting energy sources, have successfully replaced the conventional methods of electricity production. Transportation sector generates the largest share of greenhouse gas emissions [1]. Several research studies have been conducted to investigate sustainable low carbon transportation technologies that solve the carbon emission persisting problem. Electrified vehicles are among the alternative clean transportation technologies that are gaining customer's confidence these last years. This increasing interest gave birth to many research axes that share one common objective which is the elaboration of an ecologic vehicle with good performances. Control of electric propulsion systems [2], intelligent energy management [3], power electronics [4], Power train architecture [5], vehicle safety [6], intelligent vehicle control [7], optimization of fuel utilization [8] are among the biggest nowadays trends in the field of automotive engineering.

Despite their multiple advantages, electrified vehicles still have some lacks that require correction as any other engineering industrial products. Even though Proton Exchange Membrane Fuel Cells (PEMFC) are widely used in transportation sector because of their high effeciency, low operating temperature, and environmental friendliness, their sensitivity and poor transient dynamics are two serious problems that still lower electric vehicle performance. PEMFC slow transient response is due to the chemical reactions occurring at its anode and cathode prior energy deliverance. An illustration about fuel cell slowness is clearly seen in the simulation results of [9-10]. In [11-12], authors estimated fuel cell delay to be three times the time constant of the fuel cell resistive-capacitive (RC) branch. It is worth noticing that the random nature of driving conditions results in abrupt load variations and this subjects the fuel cell to large and harmful transient currents that may cause its damage. Authors in [13-16] recommended that fuel cells should be operated with protective procedures against over-current, under-voltage, abnormal-pressure and over-temperature. To summarize, most researchers in the field of fuel cell electric vehicles emphasized on some major objectives such as fuel cell protection, fuel cell lifespan enhancement, efficient FC operation and compensation of FC slow transient response.

Traction machine and drivetrain architecture are two necessary but not sufficient requirements toward the elaboration of an efficient vehicle with good performances. However, if not well managed, these two key elements will contribute in lowering further vehicle performances instead of enhancing them. Torque distribution strategies are developed to ensure

convenient torque allocation over vehicle wheels. Out of literature [17-18], the goal of most torque distribution strategies is either torque maximization through distributed drivetrains or minimize energy consumption during vehicle rides. It is true that these two last mentioned objectives enhance vehicle performance but it is at the expense of vehicle cost and weight.

The various control strategies discussed throughout this thesis seek to address some persistent issues related to electric vehicles. The major objectives targeted in this work are summarized by the following points:

- Promote the transient performances of electric vehicles via the use of metaheuristic algorithms.
- Weaken the effect of random load variations on vehicle power sources and compensation of fuel cell poor transient response.
- Elaboration of energy management strategy ensuring moderate and secure operation of vehicle power sources.
- Build a torque distribution strategy that takes maximum vehicle propulsion power as an optimization goal.

In the first chapter of this work, intelligent speed control and transient performance assessement of an electric vehicle are discussed. Speed and current controllers of the electric vehicle are tuned using two well known metaheuristic algorithms which are particle swarm optimization (PSO) and genetic algorithm (GA). Two proposed cost functions for step inputs and driving cycles were formulated to meet some design requirements which are: minimum torque and speed error for driving cycles and good tradeoff between percentage overshoot, rising time and steady state error for step inputs. It is important to point out that the two aforementioned metaheuristic algorithms were integrated on a closed loop control system that takes into account several vehicle components such as regulators, inverter, traction machine and sensors.

The second contribution made in this thesis consists of a new multi stage power management strategy that is applied to a fuel cell- battery vehicle. The proposed fuzzy energy management strategy ensures a moderate use of power sources by operating the fuel cell at several safe and predefined operating points. Furthermore, the proposed strategy is equipped with a fault detection bloc that detects possible faults at power source level and correct them. A novel coordinated switching strategy is incorporated at the last stage of the proposed energy management strategy. The aforementioned strategy relies on the use of transition functions to compensate the difference in transient dynamics between power sources and to protect them from possible damages caused by sudden load variations.

The third contribution made in this work aims to enhance vehicle performance by boosting its propulsion power via intelligent torque distribution strategies that use fuzzy logic control (FLC) and particle swarm optimization (PSO). The aforementioned metaheuristic algorithm determines the best differential arrangements and the suitable torque distributions using torque transfer ratio (TTR) as cost function. It is worth noticing that vehicle driving comfort and motor health are taken into account by incorporating the coordinated switching strategy already introduced in chapter two in the control of motors.

Chapter 1

Overview on hybrid electric
vehicles

1.1 Introduction

Transportation sector is a significant source of CO_2 emissions. In [17], it is stated that it is responsible of 22% of global CO_2 emissions in 2020 as it is pointed out in figure 1.1. To solve pollution issue or at least lower its effect, traditional vehicles that depend on exhaustible and polluting energy sources are constantly being replaced by electric vehicles because of their environmentally friendliness characteristic.
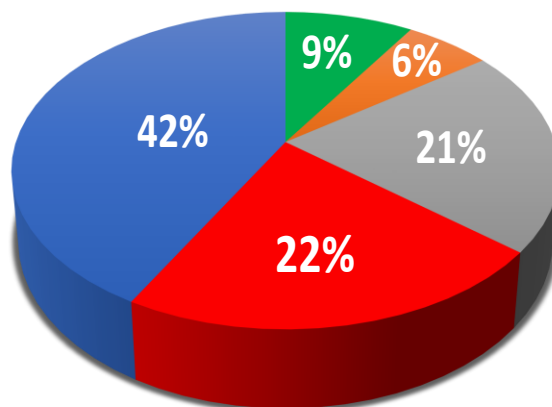
■ Other sectors ■ Residential ■ Industry ■ Transportation ■ Electricity and heat

Figure 1.1 CO_2 emissions of various sectors [18]

Electric vehicles have imposed themselves in the market of automotive engineering as a potential candidate that can successfully substitute conventional vehicles. This fact has pushed many countries around the world to reorient their policies toward the electrification of their transport sectors already suffering from greenhouse gas emissions. The growing interest given to electric vehicles is reflected by figure 1.2 which shows the global HEV sales till 2021. It could be noticed from that figure that vehicle sales reached 6.75 million units in 2021, 108 % more than in 2020. This volume includes passenger vehicles, light trucks and light commercial vehicles. The remarkable growth rate recorded in 2021 is relative to the low base volume of 2020 mainly caused by regulations and Covid 19 [18]. It is important to notice that global HEV sales of 2019 and 2020 were below the long-term trajectory and in 2021 they returned back to trend as it can be seen in figure 1.2.

Electric vehicles have dominated the market and forced many countries around the world to reorient their policies toward the electrification of their transportation sectors, which are already suffering from greenhouse gas emissions. This increasing interest given to the electrification of transportation sector gave birth to several research axes such that aim to

elaborate an ecologic and efficient electric vehicle. Extended range vehicles, Unmanned vehicles, Fuel optimization, Control of electric propulsion systems, energy management, vehicular communication systems, autonomous vehicles and vehicle security are among the biggest nowadays trends in automotive engineering. Throughout this chapter, a brief history about electrified vehicles is presented. Then, a detailed classification of electrified vehicles is discussed. After that, advantages and drawbacks of the aforementioned type of vehicles are debated. Finally, this chapter is closed by pointing out the different expectations and challenges facing the evolution of electric vehicles.
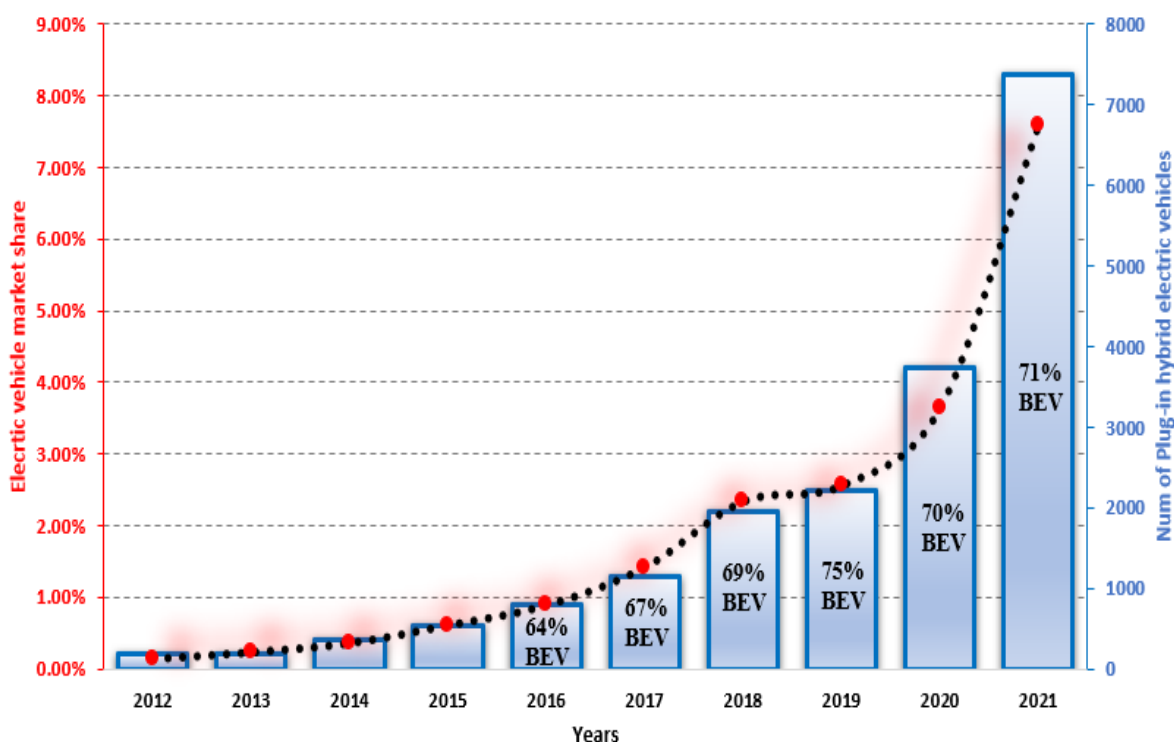
Figure 1.2 Global electric vehicle sales.

1.2 History of electric vehicles

Joint advances in energy accumulators such as batteries and electric motor as drive systems along with the predominance of the electromagnetic induction since 1831 have led to significant advances electric mobility technology. Two researchers stand out in this context: Alessandro Volta for the precursor of the battery in 1800 ("Battery Back") and Michael Faraday, who developed the homopolar motor in 1821. The first electric vehicles appear in the 1830s using non-rechargeable batteries [19]. In 1859 Mr. Gaston Plante invented the rechargeable lead-acid battery that is the nowadays most preferred type of batteries especially in automotive and storage applications. Following that, Aphonse Camille Faure enhanced the performance of the aforementioned battery type leading to its commercialization on vehicle boards in 1881 [20]. Mr. Trouvé created the first electric vehicle powered by a lead-acid battery in France in 1882. Meanwhile, other electric vehicles operated by lead-acid batteries made their

first appearance in the United States and the United Kingdom. Although steam mobility existed at the time, particularly in public transportation, the electric vehicle quickly established itself as an ideal choice for urban traffic because it produces no noise and pollutes the environment. In the early 1900s, Thomas Edison, intrigued by the potential of electric vehicles, developed the nickel-iron battery, which had a storage capacity 40 % greater than the lead battery but a much higher cost of production. To conclude, the nineteenth century is mainly characterized by important findings in battery technology such as the development of nickel-zinc and zinc-air batteries [21].

1.2.1 First cycle of electric vehicles (1837-1912)

At the beginning of the twentieth century, many researchers thought that electric and conventional vehicles could coexist together and each vehicle type will find its own customers. However, researchers' prediction was not correct and electric vehicles commercialization has decreased significantly during this period for the following reasons:

- The removal of the crank used in combustion powered vehicles as a result of electric starter invention in 1912 [22].
- In 1920, the highways in the United States interconnected several cities and this required vehicles with large autonomy capable of traveling long distances [23].
- Success of commercialization of petrol vehicles. According to [24], the number of electric power cars in 1912 in the United States reached 30 000 units and the amount of petrol cars was already thirty times larger.
- Oil discoveries in Texas have reduced gasoline prices, making it an attractive fuel for the transportation sector [25].
- The impressive progress of distillation techniques along with the low cost of petroleum products contributed together in the expansion of the automobile industry's technological development toward gasoline-powered vehicles [26].

Figure 1.3 depicts the performance achieved by the first generation of electric vehicles in terms of speed and autonomy. It can be seen that the maximum vehicle autonomy is around 65 *km* and the maximum speed is 35 km/h. It is worth noticing that at the same time period, the autonomy of vehicles using combustion engines where 3 times larger for both autonomy and speed [27]. The last mentioned reference indicates that the petrol vehicles were between 1000.00 and 2000.00 dollars with an operating cost of 0.01 dollar /mile. On the other side, electric vehicle cost at the was varying from 1250.00 to 3500 dollars with an operating cost of 0.03 dollar/mile.
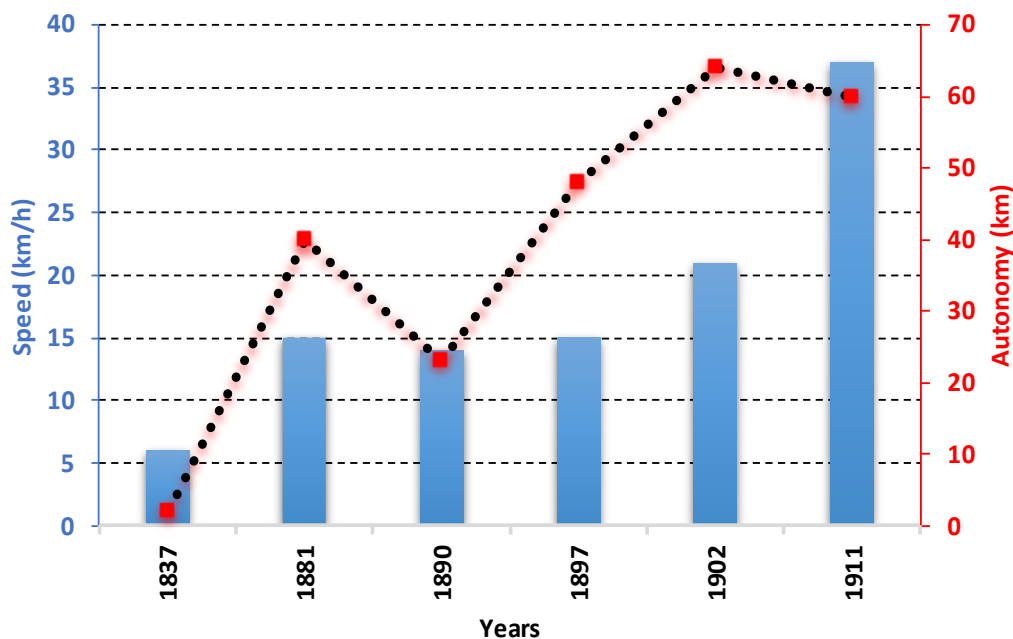
Figure 1.3 Autonomy and speed ratings for first generation of electric vehicles.

1.2.2 Second generation of electric vehicles (1912-1973)

Following the several discoveries made in oil the field, conventional vehicles based on the use of diesel and gasoline have gained a lot of momentum and they were a better choice in terms of speed, autonomy and operating cost compared to electric vehicles. The first world war in 1914 resulted in increasing oil prices and this has renewed optimism about electrified vehicles future. This enthusiasm was also amplified by the technical achievements in the favor of electric vehicles made in this period. For example, battery lifespan and storage capacity were enhanced by 35%. Despite the technical and commercial efforts spent to impose electric vehicle dominance in the vehicle market, the number of electric vehicles fell from 10% in 1913 to only 3% in 1925 according to [28] because of its limited autonomy and reduced comfort. Moreover, the long charging time of vehicle batteries has reduced its large scale commercialization.

Figure 1.4 shows the performance of the second generation of electric vehicles in terms of maximum speed and autonomy. At first look, it could be noticed that the vehicle speed and autonomy are significantly improved compared to the first generation of electric vehicles. According to [29], researchers' interests during this period were oriented toward the elaboration of vehicles with minimum energy consumption and less CO_2 emissions as issues about CO_2 usage were raised and laws discussing fuel emissions restrictions began to be adopted.
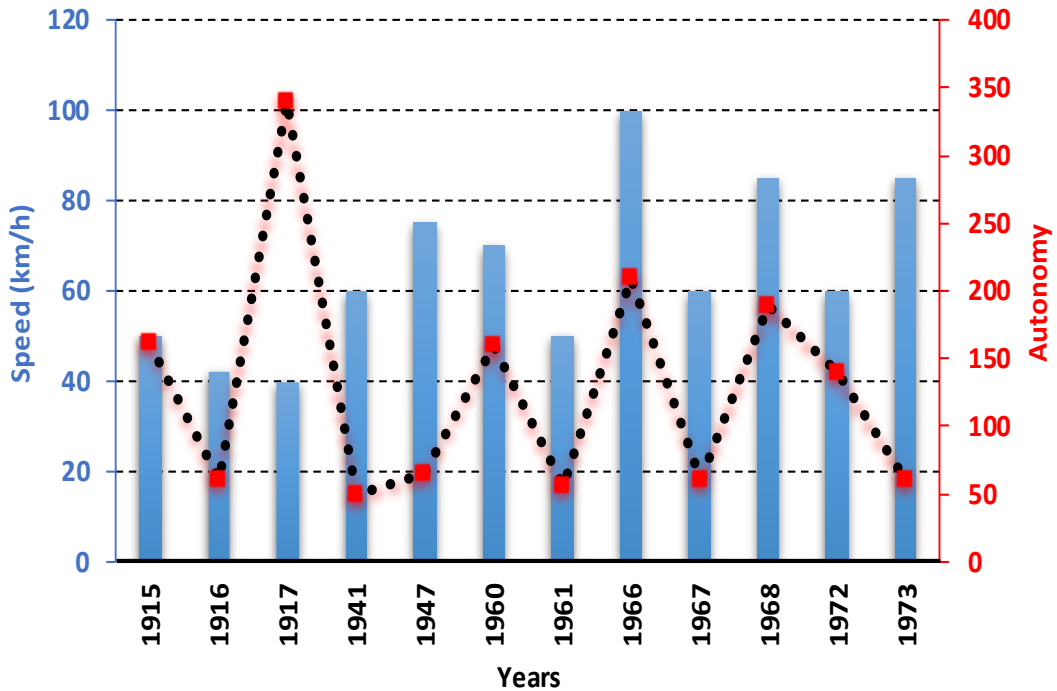
Figure 1.4 Autonomy and speed ratings for second generation of electric vehicles.

1.2.3 Third generation of electric vehicles (1973-1996)

Demand for electric vehicles grew rapidly until the late 1980s, when the issue of urban air pollution became more widely discussed [30]. The oil crisis caused by OPEC (Organization of Petroleum Exporting Countries) in 1973 had opened up new opportunities for electric vehicles. The countries which depend significantly on oil coming mainly from Arab region reconsidered their policies and have adopted some regulations and strategies to reduce oil dependence. Massive, progressive and continuous electrification of their transportation sectors was among the proposed solution for reducing oil dependence. Between the 1980s and 1990s, a number of top modern vehicles such as the General Motors EV-1, Toyota RAV4-EV, and Ford Ranger EV were commercialized and extensive research on battery costs and lifespan was conducted to evaluate the commercial prospects of these vehicles [31]. Although electric vehicles were more efficient than conventional ones, their advantages were of little value at a time when oil prices were at their lowest values [32].

Figure 1.5 highlights the performance of the third cycle of electric vehicles in terms of maximum speed and autonomy. Despite the different barriers preventing the large scale commercialization of electrified vehicle, one could notice easily from figure 1.5 that significant enhancement in terms of speed and autonomy have been made compared to the first and second generations of electric vehicles shown respectively in figures 1.4 and 1.3.
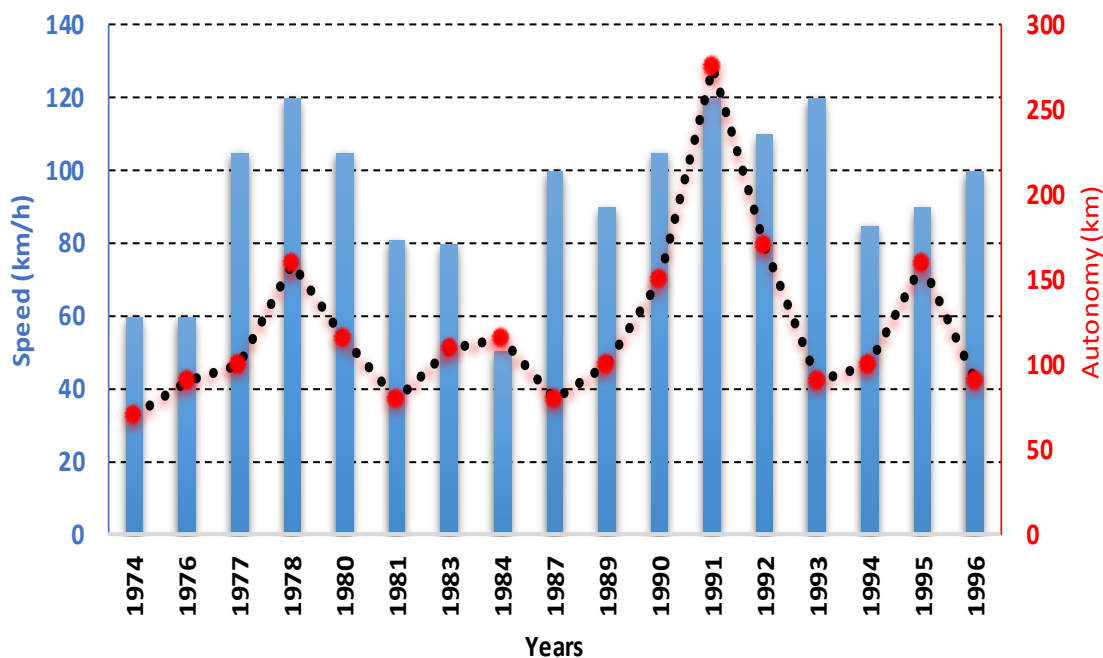
Figure 1.5 Autonomy and speed ratings of the third generation of electric vehicles.

1.2.4 Fourth generation of electric vehicles (1996-2012)

In this time period, hybrid electric vehicles and plug-in hybrid vehicles appeared as a potential solution that may solve many issues such as energy security, pollution and independency from fossil resources. The first major progress made in this period took place in 1997 when the four-door vehicles "Toyota prius" and "Insight" were launched respectively in Japan and united states markets [33]. Since the launch of the Toyota Prius in 1997, 1.9 million HEVs (Hybrid Electric Vehicles) vehicles and 60.0 thousand PHEVs (Plug-in Hybrid Electric Vehicles) and BEVs (Battery Electric Vehicles) vehicles have been sold in the North-American market [34]. This commercialization success can be attributed in large part to the encouragement of the U.S. government to manufacturers and consumers of hybrid and electric vehicles. Worldwide, over the last decade, many HEVs, PHEVs and BEVs have been sold, totaling more than 2.5 million vehicles. In early 2011, the penetration of these technologies in the market is of 2% in the U.S. and 9% were sold in Japan [35]. With the new developments in batteries, electric vehicles now have their storage capacity between 20 and 60 kWh, allowing its interconnection with the electric distribution network through the consumption of energy. Furthermore, in the very near future, this will provide energy according to the needs of network functionality through the Vehicle Connected to grid technology (V2G). Figure 1.6 depicts the performance of the fourth generation of electric vehicles in terms of maximum speed and autonomy. One can deduce from figure 1.6 that important improvements in terms of speed and autonomy have been made compared to the three first generations.
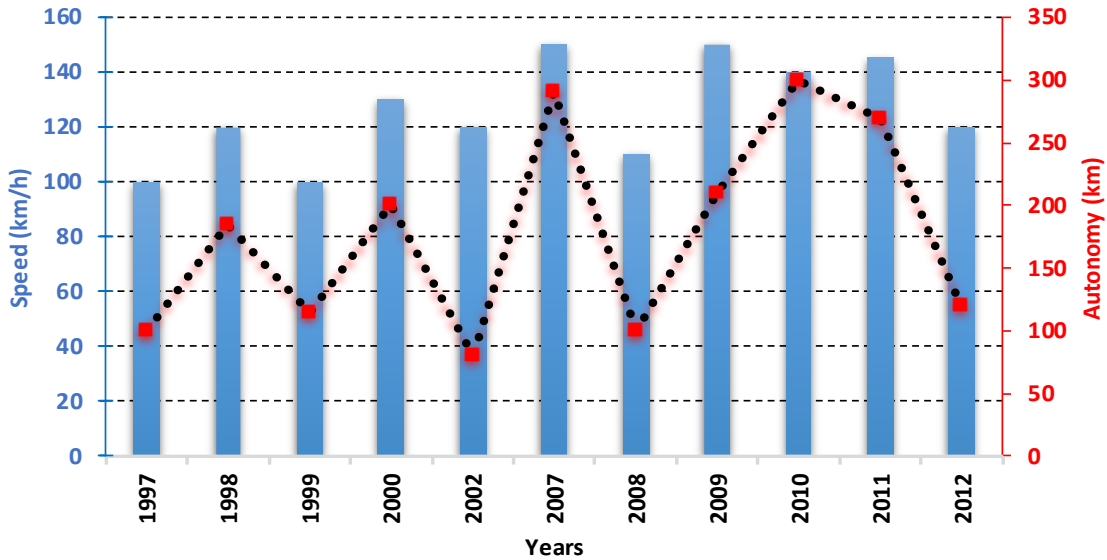
Figure 1.6 Autonomy and speed ratings of the fourth generation of electric vehicles.

1.3 Classification of electrified vehicles

There exist three main types of electric vehicles. Each type is detailed below:

1.3.1 Battery Electric Vehicle (BEV)

This type of vehicles is powered only using batteries. In comparison to the conventional fuel powered vehicle shown in figure 1.7 (a), the BEV eliminates the internal combustion engine (ICE) and relies only on rechargeable batteries packs. As it is shown in figure 1.7 (b), the battery packs supply the electric machine (M/G) (which can operate as a motor or generator) with the necessary power to drive vehicle wheels. In addition to CO_2 emissions, this type of vehicles ends the dependence to fossil fuel.

(a)   (b)
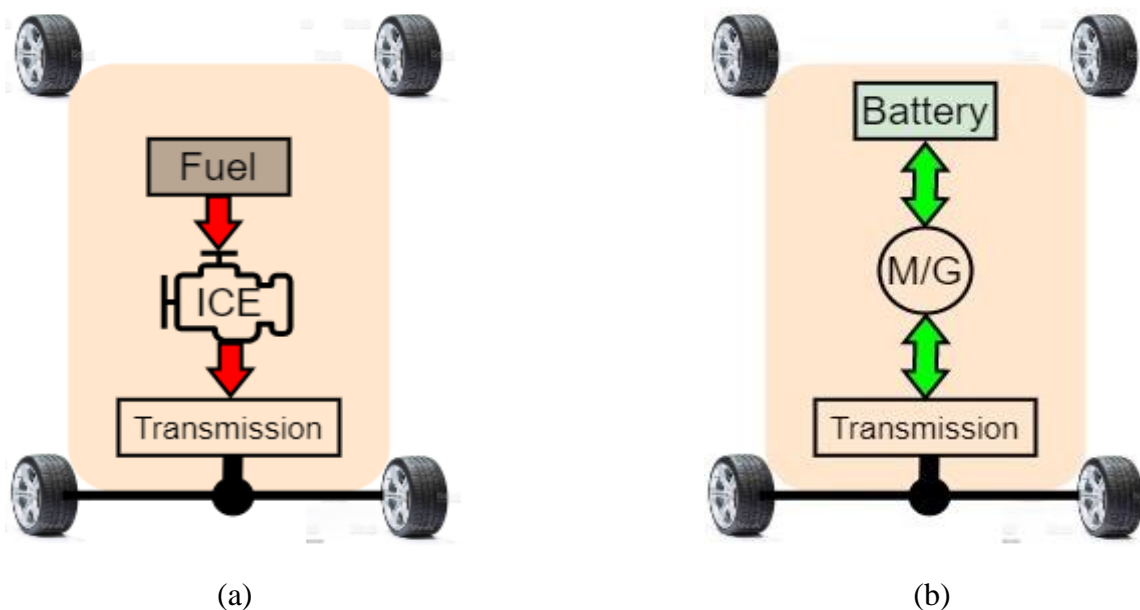
Figure 1.7 (a) Conventional vehicle, (b) Battery electric vehicle.

1.3.2 Hybrid Electric Vehicle (HEV)

Hybrid Electric Vehicles (HEV) are powered with two or more power sources which maybe of same or different nature. Figure 1.8 (a) shows a hybrid electric vehicle that is powered using two electric power sources which are: supercapacitor and battery. A hybrid electric vehicle powered by an internal combustion engine and a battery is depicted in figure 1.8 (b). Because battery packs can be recharged by recovering the vehicle's kinetic energy through regenerative braking, HEVs are better than BEVs in terms of autonomy and driving comfort. Furthermore, HEVs are very adequate for city driving which is known by the multiple starts and stops while city driving.

(a)   (b)
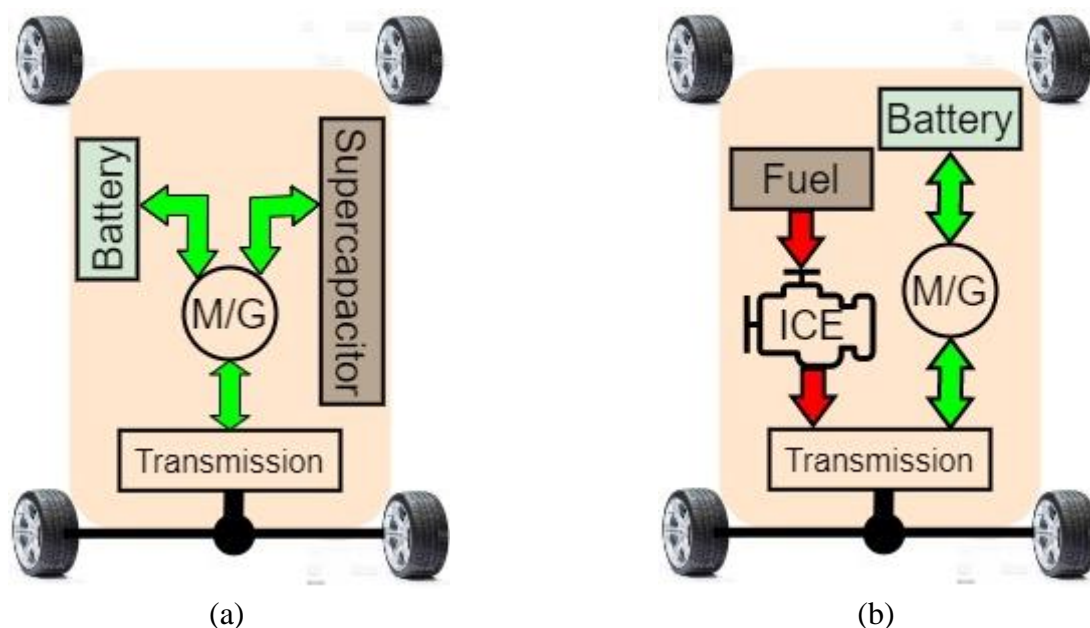
Figure 1.8 (a) HEV (Full electric), (b) HEV (electric + thermal).

1.3.3 Fuel Cell Electric Vehicle (FCEV)

Fuel Cell vehicles contain hydrogen tanks that feed the fuel cell which, in turn, power the electric motor. Based on the number of on board power sources, fuel cell vehicles are classified into Fuel Cell Electric Vehicle (FCEV) and Fuel Cell Hybrid Electric Vehicle (FCHEV). Figure 1.9 depicts the two last mentioned types of electric vehicles. Fuel cell electric vehicles are more efficient than conventional internal combustion engine vehicles and produce no tailpipe emissions. Instead, they only emit water vapor and warm air. The most common type of fuel cell type for vehicle applications is the polymer electrolyte membrane (PEM) fuel cell. In a PEM fuel cell, an electrolyte membrane is sandwiched between a positive electrode (cathode) and a negative electrode (anode). Hydrogen is introduced to the anode, and oxygen (from air) is introduced to the cathode. The hydrogen molecules break apart into protons and

electrons due to an electrochemical reaction in the fuel cell catalyst. Protons then travel through the membrane to the cathode. The electrons are forced to travel through an external circuit to perform work (providing power to the electric car) then recombine with the protons on the cathode side where the protons, electrons, and oxygen molecules combine to form water.

(a)   (b)
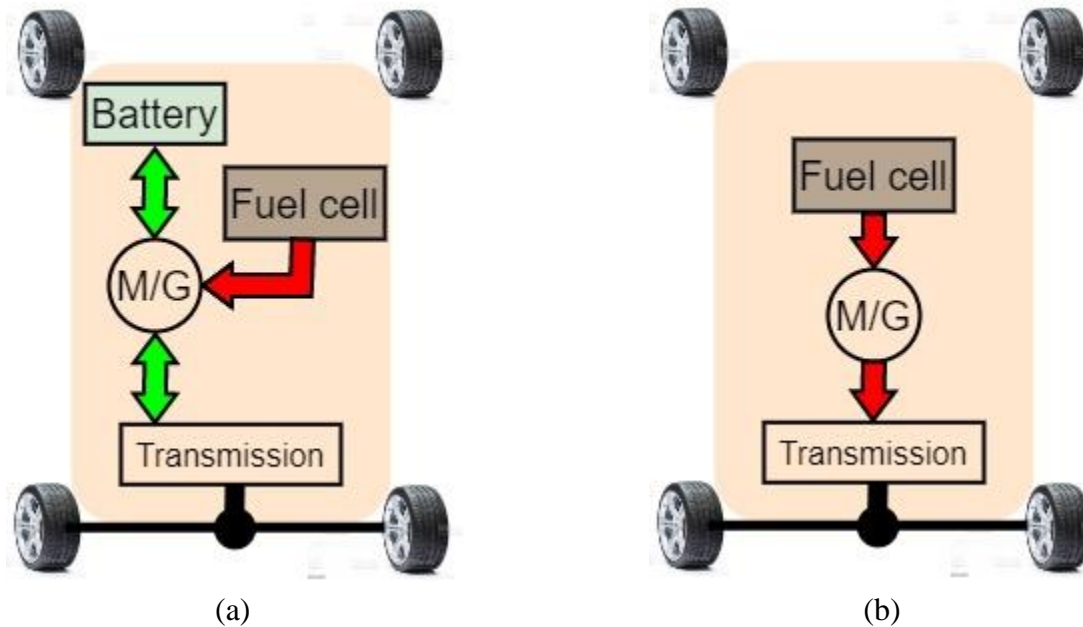
Figure 1.9 (a) Full cell hybrid electric vehicle, (b) Fuel cell electric vehicle.

To summarize, Table 1.1 shown below provides some useful information about each vehicle type.

Table 1.1 Characterestics of different electric vehicle types.

Electric vehicle Type	BEV	HEV	FCEV/ FCHEV
Propulsion	Electric machines	• Electric machines • Internal combustion engine	Electric machines
Energy sources	Battery	• Battery/Supercapacitors • Internal combustion engine	• Battery/Supercapacitors • Fuel cell
Characteristics	• Zero emission • Available on market • Independence to oil	• Very low emissions • Long autonomy • Dependence	• Zero emission • Independence to oil prices • Medium availability on markets
Major issues	Charging stations	• Management of multiple energy sources • Driving cycle dependence	• Fuel cell cost • Danger of electrical shock • Flammability of the fuel

1.4 Vehicle drivetrain architectures

Drivetrain architecture affects significantly vehicle performance [36-37]. vehicles drivetrain architectures are mainly divided into three distinct types as will be discussed below:

1.4.1 Series configuration

Figure 1.10 shows a FCHEV with series drivetrain structure. It is worth noticing that FCHEVs always have a series configuration. This makes it possible for them to operate either on fuel cell mode or it in a hybrid mode where the secondary power source (supercapacitor) assists the fuel cell. This happens usually during acceleration periods.
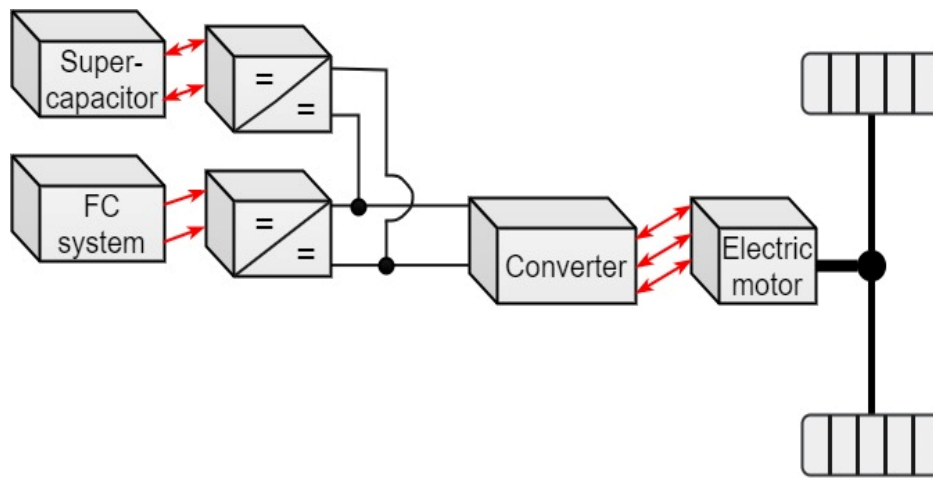
Figure 1.10 Series FCHEV.

Figure 1.11 depicts a hybrid electric vehicle with series drivetrain structure. In this architecture, the internal combustion engine (ICE) drives an electric generator which is generally associated with a three phase alternator and a rectifier. In addition to the possibility of operating under engine mode, the HEV of figure 1.11 can be powered using battery and engine in situations of high power demand. In addition to powering vehicle wheels, the generator can also charge the battery through its associated charger.
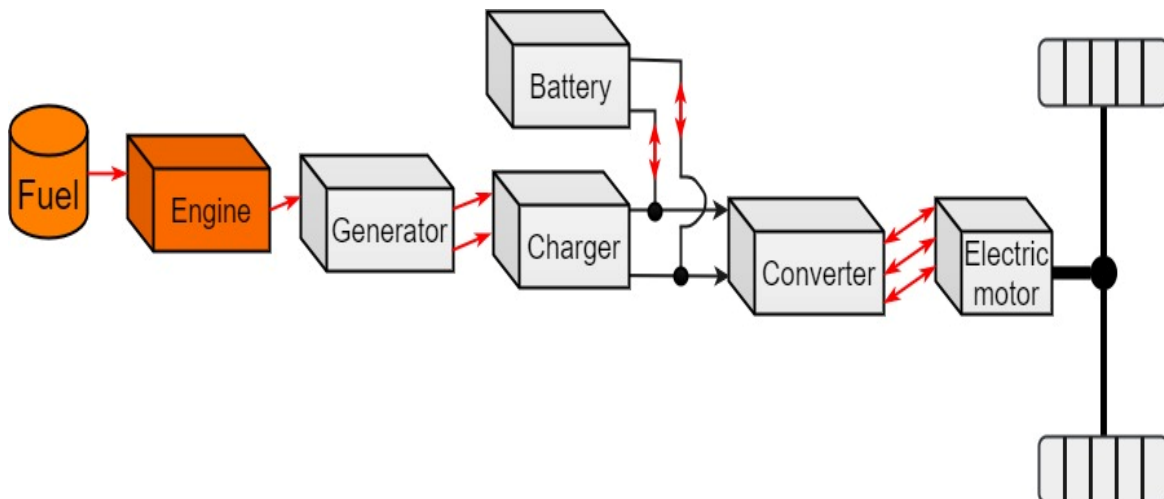
Figure 1.11 Series HEV.

1.4.2 Parallel configuration

In contrast to series configuration which has only one connection point to the mechanical transmission, parallel hybrid electric vehicles have all their power sources linked directly to a mechanical coupler which is -in turn- connected to wheels. In the case of the hybrid electric vehicle considered in figure 1.12, both the internal combustion engine and an electric motor are connected in parallel connected to the mechanical transmission. It is worth noticing that the battery will be recharged only during regenerative breaking and during situations where ICE power is higher than the required power for propulsion. However, the battery can not be charged when the vehicle is not moving and this could be seen as a drawback for some users.
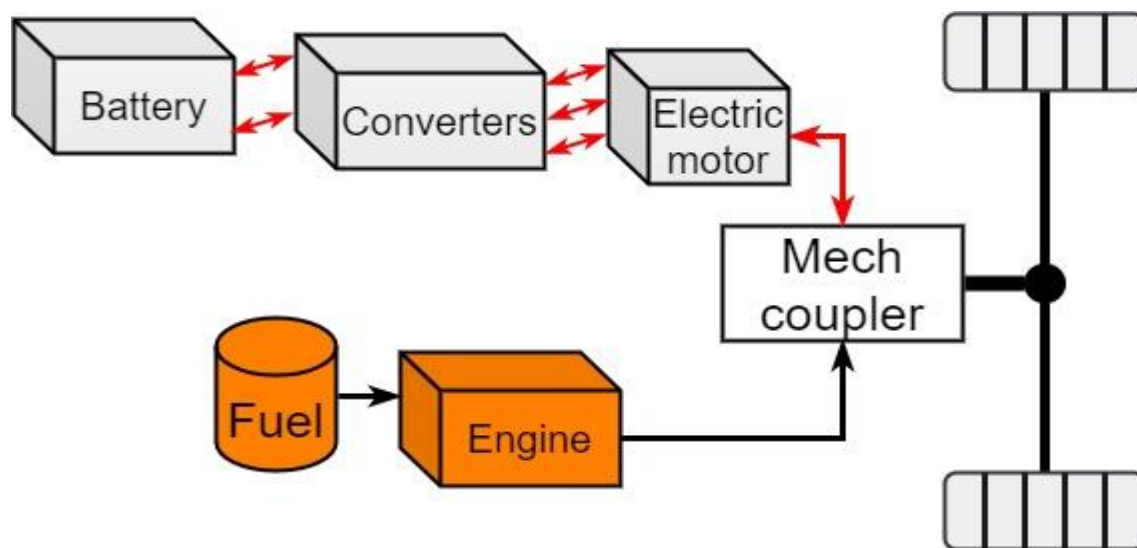
Figure 1.12 Parallel HEV.

1.4.3 Combined configuration

The structure of an electric vehicle with combined drivetrain structure is shown in figure 1.13. One can notice that the drive axle has two connections. The first one is an electric (electric motor side) and the second connection is of type mechanical (engine side). This configuration gathers the features of both series and parallel configurations. Since internal combustion engines (ICE) are not efficient at low speeds, the HEV of figure 1.13 is operated as a series HEV and power is delivered to vehicle wheels through the electric connection. At high speeds, the engine takes over vehicle propulsion as it is more efficient at high speeds. In addition to its high implementation cost, this combined driveline architecture is more complex compared to series and parallel configurations as it requires extra components such as: generator,

mechanical coupler and additional control units to manage the intervention of each power source.
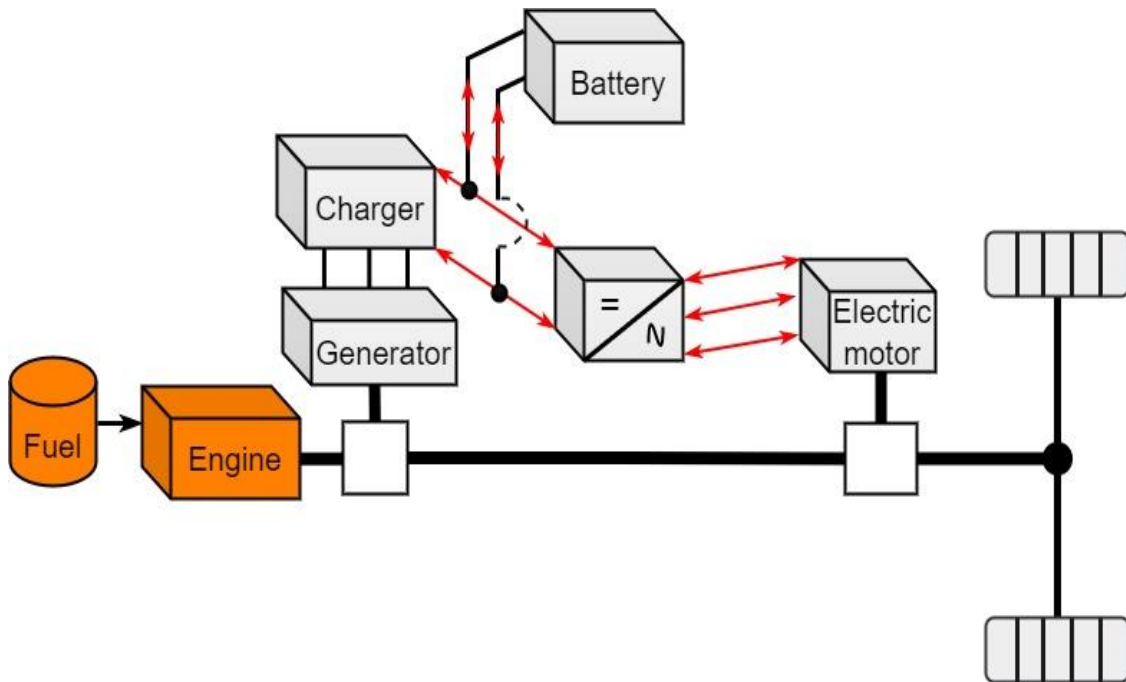
Figure 1.13 HEV with combined drivetrain architecture.

To summarize, Table 1.2 shown below discusses in details the advantages and drawbacks of each drivetrain architecture:

Table 1.2 Advantages and drawbacks of different HEV driveline architectures.

Driveline type	Advantages	Drawbacks
Series	• No mechanical link between engine and wheels. • Efficient during stop-and-go city driving.	• Excessive powertrain weight, cost and size • Multiple energy conversion stages
Parallel	• High engine efficiency during long distance driving. • Small motor size as it is only assisting traction.	• High voltages needed for good effeciency • Battery cannot be charged at standstill.
Combined	• Flexible switching between electric and ICE powers Decoupling of the power supplied by the engine from the power demanded by the driver	• Complex driveline • Very expensive

1.5 Vehicle traction machines

In the field of automotive engineering, driving comfort and high transient performance are two key factors that are achieved by the use of different types of motors and generators. In traction applications, motor type is determined by the different factors such as vehicle type (light, medium and heavy duty vehicles), drivetrain architecture (series, parallel and combined) and vehicle duty cycle. The significant advances made in the field of machine design and construction gave birth to several machine types that are used in different areas of transportation sector. Alternative current (AC) machines are classified according to their rotation method into synchronous and asynchronous machines as it is highlighted in figure 1.14. Some of these machines are discussed in the following subsections:
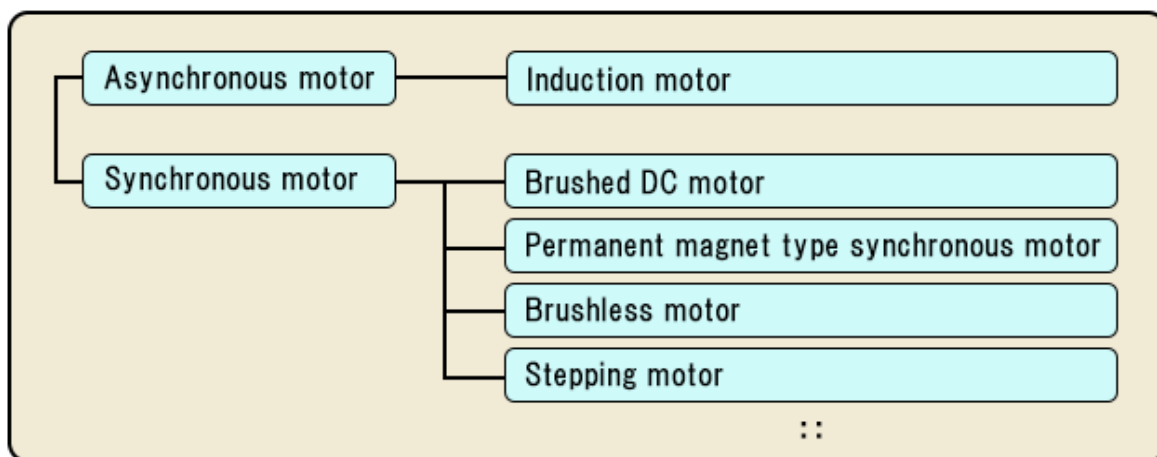
Figure 1.14 AC machine classification according to their rotation method.

1.5.1 Permanent magnet synchronous motor

Permanent magnet synchronous machines are used in a wide range of industrial applications starting from line- start pump to high performance machine tool servos, robotics, actuators and electric vehicles. PMSMs have imposed themselves as a serious concurrent to induction machines in the field of electric traction applications [38]. The advantages of using PMSMs include lesser heating, higher power density and higher efficiency along with high torque to mass ratio. Depending on how magnets are attached to the rotor and the design of the rotor, permanent magnet synchronous motor can be classified into two types: Surface permanent magnet synchronous motor (SPMSM) and Interior permanent magnet synchronous motor (IPMSM). SPMSM mounts all magnet pieces on the surface, and IPMSM places magnets inside the rotor. Also, depending on the stator design, a permanent magnet synchronous motor can be with distributed winding or with concentrated winding. Despite of the several advantages listed above, PMSMs still suffer from some problems such as: high initial cost and difficulties to start up because it is not a self-starting motor.

1.5.2 Brushless permanent magnet machines

Permanent magnet (PM) machines are divided into brushed and brushless machines. It is important to note that PM brushless machines are also divided according to several criteria such as operation mode (motor or generator), magnetic field direction (axial or radial field), rotor type (different rotor geometries). The motors can be further categorized as PM brushless DC motors (PMDC) characterised by trapezoidal back emf and PM synchronous motors (PMSM) characterised by sinusoidal back emf. Among all of these configurations of permanent magnet brushless motors, PMDC and PMSM are most popular form of PMBL motors used in various applications. These different classifications of PMBL machines are shown in Figure 1. The sinusoidal excited PMAC motor is commonly known as Permanent Magnet Synchronous Motor (PMSM). It is further subdivided into three categories based on type of rotor magnets and their excitation. The surface mounted rotor magnet PMSM is known as SPMSM, whereas interior mounted rotor magnet PMSM is known as IPMSM and inherently has additional saliency torque, suitable for some high torque requirement application. The third categories of hybrid excited PMSM has hybrid of PM and electrical excitation. In this category, provision for additional electrical excitation of rotor, results in tailor made magnetization profile of PMSM.

1.6 Electrified vehicles: challenges and expectations

Electric vehicles powered by renewable energy sources are a potential candidates that can contribute significantly in decarbonizing the transport sector and reduce the greenhouse gas emissions. However, the important growth noticed in the field of automotive engineering will result in extra energy demand. According to [39], Europe's total electricity consumption by electric vehicles is expected to rise from 0.03 % in 2014 to 9.5 % in 2050 due to increased rates of electric vehicle ownership. Figure 1.15 depicts the expected energy demand for electric vehicles as a percentage of total electricity demand. From the last mentioned figure, in case of Luxembourg, energy demand for electric vehicles is expected to be almost one third of total energy production by 2050. The energy gap which will be created by the integration of a tremendous amount of vehicles will require additional grid infrastructure. This fact gives rise to many critical questions such as: How much electricity is needed? What type of generation is used to cover this additional energy demand? How to manage the charging peaks?. The intensity of electric vehicle charging could put local grid infrastructures under substantial stress and lead to severe technical problems in network operations. Hence, the integration of electrified vehicles to the grid will come at a cost and will require additional investment such

as fast charging stations, battery swapping stations, domestic or public individual charging points for slower charging.
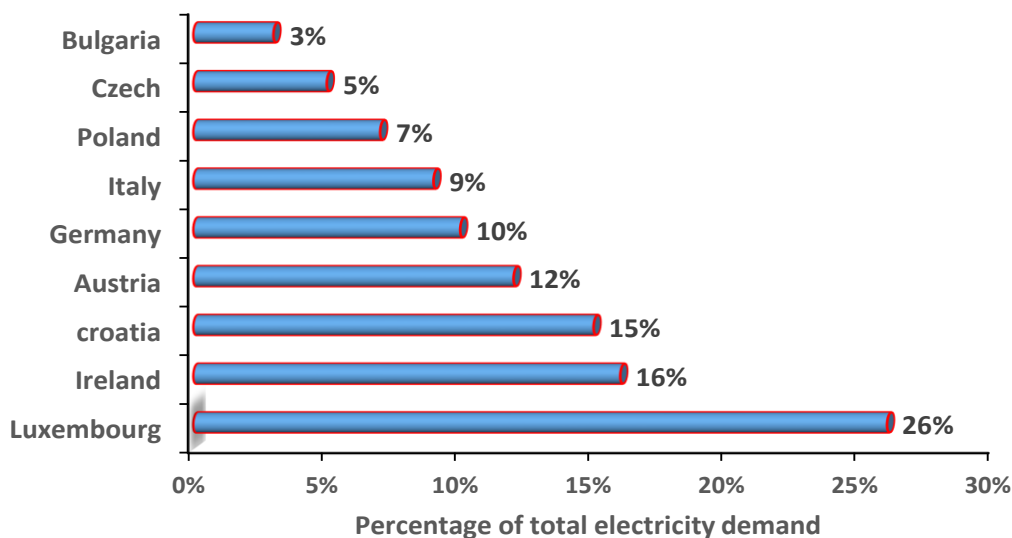
Figure 1.15 Electric vehicle energy demand as a percentage of total electricity demand in 2050 [39]

In addition to the aforementioned barriers that prevent the large-scale commercialization of electrified vehicles, there exist other challenges that still need to be faced. It is worth noticing that electrified vehicles are embedded systems that contain complex and advanced technologies which make their maintenance a complex task to be performed. Also, this type of vehicles is relatively silent in comparison to conventional vehicles and this may be dangerous especially for passengers. It is true that the autonomy of electrified vehicles is increased year after year, but it is still not sufficient for unpredicted trips as the number of charging stations is still also low and their location is not well studied.

1.7 Conclusion

In this chapter a detailed state of art concerning electrified vehicles is presented. Several cutting edge topics related to electrified vehicles are discussed. First, a detailed history that explains the advances made in the field of electrified transportation over year is presented. After that, the different driveline configuration of electrified vehicles existing on the market are pointed out and explained. Some traction machines used in vehicle traction along with their characteristics are discussed in this chapter which is concluded by a set of challenges and expectations.

Chapter 2

Intelligent electric vehicle control

2.1 Introduction

Different driving cycles are applied to electrical vehicles in order to predict the behavior and performance of electric drive systems. Some of these driving cycles are theoretically derived, as is preferred in the European Union, while others are derived from direct measurements. More information on driving cycles can be found in [40]. A driving cycle is a set of data that represents the speed of a HEV over time. The data gathered reflects the driver's behavior in various driving situations (e.g., city, highway). These cycles are used to assess various HEV performance characteristics such as battery life, fuel consumption reduction, and HEV roadside performance. The classifications of driving cycles found in the literature are summarized in Table 2.1.

Table 2.1 Different driving cycle classifications.

Criteria	Type	Characteristics
Dynamics	Transient driving cycles	Random, aggressive accelerations
	Modal driving cycles	Long periods at constant speeds.
Distance	Short	0 mile < distance ≤ 9 mile
	Medium	9 mile < distance ≤ 20 mile
	Long	20 mile < distance≤ inf
Region	Urban	0 < speed ≤ 25 mph
	Mixed	25 mph < speed ≤ 45 mph
	Highway	45 mph < speed < inf

Metaheuristic algorithms are extensively used in various areas of industrial engineering applications. In this chapter, intelligent optimization algorithms (particle swarm optimization and genetic algorithm) are used to optimize the parameters of electric vehicle controllers. This is accomplished through the use of a proposed control scheme that takes into account the real load driving conditions to which the electric vehicle is subjected. It is worth noticing that the electric vehicle is driven using a permanent magnet synchronous machine that is controlled using field oriented control. The effectiveness of the integration of metaheuristic algorithms in the control of electric vehicles is confirmed by the various robustness test performed as it will be detailed throughout this chapter.

2.2 Vehicle dynamics

When a vehicle is undergoing a given driving cycle it is subjected to some external forces which tend to attenuate or to amplify its speed [41-42]. The motion of the vehicle shown in figure 2.1 is governed by the following equation:

$$\sum \vec{F}_{ext} = m\vec{a} \tag{2.1}$$
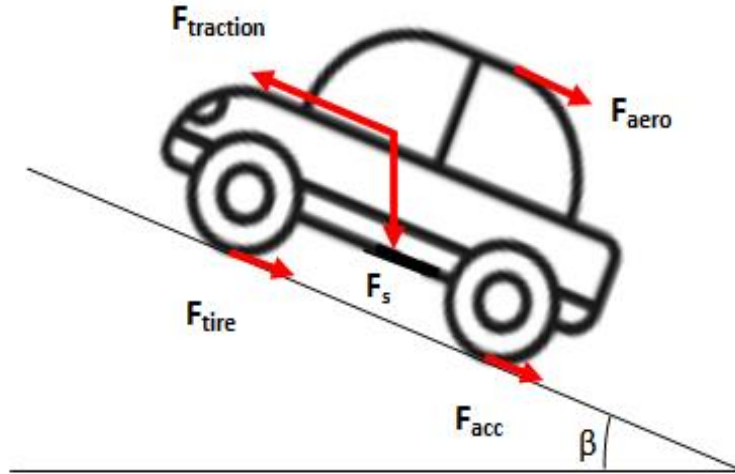
Figure 2.1 Forces exerted on the vehicle.

$\vec{F}_{ext}$ is the net external force acting on the vehicle body, m is the vehicle mass and $\vec{a}$ is the vehicle acceleration. Equation (2.1) can be rewritten as:

$$\vec{F}_{traction} - \vec{F}_r = m\,\vec{a} \tag{2.2}$$

$\vec{F}_r$ is the net resistive force which is defined as follow:

$$\vec{F}_r = \vec{F}_{aero} + \vec{F}_{slope} + \vec{F}_{rolling} \tag{2.3}$$

$\vec{F}_{aero}$ is the aerodynamic force, $\vec{F}_{slope}$ is the force due to road slope and $\vec{F}_{rolling}$ is the force due to friction between vehicle tires and ground surface.

2.2.1 Aerodynamic force

The resistance offered by the air in the atmosphere while vehicle travelling through it is known as aerodynamic drag. This force is modeled by the following mathematical expression:

$$F_{aero} = 0.5\rho A C_d (V_{wheel} + V_{wind})^2 \tag{2.4}$$

ρ is the air density *(kg/m³)*. A is the vehicle frontal area *(m²)*, C_d is the aerodynamic drag coefficient *(s²/m²)*, V_{wheel} is the vehicle longitudinal speed (*m/s*) and V_{wind} is the wind speed *(m/s)*.

2.2.2 Slope force

This force is due to road inclination and it is proportional to the mass of the vehicle. It is given by equation (2.5) where g is the gravity acceleration (m/s^2) and β is the road inclination angle (radians).

$$F_{slope} = mg\,sin(\beta) \tag{2.5}$$

2.2.3 Rolling force

This force is due to the friction between vehicle's tires and the ground surface. It depends on several parameters like: pressure, tire deflection, ground surface which may be hard or soft and vehicle speed. The rolling resistance force is given by the following expression:

$$F_{rolling} = mgf_r\,cos(\beta) \tag{2.6}$$

f_r is the rolling resistance coefficient. Typical values of the rolling resistance coefficient are provided in Table 2.2.

<p align="center">**Table 2.2** Rolling resistance values for different road types</p>

Road type	Rolling coefficient
Tarmac	0.025
Concrete	0.011
rolled gravel	0.02
Unpaved	0.05
loose sand	1.5e-4

In fact, the values provided in Table 1 do not consider the variations of f_r with respect to speed. In this work the rolling resistance is related to vehicle velocity with the following linear equation that predicts the values of the rolling resistance constant with acceptable accuracy for speeds up to 128 km/h [43].

$$f_r = 0.01\left(1 + \frac{V_{wheel}}{160}\right) \tag{2.7}$$

2.2.4 Acceleration force

It is the necessary force to accelerate from zero to maximum speed. It is given by the following equation:

$$F_{acceleration} = m\frac{(V_{wheel})_{max}}{gt_a} \tag{2.8}$$

V_{wheel} is the maximum vehicle speed (m/s), g is the gravity acceleration and t_a is the time characteristic of the vehicle(s). The HEV shown in figure 2.1 will maintain its actual position or move forward only if it develops a torque that is respectively equal or greater than the load

torque applied on it. To overcome the resistive torque applied on it, HEV wheels have to develop a minimum torque given by equation (2.9) where r is the wheel radius and G is the gear ratio.

$$T_w = \left(\frac{r}{G}\right) F_r \tag{2.9}$$

Generally, the electric motor is always connected to the drive wheels through a simple gear with a fixed ratio as shown in figure 2.2 [44]. The electromagnetic torque generated by the traction machine is transmitted through a gear box to HEV wheels which will develop a propulsion torque to move the vehicle.
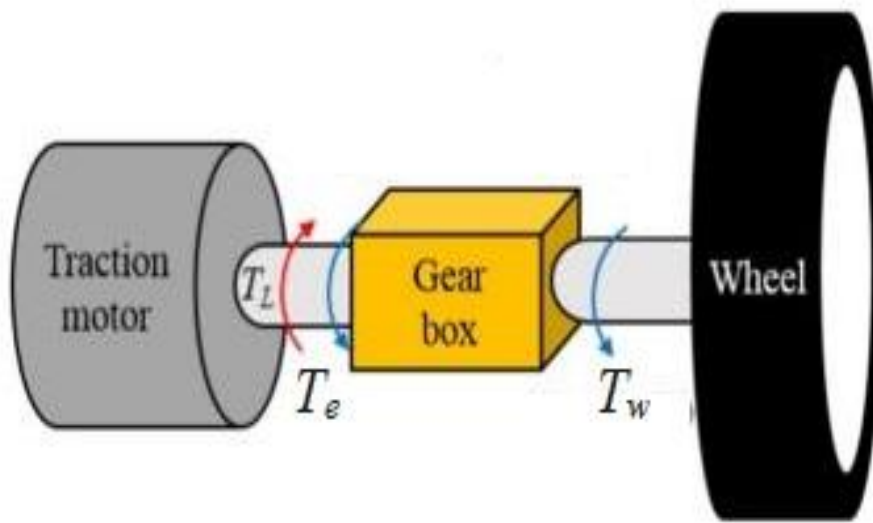
Figure 2.2 Traction motor transmitting torque to HEV wheels.

Relation between the torque generated by the traction machine and the one transmitted to HEV wheels is given by equation (2.10) in which η is the driveline effeciency and G is the total gear ratio which is defined as a ratio between the number of input teeth Z_{in} and the number of output teeth Z_{out} as illustrated by equation (2.11) shown below:

$$T_w = \eta G T_e \tag{2.10}$$

$$G = \frac{Z_{in}}{Z_{out}} \tag{2.11}$$

Relation between motor angular speed and wheel angular speed is described by equation (2.12) shown below:

$$\Omega_w = \left(\frac{1}{\eta G}\right) \Omega_m \tag{2.12}$$

2.3 PMSM modeling

Electric machines ensuring HEV traction must have high efficiency, high starting and rated torque, a wide speed range, a high overload capacity, a high power at cruising speeds, a high constant power speed range, a high specific power and power density, a fast dynamic response, a good flux weakening capability at high speeds, a high reliability, important torque to mass ratio and a high fault tolerance [45-46]. The electric machine that meets the aforementioned requirements must be of course at an acceptable cost. Table 2.1 provides useful information about traction machines used in some recently developed HEVs. Putting these data side by side, it is difficult to comment in any meaningful way the choice made about traction machine type without knowing further vehicle details such as HEV driveline system architecture. It could be noticed from Table 2.3 that most HEV constructors have migrated from the use of induction machines (IM) to permanent magnet (PM) machines. This is mainly because PMs present higher efficiency and have an important torque to mass ratio which contributes to space and weight optimization.

Table 2.3 Traction machines used in different electric vehicles [47]

Model	Motor type	Max torque (N.m)	Max speed (RPM)	Poles
Roadster	IM	370	14000	4
Tesla S60	IM	430	14800	4
Model 3	PM	410	18000	6
Prius	PM	400	6000	8
Prius	PM	207	13500	8
Prius	PM	163	17000	8
Accord	PM	136	6000	16
Accord	PM	-	14000	8
Spark	PM	540	4500	12
Volt	PM	370	12000	12
Bolt	PM	360	8810	8
Leaf	PM	280	10390	8
Leaf	PM	280	10390	8
Camry	PM	270	14000	8
Camry	PM	270	14000	8
Lexus	PM	300	10230	8
Sonata	PM	205	6000	16
BMW i3	PM	250	11400	12

The flowchart presented in figure 2.3 present a general classification of permanent magnet synchronous machines. It can be seen that depending on how magnets are attached to the rotor, permanent magnet synchronous machines are classified into interior or surface mounted permanent magnet synchronous machines.
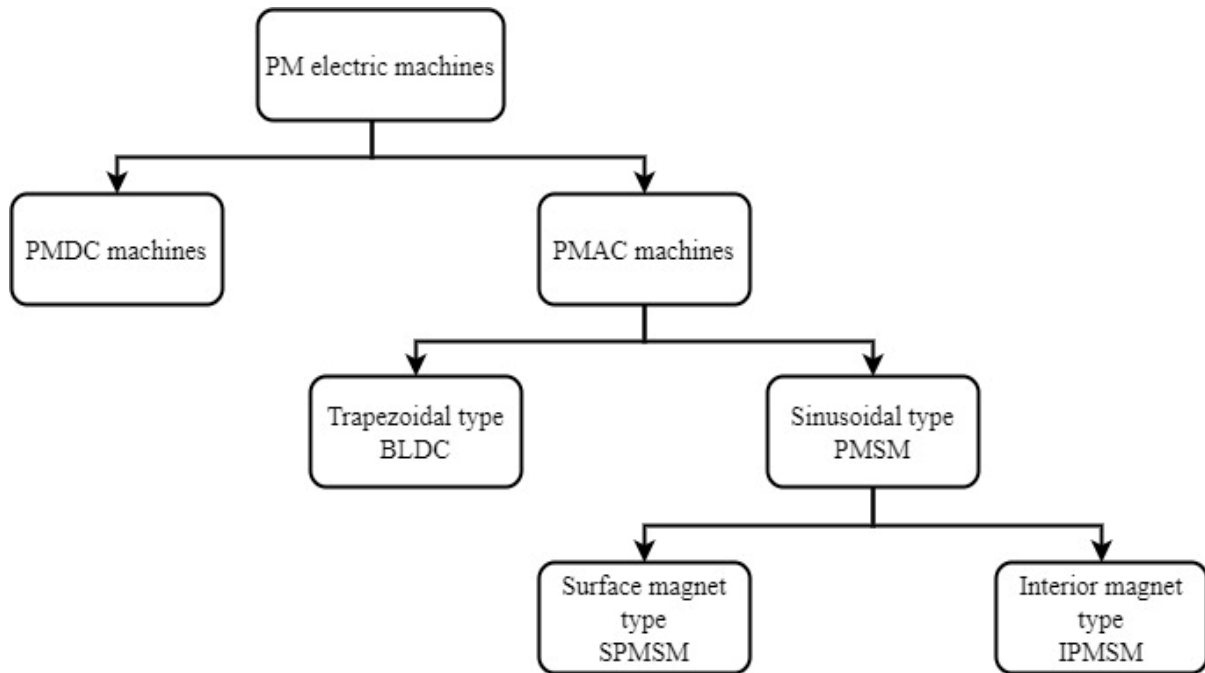
Figure 2.3 Permanent magnet synchronous classification.

The magnetic field of the stator is created by sinusoidal currents flowing through stator windings. At rotor level, the presence of magnets gives rise to a fixed magnetic field that seeks to align with the stator field. This causes the rotor to and stator to rotate at the same synchronous speed. Figure 2.4 shows the PMSM representation in three phase reference frame.
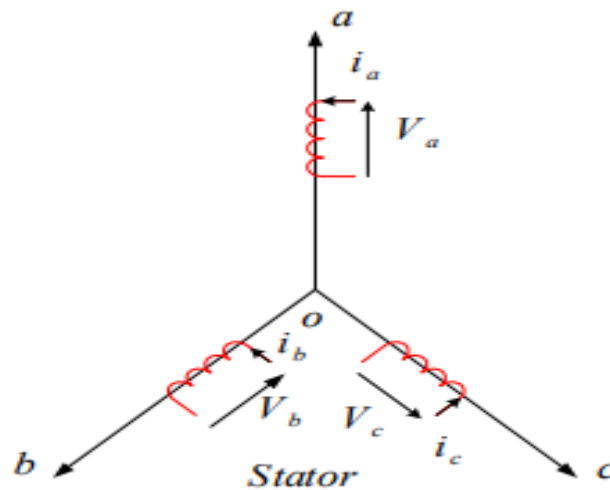
Figure 2.4 Permanent magnet synchronous in *abc* frame.

The voltage across each stator winding is given using equation (2.13) where $[V_s]_{3\times3}$ and $[R_s]_{3\times3}$ are, respectively, the voltage and resistance matrices of the stator. $[\lambda_s]_{3\times1}$ and $[I_s]_{3\times1}$ represent, accordingly, stator flux linkage and stator current column vectors.

$$[V_s] = [R_s][I_s] + \frac{d}{dt}[\lambda_s] \tag{2.13}$$

Flux linkage on each stator winding is expressed as indicated in equation (2.14):

$$\begin{bmatrix} \lambda_{sa} \\ \lambda_{sb} \\ \lambda_{sc} \end{bmatrix} = \begin{bmatrix} L_{aa} & M_{ab} & M_{ac} \\ M_{ba} & L_{bb} & M_{bc} \\ M_{ca} & M_{cb} & L_{cc} \end{bmatrix} \begin{bmatrix} I_a \\ I_b \\ I_c \end{bmatrix} + \begin{bmatrix} \Phi_{fa} \\ \Phi_{fb} \\ \Phi_{fc} \end{bmatrix} \tag{2.14}$$

L_{aa}, L_{bb} and L_{cc} are PMSM self inductances. M_{ab}, M_{ba}, M_{ac}, M_{ca}, M_{bc} and M_{cb} represent PMSM mutual inductances between different PMSM phases. In this work, since a silent pole machine is used, all the self inductances are set equal to L_s. Also all mutual inductances are equal and set to M. Taking into account the two previous informations, equation (2.12) can be rewritten as it is pointed out in equation (2.15) shown below:

$$\begin{bmatrix} V_a \\ V_b \\ V_c \end{bmatrix} = \begin{bmatrix} R_s & 0 & 0 \\ 0 & R_s & 0 \\ 0 & 0 & R_s \end{bmatrix} \begin{bmatrix} I_a \\ I_b \\ I_c \end{bmatrix} + \frac{d}{dt} \left\{ \begin{bmatrix} L_s & M & M \\ M & L_s & M \\ M & M & L_s \end{bmatrix} \begin{bmatrix} I_a \\ I_b \\ I_c \end{bmatrix} + \begin{bmatrix} \Phi_{fa} \\ \Phi_{fb} \\ \Phi_{fc} \end{bmatrix} \right\} \tag{2.15}$$

By defining PMSM cyclic inductance highlighted by equation (2.16), equation (2.15) can be rewritten as indicated in equation (2.17).

$$L_{sc} = L_s - M \tag{2.16}$$

$$\begin{bmatrix} V_a \\ V_b \\ V_c \end{bmatrix} = \begin{bmatrix} R_s & 0 & 0 \\ 0 & R_s & 0 \\ 0 & 0 & R_s \end{bmatrix} \begin{bmatrix} I_a \\ I_b \\ I_c \end{bmatrix} + \frac{d}{dt} \left\{ \begin{bmatrix} L_{sc} & 0 & 0 \\ 0 & L_{sc} & 0 \\ 0 & 0 & L_{sc} \end{bmatrix} \begin{bmatrix} I_a \\ I_b \\ I_c \end{bmatrix} + \begin{bmatrix} \Phi_{fa} \\ \Phi_{fb} \\ \Phi_{fc} \end{bmatrix} \right\} \tag{2.17}$$

In this work the modeling, control and analysis of PMSM is performed in the dq synchronous rotating frame as the one shown in figure 2.5. The fundamental reason to transform the three-phase instantaneous voltages and currents into the synchronously rotating reference frame is to make computations much easier. Furthermore, it allows the system operator to independently control the active (d-axis) and reactive (q-axis) components of the currents.
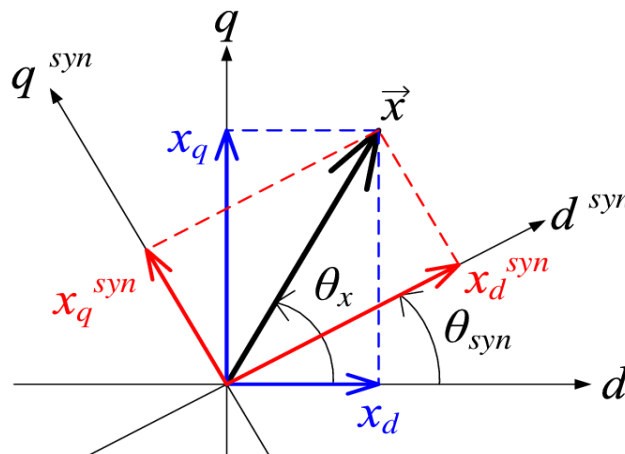
Figure 2.5 abc to dq axis transformation.

Stator voltage is expressed by the following set of equations:

$$\begin{cases} V_d = r_s i_d + \dfrac{d\lambda_d}{dt} + w_e \lambda_q \\ V_q = r_s i_q + \dfrac{d\lambda_q}{dt} - w_e \lambda_d \end{cases} \tag{2.18}$$

Stator flux in both direct and quadrature axes is expressed by equation (2.19) shown below:

$$\begin{cases} \lambda_d = L_d i_d + \varphi \\ \lambda_q = L_q i_q \end{cases} \tag{2.19}$$

Where r_s is the stator resistance, i_d is the d-axis stator current, i_q is the q-axis stator current, λ_d is the d-axis flux linkage, λ_q is the q-axis stator flux linkage. L_d is the d-axis inductance, L_q is the q-axis inductance, φ is the flux linkage due permanent magnets. w_e is the electrical speed and w_r is the motor mechanical speed. For a machine with p pair of poles, electrical and mechanical speed are related by the following mathematical formula:

$$w_e = p w_r \tag{2.20}$$

Substitution by equation (2.19) and (2.20) in equation (2.21) yield the set of equations shown below:

$$\begin{cases} \dfrac{di_d}{dt} = -\dfrac{r_s}{L_d} i_d + p w_r i_q + \dfrac{V_d}{L_d} \\ \dfrac{di_q}{dt} = -\dfrac{r_s}{L_q} i_q - p w_r i_d - \dfrac{p w_r \varphi}{L_q} + \dfrac{V_q}{L_q} \end{cases} \tag{2.21}$$

Converting the two last equations to Laplace domain yields:

$$\begin{cases} V_d = (r_s + Ls)i_d - L w_e i_q \\ V_q = (r_s + Ls)i_q + w_e(L i_d + \varphi) \end{cases} \tag{2.22}$$

The electromagnetic torque developed by the PMSM is given by the following expression:

$$T_e = \left(\dfrac{3p}{2}\right)\left(\lambda_d i_q - \lambda_q i_d\right) \tag{2.23}$$

It is worth noticing that rotor's rotation produces a mechanical torque given by the following equation where T_e represents the electromagnetic torque and T_r is the mechanical load torque.

$$T_e - T_r = J\dfrac{dw_r}{dt} + B w_r \tag{2.24}$$

Equation (2.23) can be expressed in Laplace domain as follow where J is the inertia of the rotor ($Kg.m^2$) and B is the mechanical damping coefficient. The parameters of the PMSM motor used in this work are shown in Table 2.4:

$$w_r = \dfrac{T_e - T_r}{(Js + B)} \tag{2.25}$$

Table 2.4 HEV and environment parameters

Parameter	Value
P	35 kW
Tn	111 N.m
rs	0.05 Ohm
L	6.35 e-4 mH
Φ	0.192 Wb
J	0.011 kg.m^2
B	0.002 N.m.s
P	4

2.4 Field oriented controlled PMSM

AC machine control is a difficult task due to several reasons like the nonlinearity of the machine model and the strong coupling and interaction that exists between stator and rotor fields [48]. The idea behind field oriented control is to always keep the stator field perpendicular to the rotating rotor field as it is shown in the figure 2.6.
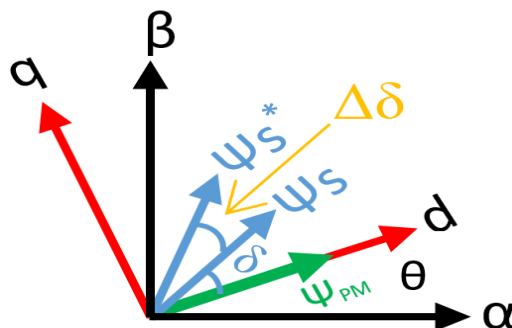
Figure 2.6 Stator and rotor field orientations in dq axis.

Nowadays, several control techniques are used for the control of PMSM such as direct torque control [49-50] and field oriented control [51]. This last control technique is used for obtaining large instantaneous speed regulation without developing current and torque ripples for low speeds as it is the case in DTC. Figure 2.7 shows a general scheme of field oriented control technique applied to a PMSM driving an HEV. A current feedback loop is formed by sensing then transforming the stator phase currents to a coordinate system rotating with the rotor of the machine. Vehicle speed is also measured then compared with its reference forming a speed loop. This speed error is fed into a PID controller which generates the reference torque.
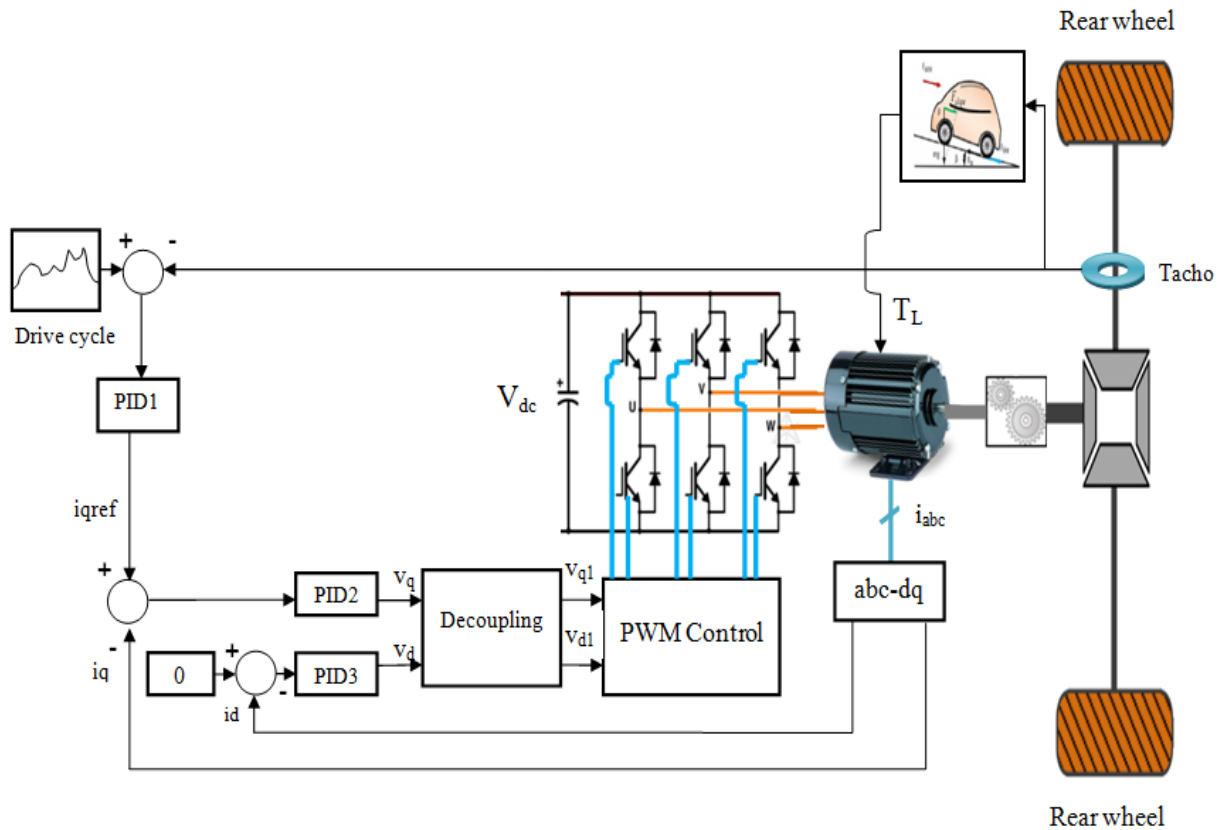
Figure 2.7 Electric vehicle field oriented controlled scheme.

Setting the d-axis current to zero in equation 2.23 maximizes the electromagnetic torque of the PMSM and provides the following linear relationship between stator current and motor torque:

$$T_e = \left(\frac{3p}{2}\right)(\lambda_d i_q) \tag{2.26}$$

From equation (2.26), one can see that the control of vehicle torque comes back to the control of the q-axis component of the stator current. The inputs to the decoupling block shown in figure 2.7 are given by equation (2.27) where a strong coupling between direct and quadrature axes can be noticed. Decoupling by compensation procedure is performed via the use of equation (2.27) shown below:

$$\begin{cases} V_d = V_{d1} - Lw_e i_q \\ V_q = V_{q1} + w_e(Li_d + \varphi) \end{cases} \tag{2.27}$$

Equating equation (2.22) and equation (2.27) yields the following set of equations:

$$\begin{cases} i_d = \dfrac{V_{d1}}{(r_s + Ls)} \\ i_q = \dfrac{V_{q1}}{(r_s + Ls)} \end{cases} \tag{2.28}$$

Setting i_d to zero for torque maximization yields a decoupling that enables us to analyze, separately, the performance of the PMSM driving the HEV on the quadrature axis. Based on the previously derived equations, a control system model of an HEV driven by PMSM is derived and it is shown in figure 2.8. The outer loop of the control system shown below controls the speed of the electric vehicle, whereas the inner loop highlighted with red dashed lines is used to control PMSM currents. Out of figure 2.8, one can notice that dynamics of the inverter, PMSM and the tachometer are all described using first order transfer functions. Each of these aforementioned elements is discussed in details as it will be shown below:
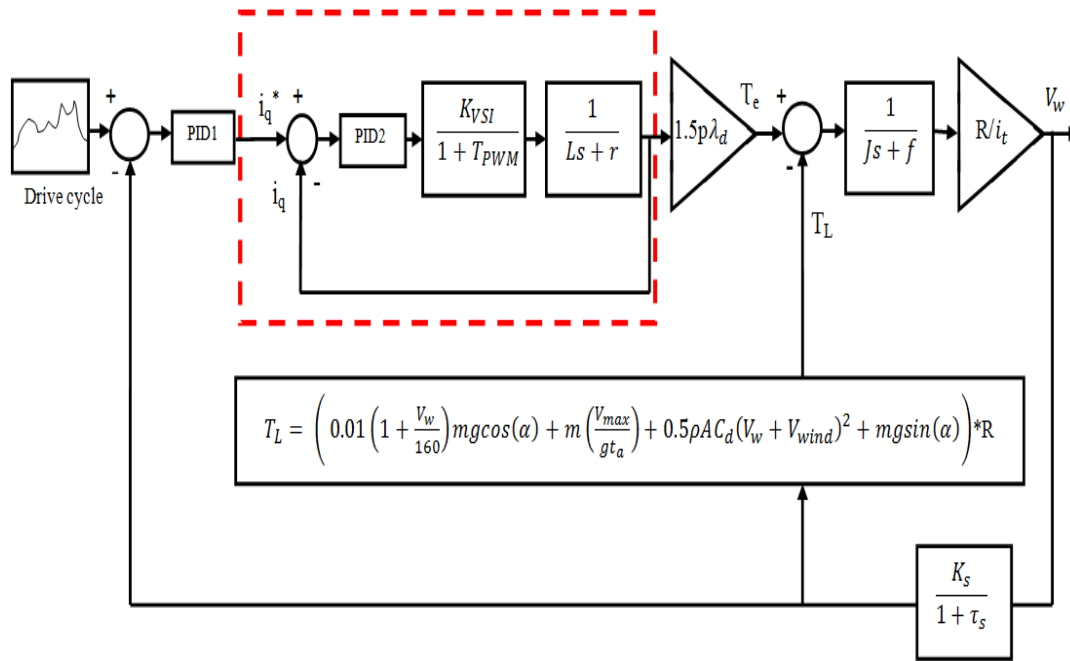
Figure 2.8 Decoupled control scheme of the electric vehicle driven by PMSM.

2.4.1 Inverter model

The output of the decoupling block is supplied to a the three-phase SPWM inverter whose transfer function is given as follow:

$$T_{vsi}(s) = \frac{K_{vsi}}{1 + T_{pwm}} \tag{2.29}$$

Where K_{VSI} is the inverter gain which is given by:

$$K_{vsi} = \frac{V_{dc}}{2V_t} \tag{2.30}$$

Where V_{DC} is the DC voltage input to the inverter and V_T is amplitude of the triangular modulation signal. The inverter time constant is given by the following equation where f_m is the frequency of the triangular modulation signal

$$T_{pwm} = \frac{1}{2f_m} \tag{2.31}$$

2.4.2 PID controller model

PID controllers are used to provide an output which is as close as possible to the input reference value with minimum overshoot for a given input. The transfer function of the PID controller shown in Figure 2.9 which is used in the outer loop for speed and current regulation is given by the following equation:

$$T_{pid}(s) = K_p + \frac{K_i}{s} + K_D s \qquad (2.32)$$
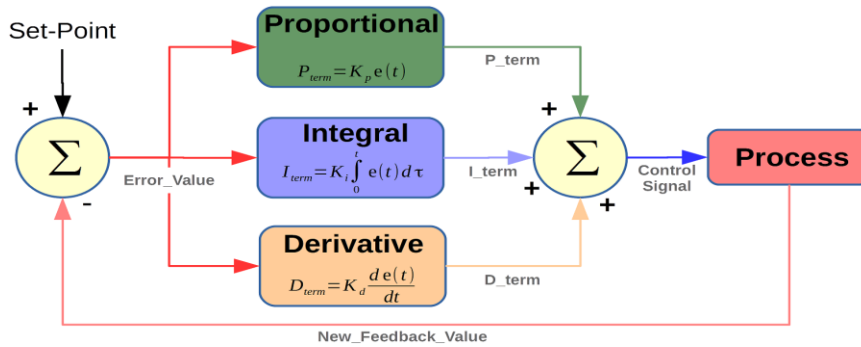
Figure 2.9 PID control scheme.

2.4.3 Sensor model

A tachometer is used as a tool to sense wheel's speed. This device can be represented by a simple first order transfer function with a static gain K_s and time constant T_s as it is given in equation (2.33):

$$T_{vsi}(s) = \frac{K_s}{1 + \tau_s} \qquad (2.33)$$

The parameters of the previously defined models are as follow: $K_S = 1$, $\tau_s = 0.02$, $K_{VSI} = 1$ and $T_{PWM} = 1$.

2.5 Direct torque control

DTC is a vector control method which was first proposed by Takahashi and M. Depenbrock [52] in 1980s. The principle of operation of this control strategy is the selection of suitable voltage vectors from the switching table based on the output of torque and flux hysteresis controllers which will keep the input error within a tolerated error band. Figure 2.10 points out direct torque control technique applied to an electric vehicle driven by a PMSM.

The stator flux is estimated using the following equation:

$$\varphi_s(t) = \varphi_{PM} + \int_0^t (V_s(t) - R_s i_s(t)) dt \qquad (2.34)$$

R_s is the stator resistance and V_s is the stator voltage which is expressed in $\alpha\beta$ frame as follow:

$$V_s = V_{s\alpha} + jV_{s\beta} \qquad (2.35)$$
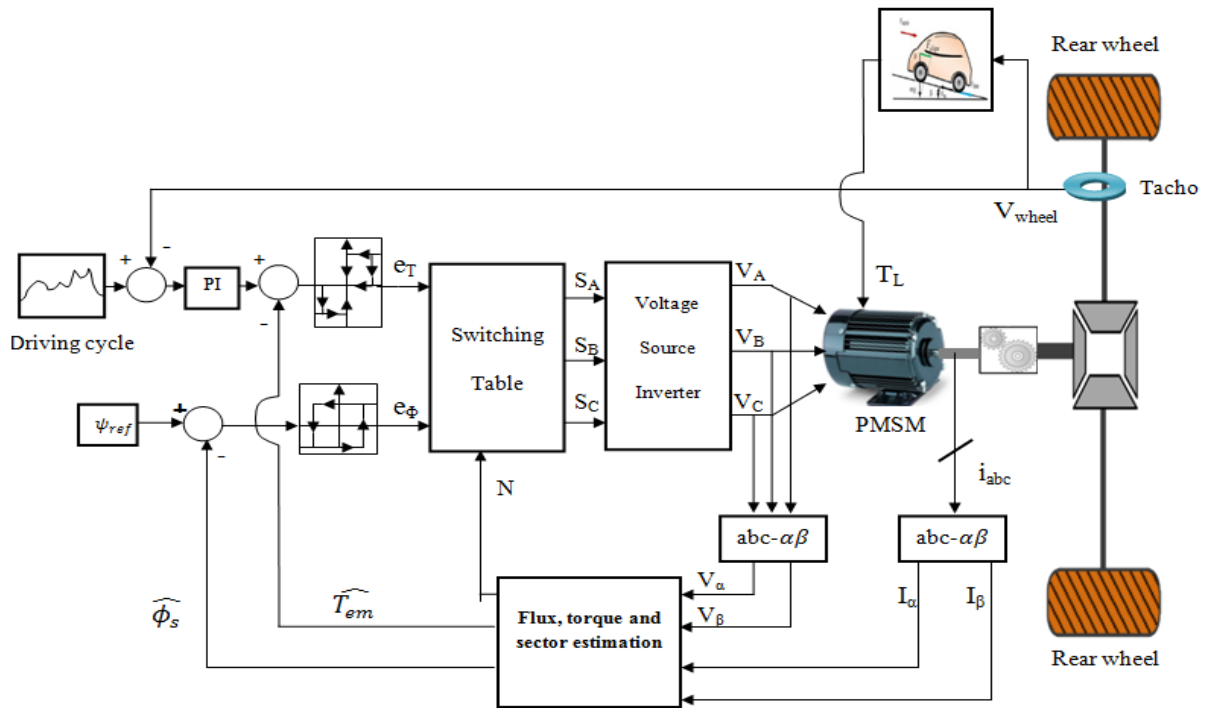
Figure 2.10 DTC scheme for an electric vehicle.

The integration of difference between stator voltage and the voltage drop across the stator resistance in $\alpha\beta$ frame yields equation (2.36):

$$\begin{cases} \varphi_{s\alpha}(t) = \varphi_{PM} + \int_0^t (V_{s\alpha}(t) - R_s i_{s\alpha}(t))dt \\ \varphi_{s\beta}(t) = \int_0^t (V_{s\beta}(t) - R_s i_{s\beta}(t))dt \end{cases} \tag{2.36}$$

Where ϕ_{PM} is the permanent magnet flux. The estimated stator flux and angle are given by equation (2.37) and equation (2.38) respectively.

$$\hat{\varphi}_s = \sqrt{\varphi_{s\alpha}^2 + \varphi_{s\beta}^2} \tag{2.37}$$

$$\hat{\theta}_s = tan^{-1}\left(\frac{\varphi_{s\beta}}{\varphi_{s\alpha}}\right) \tag{2.38}$$

A two level and three level hysteresis controllers are used for flux and torque control respectively. After comparing the stator reference flux to its estimated value, the hysteresis flux controller will output 1 if the input flux error is greater than the upper hysteresis limit ε_U and will output 0 if the flux error less than the lower hysteresis limit ε_L. The hysteresis torque controller will output -1 if the estimated torque is greater than the reference value, the output is 1 for torque values below the reference torque and 0 for estimated torque values laying between the lower and the upper torque hysteresis bands
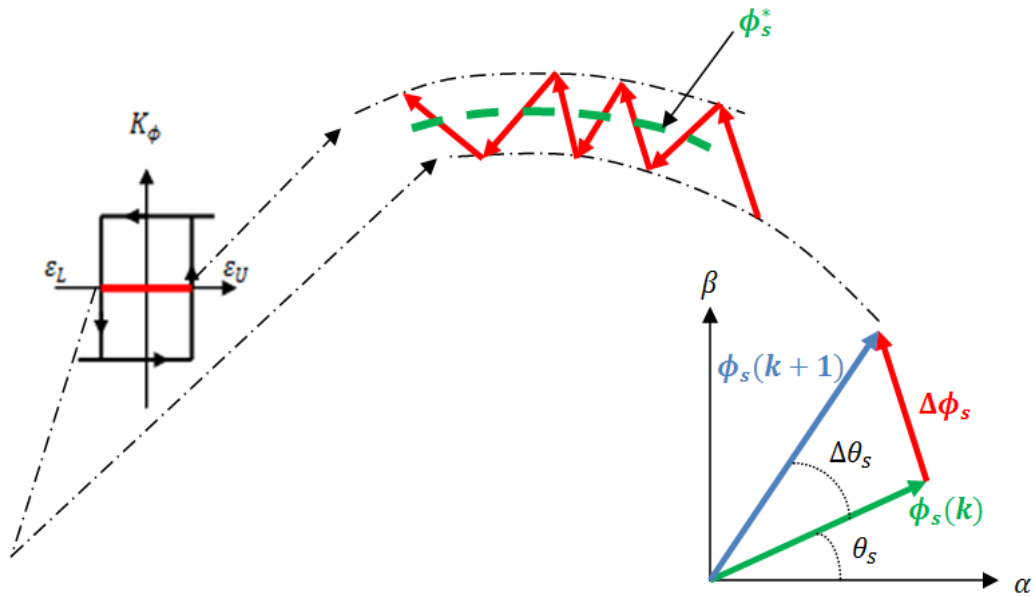
Figure 2.11 Stator flux vector evolution in the αβ subspace.

Based on H_T, H_Φ and N, the commutation table will output three control signals S_a, S_b and S_c that will control the opening and the closing of inverter IGBTs as it is highlighted in figure 2.10. The commutation table depicted in table 2.5 points out the appropriate voltage vector to be applied at each sector.

Table2.5 Direct torque control commutation table.

H_Φ	H_T	S_1	S_2	S_3	S_4	S_5	S_6
	1	$V_2(110)$	$V_3(010)$	$V_4(011)$	$V_5(001)$	$V_6(101)$	$V_1(100)$
1	0	$V_7(111)$	$V_0(000)$	$V_7(111)$	$V_0(000)$	$V_7(111)$	$V_0(000)$
	-1	$V_6(101)$	$V_1(100)$	$V_2(110)$	$V_3(010)$	$V_4(011)$	$V_5(001)$
	1	$V_3(010)$	$V_4(011)$	$V_5(001)$	$V_6(101)$	$V_1(100)$	$V_2(110)$
0	0	$V_0(000)$	$V_7(111)$	$V_0(000)$	$V_7(111)$	$V_0(000)$	$V_7(111)$
	-1	$V_5(001)$	$V_6(101)$	$V_1(100)$	$V_2(110)$	$V_3(010)$	$V_4(011)$

2.6 Intelligent controller tuning

In electrical engineering or more precisely in drive control, PMSM speed regulation is usually ensured by PI controllers. Finding those optimum controller parameters is too time consuming and risky task at the same time since some the PI gains may damage the system or make it unstable. To overcome these problems, PI gains should be automatically adjusted using the idea that only the best proportional and integral gains should be provided to the PI controller at each instant. This is usually performed using population based optimization algorithms such as particle swarm optimization [53] or genetic algorithm [54]. These two aforementioned naturally inspired algorithms have been used in this work to tune the PI speed controller and optimize its parameters as it will be discussed in the forthcoming section.

2.6.1 Particle swarm optimization

Particle swarm optimization is a population-based algorithm inspired from the social behavior of organisms such as birds and fishes. It was first introduced by Eberhart and Kennedy in 1995 [55]. It is similar to other population-based algorithms like (GA) in that the algorithm is initialized with a population of random solutions. To optimize the time complexity of the algorithm the idea of several evaluations at one iteration was adapted, this means that all the particles in the population are all exploring the search space at the same time attempting to find an optimal location (solution) with respect to a cost function.

For a population of N particles. The personal and global bests are given by:

$$P_{best,i}^{t+1} = \begin{cases} P_{best,i}^t & if \quad f(x_i^{t+1}) > P_{best,i}^t \\ x_{best,i}^{t+1} & if \quad P_{best,i}^t \geq f(x_i^{t+1}) \end{cases} \tag{2.39}$$

$$G_{best}^t = \text{Min}\left(P_{best,1}^t P_{best,2}^t \dots P_{best,n}^t\right) \tag{2.40}$$

Where $P_{best,i}^t$ and G_{best}^t are the personal and global best position of particle i at iteration t.

Particles' position is updated using equation (2.41):

$$v_i^{t+1} = w^t v_i^t + c_1 r_1 \left[P_{best,i}^t - x_i^t\right] + c_2 r_2 [G_{best}^t - x_i^t] \tag{2.41}$$

Where: v_i^t is the ith Particle's velocity at iteration t, x_i^t is the ith Particle's position at iteration t. $P_{best,i}^t$ is the personal best position of particle i, G_{best}^t is the global best position of particle i found in [0 t]. c_1, c_2 represent respectively the cognitive and social influence on particle's decision, r_1, r_2 are two random coefficients and w^t is an inertia weighting factor that is linearly decreasing [0.4, 0.9].

All the particles update the position is given by:

$$x_i^{t+1} = x_i^t + v_i^{t+1} \tag{2.42}$$

Table 2.6 represents all the PSO parameters that have been used when performing the different simulations and PSO pseudocode is shown in figure 2.10.

Table 2.6 PSO parameters.

Population	32
Iterations	50
c_1	2
c_2	2
w_{min}	0.4
w_{max}	0.9

```
--------------------Pseudo code for PSO algorithm------------------
Inialize all the particles
Do
  For each particle
    Calculate the new cost
      If the new cost is better than the one in history(Pbest)
      Set the new cost as the new Pbest value
End
Choose particle with best cost of all particles as Gbest
While max iteration or min error is not satisfied
  for each particle
    Update position and velocity based on Pbest and Gbest
  end
end
----------------------------------------------------------------------
```

Figure 2.12 Pseudo code of PSO algorithm.

2.6.2 Genetic algorithm

GA is a stochastic universal adaptive search optimization technique based on the procedure of inherent selection. Darwin also stated that the survival of an organism can be maintained through the process of selection, crossover and mutation. The solution generated by GA is called a chromosome, while collection of chromosomes is referred as a population which will undergo a process called evaluation to measure the suitability of solution. Some chromosomes will mate through a process called crossover producing offspring's which are the combination of their parent's genes. In a generation, few chromosomes will undergo mutation in their genes. The number of chromosomes which will undergo crossover and mutation is controlled by crossover rate and mutation rate value. The chromosomes that will be maintained for the next generation will be selected based on Darwin's rule, the chromosome with higher fitness or lower cost value will have greater probability of being selected again in the next generation.

After several generations, the chromosome value will converge to a certain value which is the best solution for the problem. Figure 2.13 shown below points out GA flowchart which explains the different major steps of this algorithm.
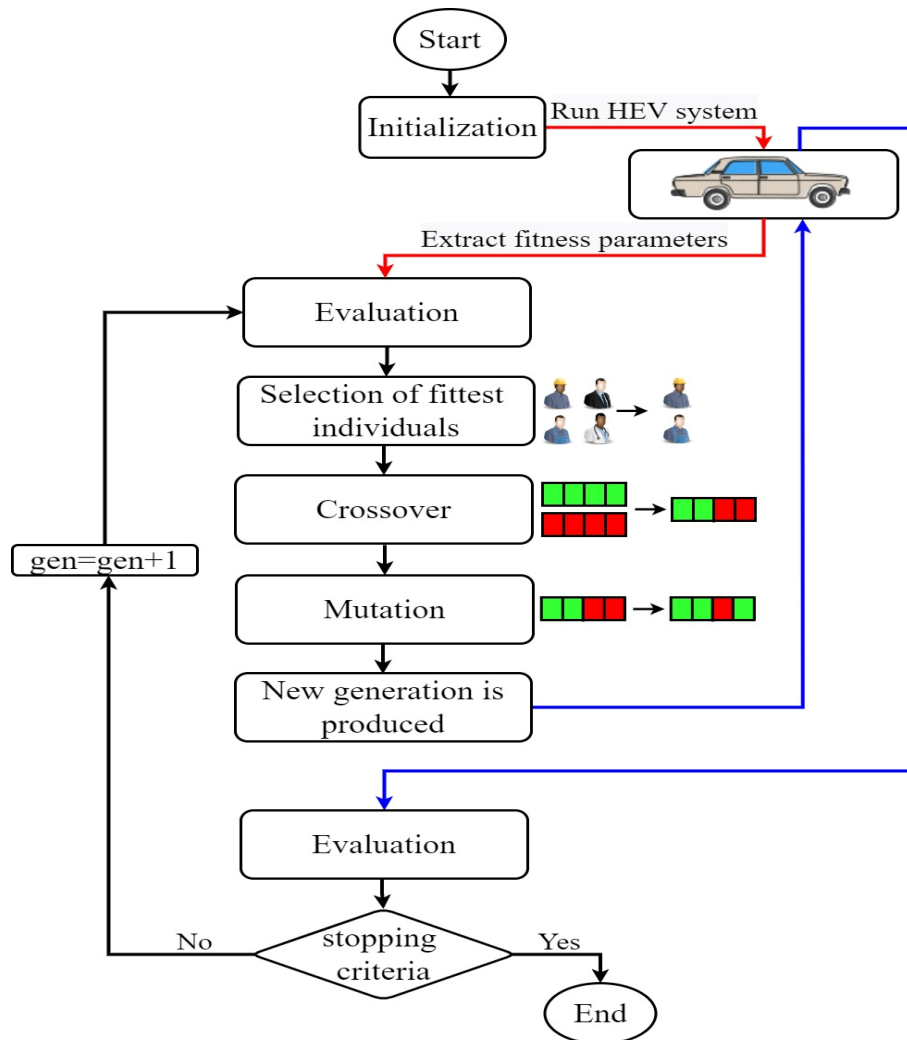
Figure 2.13 Genetic algorithm flowchart.

Each of the genetic algorithm steps shown in flowchart 2.11 are detailed below:

2.6.2.1 Search space initialization

In solving problems, some solutions will be the best among others. The space of all feasible solutions (among which the desired solution resides) is called search space. Each point on this state space is a possible solution which is characterized by its cost for the problem. Figure 2.12 shows a GA population in a four dimension search space. One can remark that the first two dimensions are dedicated for the speed regulator and the last two ones are reserved for PI current controller.
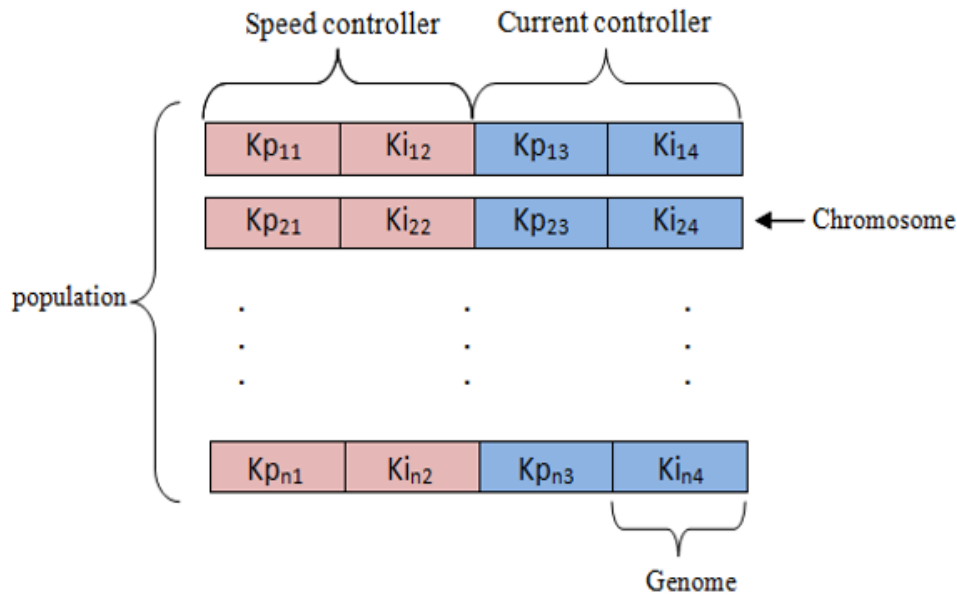
Figure 2.14 GA PI controller.

2.6.2.2 Selection

It is the process of choosing the fittest chromosomes based on their cost. The number of chromosomes selected for crossover is decided by the selection factor. There exist many techniques for selecting chromosomes like roulette Wheel selection, rank selection and tournament selection. Roulette wheel selection which is the most commonly used technique for chromosome selection is the technique that has been used in this work, for this reason we will explain below its principal of operation.

✓ Calculate the cost of each chromosome F(i).

✓ Calculate the selection probability for each chromosome using the equation (2.36):

$$P = \frac{F(i)}{\sum_{i=1}^{m} F(i)} \tag{2.43}$$

✓ Compute the cumulative probability values.

✓ Generate two random vectors R1 and R2.

✓ Based on R1 and R2 we select two sets of chromosomes (parents) for crossover. In this method, each individual is allocated a section of a roulette wheel. The size of the section is proportional to the cost of the individual. A pointer is spun and the individual to whom it points is selected. This continues until the selection criterion has been met. The probability of an individual being selected is related to its cost ensuring that fitter individuals are more likely to leave offspring. Figure 2.15 shown in the next page illustrates the roulette wheel selection:
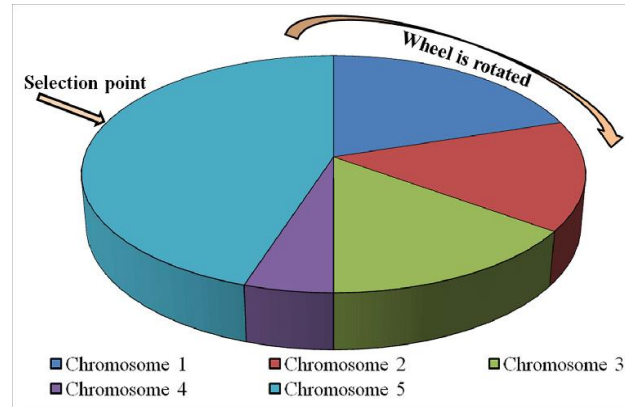
Figure 2.15 Roulette wheel selection.

2.6.2.3 Crossover

It is a genetic operator that combines (mates) two chromosomes (parents) to produce a new chromosome (offspring). The idea behind crossover is that the new chromosome may be better than both of the parents if it takes the best characteristics from each of the parents. There exist two types of crossover: single point crossover and two point crossover. When performing single point crossover, both parental chromosomes are split at a randomly determined crossover point, then a new child genotype is created by appending the first part of the first parent with the second part of the second parent. A single crossover point on both parents' organism strings is selected. All data beyond that point in either organism string is swapped between the two parent organisms. The advantage of having more crossover points is that the search space may be searched more thoroughly. However, adding further crossover points reduce the performance of the GA.

2.6.2.4 Mutation

Mutation means the flipping of variable values. For every chromosome, the variable value which will change is randomly selected. Using selection and crossover on their own will generate a large amount of different strings. However the following problem will be faced when using only selection and crossover: Depending on the initial population chosen, there may not be enough diversity in the initial strings to ensure the Genetic Algorithm searches the entire search space. Furthermore, The Genetic Algorithm may converge to sub-optimum strings due to a bad choice of initial population. These problems may be overcome by introducing a mutation operator into the Genetic Algorithm.

Table 2.5 points out all the GA parameters used when performing the different simulations

Table 2.7 GA parameters

Parameters	Values
Population size	32
Number of iterations	50
Selection rate	0.5
Mutation rate	0.5
Crossover rate	Single point

2.7 Cost function formulation and performance assessement

A cost function is a mathematical formula used to measure and evaluate the goodness or the performance of a given particle (potential solution). In most of cases, the cost function is constructed from the different parameters that do affect the system output or simply by using some well defined error functions. In general, four criteria are employed to judge the goodness of the PID parameters. The performance criteria which are mostly used in control system design and summarized as follows:

$$ISE \ = \int_0^T e^2(t)dt \tag{2.44}$$

$$IAE \ = \int_0^T \left| e(t) \right| dt \tag{2.45}$$

$$ITSE = \int_0^T t\, e^2(t)dt \tag{2.46}$$

$$ITAE = \int_0^T t \left| e(t) \right| dt \tag{2.47}$$

The performance of our system is measured with a cost function. It is used to provide a measure of how good the solution is and how the potential solutions have performed in the problem domain. A good formulation of the cost function will have a positive impact on the HEV system by enhancing its performances. In this work, we have considered two types of speed inputs: step input reference (simple) and driving cycles (complex). For simple speed inputs, one can use system performance indices such as rising time, percentage overshoot and steady state speed and torque errors to formulate a good fitness function that optimizes HEV system response. When driving cycles are used as reference speed, it is meaningless to use the performance indices mentioned above since the input is a set of random data points which does not settle during all the simulation time. This is why two cost functions were formulated for

the two different types of inputs in terms of instantaneous errors, steady state errors and other quantities that we want to optimize.

The cost function proposed for simple step input is given by equation (2.48). Its first term includes steady state torque error e_{ssT} and steady state speed error $e_{ss\Omega}$ that are both multiplied by a weighting factor α. The second term includes percentage overshoot PO and settling time Ts which are all multiplied by a weighting factor of (1- α).

$$J_1 = \alpha(|e_{ss\Omega}| + |e_{ssT}|) + (1 - \alpha)(PO + T_S) \tag{2.48}$$

For driving cycles reference speed, the proposed cost function is given by equation (2.49). It is a weighted sum of average mean speed error and average mean torque error. This cost function is a tradeoff between vehicle speed and torque. So, it gives the designer the freedom of prioritizing either vehicle speed or vehicle torque by attributing a larger weighting factor to it. In this work, the weighting factor α was set to 0.5 so that an equivalent importance will be attributed to both speed and torque.

$$J_2 = \alpha\overline{|e_\Omega|} + (1 - \alpha)\overline{|e_T|} \tag{2.49}$$

Average absolute speed error $\overline{|e_\Omega|}$ and average absolute torque error $\overline{|e_T|}$ are respectively calculated using equations (2.50) and equation (2.51) where Ω_i and T_i represent, respectively, HEV reference speed and torque. $\widehat{T_i}$ and $\widehat{\Omega_i}$ represent the measured HEV speed and torque respectively.

$$\overline{|e_\Omega|} = \frac{1}{n}\sum_{k=1}^{n}\left|\Omega_i - \widehat{\Omega_i}\right| \tag{2.50}$$

$$\overline{|e_T|} = \frac{1}{n}\sum_{k=1}^{n}\left|T_i - \widehat{T_i}\right| \tag{2.51}$$

It is worth noticing that N in the two above equations is the length of the torque and speed vectors during a given driving cycle. N is given equation (2.52) where T_d^{cy} is the duration of the speed profile.

$$N = \frac{T_d^{cy}}{T_s} \tag{2.52}$$

The flowchart presented in figure 2.16 explains how PSO is adapted for use to find the optimum controller gains that satisfy the design requirements established via the proposed cost functions.
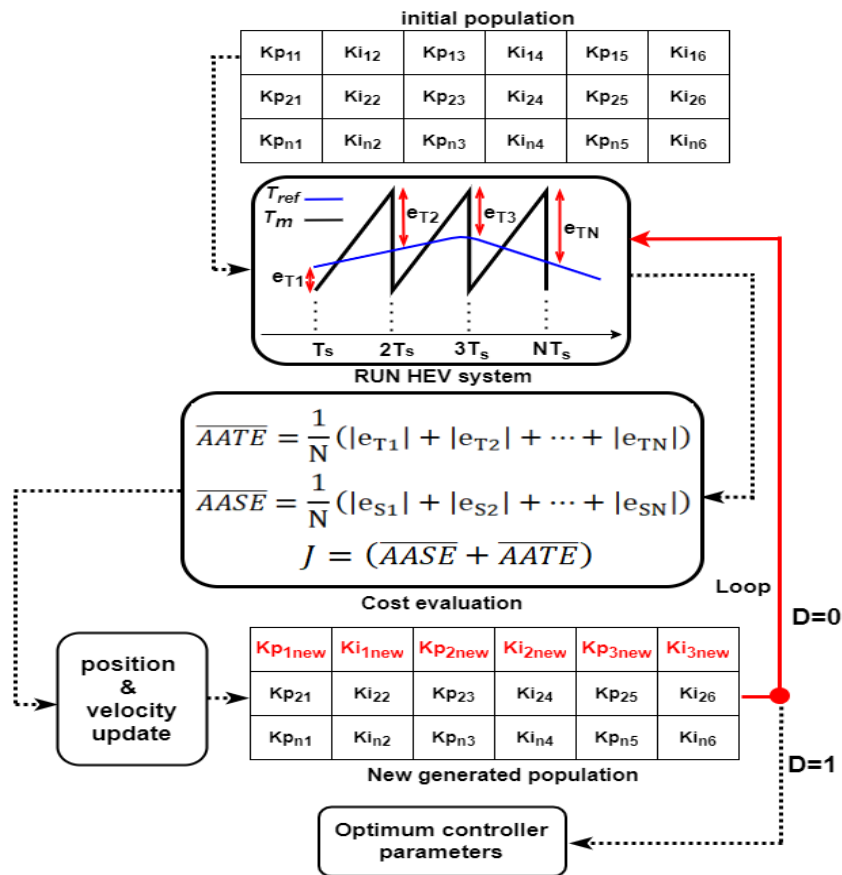
Figure 2.16 EV controller tuning with PSO

The following steps explain point by point how optimum controllers' gains are found using PSO algorithm. It is worth noticing that the same steps are almost followed while using genetic algorithm only the algorithm philosophy differs:

- Initialize the swarm in a six dimensions search space.

- For each population particle, run the HEV system for a complete speed profile and evaluate particle's performance using equation (2.49).

- Apply penalty function to exclude unstable PI combinations that resulted in infinite cost values. Infinite or large cost values mean that the actual PMSM speed or torque values are too far from their references.

- Update particles'speed and position.

- Evaluate the cost of the particle at its new location. If is smaller than the previous cost value then update it.

- Keep iterating until the decison signal D (figure 2.16) is 1. This last mentionned signal is equal to 1 when the maximum number of iterations is elapsed or the minimum cost is reached.

- Extract the particles that resulted in smallest cost value.

- Apply the optimum gains to the HEV system of figure 2.8.

2.8 Simulation and results

    To test PSO and GA performance before their integration to the HEV system, the convergence of the two bio inspired algorithms is evaluated using the two benchmark test functions given by equations (2.48) and (2.49) for which the optimum is already known. It is worth noticing that the minimums of F1 and F3 are respectively -18.56 and -0.5231. Equations 2.53 and 2.54 are respectively depicted in figures 2.17 and 2.18.

$$F_1 = x_2 \sin(4x_1) + x_1 \sin(4x_2) \tag{2.53}$$

$$F_3 = 0.5 + \frac{sin^2\sqrt{x^2 + y^2} - 0.5}{1 + 0.1(x^2 + y^2)} \tag{2.54}$$

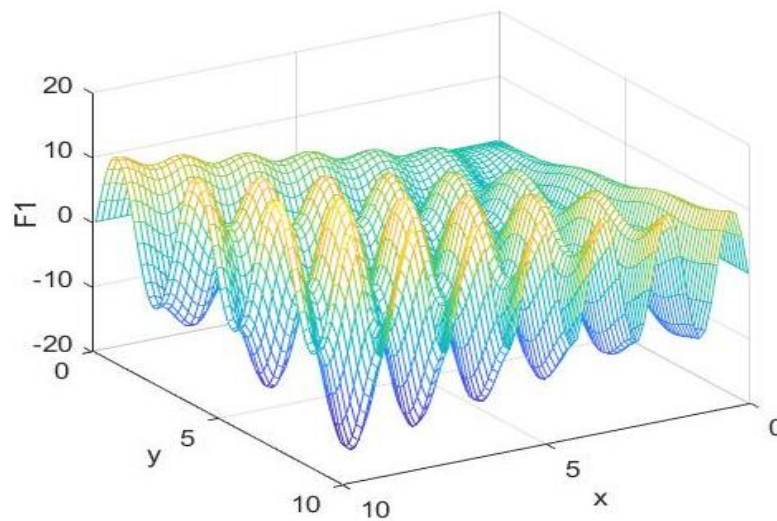**Figure 2.17** First used test function
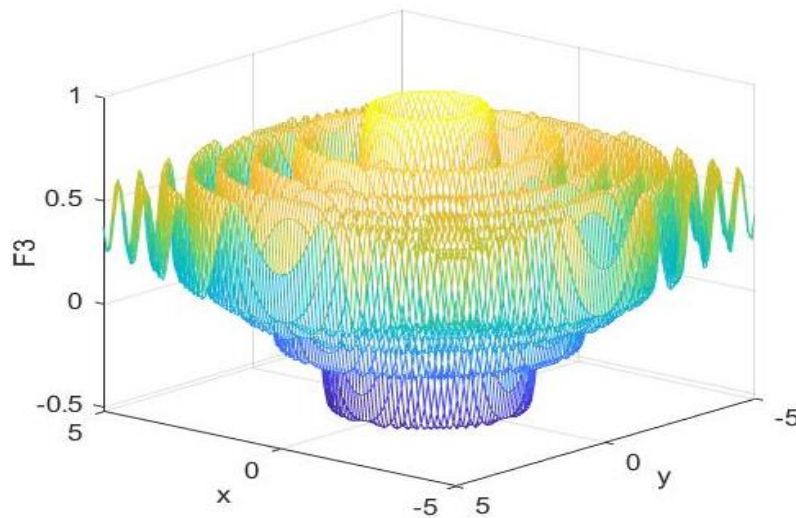
Figure 2.18 Second used test function.

    The results of minimization of F1 and F3 using GA and PSO algorithms are depicted in figure 2.17 and 2.18. It could be noticed that both algorithms have converged to the minimum of used test functions with a slight tolerable error and this confirms that the convergence of PSO and GA.
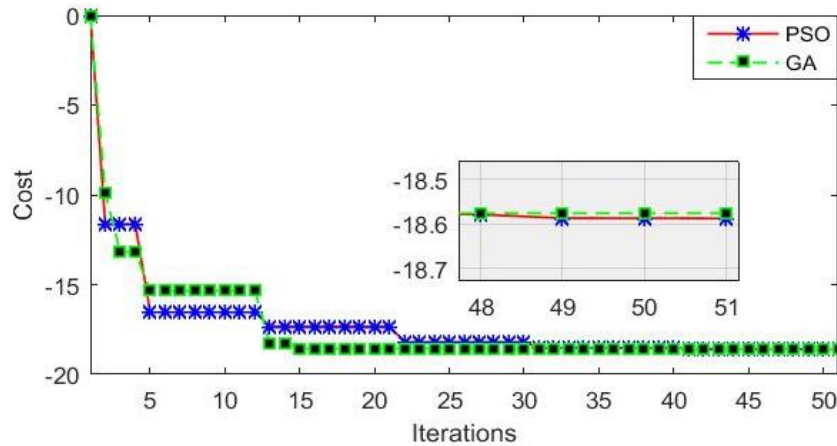
Figure 2.19 Cost minimization of F1.
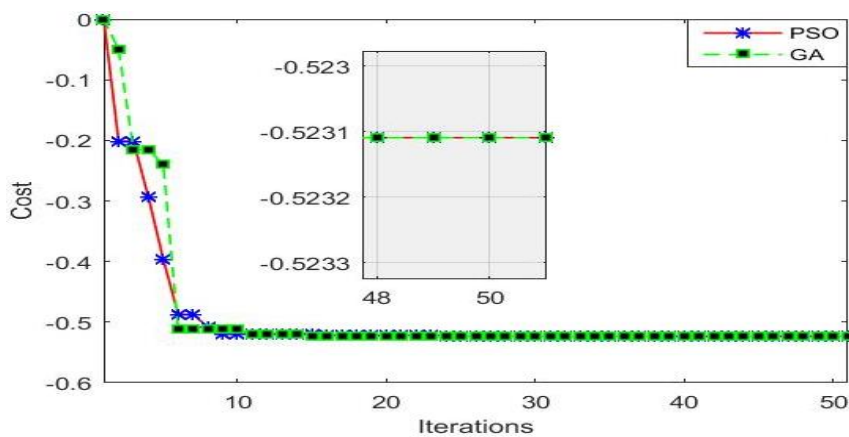
Figure 2.20 Cost minimization of F3.

All the simulations carried out through this chapter are under a constant wind speed of 10 *Kph* against vehicle motion and a road slope of 10°. The HEV is subjected to two speed inputs: step speed input: we want our response to have minimum overshoot, minimum settling time and minimum speed and torque steady state error. For driving cycle input speed: since the UDDS driving cycle is a series of data points that does not settle so it is meaningless to include peak overshoot or settling time in the design specification. This is why the design specifications for driving cycle input speed are minimum instantaneous absolute torque and speed errors.

2.8.1 Simple step reference input speed

Figure 2.21 shows the electric vehicle response when it is subjected to a simple reference speed input of 50 km/h. One can remark form figure 2.21 that PSO and GA algorithms yielded a speed response with almost a null peak overshoot but trial and error approach yielded a response relatively faster response with 5% overshoot. From figure 2.22 to 2.27, one can state that the absolute speed error gotten either using trial and error approach or intelligent tuning approach is approximately the same and it is in the order of 1e-5 km/h. For absolute torque error the trial and error approach yielded a mean error of 1.5 N.m whereas genetic algorithm

and particle swarm optimization resulted respectively in an average absolute torque error of 0.007 N.m and 0.01 N.m.
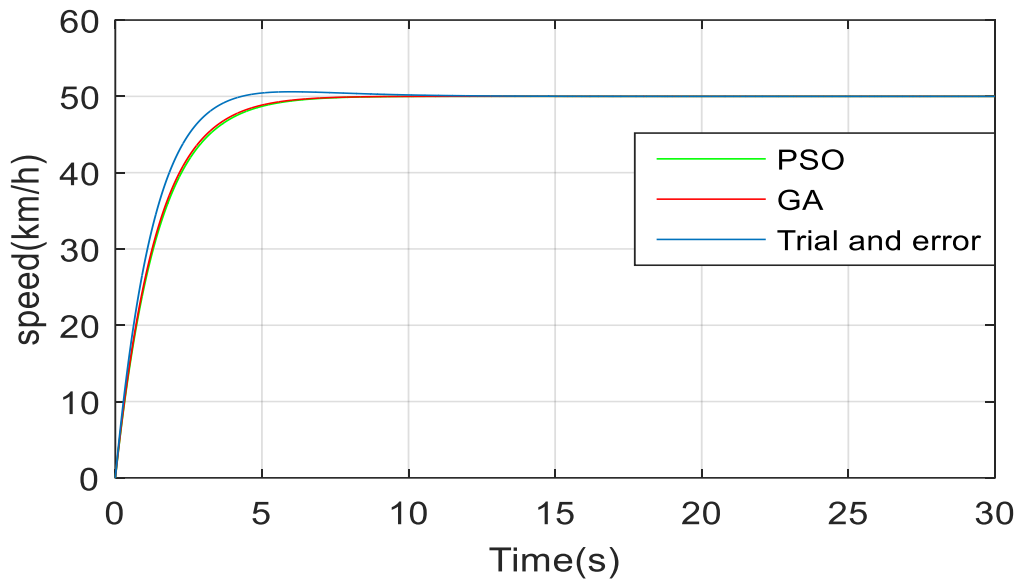
Figure 2.21 BEV speed response for simple input speed reference.
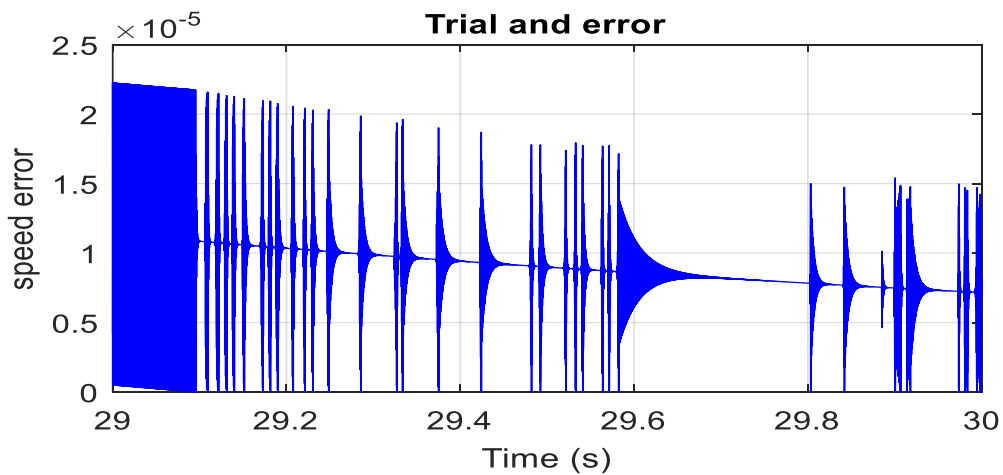
Figure 2.22 BEV absolute speed error based on trial and error.
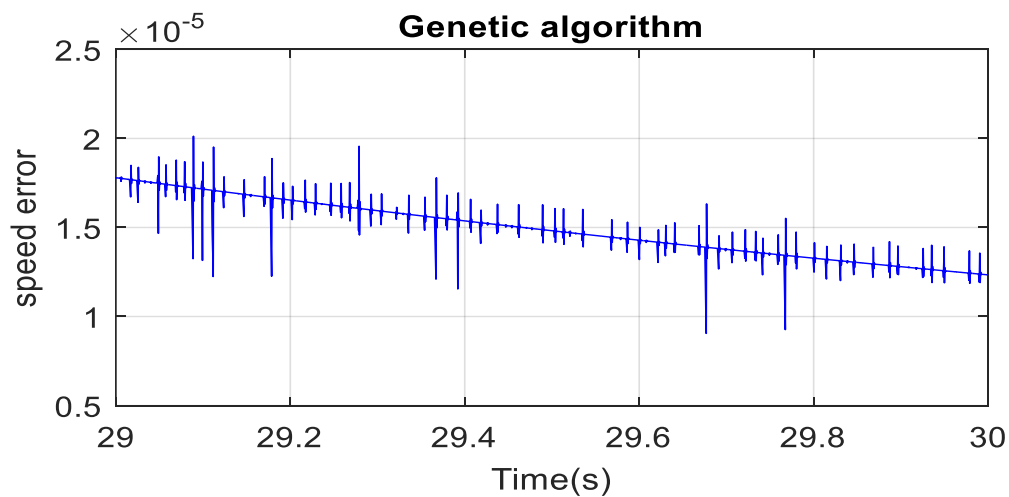
Figure 2.23 BEV absolute speed error using genetic algorithm.
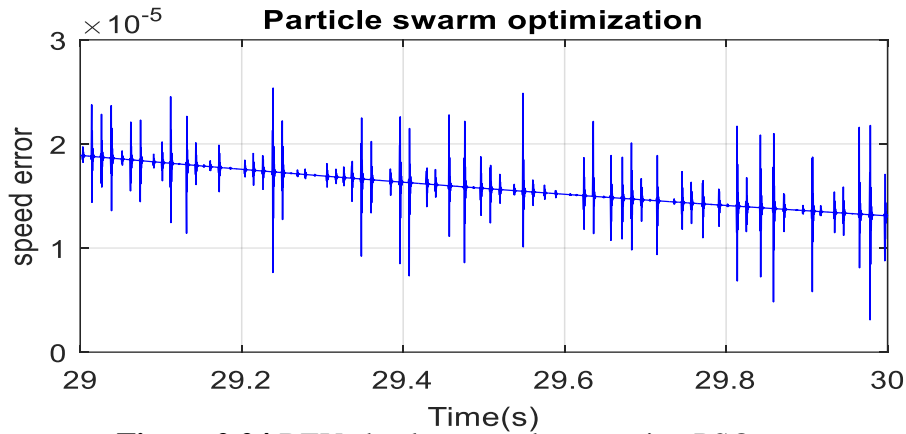
Figure 2.24 BEV absolute speed error using PSO.
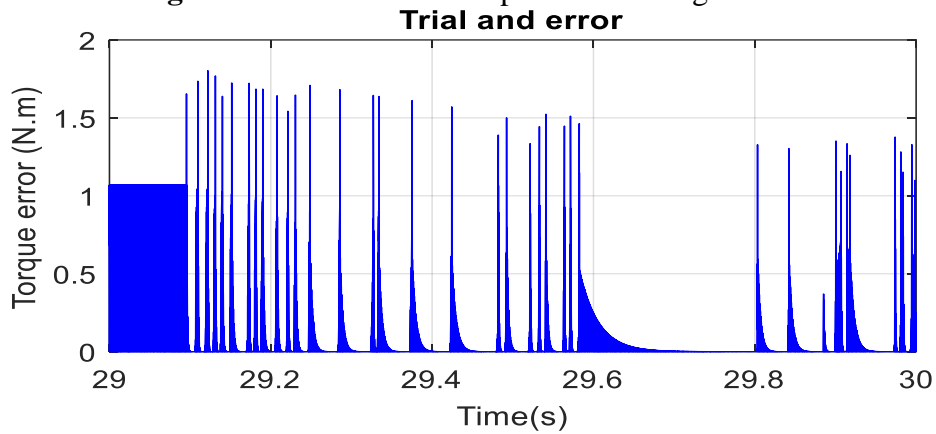
Figure 2.25 BEV absolute torque error based on trial and error.
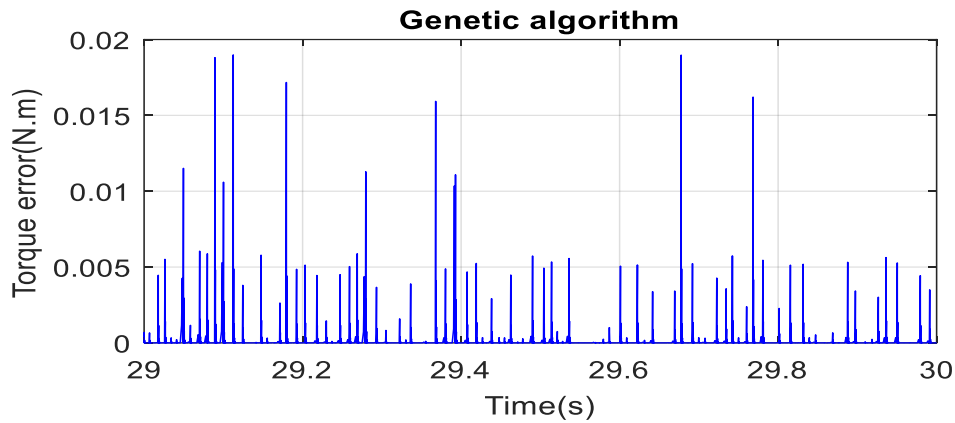
Figure 2.26 BEV absolute torque error using GA.
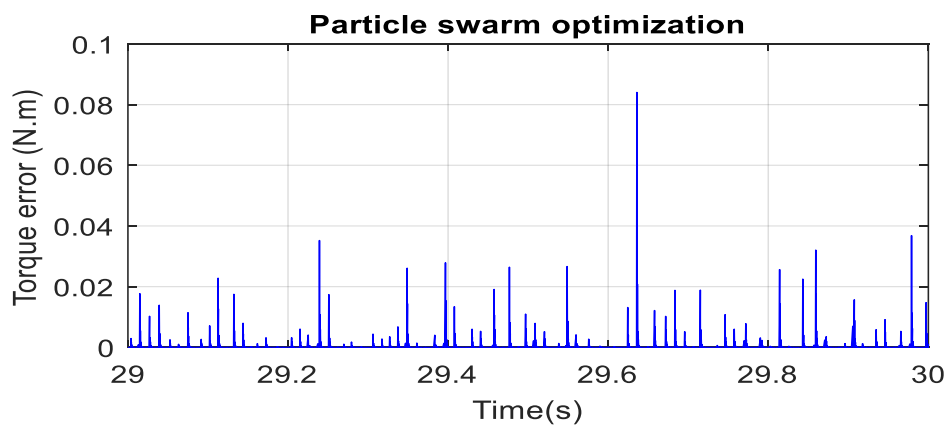
Figure 2.27 BEV absolute torque error using PSO.

Figure 2.28 highlights the cost value for PSO and GA algorithms while minimizing the fitness function J_1 given in equation (2.48). One can notice the cost value for both algorithms keeps decreasing as the number of iterations increases which mean that the used cost function was effectively optimized. From figure 2.28 also, one can remark that both algorithms converged to the same value only that GA converged faster.
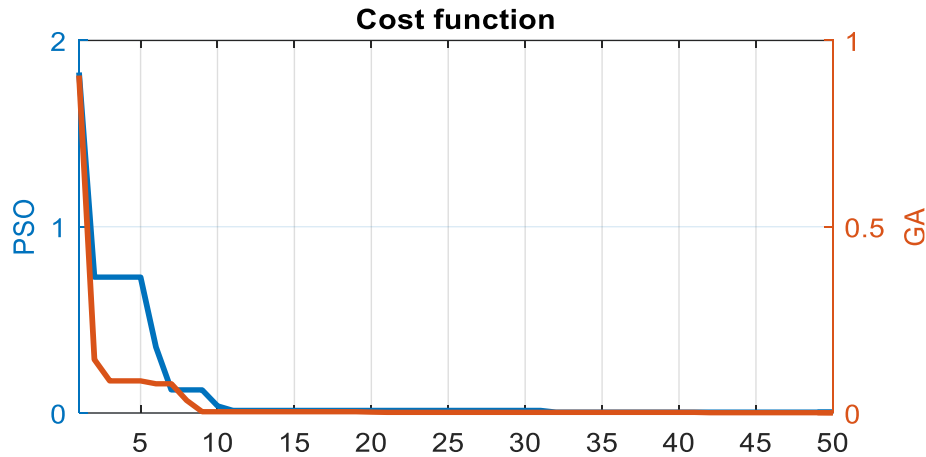
Figure 2.28 Cost value for PSO and GA algorithm

Figure 2.29 shows the evolution of controller parameters using PSO and GA algorithms. After each iteration, the PID parameters resulting in minimizing the cost function given by equation (2.48) are kept. After that, the best global cost is deduced using equation (2.40).
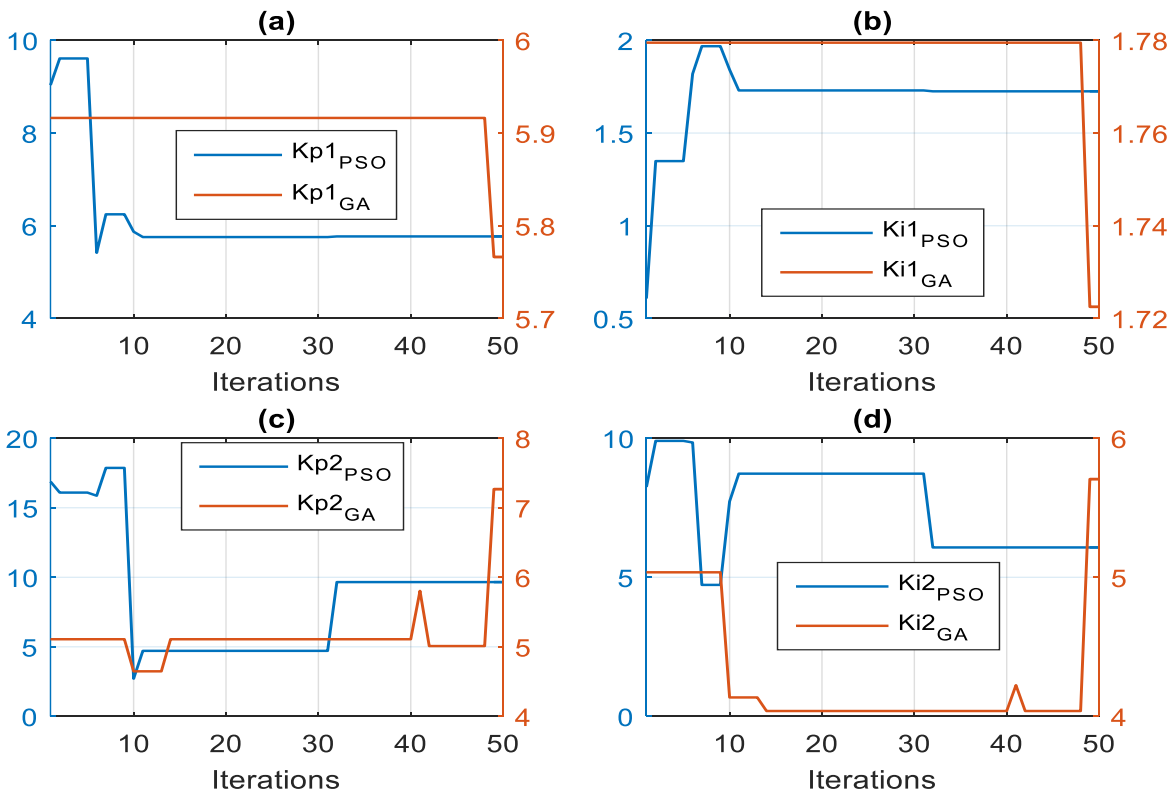
Figure 2.29 Best controller position for PSO and GA algorithm

2.8.2 ECE 15 driving cycle

   Figure 2.30 shows the HEV speed response and its reference when ECE15 driving cycle is applied. One can notice that there is almost a perfect matching between the actual HEV speed and its reference. This is confirmed by figure 2.31 which highlights that the maximum absolute speed error is 3.5e-3. From figure 2.32, it can be remarked that the HEV torque response follows precisely its reference with a maximum absolute torque error of 0.42 N.m as it is shown in figure 2.33.

Figure 2.30 BEV speed response and its reference for ECE driving cycle
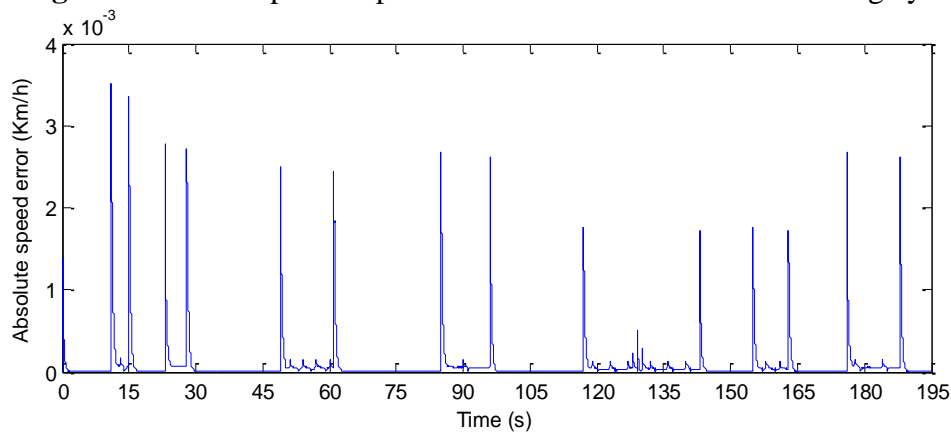
Figure 2.31 BEV absolute speed error for ECE driving cycle.

Figure 2.32 BEV torque response and its reference for ECE driving cycle.
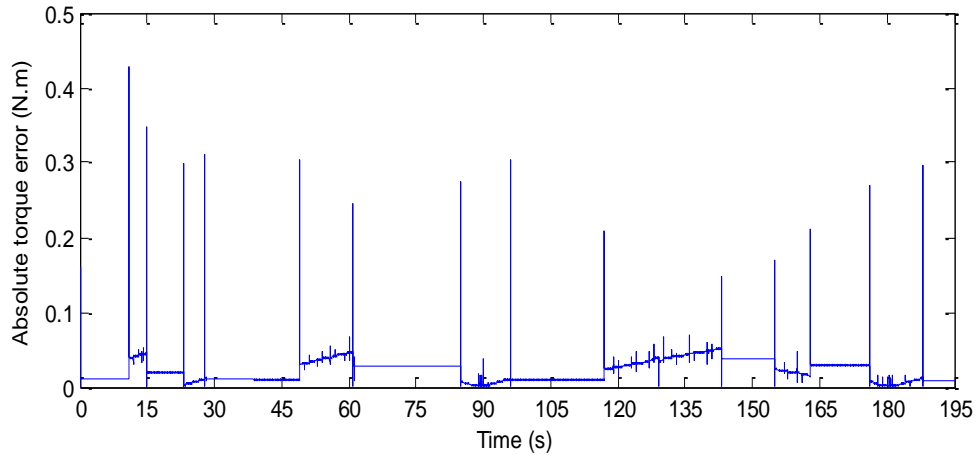
Figure 2.33 BEV absolute speed error for ECE driving cycle

PMSM phase currents are shown in figure 2.34, the zooms on that figure shows that they are pure sinusoidal and 120 degree apart which means that the traction motor operates under balanced or normal conditions. The amplitude of PMSM phase currents depends on HEV torque and both of them vary in the same manner. When the HEV torque is constant, phase currents amplitude is also are constant, when HEV torque increases, phase currents amplitude increases and when HEV torque decreases, so does phase current amplitude. One can also conclude from the zooms of figure 2.34 that the frequency of PMSM phase currents is variable and depends on vehicle speed. To confirm this, let's first mention that PMSM rotor speed is related to frequency as follow:

$$f = \frac{p\Omega}{60} \tag{2.54}$$
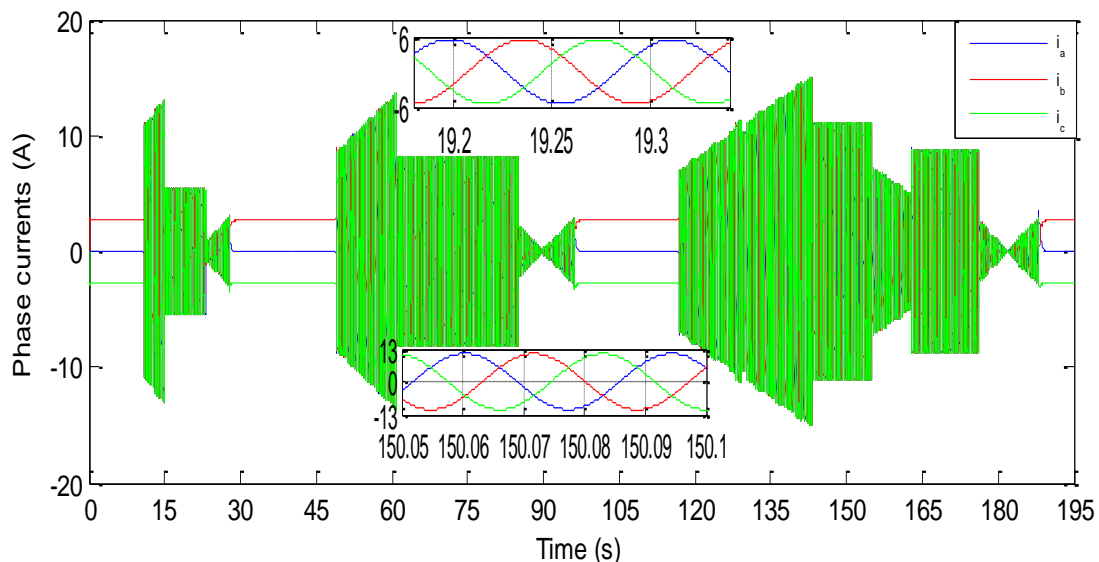
Figure 2.34 PMSM phase currents and their zooms.

When t ϵ [96 s, 117 s] in figure 2.30, the HEV speed or rotor speed is null. According to equation (2.54), this means that the *f=0* Hz which means that the PMSM currents must be constant at that time interval. Indeed, in figure 2.34, PMSM phase currents are constant at that

time interval and their sum is null which means that there is no current flowing to the motor because the vehicle is at rest.

2.8.3 HWFET driving cycle

Figure 2.35 shows the HEV speed response and its reference when HWFET driving cycle is used as input speed reference. The vehicle absolute speed error is shown in figure 2.36 where one can see that the speed error is satisfactory and it is in the order of 1e-3. Figure 2.37 shows that the HEV torque follows its reference during all the driving cycle period. The absolute torque error lays in a narrow band as it is shown in figure 2.38 where one can see that the maximum torque error is 0.6 N.m. Figure 2.39 shows PMSM phase currents during the HWFET driving cycle, their zoom provided in figure 2.40 shows a sinusoidal shape with variable amplitude and frequency. From equation (2.54), one can conclude that the variable current frequency is due to HEV speed variation. The amplitude of PMSM phase currents depends on HEV torque and both of them vary in the same manner. When the HEV torque is constant, phase currents amplitude is also are constant , when HEV torque increases, phase currents amplitude increases and when HEV torque decreases, so does phase current amplitude.
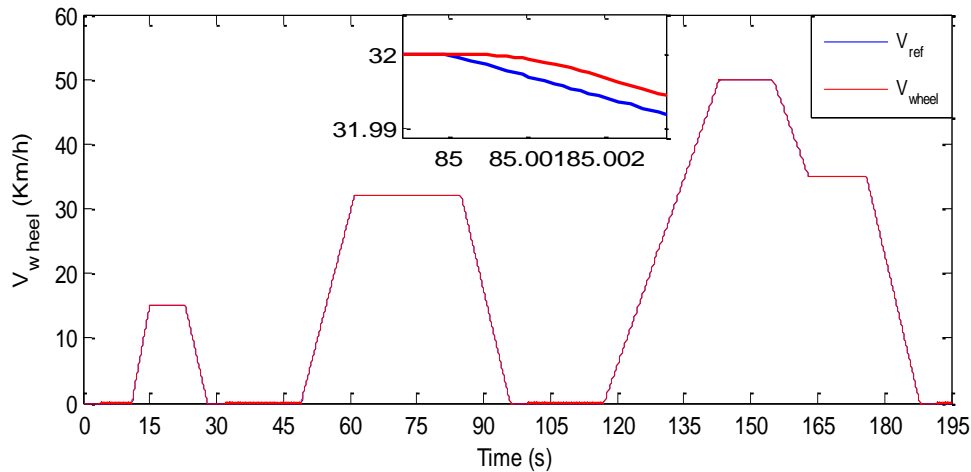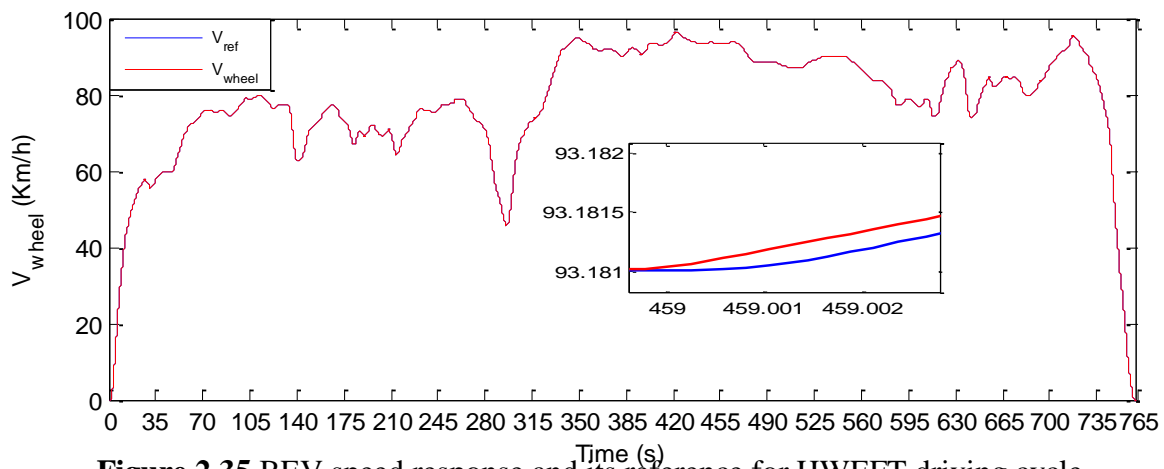

Figure 2.35 BEV speed response and its reference for HWEFT driving cycle.

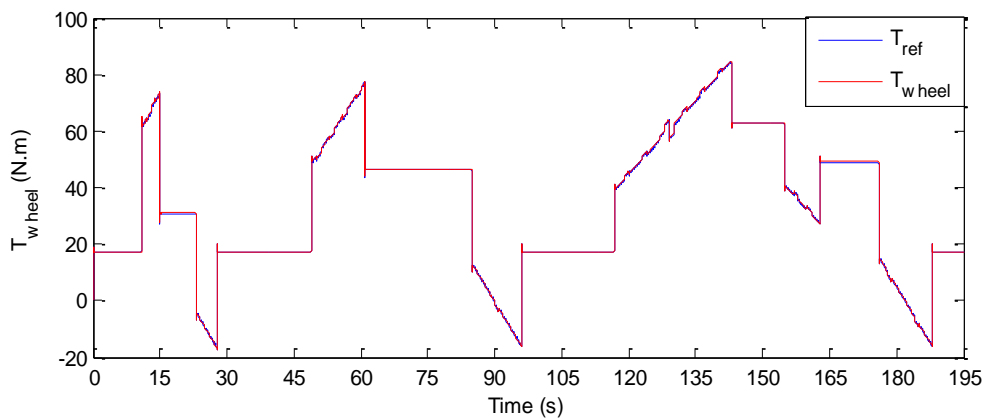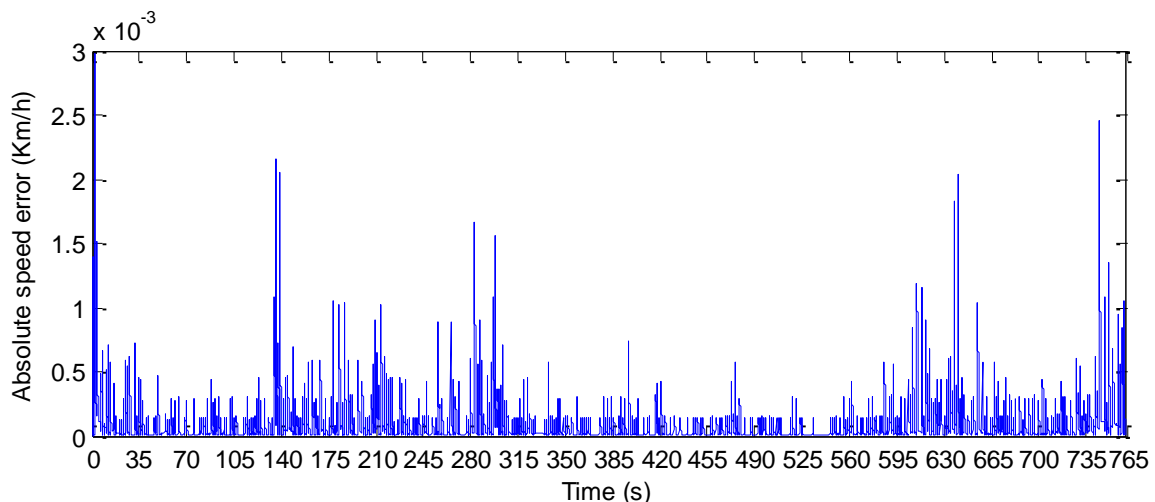**Figure 2.36** BEV absolute speed error for HWEFT driving cycle.
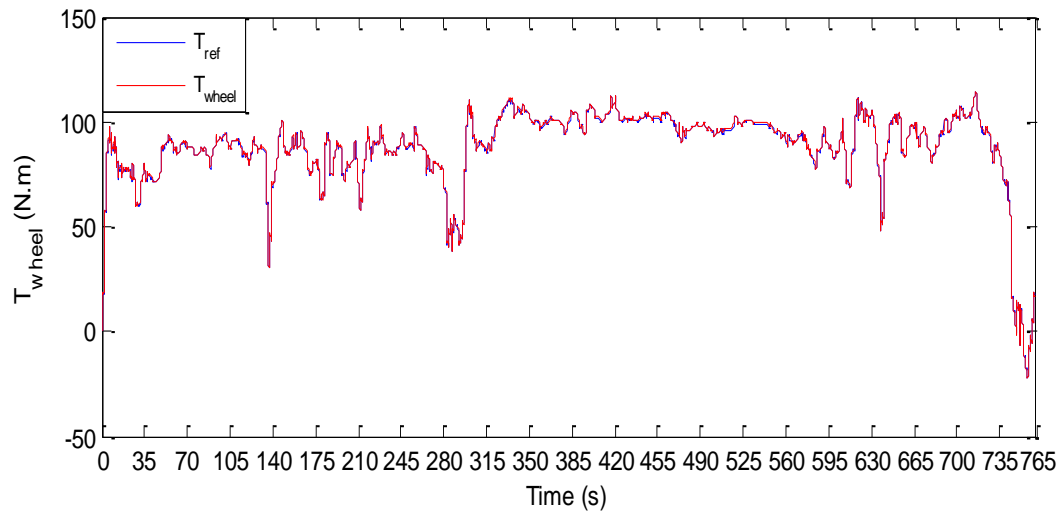
Figure 2.37 BEV torque response for HWEFT driving cycle.
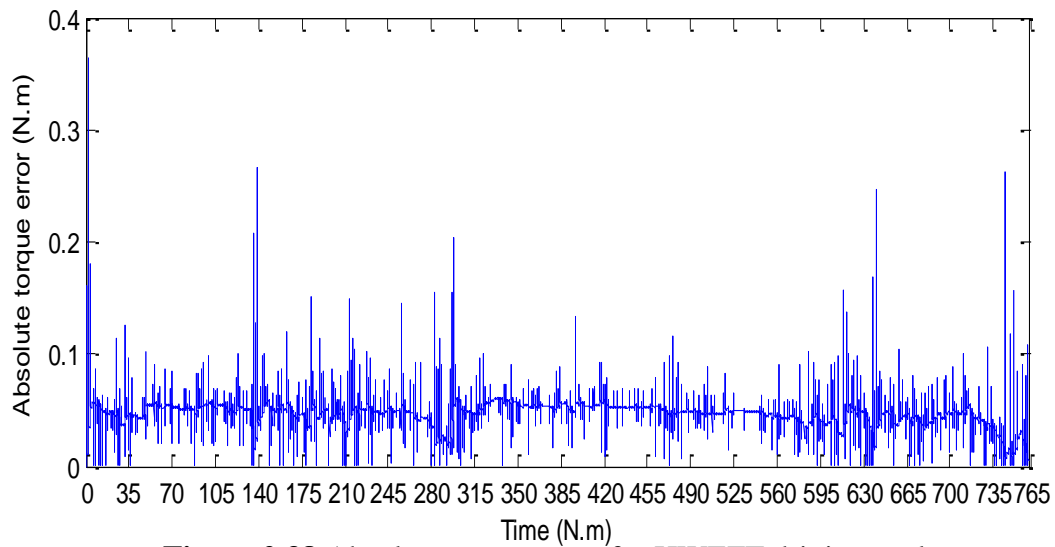
Figure 2.38 Absolute torque error for HWEFT driving cycle.
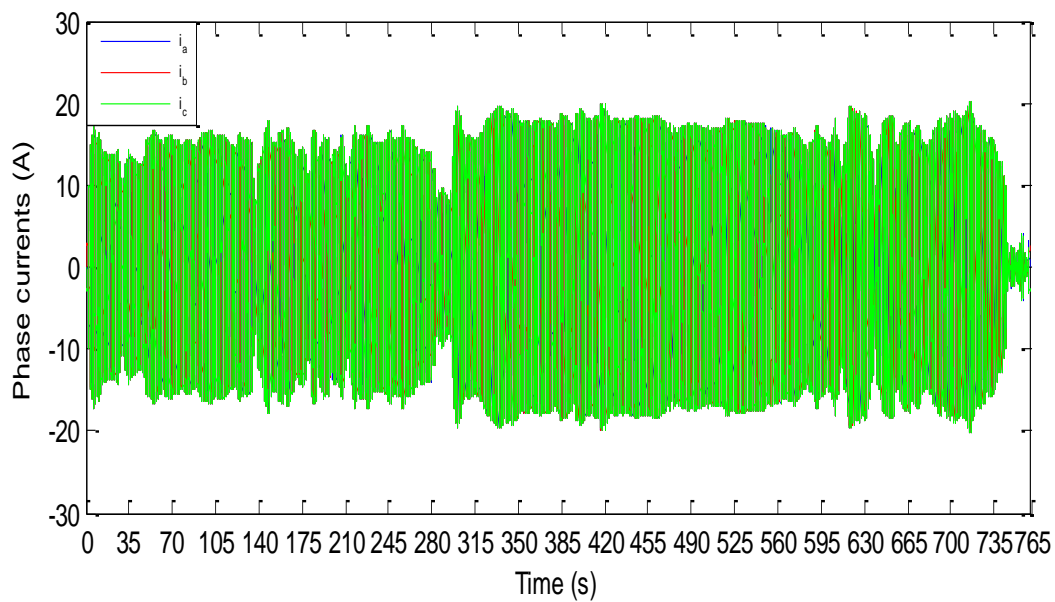
Figure 2.39 PMSM phase currents for HWEFT

(a)   (b)
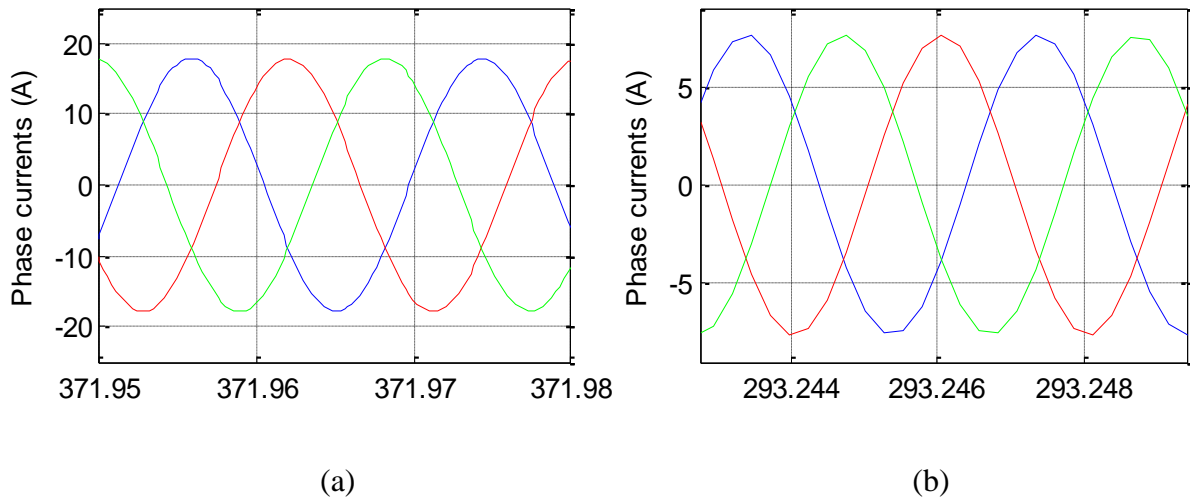
Figure 2.40 Zoom of PMSM phase currents for HWEFT

2.8.4 Robustness against environmental parameters

As mentioned in the previous section, the load torque is varying as the vehicle is undergoing a given path. This variation is due to some external and environmental parameters such as road type which maybe concrete, snowy or sandy road. Road slop and wind are also crucial factors that affect the system response. The impact of surface friction on HEV response is shown in figure 2.39 where one can see that the HEV response remains always stable with zero steady state error which means that the HEV response is robust. Figure 2.40 shows that the road slope does have an impact on vehicle dynamics which tend to become slower as the slope angle becomes larger. From figure 2.41, it can be concluded that when the speed is negative (which means that the speed is in the same direction as the vehicle response becomes faster and when the speed is against vehicle motion, vehicle dynamics become slower.
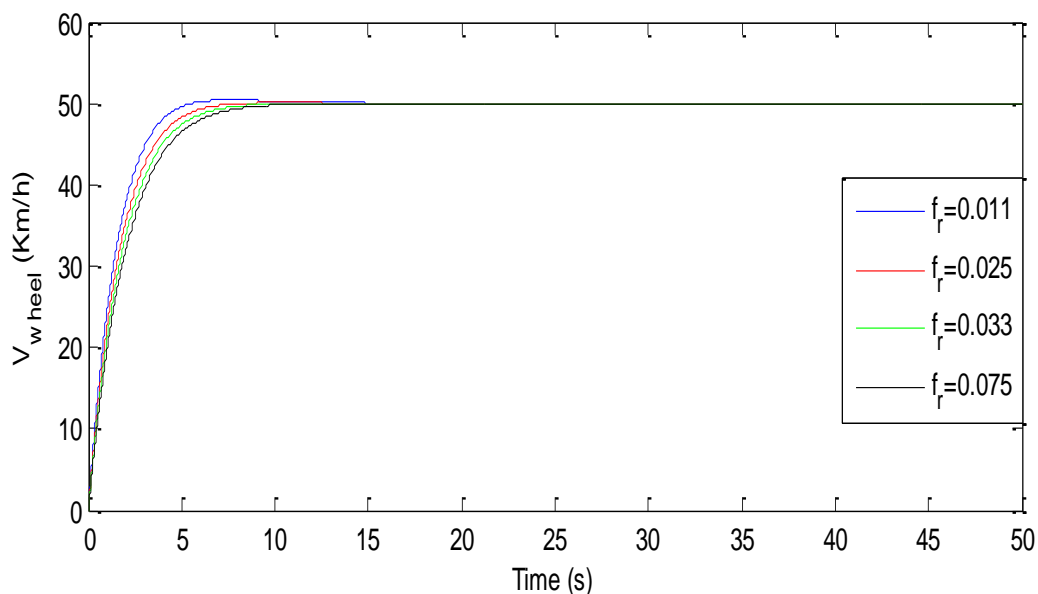
Figure 2.41 Effect of variation of surface-friction coefficient on BEV speed response.
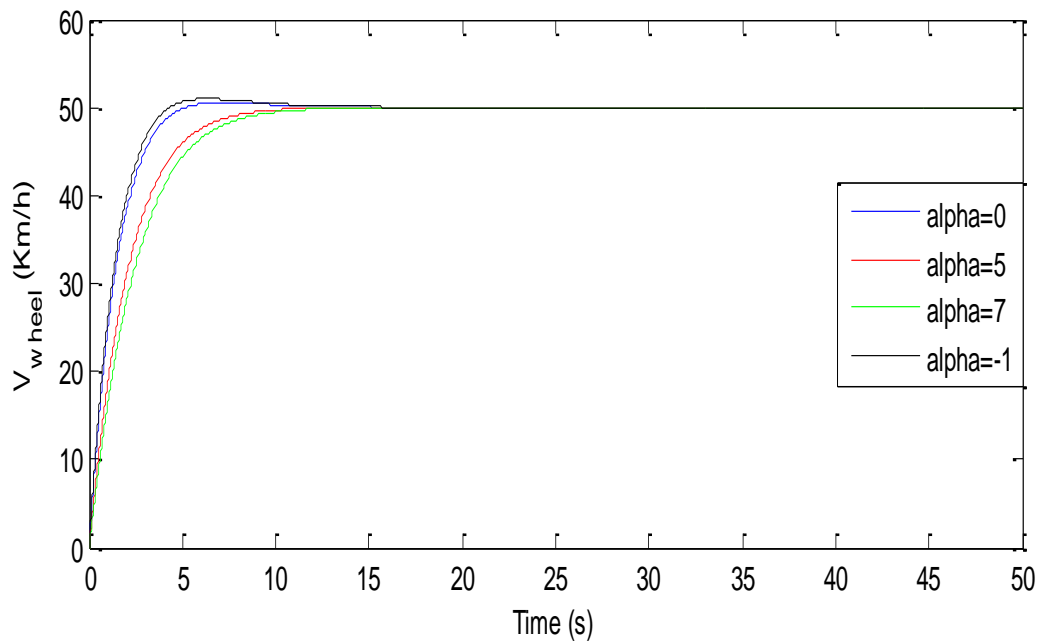
Figure 2.42 Effect of variation of road slope on BEV speed response.
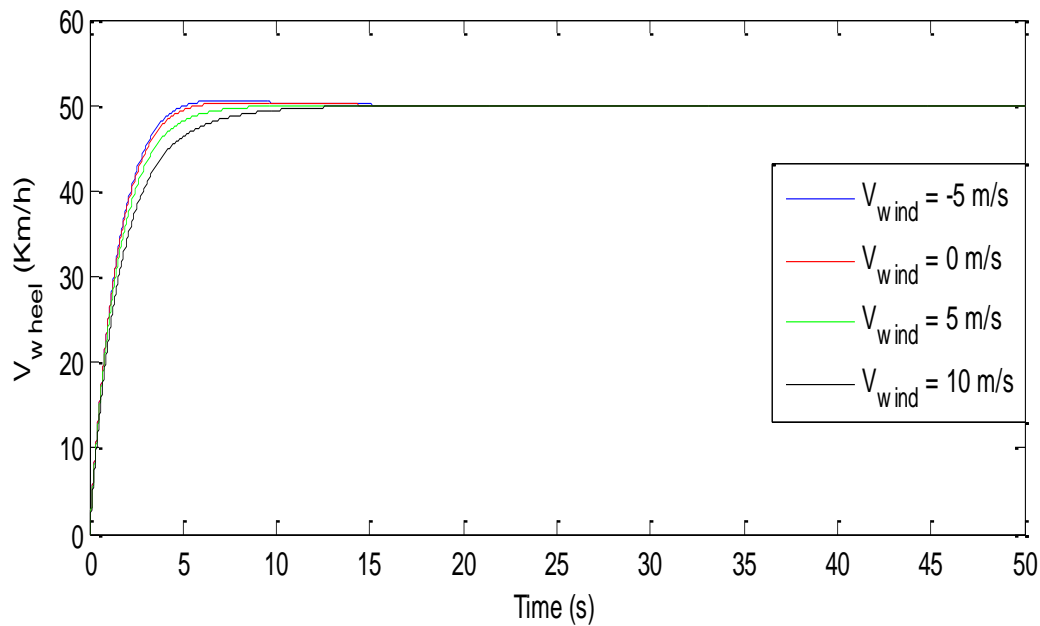
Figure 2.43 Effect of variation of wind speed on BEV speed response

From figure 2.44 one can deduce that when wind speed is in the same direction as HEV motion, its response becomes faster and this increases the performance of its speed response in terms of rising and settling time. However, when wind speed is against vehicle motion, the overshoot of the speed response gets lowered and its dynamics becomes relatively slow. Figure 2.45 confirms that HEV performances gets slow as road slope increases and the inverse is correct. Figure 2.46 confirms that road type does affect HEV speed response.
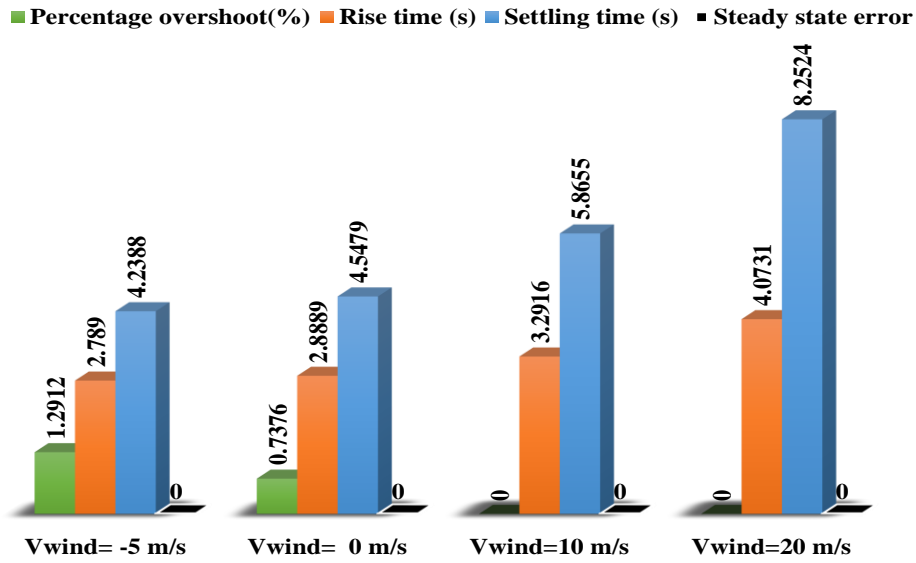
Figure 2.44 Effect of wind speed variation on BEV performance
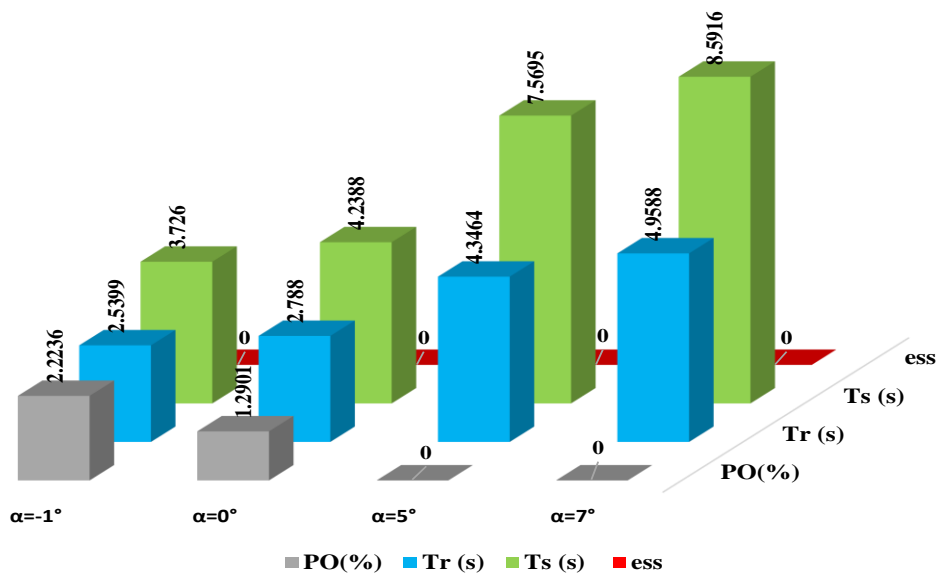
Figure 2.45 Effect of road slope variation on BEV performance
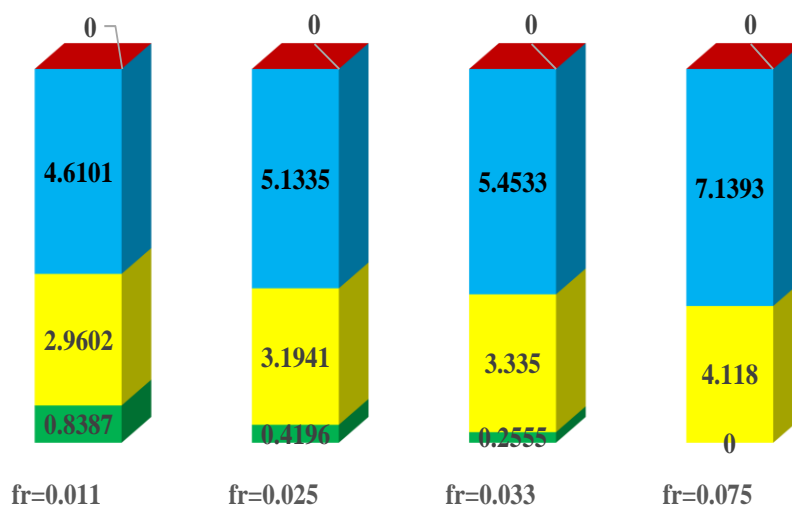
Figure 2.46 Effect of road friction coefficient variation on BEV performance.

2.8.5 Robustness against vehicle parameters variation

The parameters of any electrical system may be subjected to variations due to different factors such as heat, moisture and uncertainty of the measurement device. In this section a robustness analysis is carried out by varying the time constant of some of the EV components which are vehicle sensor and inverter. Table 2.6 shows that the effect of parameter variation is very small. Figure 2.47 and figure 2.48 show respectively the HEV speed response for different inverter and sensor time constants. Changes in inverter and sensor time constants have been made in the interval of -50% to +50% in steps of 25%.
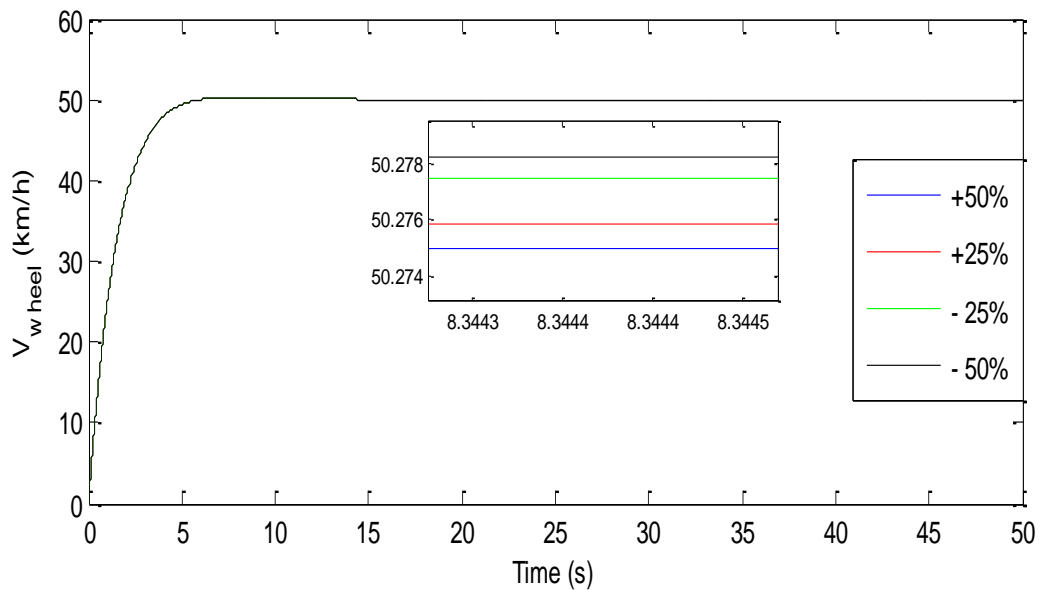
Figure 2.47 Effect of inverter time constant variation on BEV performance.
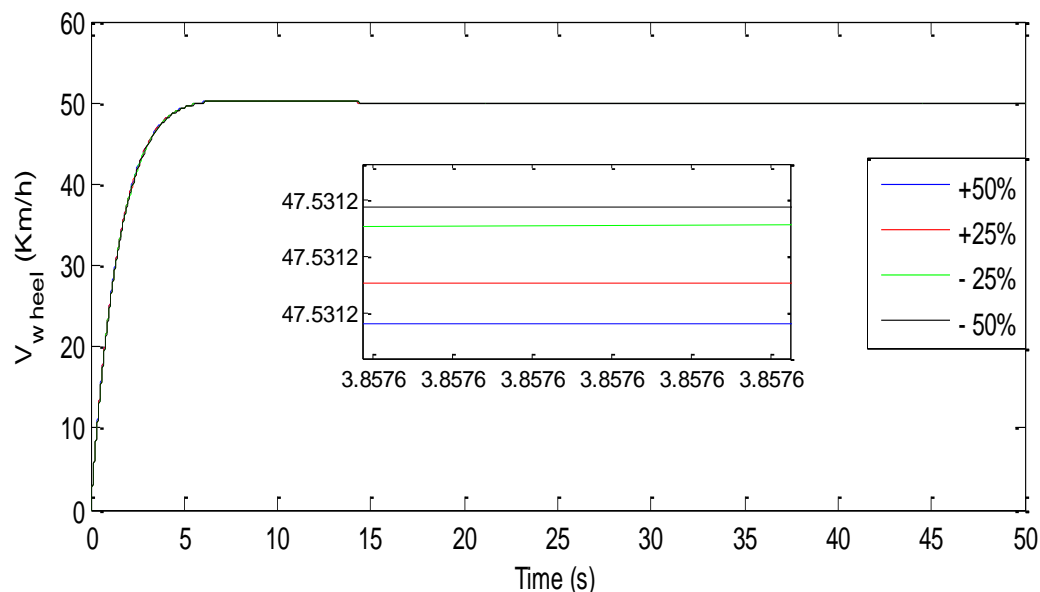
Figure 2.48 Effect of inverter time constant variation on BEV performance.

Table 2.8 Results of robustness analysis against HEV parameter variation.

Parameter	Degree of variation	Percentage overshoot (%)	Rise time (s)	Settling time (s)	Steady state error
T_{PWM}	+50%	0.8798	2.9021	4.5091	0
	+25%	0.8798	2.9020	4.5102	0
	-25%	0.8798	2.9013	4.5091	0
	-50%	0.8798	2.9019	4.5090	0
τ_s	+50%	0.8824	2.8794	4.4761	0
	+25%	0.8811	2.8909	4.4926	0
	-25%	0.8786	2.9130	4.5264	0
	-50%	0.8775	2.9237	4.5420	0

2.9 Conclusion

In this chapter, the speed of the electric vehicle is controlled using FOC technique which simplicity to the control task by providing decoupling between direct and quadrature axes. The PI speed and current regulators were simultaneously tuned using the classical method based on trial and error then using PSO and GA algorithms. These two last mentioned algorithms have succeeded to provide better results and they have also succeeded to provide a good tradeoff between speed and current control which was the main problem of trial and error method. This last mentioned achievement was reached thanks to the two proposed objective functions that provided a good trade off between the parameters to be minimized.

Coordinated power management strategy

3.1 Introduction

Fuel cell based electric vehicles hold great promise for eventually replacing conventional fuel vehicles in the long run. Although the fuel cells are environmentally friendly power sources, there are still some challenges that prevent their large commercialization such as their high cost per unit of power, inability to allow bi-directional power flow, and slow transient response during abrupt load variations [56]. The randomness of road conditions results in sudden load variations which subject fuel cells to harmful transient currents that have a negative impact on their performance and lifespan. Oxygen starvation is a dangerous consequence caused by abrupt load variation that may result in fuel cell damage as it is stated in [58-59]. Authors in [60] have summarized the various control strategies adopted to address the problem of fuel starvation as a result of sudden current demand. Unlike most of the energy management strategies [61-64] which take minimum energy consumption as a design objective, the novel fuzzy multi stage power management strategy that will be presented in this chapter takes into account poor fuel cell transient dynamics, improves vehicle security, compensates the difference, enhances vehicle transient performance and provides moderate usage of power sources. The first stage of the proposed strategy is made of a new developed power management algorithm that offers precise control over fuel cell power by operating it at safe and defined operating points. Since vehicle power sources are sensitive and subjected to harsh external conditions, fault detection algorithms are incorporated in the second stage of the power management strategy to detect and correct possible fuel cell failures and guarantee continuous and safe vehicle operation. The last stage of the proposed power management strategy is a new coordinated switching technique that protects fuel from high and abrupt load power variation suppresses large transient switching ripples and compensates for the poor fuel transient dynamics as it will be demonstrated throughout this chapter

3.2 Power Sources Transient Dynamics

Because of the randomness and unpredictability of driving conditions, load power varies in amplitude and frequency. To address the sudden changes occurring in vehicle load power, the use of power sources is related to the frequency of load power demand as shown it is illustrated in figure 3.1. Supercapacitors are generally used for high frequency power variations, batteries for medium frequency power variations and FC for low frequency power variations due to their slow transient dynamics. Details about the power sources transient will be detailed in the following subsections.
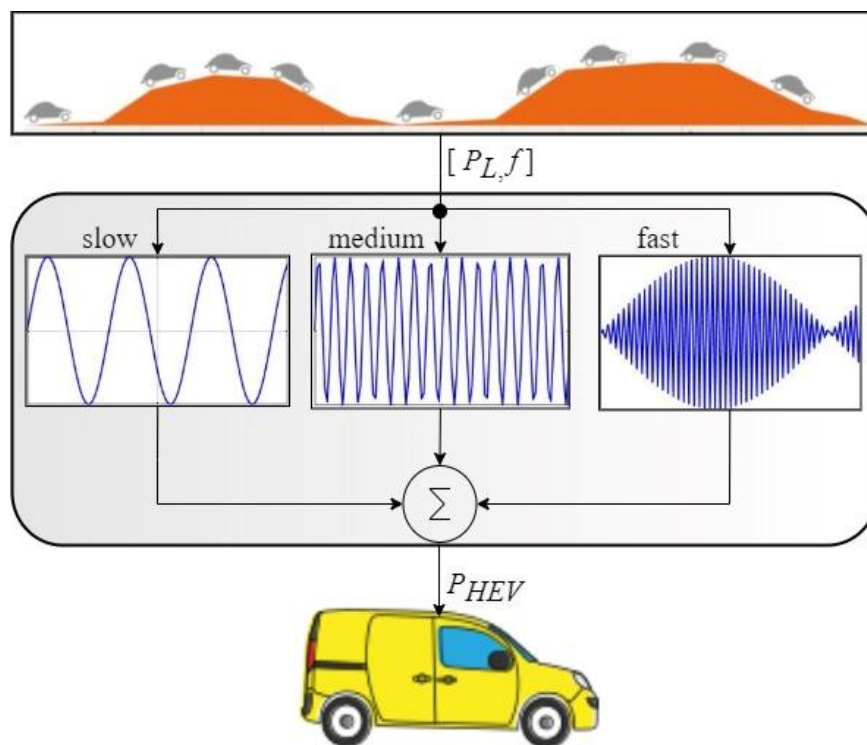
Figure 3.1 Classification of power sources usage.

3.2.1 Fuel cell transient dynamics

FC delivers power after chemical reactions and this causes important delay toward fast load variations. In [65], it has been stated that the reformer or the purifier, which is responsible of transforming fuel to pure hydrogen causes a time delay of several seconds. Purifier's dynamics are estimated to be of first order as it is highlighted in Figure 3.2,
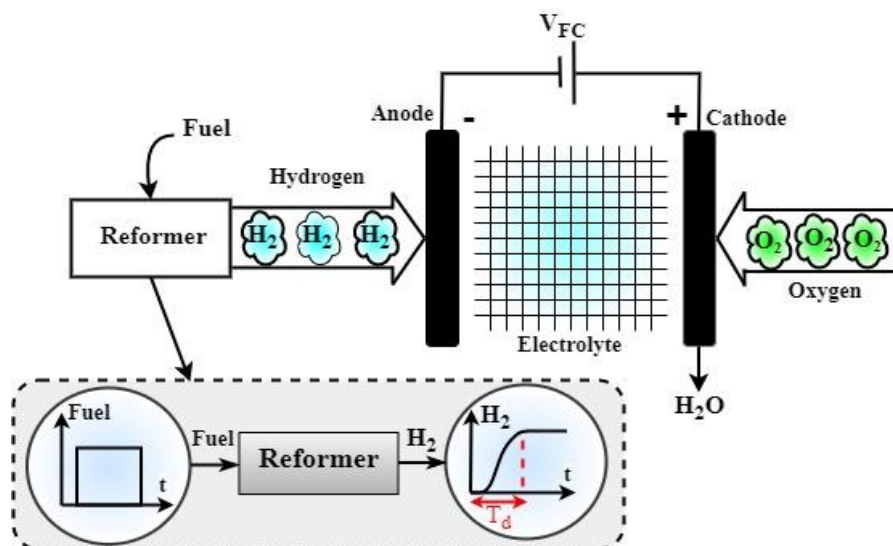
Figure 3.2 PEMFC scheme and reformer's dynamics.

The attenuation caused by the reformer will delay the whole FC response. To determine FC time constant, the no load and full load FC voltage equations are expressed using equations (3.1) and equation (3.2) respectively:

$$V_{FC,CELL} = E_{Nernst} - U_{act} - U_{con} - U_{ohm} \tag{3.1}$$

$$V_{FC,CELL} = E_{Nernst} - U_{act} - U_{con} - U_{ohm} - R_L i(t) \tag{3.2}$$

Where U_{con} is the concentration polarization due to the variation in gradients' concentration at FC anode and cathode and U_{act} is the activation polarization due to the slowness of chemical reactions at the two electrodes. U_{ohm} is the ohmic polarization that represents the voltage drop caused by the specific FC conductivity. Mathematical expressions that relate concentration, activation and ohmic polarizations to current are respectively given by equations (3.3, 3.4, 3.5).

$$U_{act} = \frac{RT}{znF} ln(i_0[i(t)]^{2.303}) \tag{3.3}$$

$$U_{con} = \frac{RT}{nF} ln\left(\frac{i_L - i(t)}{i_L}\right) \tag{3.4}$$

$$U_{ohm} = \frac{nFD}{\sigma(1 - t_i)} ln\left(\frac{i_L - i(t)}{i_L}\right) \tag{3.5}$$

Where R is the gas constant (8.314 Jmol^{-1}K^{-1}), T is the fuel cell temperature (K), z is the activity coefficient, n is the number of electrons in the FC reaction, F stands for Faraday's constant (96485.3 Cmol^{-1}), i_0 is the exchange current (A), $i(t)$ is the FC current (A), i_L is the limit current (A), σ is the equivalent conductance (m$^2\Omega^{-1}$) and t_i is the transference number. The linearization of FC current around an operating current i_X and the definition of three resistances $R_{act}(T)$, $R_{con}(T)$ and $R_{ohm}(T)$ yield the following set of the equation:

$$\begin{cases} \frac{\partial}{\partial i(t)}[U_{act}] = R_{act}(T)i(t) \\ \frac{\partial}{\partial i(t)}[U_{con}] = R_{con}(T)i(t) \\ \frac{\partial}{\partial i(t)}[U_{ohm}] = R_{ohm}(T)i(t) \end{cases} \tag{3.6}$$

Substituting equation (3.6) in equations (3.1) and (3.2) yield the following:

$$V_{FC,CELL} = E_{Nernst} - R_{act}(T)i(t) - R_{con}(T)i(t) - R_{ohm}(T)i(t) \tag{3.7}$$

$$V_{FC,CELL} = E_{Nernst} - R_{act}(T)i(t) - R_{con}(T)i(t) - R_{ohm}(T)i(t) - R_L(T)i(t) \tag{3.8}$$

From these two previous equations and by modeling the electric field that arises between the anode and the cathode by a capacity C, the FC equivalent circuits in cases of no and full loads are respectively presented in figures 3.3.a and 3.3.b.
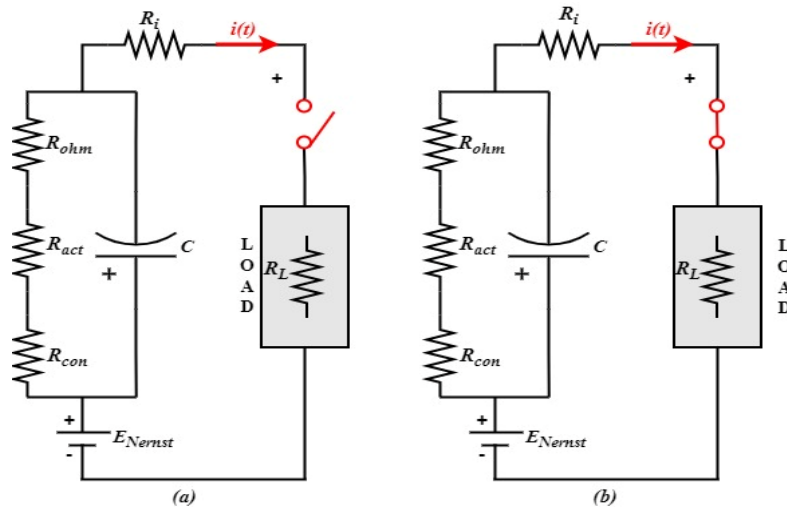
Figure 3.3 PEMFC electric circuit. (a)No load, (b)Full load.

From Figure 3.3, one can notice that, under no load connected to it, FC has no load time constant, τ_{FC}^{NL}, given by Equation (3.9) and when it is loaded, its time constant τ_{FC}^{FL} expressed using equation (3.10). These two last mentionned equations highlight the slowness of FC and show that it takes a well defined time to respond to transient peak demands. In [68], fuel cell transient delay is estimated to be $2.2\tau_{FC}^{NL}$. In [66-67], it is approximated to be $3\tau_{FC}^{NL}$.

$$\tau_{FC}^{NL} = (R_{act} + R_{con} + R_{ohm})C \tag{3.9}$$

$$\tau_{FC}^{FL} = \left[\frac{(R_{act} + R_{con} + R_{ohm})(R_i + R_L)}{(R_{act} + R_{con} + R_{ohm} + R_i + R_L)}\right]C \tag{3.10}$$

The voltage-current and power-current characteristics of one fuel cell stack are depicted in Figure 3.4. The green points on curves represent the nominal current, voltage and power of the used FC and the red points depict the maximum FC values, The FC is formed by a series connection of six FC stacks and each one is formed by serial grouping of N_s =68 which makes the stack nominal voltage approximately 48V.
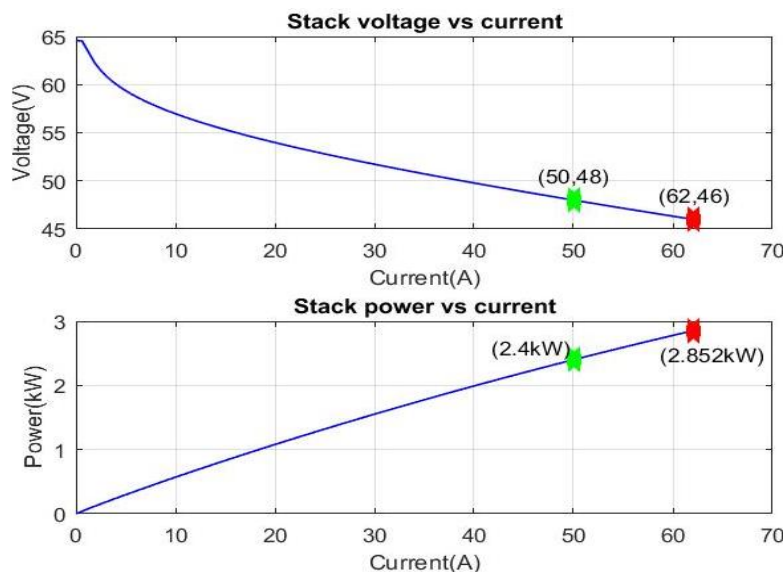
Figure 3.4 Fuel cell characteristic curves.

3.2.2 Battery dynamics

Batteries power HEVs and they are used as a storage element too. Even though lithium-ion battery is todays' preferred choice in the field of automotive engineering, there exist nonetheless a variety of other technologies such as lead-acid, nickel-cadmium, nickel-metal hybrid and solid-state batteries. The equivalent circuit of the Li-Ion battery used in this work is shown in Figure 3.5. It can be seen that Li-Ion battery model is made of charge and discharge models given respectively using equations (3.11) and (3.12).

$$V_{batt} = E_0 - \left(K\frac{Q}{Q-it}i^*\right) - \left(K\frac{Q}{Q-it}it\right) + Ae^{-Bit} \tag{3.11}$$

$$V_{batt} = E_0 - \left(K\frac{Q}{it+0.1Q}i^*\right) - \left(K\frac{Q}{Q-it}it\right) + Ae^{-Bit} \tag{3.12}$$

The low pass filter and the first order transfer function used in Li-ion battery model shown in Figure 3.5 represent the time delay required by the battery for the evolution and establishment of the reference voltage at its terminals. Authors in [65] estimated this delay using the battery equivalent model shown in Figure 3.6. They have concluded that the time required by the battery before the deliverance of reference current or power is nothing more than its full load time constant given by Equation (3.13) below:

$$\tau_1 = \left[\frac{(R_i + R_L)R_p}{(R_i + R_L) + R_p}\right]C_p \tag{3.13}$$
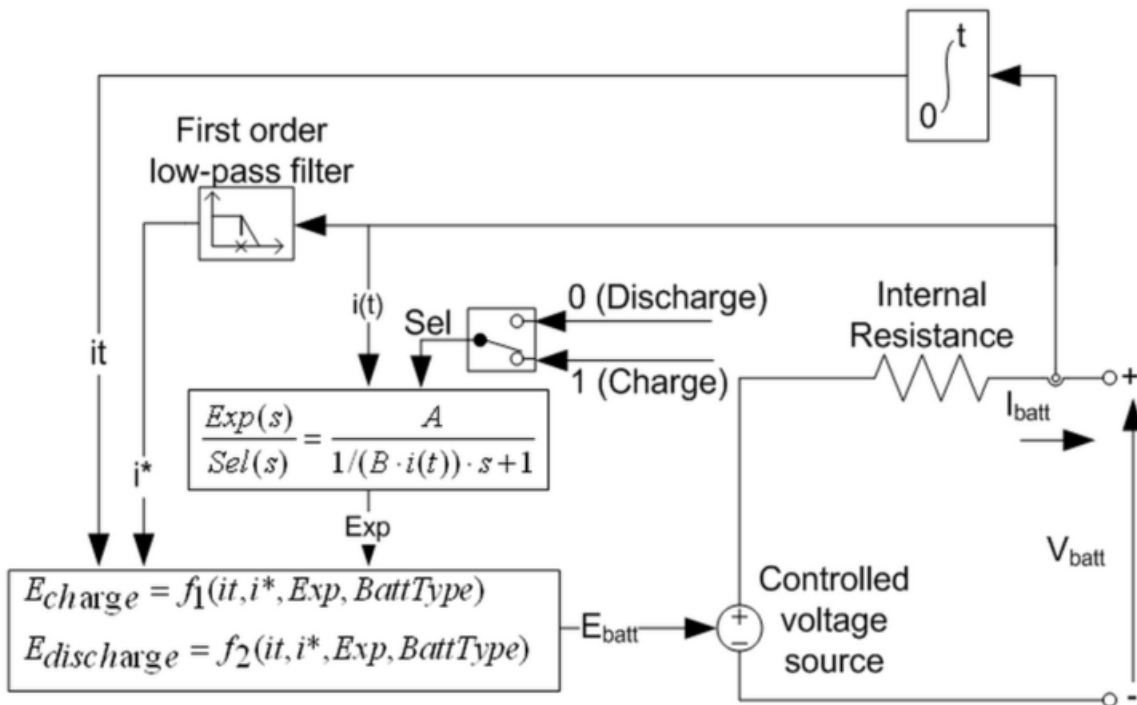
Figure 3.5 Fuel cell characteristic curves.
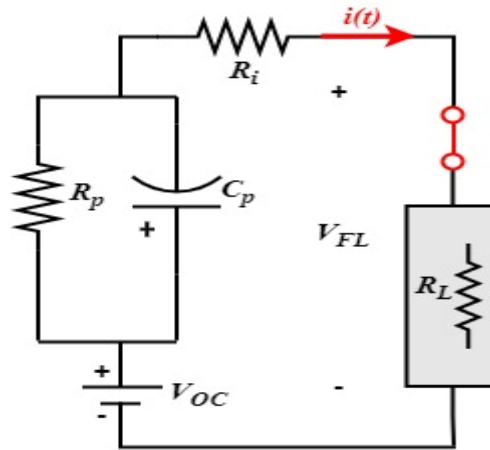
Figure 3.6 Li-Io battery electric circuit. (a) No load, (b) Full load.

The parameters of equations (3.11) and (3.12) are depicted in Figure 3.7 which represents the nominal discharge curve at nominal discharge current and the discharge curves at the specified discharge currents.
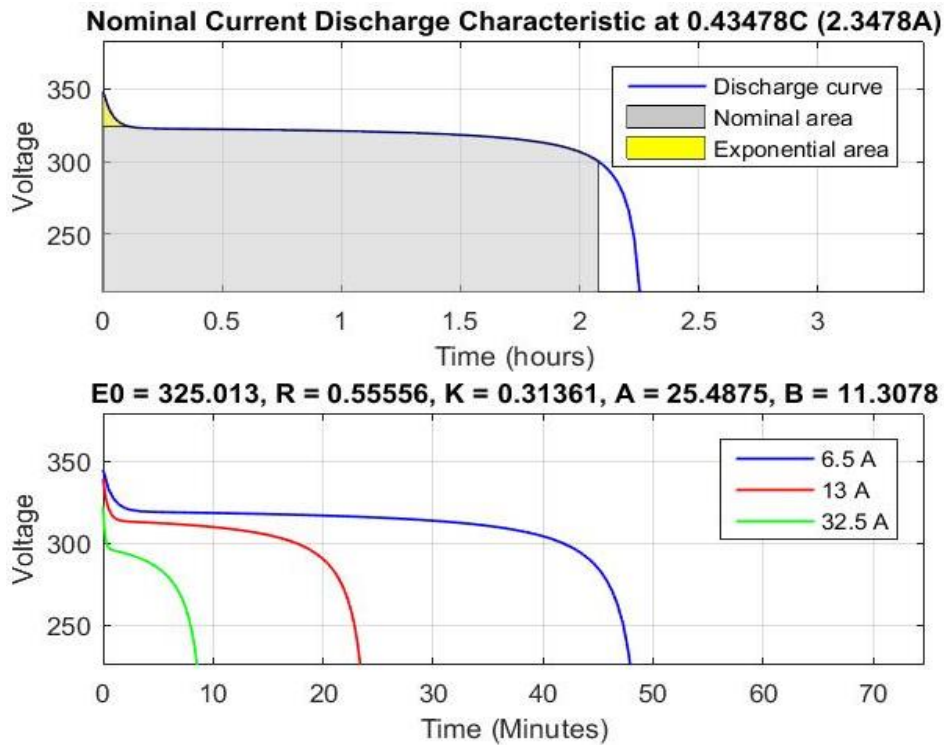
Figure 3.7 Li-Io battery discharge characteristics

Out of equations (3.9), (3.10) and (3.13), one can deduce that the transient response of FCs and Li-Ion batteries are different from each other. This causes miscoordination during switching instants and gives rise to undesired transient ripples. Furthermore, Some HEV power sources such as FC are sensitive and have a poor transient response. As it will be discussed in the forthcoming sections, these problems are addressed by a proposed coordinated switching strategy that considers power sources' slowness and protects them from damages that may be caused by sudden load variation.

3.3 Multi Stage Energy Management Strategy

The global HEV scheme is shown in Figure 3.8 in which the proposed multi stage energy management strategy is highlighted in dashed red lines. It can be seen that it is made of three main stages. In the first stage, a developed energy management algorithm determines the percentage of total power that will be delivered by FC based on BAT state of charge, level of required power (P_{HEV}) and power slope. The second stage detects possible failures in HEV power sources and corrects them via the reconfiguration of FC and BAT control loops to ensure continuous HEV operation. The control loops associated with HEV power sources are pointed out with blue dashed lines as it is shown in Figure 3.8. A new coordinated switching strategy is integrated into the third stage of the proposed energy management strategy to protect FC from the harmful transient power ripples noticed during power source switching and abrupt load variations. The last stage of the proposed energy management strategy is also intended to compensate for the difference in power sources transient dynamics and to ensure switchings with minimum transient ripples. Notice that FC and BAT are, respectively, connected to DC bus through bidirectional and unidirectional DC/DC converters. The inverter feeds the traction machine which will in turn drive the HEV wheels.
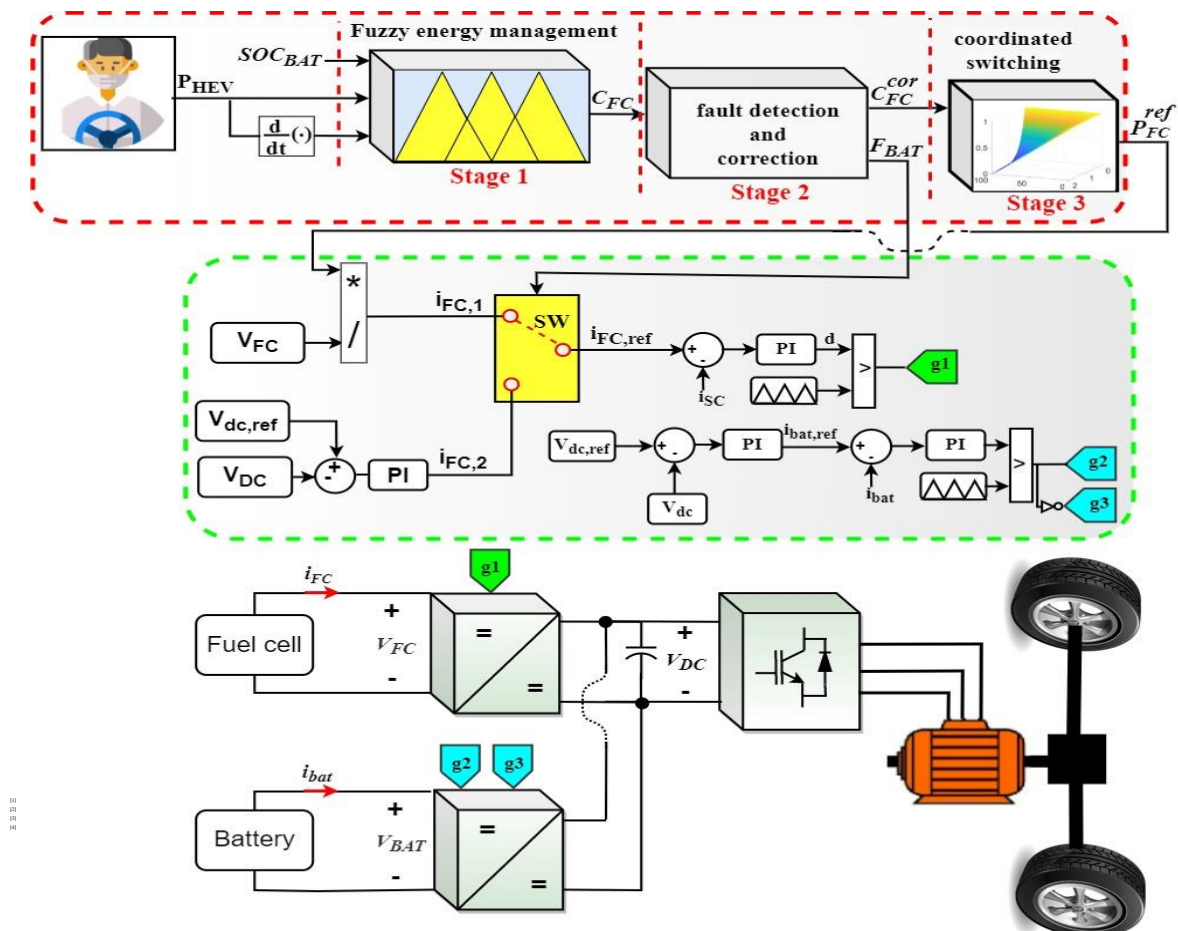
Figure 3.8 Global HEV system scheme.

The internal structure and the working principles of each stage of the proposed multi stage energy management strategy are explained in detail in the forthcoming sections:

3.3.1 Fuzzy energy management

At any instant, HEV power is expressed as the sum of FC and BAT powers as it is given in equation (3.14).

$$P_{HEV} = P_{FC}^{ref} + P_{FC}^{ref} \qquad (3.14)$$

In this work, the proposed power management algorithm is summarized by the following sentence: "At any driving instant, FC and BAT can deliver any desired fraction of the total power required for traction". This last sentence can be expressed mathematically as follow:

$$P_{HEV} = (C_{FC}^{cor} + C_{BAT}^{cor}) \ P_{HEV} \qquad (3.15)$$

Where C_{FC}^{cor} and C_{BAT}^{cor} are, respectively, the corrected FC and BAT power contribution factors that represent the percentage of total traction power that FC and BAT will deliver. These two factors are defined by equations (3.16) and (3.17) shown below.

$$C_{FC}^{cor} = \frac{P_{FC}^{ref}}{P_{HEV}} \qquad (3.16)$$

$$C_{BAT}^{cor} = 1 - C_{FC}^{cor} \qquad (3.17)$$

The fuzzy logic controller (FLC) shown in Figure 3.9 determines the amount of total power that will be delivered by the FC. To do so, BAT state of charge, traction power level and its slope are fuzzified using adequate membership functions. Figure 3.10 highlights the three trapezoidal membership functions used to fuzzify HEV power level. Notice that three fuzzy sets are used: P means low power, pM stands for medium power and pH signifies high power. The membership functions shown in Figure 3.11 fuzzify battery state of charge using four membership functions of type triangular and trapezoidal. The four sets used for battery SOC fuzzification and their corresponding symbols are as follow: L means low power, pM stands for medium power and pH signifies high power. Figure 3.12 shows the singleton membership functions used for C_{FC} deffuzification. Each singleton operates the FC at a given defined operating point. In this work, the FC can be operated at five distinct contribution factors. The surface maps shown in Figure 3.13 better explain the dependency between FLC inputs and outputs presented by their corresponding membership functions and the set of established fuzzy rules.
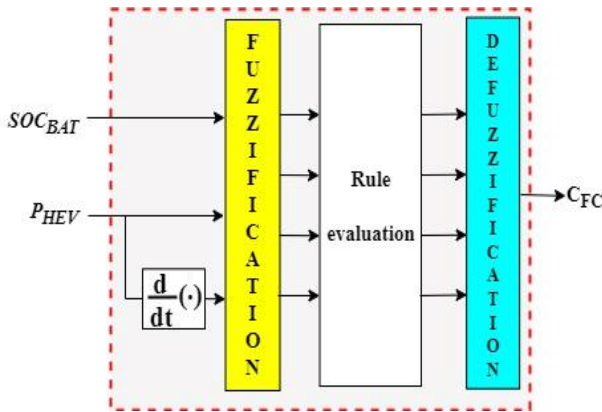
Figure 3.9 Fuzzy logic controller.
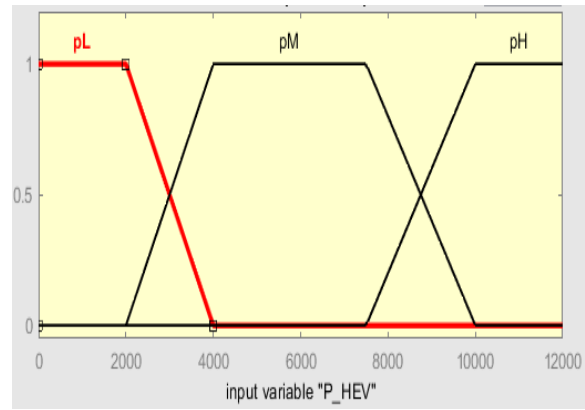
Figure 3.10 Fuzzification of HEV power.
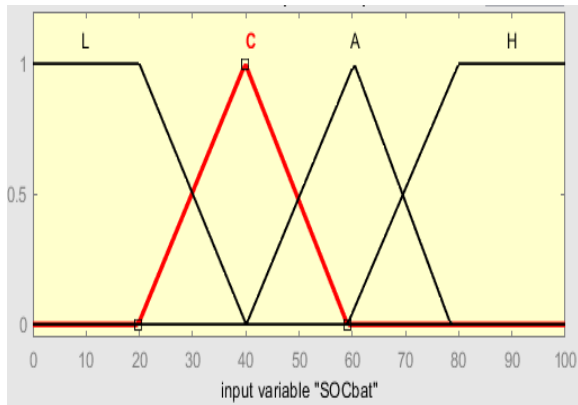
Figure 3.11 Battery SOC fuzzification.
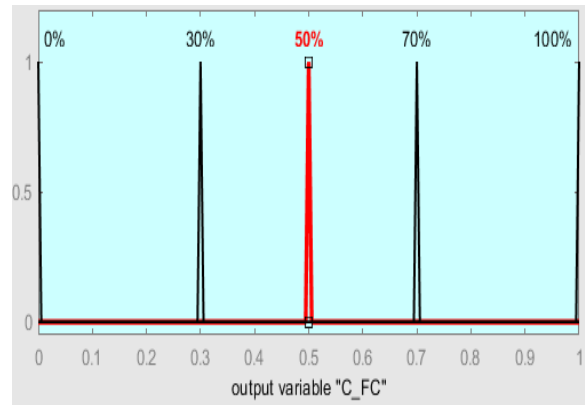
Figure 3.12 C_{FC} membership functions.
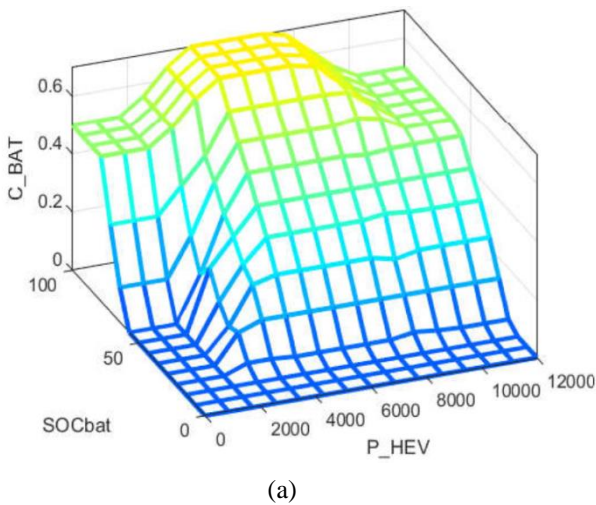
(a)
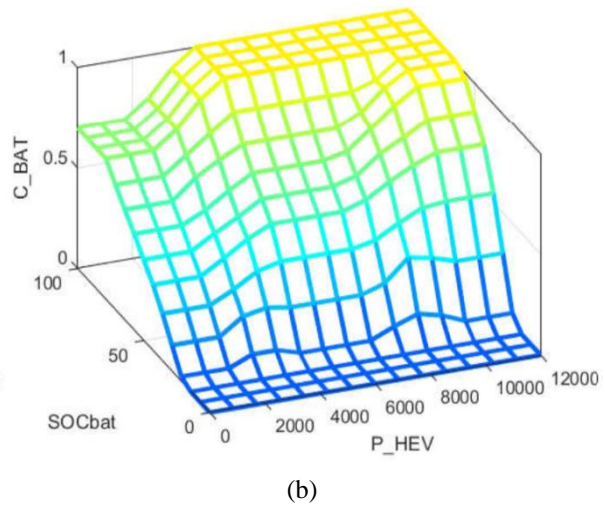
(b)

Figure 3.13 FLC surface map during: (a) acceleration; (b) deceleration

3.3.2 Failure detection and correction

Many research works [70-71] designed correction strategies for possible failures in HEV components that are more robust than FC and BAT. In this chapter, possible failures in HEV power sources are considered during the design of the design of the proposed energy management strategy. Table 3.1 shown below explains the operating principle of the fault detection and correction bloc.

Table 3.1 Fault correction truth table.

F_{FC}	F_{BAT}	C_{FC}^{cor}	C_{BAT}^{cor}	$i_{FC,ref}$	$i_{BAT,ref}$
0	0	C_{FC}	C_{BAT}	$\dfrac{P_{FC}^{ref}}{V_{DC}}$	$C_{BAT}\dfrac{P_{HEV}}{V_{DC}}$
0	1	100%	isolated	$\dfrac{P_{HEV}}{V_{DC}}$	0
1	0	isolated	100%	0	$\dfrac{P_{HEV}}{V_{DC}}$

Note that in the absence of failures ($F_{BAT} = F_{FC} = 0$), the output of the fault detection and correction bloc shown in Figure 3.14 is equal to one of the fuzzy energy management defined by equation (3.18). Under normal operating mode ($F_{BAT}=0$, $F_{FC}=0$), the BAT regulates DC bus voltage and FC receives a reference current $i_{FC,ref}=i_{FC,1}$ that allows it to deliver C_{FC}^{cor} of the total power required for traction. When a failure occurs at battery level ($F_{BAT}=1$), the FC control loop will be reconfigured and the FC will receive a reference power $i_{FC,ref} = i_{FC,2}$ that lets it deliver all the required power for traction ($C_{FC}^{cor}=100\%$) while ensuring dc bus voltage stability. When a failure occurs at FC level ($F_{FC}=1$), C_{BAT}^{cor} will toggle from its value to 100% and the battery current will also increase. Figure 3.14 depicts the internal structure of FC fault detection bloc used in this work.
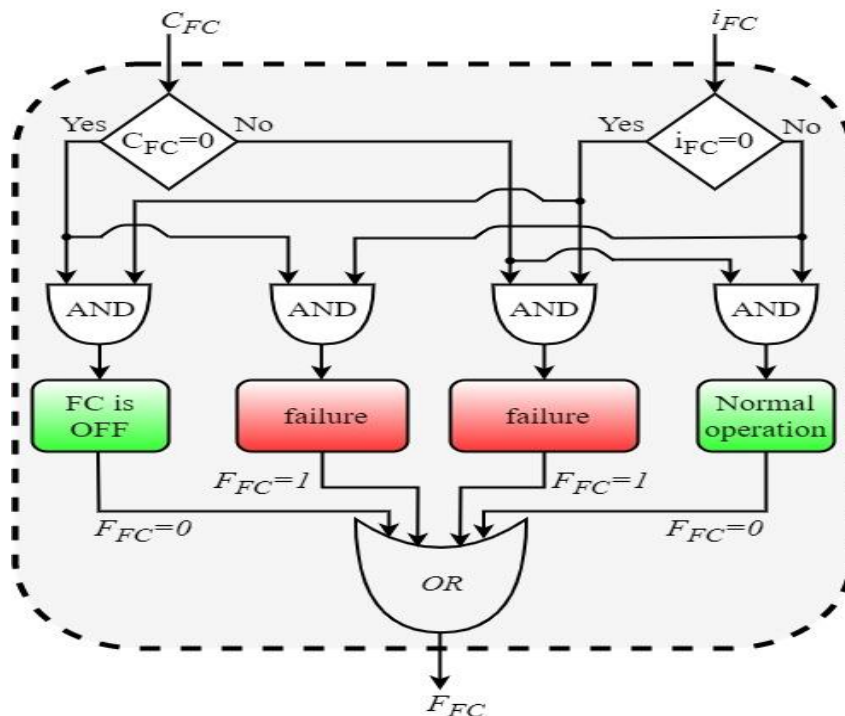
Figure 3.14 Internal structure of FC failure detection bloc.

3.3.3 Coordinated switching strategy

Large transient ripples are observed during abrupt power source switching [72-73]. These ripples, which reduce riding comfort, are primarily caused by differences in the transient responses of HEV power sources. To address this problem, a coordinated switching strategy is proposed in this chapter to improve low HEV performance during switching instants. Mathematically, variations in FC reference power $P_{FC}(t)$ between two distinct instants t_1 and t_2 are expressed using equation (3.18):

$$\frac{\Delta P_{FC}}{\Delta t} = \frac{P_{FC}(t_2) - P_{FC}(t_1)}{t_2 - t_1} \tag{3.18}$$

For the sake of real time implementation of equation (3.18), only fixed step solvers, with sampling time T_s, are considered. Hence, the last mentioned equation becomes:

$$\frac{\Delta P_{FC}}{\Delta t} = \frac{P_{FC}(t + T_s) - P_{FC}(t)}{T_s} \tag{3.19}$$

Fast FC power variations can be expressed at any instant using equation (3.20):

$$\lim_{T_s \to 0} \left[\frac{P_{FC}(t + T_s) - P_{FC}(t)}{T_s} \right] = \frac{dP_{FC}(t)}{dt} \tag{3.20}$$

Using equation (3.14- 3.17), the instantaneous transient ripples arising during switching instants are expressed using equation (3.21) shown below:

$$\frac{dP_{HEV}}{dt} = \left[C_{FC}^{cor} \frac{dP_{FC}}{dt} + P_{FC} \frac{dC_{FC}^{cor}}{dt} \right] + \left[C_{BAT}^{cor} \frac{dP_{BAT}}{dt} + P_{BAT} \frac{dC_{BAT}^{cor}}{dt} \right] \tag{3.21}$$

Equation (3.22) provides a numerical approximation of each left-hand side term of equation (3.21). T_s in Equation (3.22) represents the calculation step. Derivative of T_{m1} and T_{m2} are equal to zero because the torque developed by PMSM1 and PMSM2 between t and $t+T_s$ is nearly the same.

$$\begin{cases} \frac{dP_{FC}}{dt} \approx \left[\frac{P_{FC}(t + T_s) - P_{FC}(t)}{T_s} \right] \approx 0 \\ \frac{dP_{BAT}}{dt} \approx \left[\frac{P_{BAT}(t + T_s) - P_{BAT}(t)}{T_s} \right] \approx 0 \\ \frac{dC_{FC}^{cor}}{dt} \approx \left[\frac{C_{FC}^{cor}(t + T_s) - C_{FC}^{cor}(t)}{T_s} \right] \approx \frac{\Delta C_{FC}^{cor}}{T_s} \\ \frac{dC_{BAT}^{cor}}{dt} \approx \left[\frac{C_{BAT}^{cor}(t + T_s) - C_{BAT}^{cor}(t)}{T_s} \right] \approx \frac{\Delta C_{BAT}^{cor}}{T_s} \end{cases} \tag{3.22}$$

Equation (3.22) can be rewritten using the approximations of Equation (3.23) as follows:

$$\frac{dP_{HEV}}{dt} \approx C_{FC}^{cor}\left(\frac{\Delta C_{FC}^{cor}}{T_s}\right) + C_{BAT}^{cor}\left(\frac{\Delta C_{BAT}^{cor}}{T_s}\right) \tag{3.23}$$

Because T_s is in the order of 10^{-6}, the two ratios on the right-hand side of equation (3.21) will result in significant transient ripples that reduce HEV driving comfort during drive mode switchings and reduce HEV power source lifespan. To avoid the aforementioned drawbacks, a coordinated switching strategy that smoothens drive mode switchings is proposed in this work and its basic steps are shown in the flowchart of figure 3.15.
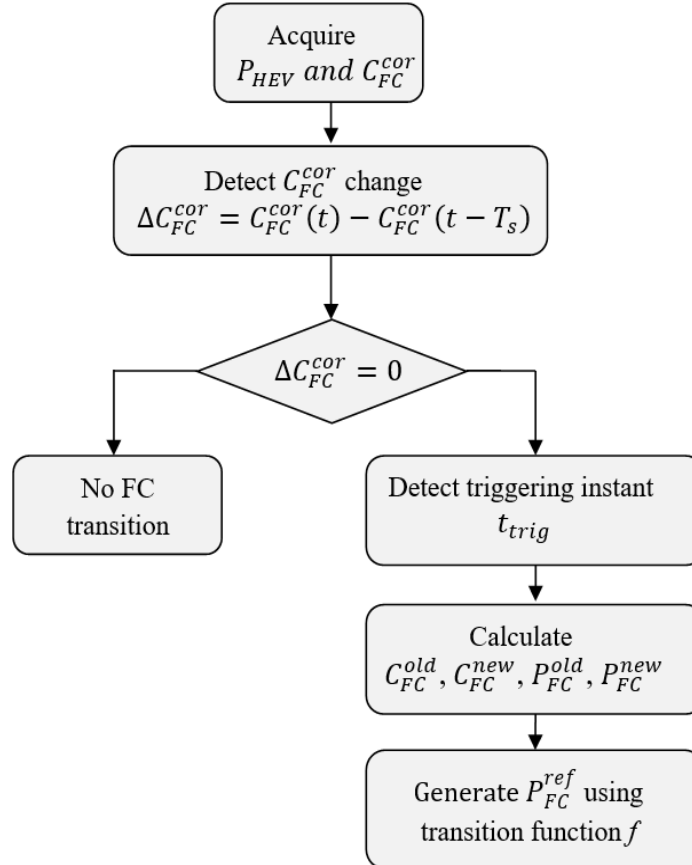
Figure 3.15 FC coordinated the switching flowchart.

The old and the new FC operating points are calculated as given in Equation (3.24) where t_{trig} is the time instant at which a change in C_{FC} is detected.

$$\begin{cases} C_{FC}^{new} = C_{FC}^{cor}(t_{trig}) \\ C_{FC}^{old} = C_{FC}^{cor}(t_{trig} - T_s) \end{cases} \tag{3.24}$$

Old and new FC power references are then calculated as given in equation (3.25):

$$\begin{cases} P_{FC}^{old} = C_{FC}^{old} P_{HEV} \\ P_{FC}^{new} = C_{FC}^{new} P_{HEV} \end{cases} \tag{3.25}$$

The exponential transition function given by equation (3.26) is used to provide coordinated FC and BAT switching. This function is used mainly because many electric phenomena follow

exponential law during their evolution. Using Equation (3.24) and Equation (3.25), FC and BAT reference powers can be expressed as given in Equations (3.27) and (3.28) respectively. Figure 3.16 illustrates how FC operating point is toggled from its actual to its new operating point smoothly following an exponential transition function.

$$P_{FC}^{ref}(t) = \left[\left(P_{FC}^{old} - P_{FC}^{new}\right)e^{-\frac{(t-t_{trig})}{\tau_{FC}^{FL}}} + P_{FC}^{new} \right] \qquad (3.26)$$

$$P_{FC}^{ref}(t) = \left[\left(C_{FC}^{old} - C_{FC}^{new}\right)e^{-\frac{(t-t_{trig})}{\tau_{FC}^{FL}}} + C_{FC}^{new} \right] P_{HEV} \qquad (3.27)$$

$$P_{BAT}^{ref}(t) = \left[1 - C_{FC}^{new} - \left(C_{FC}^{old} - C_{FC}^{new}\right)e^{-\frac{(t-t_{trig})}{\tau_{FC}^{FL}}} \right] P_{HEV} \qquad (3.28)$$
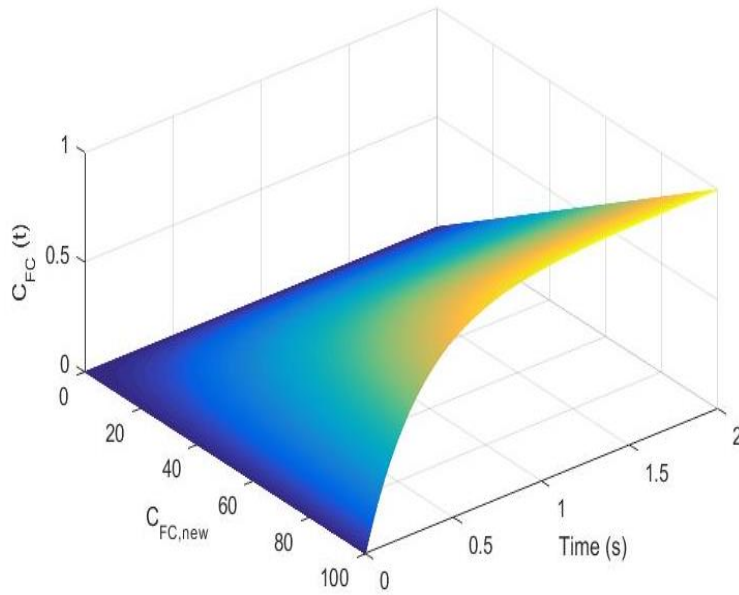
Figure 3.16 Three dimensional exponential C_{FC} evolution.

3.4 Numerical Simulation Results

SOC$_{SC}$ is depicted in Figure 3.17 along with FC contribution factor C_{FC}. One can note that SOC$_{SC}$ is maintained within safe limits during all HEV rides and this is the result of good power management. A zoom of figure 3.17 during [0; 8 s] is presented in figure 3.18. The green waveform on it represents C$_{FC}$ which is shifted on the y axis for more figure clarity. The battery discharge rate in zone 3 (Z$_3$) is greater than the one in Z$_1$. This is because the battery is delivering 100% of the required power for traction in Z$_3$ whereas in Z$_1$, it is delivering only 70% of the required power for traction. One can conclude that the proposed power management

strategy controls BAT depth of discharge via the control of C_{FC}. The greater C_{FC} value, the slower the BAT depth of discharge will be. In Z_2, $C_{FC}=100\%$. This means that FC is off and its SOC will remain constant.
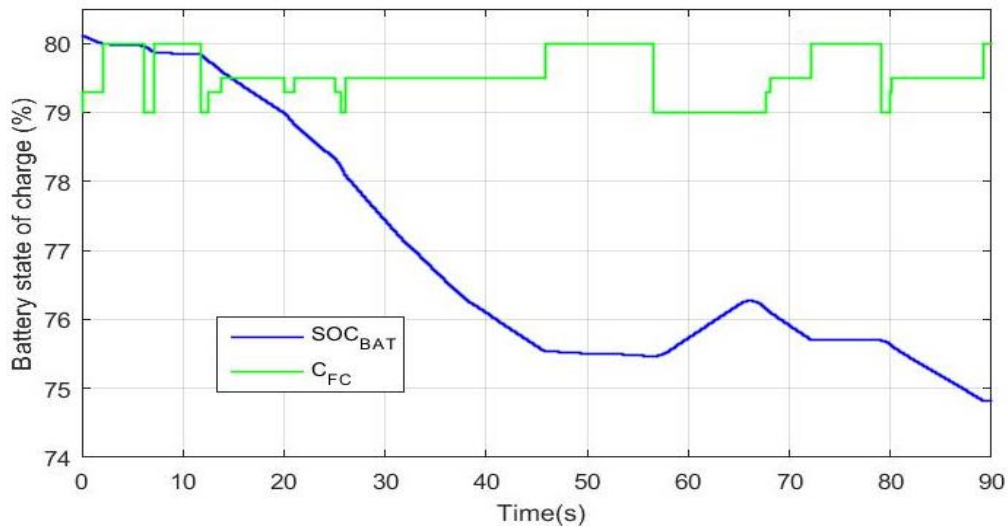
Figure 3.17 Battery state of charge.
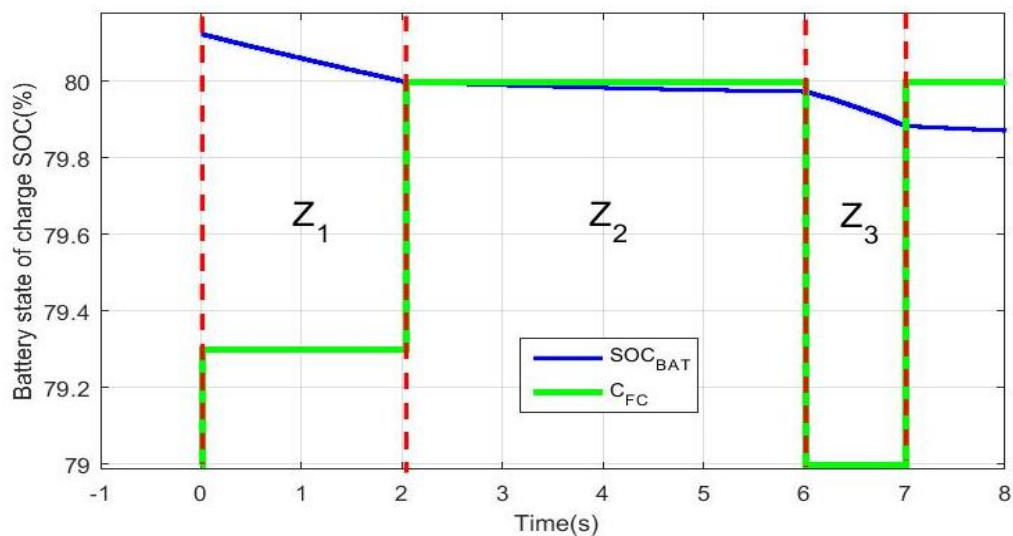
Figure 3.18 Zoom of battery state of charge.

The Initial FC and BAT contribution factors generated by the power management algorithm are respectively shown in figures 3.19.a and 3.19.b. FC and BAT fault signals are depicted in figures 3.19.c and 3.19.d respectively. The corrected FC and BAT contribution factors are respectively shown in figures 3.19.e and 3.19.f. One can remark that in the absence of faults, C_{BAT} equals corrected C_{BAT} and C_{FC} equals corrected C_{FC} and this means that the decision generated by the power management algorithm doesn't have to be corrected.

- A temporary failure occurred in BAT during [69; 71] as it is highlighted with magenta dashed lines. The fault detection algorithm has detected the fault and set $F_{BAT}=1$. This setting has isolated the faulty power source by setting C_{BAT} to zero and caused C_{FC} to change from 50%

to 100% through the reconfiguration of FC control loop shown in Figure 3.8.

- The green dashed lines highlight a permanent FC failure as it was delivering 50% of the required traction power. As the fault occurred, F_{FC} state toggled to 1 and this has modified the C_{BAT} to 100% which means that BAT will regulate DC bus voltage and provide all the required traction. It can be concluded that the proposed multi stage power management strategy increases the security of the electric vehicle and reduces the failure possibility.
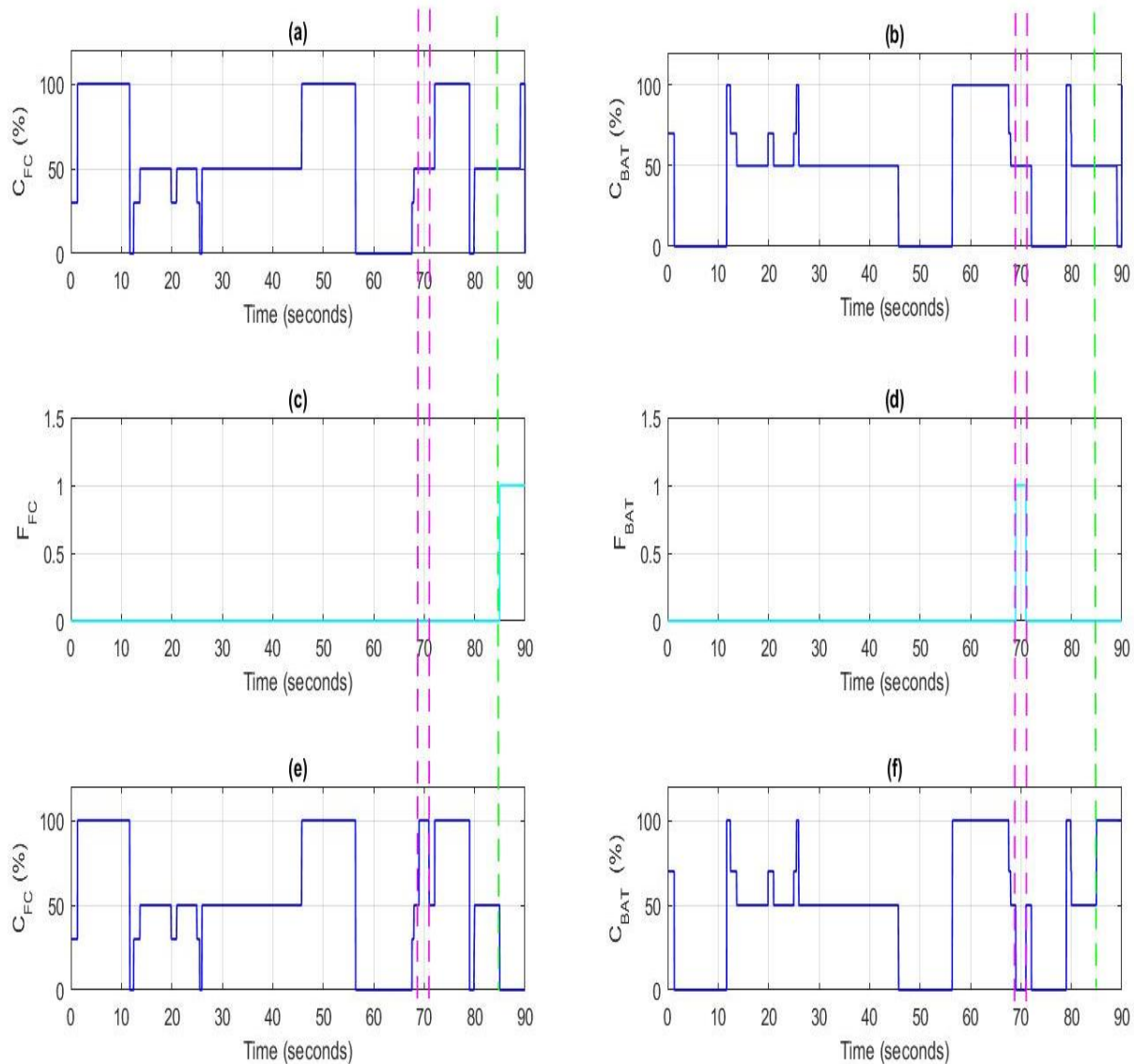
Figure 3.19 Initial and final FC-BAT contribution factors.

FC and BAT powers are highlighted respectively in figure 3.20.a and 3.20.b. The behavior of FC and BAT during each of the highlighted zones is as follows:

Zone 01: FC delivers 0.9 kW and BAT delivers 3.5 kW. This means that FC delivers 30% of the required power and BAT delivers the remaining.

Zone 02: FC delivers 100% of the required traction power and BAT is off

Zone 03: FC and BAT deliver 3.7 kW which represents half the total required power.

Zone 04: BAT delivers 3.7 kW which is the total required power and the FC is off

Zone 05: FC is off and BAT is charging (regenerative braking).

BAT fault: Before fault occurrence, both FC and BAT were delivering 50% of the required traction power. When BAT is in a failure state ($F_{BAT}=1$), it is disconnected and FC toggles from 50% to 100% contribution which means that it delivers all the required traction power.

FC fault: Before fault occurrence, both power sources deliver 50% of the required traction power. When FC is in a failure state ($F_{FC}=1$), it is isolated and BAT delivers 100% of the required traction power.
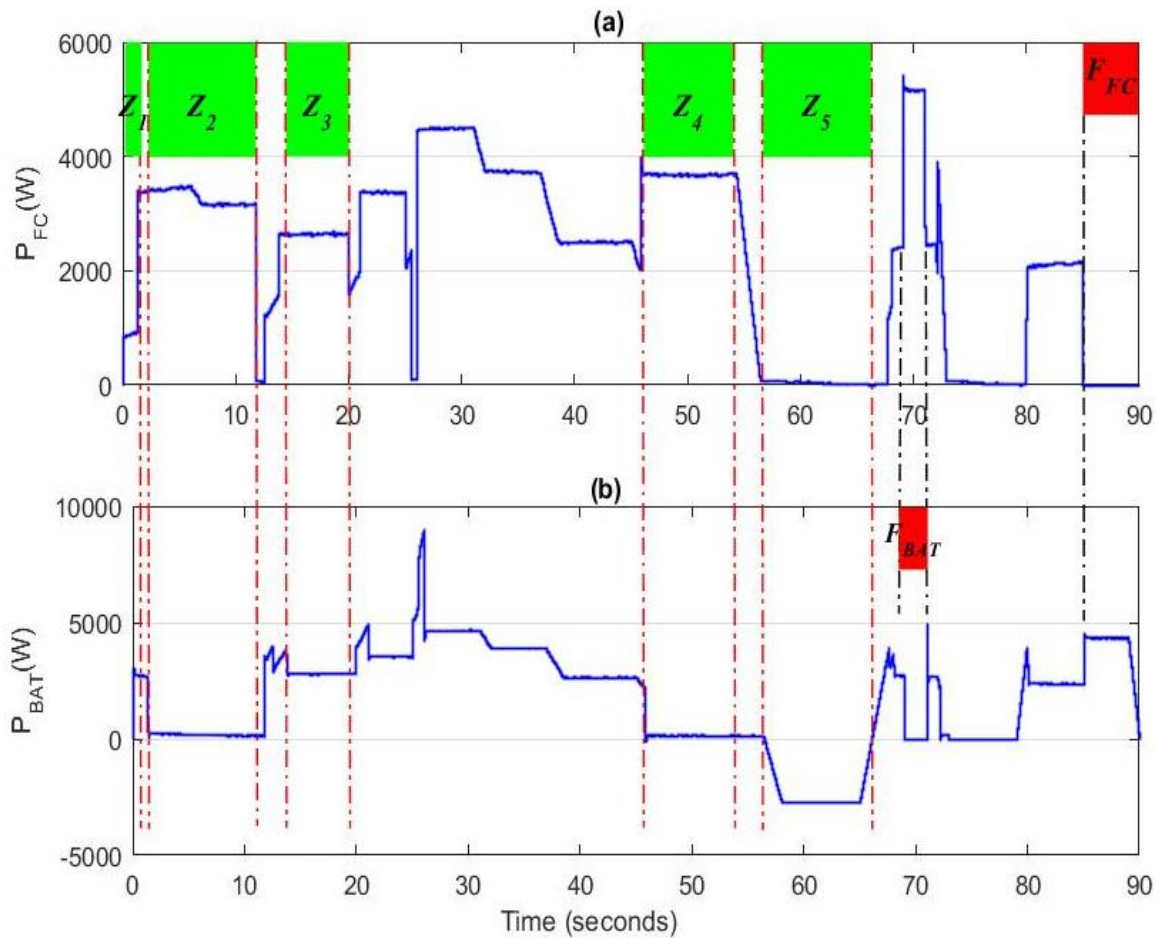
Figure 3.20. FC and *BAT* powers.

One can deduce that the proposed management algorithm reduces the stress applied to the primary power source (FC) and controls precisely the amount of power to be delivered by each power source. Figures 3.21 and 3.22 present respectively the sum of FC and BAT powers along with the required traction power using coordinated and non coordinated switching. In both cases, the sum of FC and BAT powers tracks the reference traction power. Large and harmful transient ripples are noticed during each non coordinated C_{FC} variation. However, coordinated switching eliminated the transient peaks.
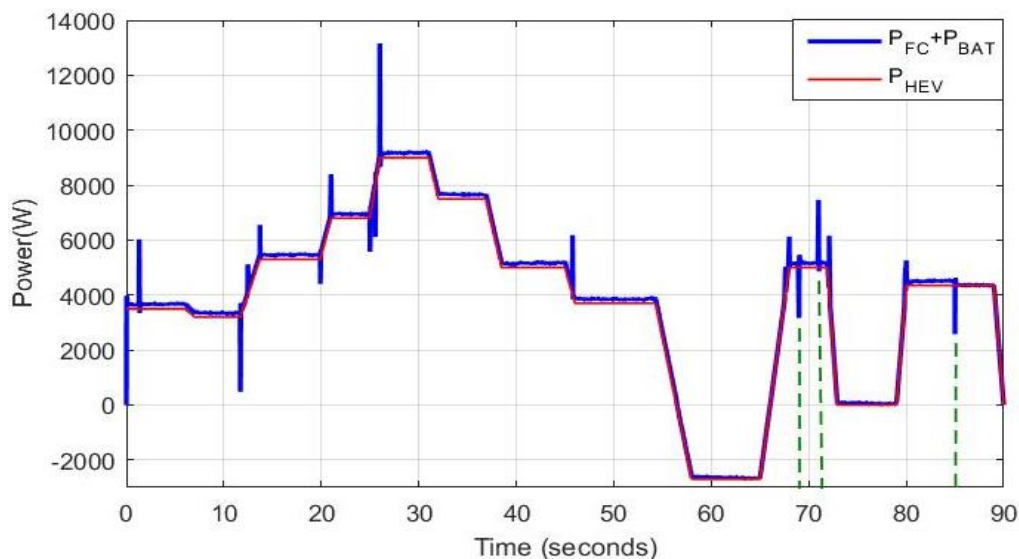
Figure 3.21 HEV power without coordination.
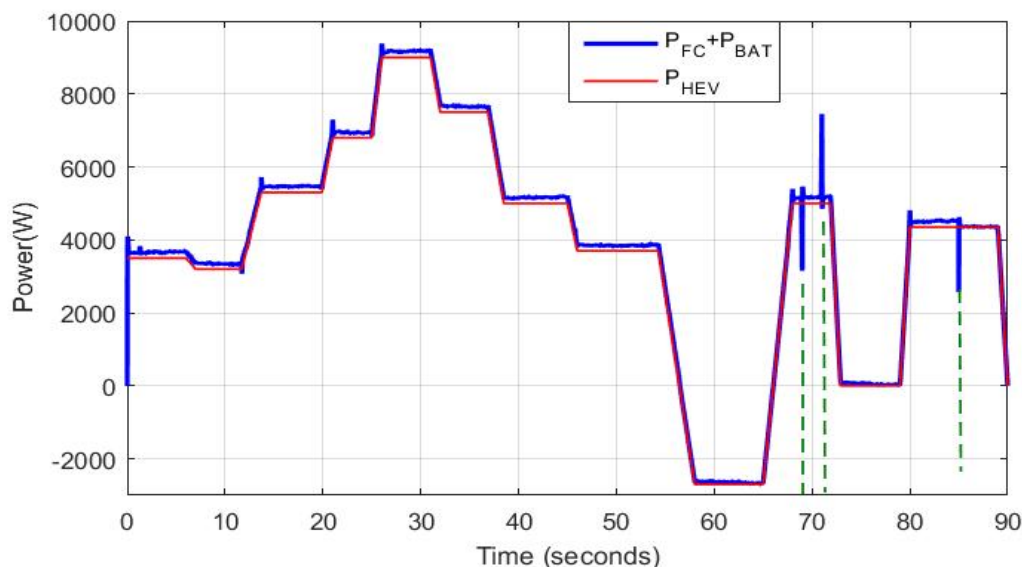
Figure 3.22 HEV developed power with coordination.

Figure 3.23.a and 3.23.b are zooms of figure 3.21 and figure 3.22, respectively. During the time instants [11.65; 11.82]. It can be seen that the proposed coordinated switching strategy inserted in the last stage of the energy management strategy compensated for the difference between FC and BAT transient responses and has compensated for FC slowness also. From Figure 3.23.b, switchings between FC and BAT are performed within T_{FC} and this protects sensitive power sources such as FC from large and abrupt currents that may cause their damage. Using non coordinated switching, the power conservation equation given by equation (3.14) is violated and it can be seen that at $t=11.71$ s, P_{HEV} is 3.1 kW whereas the sum of FC and BAT power is less than that value. This power lack caused the significant transient peak shown in figure 3.22 at $t=11.71$ s. Figure $24.b$ shows that FC/BAT switching performed using the

coordinated switching respected the power conservation equation given by equation (3.14). At each instant, during the transition period [t_{trig}; $t_{trig}+T_{FC}$] the developed power sources and the required traction power are almost the same and this suppressed the transient peak at t=11.71 as can be seen in figure 3.23.b.
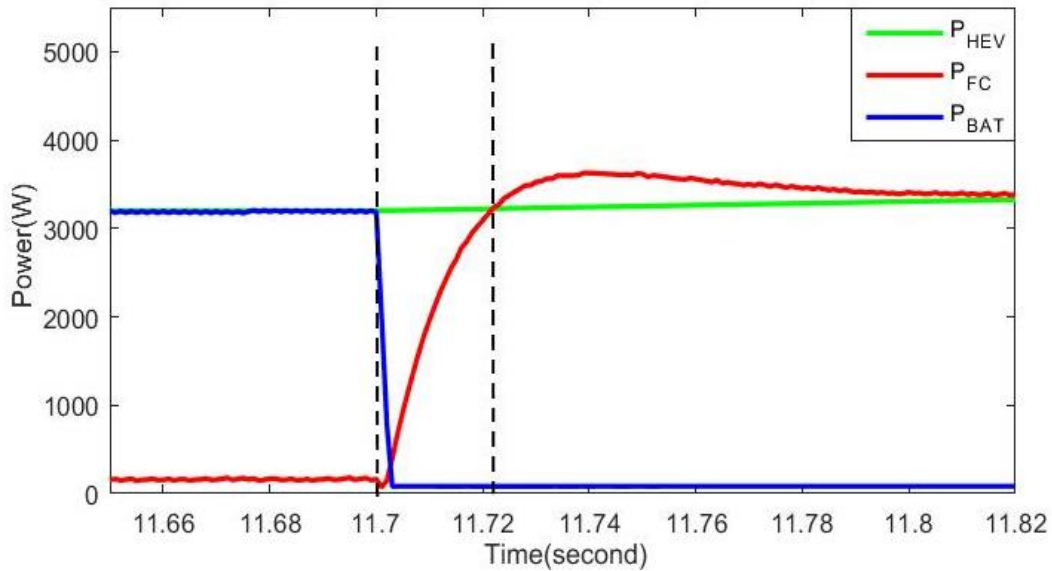
(a)
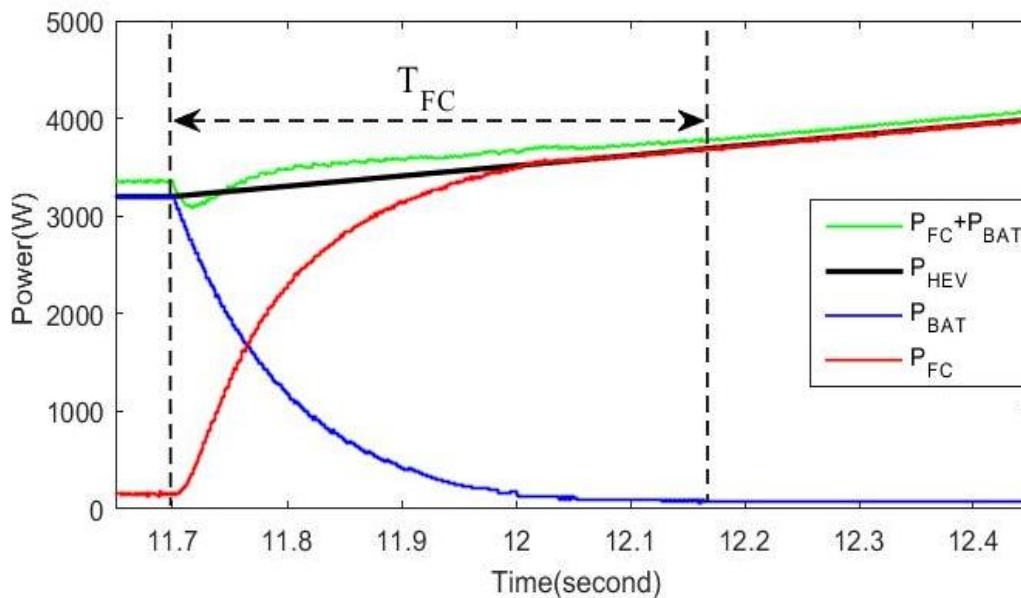
(b)

Figure 3.23. Zoom of switching instant: (a) non coordinated (b) coordinated.

Figure 3. 24 shows the DC bus voltage when FC and BAT are switched using coordinated and non-coordinated switching. One can see that coordinated switching has contributed to the reduction of DC voltage ripples in comparison to non-coordinated switching.
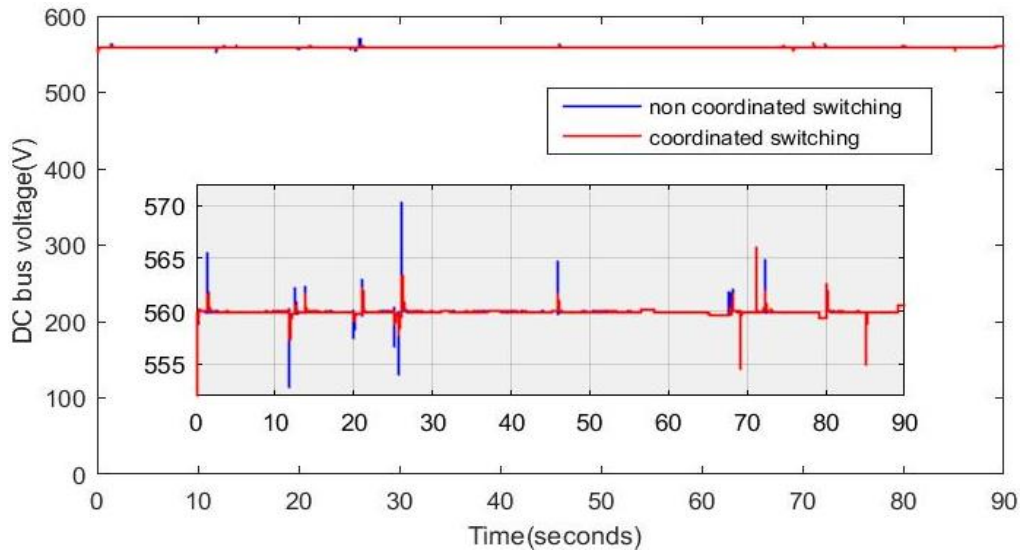
Figure 3.24. DC bus voltage.

To point out the added value provided by the third stage of the proposed energy management strategy, a comparison is performed to other published works as it is shown in Figure 3.25. The comparison is made in terms of voltage percentage overshoot and transient power peaks defined, respectively, using equations (3.29) and (3.30). It could be seen that the coordinated switching strategy via the proposed transition function has resulted in the significant and simultaneous reduction of DC bus voltage and transient power ripples. Note that the proposed coordinated strategy resulted in a voltage percentage overshoot of 0.4% and a maximum transient power ripples of 480 W.

$$PO_V = 100 * \max \left| \frac{V_{DC} - V_{DC,ref}}{V_{DC,ref}} \right| \tag{3.29}$$

$$\Delta P = \max \left| P_{HEV} - \left(P_{FC} + P_{BAT} \right) \right| \tag{3.30}$$
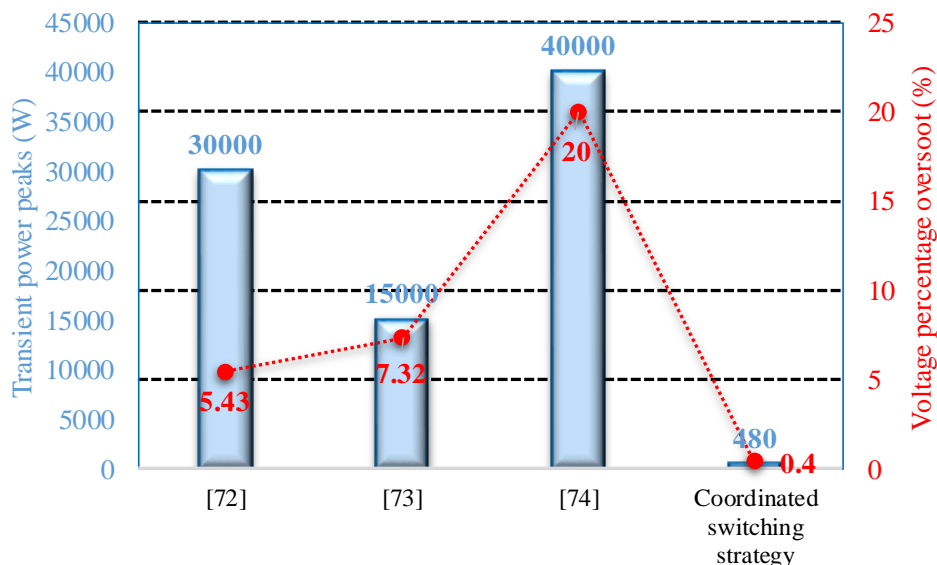
Figure 3.25 Comparison to other published works.

To investigate the effect of the transition function on HEV transient performances during switching instants during C_{FC} variations, a comparison is made between the used exponential transition function given by Equation 3.26 and 3.27, stair based transition function given by equation (3.31) and the linear transition function highlighted by equation (3.32). The comparison results are shown in Figure 3.27. It can be deduced that all the transition functions resulted in minimizing transient power ripples and DC bus voltage. In particular, the exponential transition function resulted in minimum DC bus voltage ripples of 6 V and a transient power peak of 608V.

$$
\begin{cases}
P_{FC}^{ref}\left(t_{trig} + i\delta_{FC}\right) = \left[C_{FC}^{old} + i\left(\frac{C_{FC}^{new} - C_{FC}^{old}}{m}\right)\right] P_{HEV} \\[4mm]
P_{BAT}^{ref}\left(t_{trig} + i\delta_{FC}\right) = \left[1 - C_{FC}^{old} - i\left(\frac{C_{FC}^{new} - C_{FC}^{old}}{m}\right)\right] P_{HEV} \\[4mm]
T_{FC} = m\delta_{FC}
\end{cases}
\tag{3.31}
$$

$$
\begin{cases}
P_{FC}^{ref}(t) = \begin{cases} \left[\left(\dfrac{C_{FC}^{new} - C_{FC}^{old}}{T_{FC}}\right)\left(t - t_{trig}\right) + C_{FC}^{old}\right] P_{HEV} & t_{trig} \leq t \leq t_{trig} + T_{FC} \\[3mm] P_{FC}^{new} & t_{trig} > t_{trig} + T_{FC} \end{cases} \\
\text{-----------------------------------} \\
P_{BAT}^{ref}(t) = \begin{cases} \left[\left(\dfrac{C_{SC}^{new} - C_{SC}^{old}}{T_{FC}}\right)\left(t - t_{trig}\right) + C_{SC}^{old}\right] P_{HEV} & t_{trig} \leq t \leq t_{trig} + T_{FC} \\[3mm] P_{BAT}^{new} & t_{trig} > t_{trig} + T_{FC} \end{cases}
\end{cases}
\tag{3.32}
$$
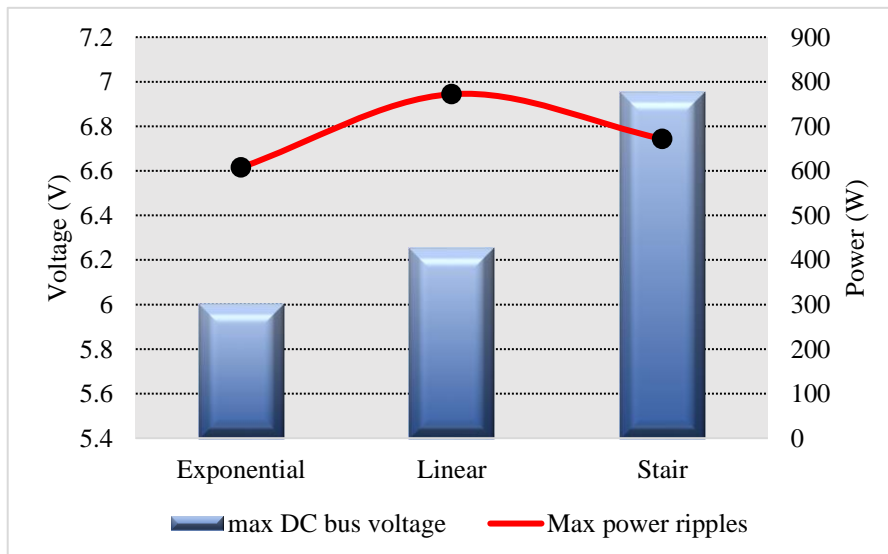
Figure 3.26 Comparison between the used switching techniques.

3.5 RT LAB Simulation

This section discusses the real time feasibility of each stage of the proposed multi stage power management strategy. Real time simulation is performed using OPAL RT LAB simulator. As is shown in figure 3.27, the first step toward real time simulation is the model separation. HEV system is splitted into computation and console blocs. Blocs that contain computations such as the coordination control strategy, HEV model, FC and SC models are placed on the computation subsystem. Scopes and constants are placed in the console bloc. *Each* computation subsystem will be executed on one CPU core of the RT simulator. Data between the computation subsystem and console are exchanged asynchronously through the TCP/IP link but data exchange between the two computation subsystems is performed synchronously through shared memory. Data from RT simulator are displayed on the digital oscilloscope using BNC to BNC cable.
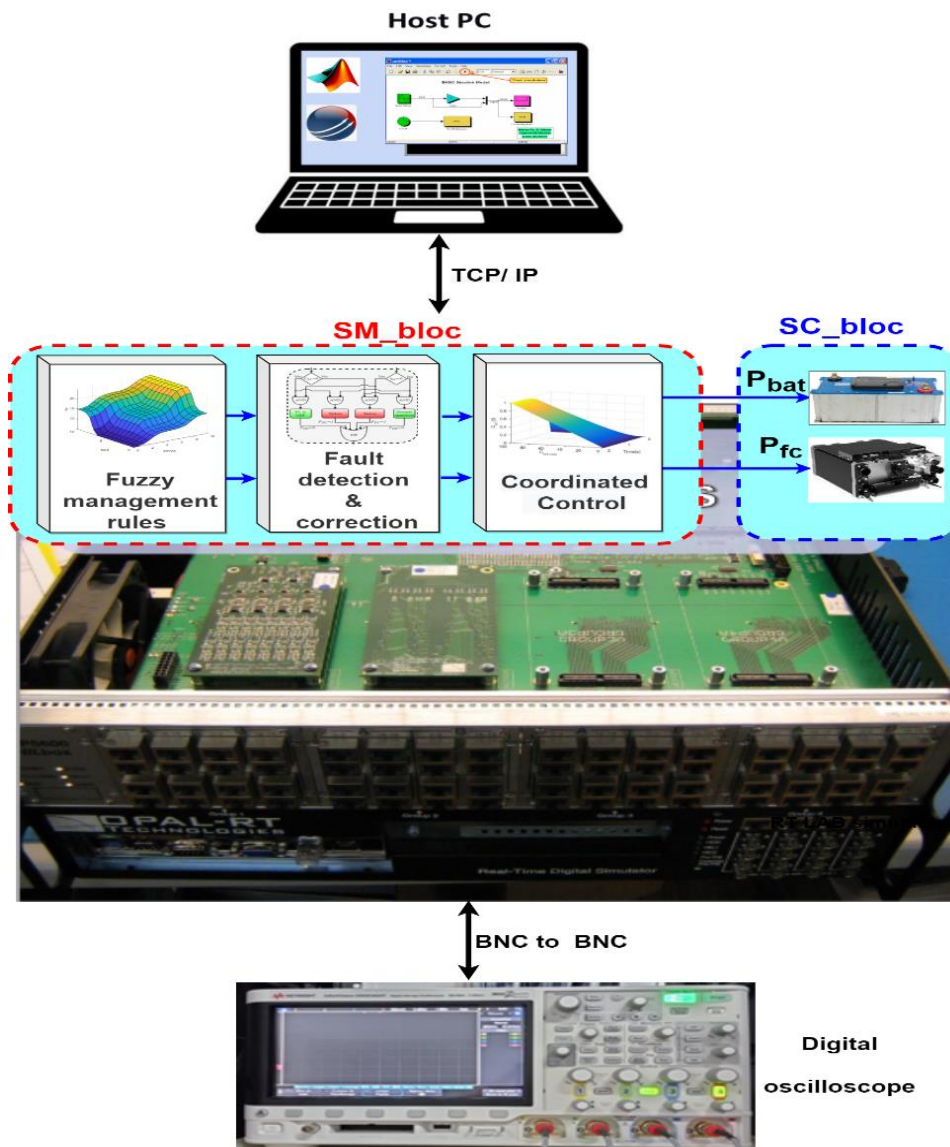
Figure 3.27. General scheme of real time simulation model.

Figure 3.28 shows the real time simulation bench established in our research laboratory in which element 1 represents the host PC, element 2 shows the FPGA based real time simulator (OP 5700), element 3 highlights the unit measurement a data acquisition interface (OP8660) and element 4 is a digital oscilloscope.
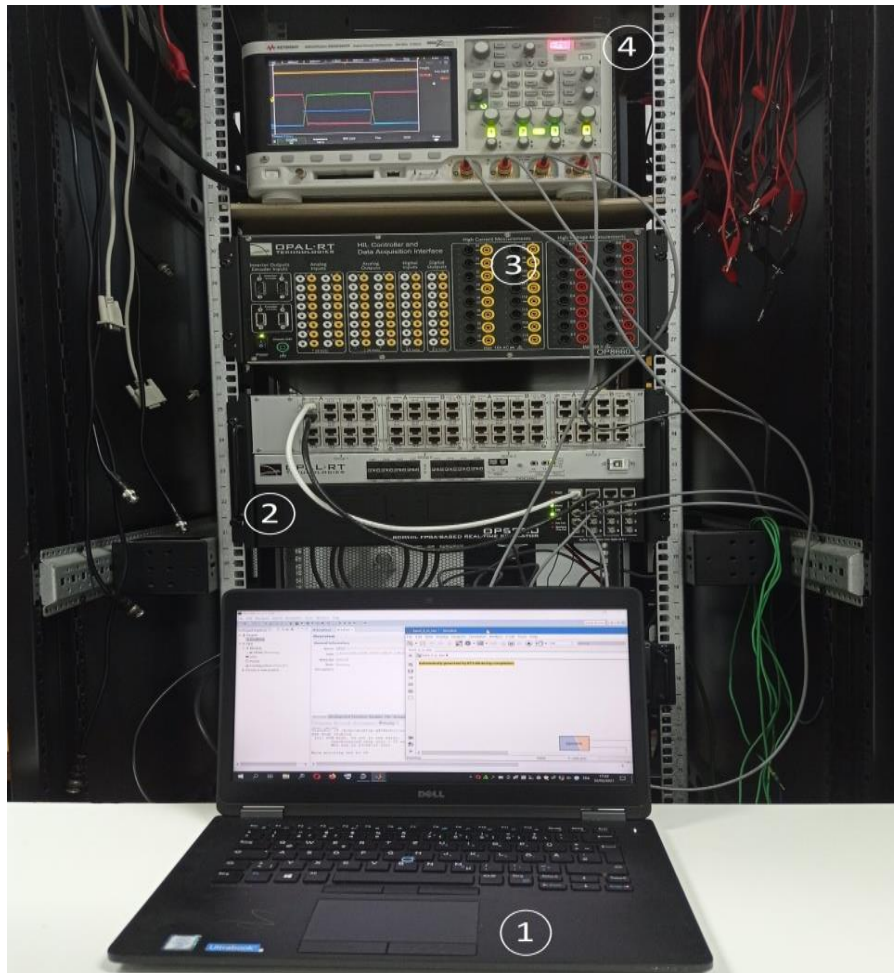
Figure 3.28 RT LAB simulation workbench.

A load profile of 5 kW that emulates HEV power demand is applied on FC and Li-Ion battery to test in real time the effectiveness of each stage of the proposed energy management strategy. Figure 3.29 highlights the power developed by FC and Li-Ion battery. One can notice that the proposed multi stage energy management strategy controls precisely the amount of power delivered by each power source. For instance, at region 6, the Li-Ion battery delivers 30% of the total required power whereas FC furnishes the remaining 70%. Table 3.2 shown below highlights clearly the different percentages of the total power delivered HEV power sources at each of the eight regions highlighted in Figure 3.29.
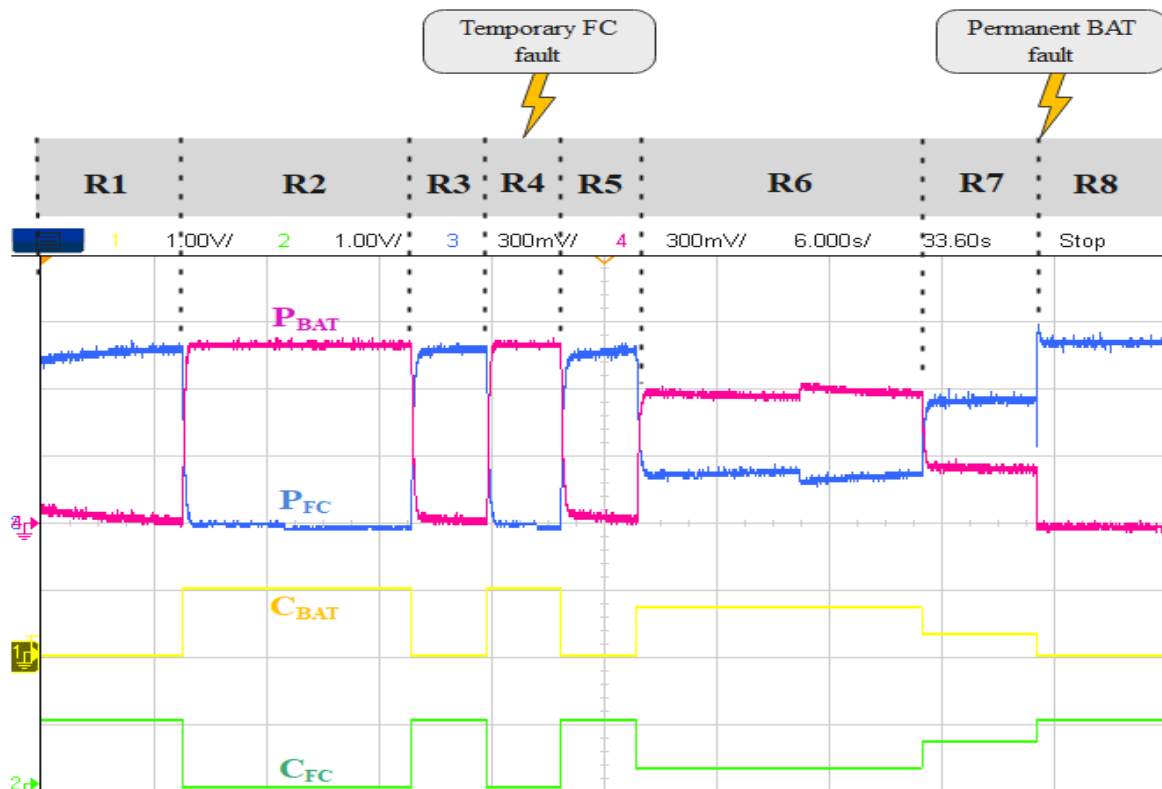
Figure 3.29 FC and Li-Ion battery delivered power.

Table 3.2 HEV power sources contribution in each region.

Region	C_{FC}	C_{BAT}	Operation
Region 1	100%	0%	BAT delivers all the required traction power during the starting and fixes DC bus voltage
Region 2	0%	100%	FC delivers all the required power for traction and SC fixes DC bus voltage
Region 3	100%	0%	BAT delivers all the required power for traction and fixes DC bus voltage. FC is off
Region 4	0%	100%	Temporary fault occurred at FC level. BAT is set to deliver all the required power for traction and fixes DC bus voltage
Region 5	100%	0%	FC delivers 100% of required traction power and BAT delivers the remaining 0%
Region 6	30%	70%	FC delivers 30% of the required power for traction and BAT fixes DC bus voltage and deliver the remaining power for traction
Region 7	70%	30%	FC delivers 70 % of the required power for traction and BAT fixes DC bus voltage while delivering 30% of the required power.
Region 8	100%	0%	Fault occurred at BAT level as it was ensuring 30% of the required traction power. It was isolated and CFC toggled from 70% to 100%

As indicated already in Figure 3.8, the second stage of the proposed power management strategy verifies whether HEV power sources are operating under normal operating conditions or not. Figure 3.30 shows the actual and corrected power sources' contribution factors. Note that in the absence of faults at the power sources level, C_{FC} and C_{BAT} generated by the fuzzy power management algorithm are equal to C_{FC}^{cor} and C_{BAT}^{cor}. The brown dashed lines in Figure 30.b highlight the instant of fault occurrence at FC level ($F_{FC}=1$). Note that as soon as the fault

is detected, FC was turned off by setting its contribution factor to zero ($C_{FC}=0$). According to Equation (3.17), this correction caused the modification of battery contribution factor from 0 to 1 as it is pointed out with dashed brown lines in Figure 3.30.a. It can be seen that just after the FC temporary fault disappeared, C_{FC}^{cor} went back to its previous value which is equal to C_{FC}. The dark dashed lines in Figure 3.30 show the instant of battery fault occurrence at battery level ($F_{bat}=1$). Before the fault takes place, C_{FC} and C_{BAT} are respectively equal to 70% and 30%. Once the fault was detected, the battery was turned off and the FC control loop was reconfigured to ensure DC bus voltage regulation and to ensure all the power required for traction. This was done by setting C_{FC}^{cor} and C_{BAT}^{cor} to 100% and 0%, respectively. FC control loop reconfiguration has resulted in a transient power peak as can be noticed in Figure 3.29 (region 8).
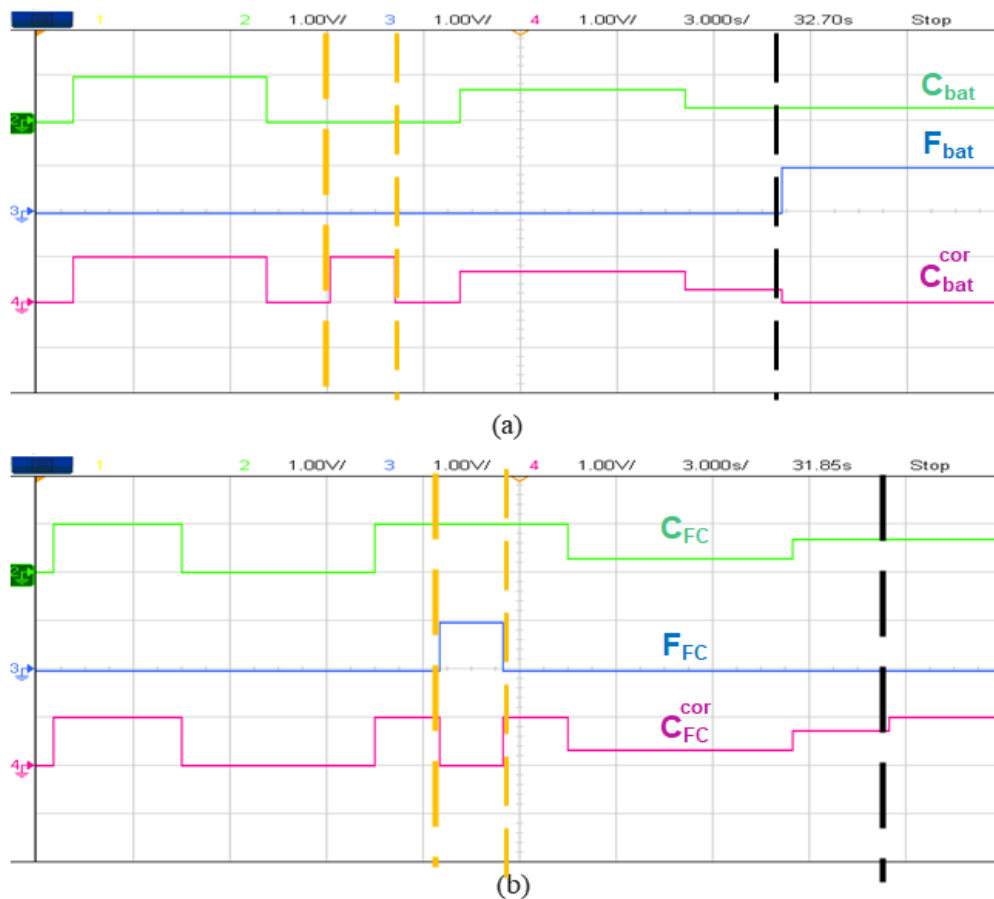
Figure 3.30 Power sources' contribution factors: (a) fuel cell, (b) battery.

To investigate the advantages provided by the third stage of the proposed energy management strategy, the HEV system is simulated with and without coordinated switching and the results are shown in Figures 3.31 and 3.32. Note that without the addition of a coordinated switching strategy bloc, important power ripples are noticed during each C_{FC} variation. This reduces power sources' lifespan and subjects them to dangerously high and

abrupt currents. From Figure 3.32, one can notice that the coordinated switching strategy reduced significatively the large transient power ripples noticed during power source switchings.
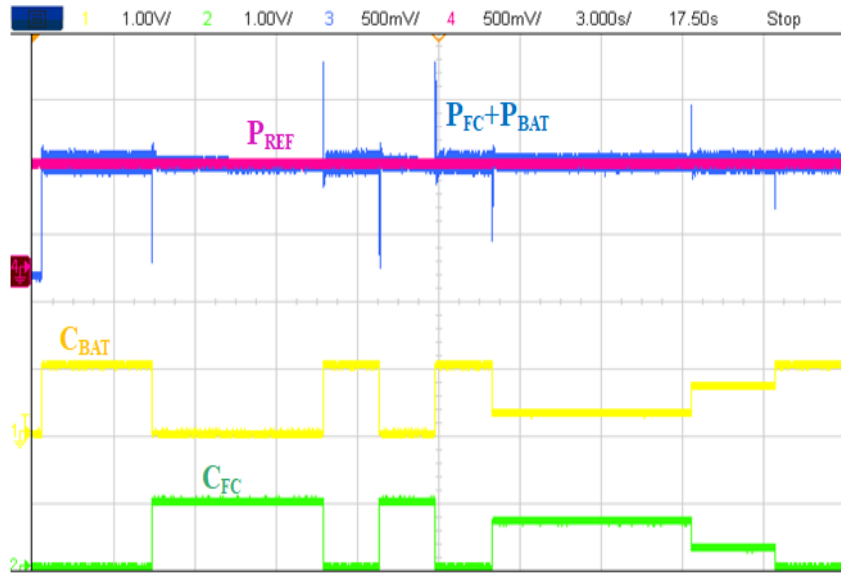
Figure 3.31 Abrupt switching of HEV power sources.
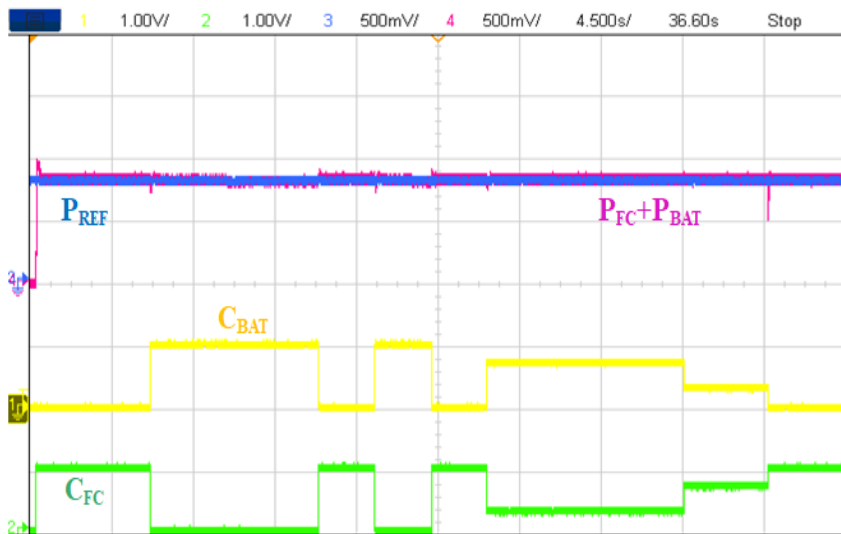
Figure 3.32 Coordinated switching of HEV power sources.

Figures 3.33 and 3.34 show respectively zooms of non coordinated and coordinated switchings. From figure 34, the difference between FC and BAT transient dynamics caused transient power lack that yielded the power ripples seen in Figure 3.31. For instance, at P_1, the sum of FC and BAT powers is only half of the required power for traction which is equal to *5 kW* and this causes transient ripples and reduces HEV transient performance. From Figure 3.34 one can see that a coordinated switching strategy via the proposed exponential transition function compensates for the difference in transient dynamics between power sources.

Furthermore, it protects them from the high and abrupt currents resulting from sudden load variations.
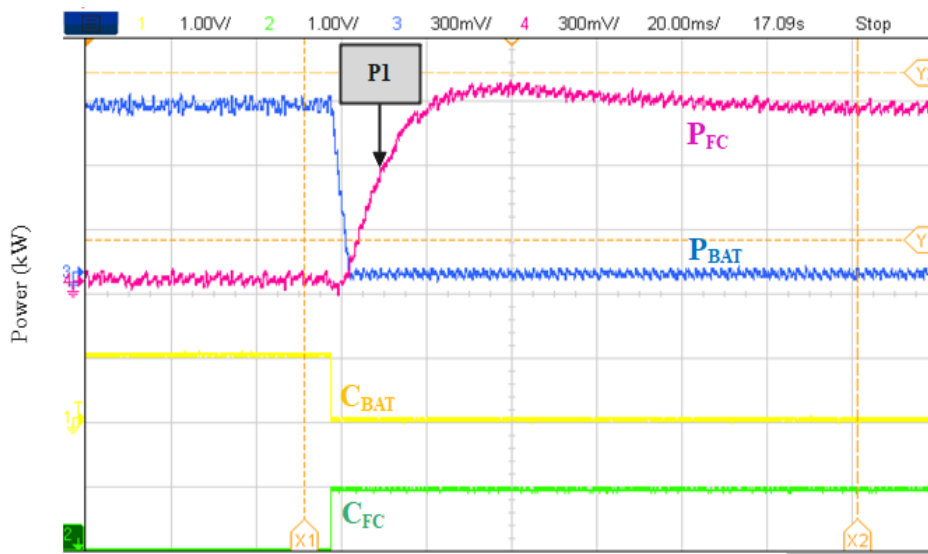
Figure 3.33 Zoom of non coordinated power sources switching.
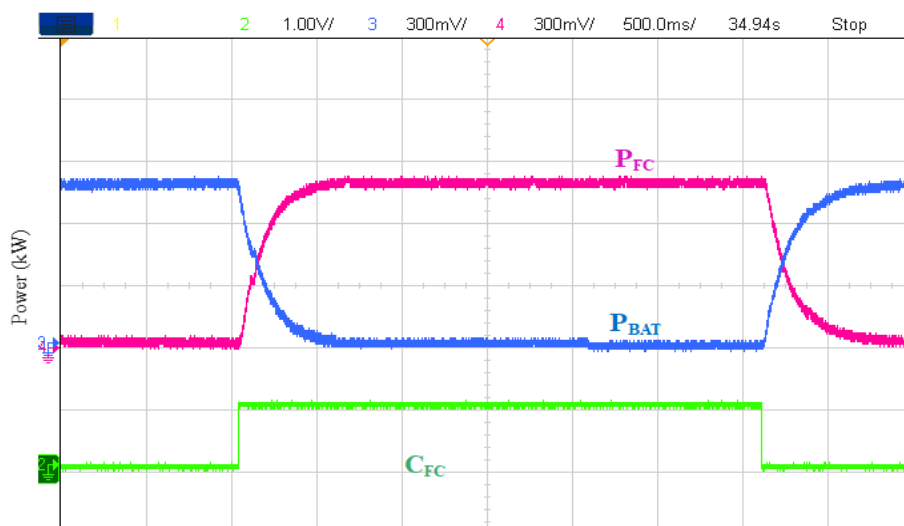
Figure 3.34 Zoom of coordinated power sources switching.

3.6 Conclusion

The developed multi stage power management strategy has improved vehicle security since failures on its power sources will be detected, identified and corrected. The problem of high transient ripples due to the difference in transient dynamics between FC and SC is resolved by a proposed coordinated switching strategy that compensates for the difference in power sources dynamics via the use of an exponential transition function that governs the different FC operating points variations. In addition to ripple suppression, the proposed coordinated switching has reduced the stress applied on FC during vehicle starting and this enhances its lifetime. Real time simulation results obtained using RT LAB simulator confirms the numerical simulation results.

Chapter 4

Intelligent torque allocation strategies

4.1 Introduction

Powertrain architectures are among the characteristics that have been strongly diversified since the invention of HEVs because it is the key factor toward HEV performance enhancement. The number and the location of the used electric machines is used as a scale in HEV classification which is extensively discussed in [75]. The most used HEV drivelines are depicted in figure 1. From the last mentioned figure, one can be notice that in order to enhance HEV propulsion power, the number of electric traction machines is increased on HEV board. This solution enhances vehicle performance at the expense of its cost and weight. Furthermore, one can notice that the torque to be received by each vehicle wheel is fixed and this is not suitable in cases where HEV is on ground surfaces with different friction coefficients. The idea of equal torque distribution is very common, in [76], HEV propulsion is ensured by a unique PMSM connected to rear wheels. The limitation of such drivetrain architecture appears when most of load torque is exerted on the front driven wheels instead of the rear driving wheels. In [77-78], both HEV rear wheels are driven by a five phase PMSM. This driveline structure will increase HEV propulsion power, but in case of failure of one traction machines the vehicle may skid away. Added to that, if the rear driving wheels are on an icy surface with low friction coefficient, the torque attributed to them will not develop significant propulsion power. Four traction machines are used for HEV traction in [79], this will increase HEV propulsion power but it will be at the expense of vehicle price and weight. The limitation of all the previously mentioned research works is that all the generated torque is either sent to rear or front wheels or it is equally distributed over all HEV wheels which is unsuitable in non-uniform ground surfaces. For that reason, researchers have developed several torque distribution strategies [80].
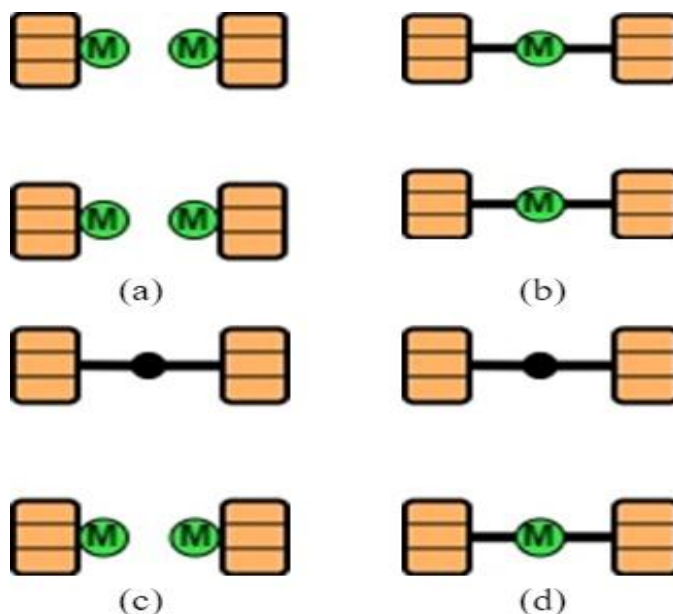
Figure 4.1 Frequently used HEV drivetrains architectures.

4.2 Proposed HEV structure

Figure 4.2 shows the drivetrain structure of the HEV considered in this work which can be powered using one or two power sources and maybe driven by either one or two permanent magnet synchronous machines (PMSM) choosed mainly for their high torque to mass ratio [81]. The turn on and extinction of FC and supercapacitor (SC) responsible of powering the HEV is governed by a proposed coordinated power management strategy. When the load torque, T_L, applied on the vehicle is less than the specified threshold torque value T_{TH}, the HEV will be driven only using PMSM1. As soon T_L exceeds the defined threshold, SW will be closed and PMSM2 will be turned on letting both motors share equally the load torque applied on the HEV. Transitions from single motor drive mode to dual motor mode is performed via a proposed coordinated switching strategy that will be discussed in details in the forthcoming sections. Two proposed TDS are used in this chapter to distribute the generated torque, T_{HEV}, to front and rear HEV wheels so that to maximize its propulsion as it will be seen throughout this chapter.
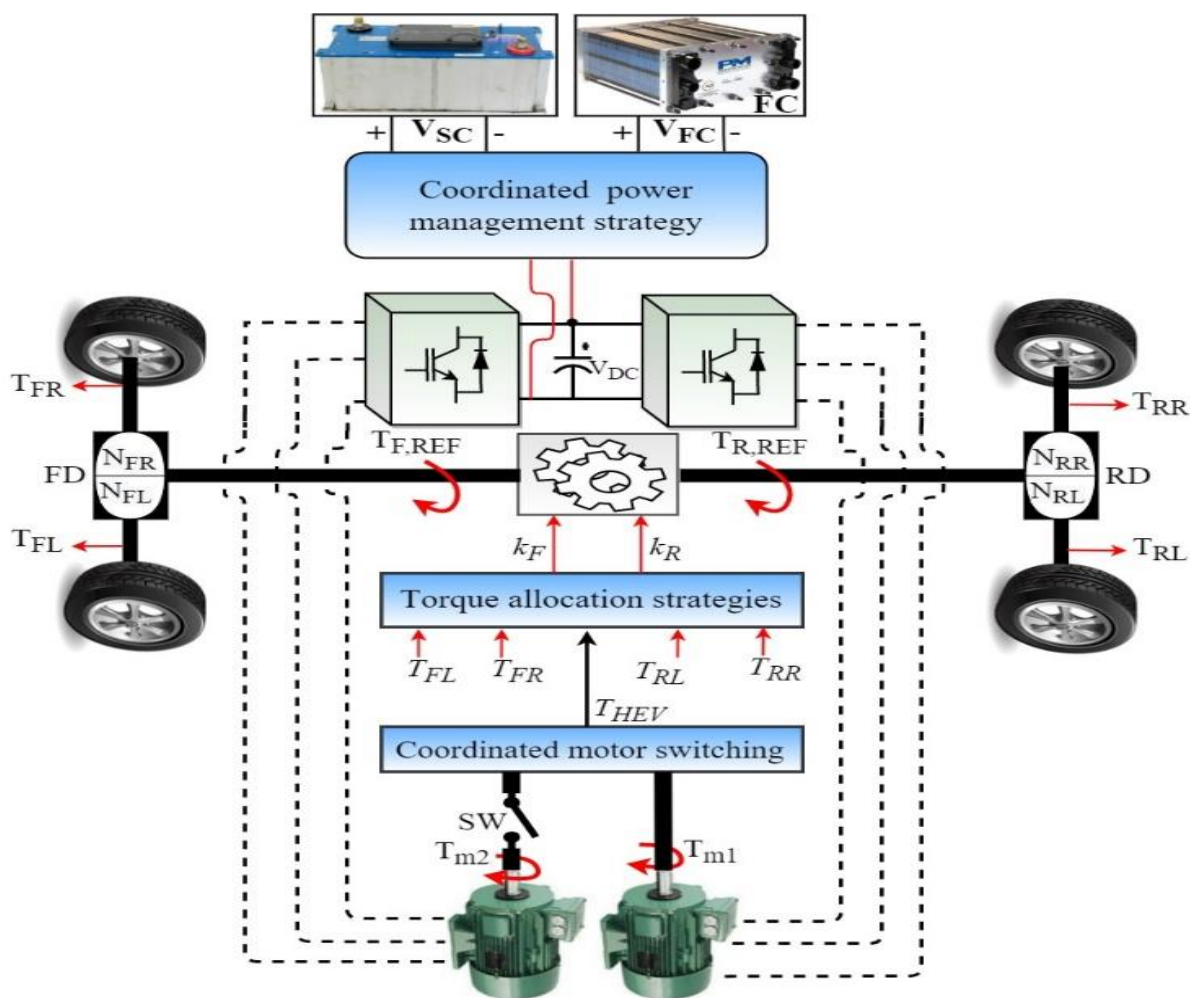
Figure 4.2 power source, multi traction motor HEV.

The torque allocation bloc shown in figure 4.2 outputs k_R and k_F which represent, respectively, the percentage of total torque attributed to rear and front differentials. Relation between k_F and k_R at every time instant is given by equation (4.1).

$$k_F = 1 - k_R \tag{4.1}$$

$T_{F,REF}$ and $T_{R,REF}$ in figure 4.2 represent, respectively, the amount of torque sent to front and rear differentials. They are defined by the set of equations given in equation (4.2) where T_{m1} and T_{m2} are the electromagnetic torque values developed by $PMSM_1$ and $PMSM_2$. η is the transmission effeciency of the front and rear differentials and center gear system.

$$\begin{cases} T_{R,REF} = \eta \, k_R \left[T_{m1} + T_{m2} \right] \\ T_{F,REF} = \eta \, k_F \left[T_{m1} + T_{m2} \right] \end{cases} \tag{4.2}$$

The center differential shown in figure 4.2 performs the first torque orientation by sending the reference torque values $T_{F,REF}$ and $T_{R,REF}$ to HEV front and rear wheels. After that, RD and FD, which are bistate differentials, perform the second and last torque vectoring. When they are open, RD and FD provide an equal torque split over HEV right and left wheels. If FD and RD are closed, 95% of the front or rear reference torque will be allocated to the HEV wheel on which more load torque is applied and the remaining 5% will be allocated to the other wheel so that to ensure its rotation. The torque transmitted to each vehicle wheel is by equation (4.3) where N_{RR}, N_{RL}, N_{FR} and N_{FL} are respectively gear ratios of rear right, rear left, front right and front left wheels that are defined using equation (4.4).

$$\begin{cases} T_{RR} = \eta^2 k_R N_{RR} \left(T_{m1} + T_{m2} \right) \\ T_{RL} = \eta^2 k_R N_{RL} \left(T_{m1} + T_{m2} \right) \\ T_{FR} = \eta^2 k_F N_{FR} \left(T_{m1} + T_{m2} \right) \\ T_{FL} = \eta^2 k_F N_{FL} \left(T_{m1} + T_{m2} \right) \end{cases} \tag{4.3}$$

$$\begin{cases} N_{RR} = \dfrac{T_{RR}}{T_{R,REF}} \\\\ N_{RL} = \dfrac{T_{RL}}{T_{R,REF}} \\\\ N_{FR} = \dfrac{T_{FR}}{T_{F,REF}} \\\\ N_{FL} = \dfrac{T_{FL}}{T_{F,REF}} \end{cases} \tag{4.4}$$

Relation between the torque allocated to an HEV wheel and the maximum propulsion torque that can be produced by an HEV wheel depends on the surface fiction coefficient μ that exists between vehicle tire and ground surface. In reference [82], it is stated that tire friction coefficient is a function of several parameters such as tire inflation and wheel slip. According to [83], the estimate of the road friction coefficient can be performed using equation (4.5) where F_x and F_z are the longitudinal and normal forces applied on the tire, C_s is the tire stiffness and λ is the HEV wheel slip given by equation (4.6) in which R represents wheel radius, w stands for motor angular speed and v highlights wheel speed.

$$\mu = \frac{F_x}{F_z} = C_s \lambda \tag{4.5}$$

$$\lambda = \frac{v - \omega R}{v} \tag{4.6}$$

Using equation (4.5), the total propulsion torque that can be developed by HEV is rewritten as given by equation (4.7) where $\mu_{RR}, \mu_{RL}, \mu_{FR}$ and μ_{FL} are respectively the rear right, rear left, front right and front left surface friction coefficients between HEV tires and the ground surface.

$$T_{prop} = \mu_{RR} T_{RR} + \mu_{RL} T_{RL} + \mu_{FR} T_{FR} + \mu_{FL} T_{FL} \tag{4.7}$$

Equation (4.8) highlights the torque transfer ratio (*TTR*) which is used in this chapter as a performance measure to evaluate the goodness of the proposed TDS. It can be seen that TTR is nothing than the ratio between the total propulsion torque developed by vehicle wheels, T_{prop}, and the electromagnetic torque generated by the two traction machines, T_{HEV}. As pointed out by equation (4.8), TTR ranges between 0 and 1 and the greater it is, the more effective the TDS will be and vice versa.

$$\begin{cases} TTR = \dfrac{T_{prop}}{T_{HEV}} \\ 0 \leq TTR \leq 1 \end{cases} \tag{4.8}$$

The term ETD (equal torque distribution) stands for HEVs whose generated torque is equally splitted over vehicle wheels as it is the case in [84-89]. The TTR of these last-mentioned reference works gets significantly reduced in non-uniform ground surfaces. In order to prevent TTR deteriorations, two TDS that rely on the use of PSO and FLC discussed in this chapter and they are presented in the next section.

4.3 Proposed torque distribution strategies

4.3.1 PSO based torque allocation

To do so, first, we generate a randomly population of n torque candidate solutions in a four-dimensional search space as given in equation (4.9). Each matrix column represents a set of all possible torque values that may be allocated to a given HEV wheel. Each matrix row represents a torque vector combination that may be applied to HEV wheels. At any instant k, the population matrix T should satisfy two simultaneous conditions given by equation (4.10):

$$
T = \begin{bmatrix} T_{11} & T_{12} & T_{13} & T_{14} \\ T_{21} & T_{22} & T_{23} & T_{24} \\ \vdots & \vdots & \vdots & \vdots \\ T_{n1} & T_{n2} & T_{n3} & T_{n4} \end{bmatrix}
\tag{4.9}
$$

$$
\begin{cases} T(i,j) \leq T_{HEV}(k) \\ \sum_{j=1}^{4} T(:,j) = T_{HEV}(k) \end{cases}
\tag{4.10}
$$

Notice that the fitness function J given by equation (4.11) which is nothing more than the TTR already defined in equation (4.8) which is evaluated for each population candidate solution [$T(i,1), T(i,2), T(i,3), T(i,4)$] and for every possible differentials arrangement.

$$
J(i,j) = \frac{\begin{bmatrix} \mu_{RR} \\ \mu_{RL} \\ \mu_{FR} \\ \mu_{FL} \end{bmatrix}^{T} .* \begin{bmatrix} N(j,1) \\ N(j,2) \\ N(j,3) \\ N(j,4) \end{bmatrix}^{T} .* \begin{bmatrix} T(i,1) \\ T(i,2) \\ T(i,3) \\ T(i,4) \end{bmatrix}^{T}}{T_{HEV}}
\tag{4.11}
$$

As already discussed in the previous section, the set of possible values that N_{RR}, N_{RL}, N_{FR} and N_{FL} can take is given by equation (4.12). Mathematically, If S is a finite set whose cardinality is $n(S) = k$, then the number of subsets in S is 2^k. Considering four HEV wheels and applying this last mentioned theorem to equation (4.12) we deduce that 8 differential arrangements or 8 torque orientations are possible for each load torque value T_L. Equation (4.13) depicts the matrix of all possible differential configurations N whose row number is 2^S and column number is equal to HEV wheel number.

$$S = \{0.05, 0.5, 0.95\} \tag{4.12}$$

$$N = \begin{bmatrix} N_{11}^{RR} & N_{12}^{RL} & N_{13}^{FR} & N_{14}^{FL} \\ N_{21}^{RR} & N_{22}^{RL} & N_{23}^{FR} & N_{24}^{FL} \\ \vdots & \vdots & \vdots & \vdots \\ N_{81}^{RR} & N_{82}^{RL} & N_{83}^{FR} & N_{84}^{FL} \end{bmatrix} \tag{4.13}$$

The best torque distribution and the best differential arrangement are respectively updated after each iteration as given using equations (4.14) and (4.15). Notice that only candidate solutions that maximizes the TTR of HEV are kept.

$$T_{opt}^{i} = \begin{cases} T_{opt}^{new} & if \quad J^{new} > J^{old} \\ T_{opt}^{old} & if \quad J^{new} < J^{old} \end{cases} \tag{4.14}$$

$$N_{opt}^{i} = \begin{cases} N_{opt}^{new} & if \quad J^{new} > J^{old} \\ N_{opt}^{old} & if \quad J^{new} < J^{old} \end{cases} \tag{4.15}$$

The global optimum differential arrangement and the global optimum torque distribution that resulted in the highest fitness value (TTR) are respectively given using equations (4.16) and (4.17). Optimal torque percentages to be allocated to front and rear wheels are given using equation (4.18). Before the use of PSO for torque distribution, its convergence is tested using the benchmark test function shown in figure (4.3) whose expression is given by equation (4.19). This benchmark function is full of local minima and has a unique global optimum as highlighted on the figure and this may trap the algorithm if it is not well conceived. Figure (4.4) shows the result of minimization of equation (4.19) using PSO algorithm. Notice that after 72 iterations PSO converged to the same global optimal solution which is -18.59.

$$T_{opt}^{G} = \begin{pmatrix} T_{opt,1} \\ T_{opt,2} \\ \vdots \\ T_{opt,n} \end{pmatrix}^{T} = \begin{bmatrix} T_{RR}^{opt} \\ T_{RL}^{opt} \\ T_{FR}^{opt} \\ T_{FL}^{opt} \end{bmatrix}^{T} \tag{4.16}$$

$$N_{opt}^{G} = \begin{pmatrix} N_{opt,1} \\ N_{opt,2} \\ \vdots \\ N_{opt,n} \end{pmatrix}^{T} = \begin{bmatrix} N_{RR}^{opt} \\ N_{RL}^{opt} \\ N_{FR}^{opt} \\ N_{FL}^{opt} \end{bmatrix}^{T} \tag{4.17}$$

$$\begin{cases} k_R^{opt} = \dfrac{\sum\limits_{i=1}^{2} T_{opt}^{G}(1,i)}{\sum\limits_{i=1}^{4} T_{opt}^{G}(1,i)} \\[4mm] k_F^{opt} = 1 - \dfrac{\sum\limits_{i=1}^{2} T_{opt}^{G}(1,i)}{\sum\limits_{i=1}^{4} T_{opt}^{G}(1,i)} \end{cases} \tag{4.18}$$

$$f(x,y) = y\sin(4x) + 1.1x\sin(4y) \tag{4.19}$$
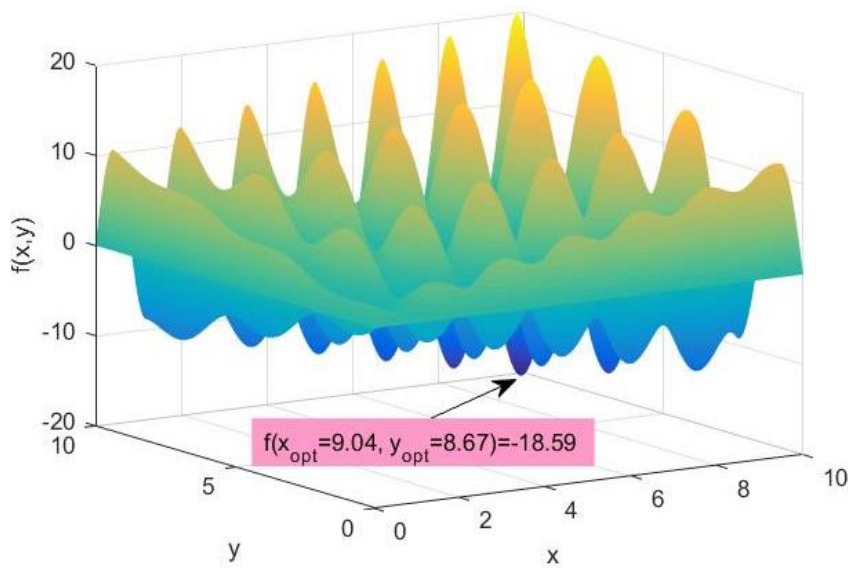
Figure 4.3 Used benchmark test function.

The flowchart shown in figure 4.5 explains how PSO was integrated to provide an optimum torque allocation and to maximize HEV propulsion power in non uniform ground surfaces. Notice that PSO is initiated only when the road conditions are not uniform.
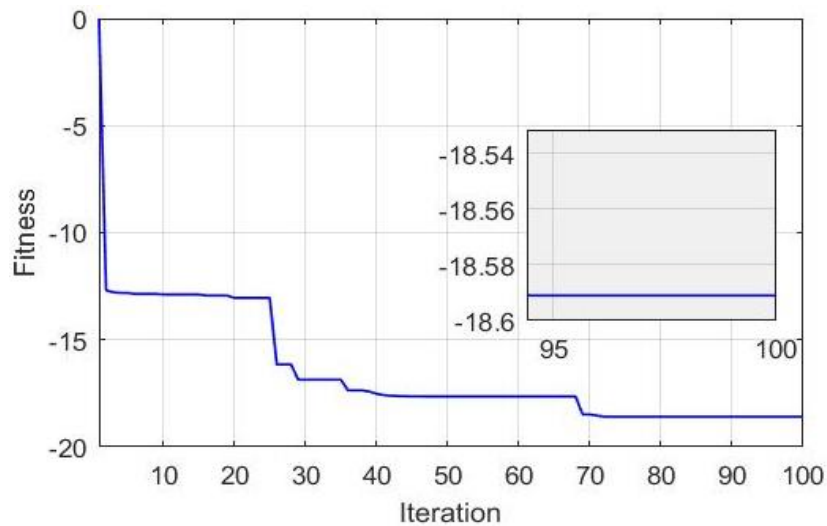
Figure 4.4 Convergence PSO test function.
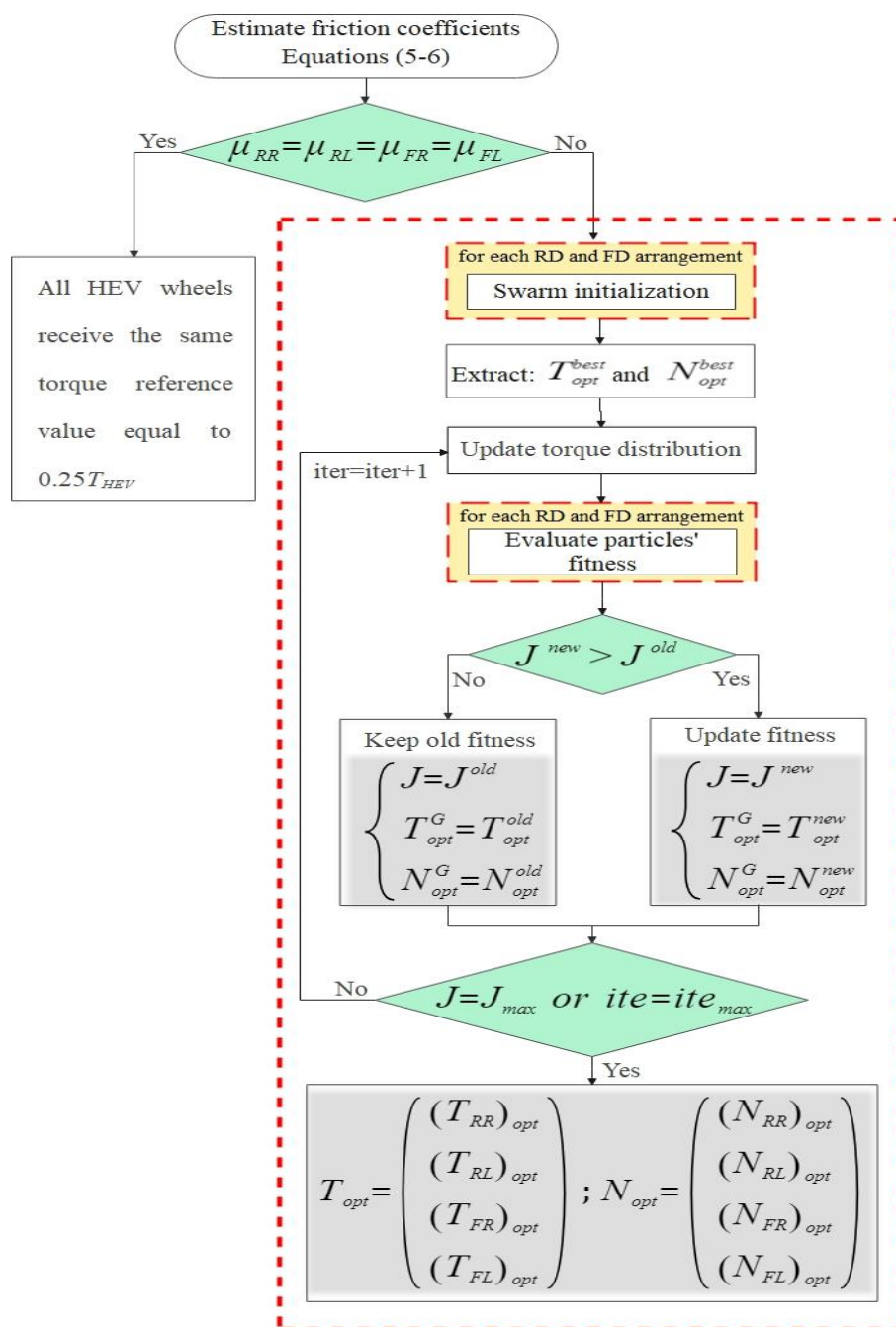
Figure 4.5 PSO based torque distribution.

4.3.2 Fuzzy torque allocation

The load torque applied on each HEV wheel is sensed. After that, the total load torque applied to rear and front HEV wheels are fed to the designed fuzzy logic controller. The used FLC controller fuzzifies the sensed front and rear load torque applied on the vehicle using six fuzzy sets which are: very low *"VL"*, low *"L"*, below average *"BA"*, average *"A"*, high *"H"* and very high *"VH"* .This is performed using two trapezoidal and four triangular membership functions as it is shown in figure 6 from which one can see that the universe of discourse is between zero

and maximum torque supported by PMSM1 and PMSM2. After rule evaluation, deffuzification is performed using two triangular and two trapezoidal membership functions as shown in figure 8. *VLG, LG, MG* and *HG* stand, respectively, for very low, low, medium and high gears. Physically, each membership function represents a gear ratio level that will result in a given torque split. The most important part in FLC design is the establishment of a rule base system that governs its operation and stores the expert knowledge on how to split the torque over HEV wheels. Dependency between FLC inputs and outputs presented by their corresponding membership functions and the set of established fuzzy rules is better explained by the surface map shown in figure 4.9.
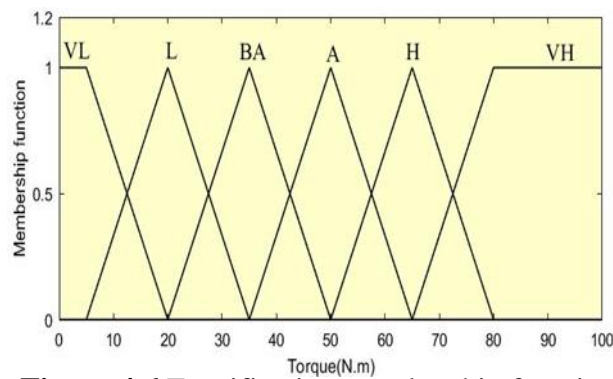
Figure 4.6 Fuzzification membership function.
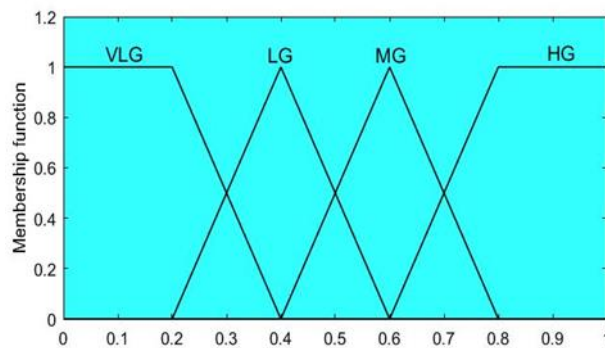
Figure 4.7 Deffuzification membership function
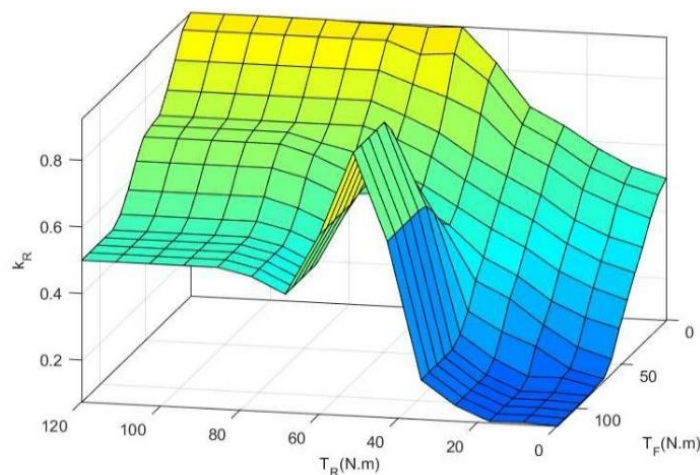
Figure 4.8 FLC surface map.

Table 4.1 shown below points out the set of fuzzy rules used to generate the reference torque to be sent to HEV front wheels ($T_{F,REF}$). Notice that when the same load torque is applied on front and rear vehicle sides, the generated torque (T_{HEV}) will be shared equally between front and rear wheels. After $T_{F,REF}$ determination using the set of fuzzy rules given in table 4.1, $T_{R,REF}$ is concluded using equation (4.20) shown below:

$$T_{R,REF} = T_{HEV} - T_{F,REF} \qquad (4.20)$$

Table 4.1 Fuzzy rules for front torque allocation.

T_F / T_R	VL	L	BA	A	H	VH
VL	MG	MG	HG	HG	HG	HG
L	LG	MG	MG	HG	HG	HG
BA	VLG	LG	MG	HG	HG	HG
A	VLG	LG	LG	MG	HG	HG
H	VLG	VLG	LG	LG	MG	HG
VH	VLG	VLG	VLG	LG	LG	MG

4.4 Coordinated switching strategy

4.4.1 Coordinated motor switching

Drive mode switching problems are extensively studied in the last years [90-91] as they subject traction machines to abrupt and high currents that may cause their damage. Furthermore, abrupt drive mode switching gives rise to large undesired torque ripples that reduce HEV drivability and produce undesired passenger-felt jerks. Figure 4.9 shows one of the negative impacts occurring when the drivetrain structure shown in figure 4.1 toggles from single to dual motor traction mode. Notice that when PMSM$_2$ is abruptly turned on at *t=4.4*s, large transient torque ripples reaching 45 N.m are observed as it can be seen in figure 4.9.a. The same unwanted transient behavior is noticed during abrupt PMSM$_2$ extinction when switching from dual to single traction mode. To address these undesired torque jerks that reduce driving comfort, a proposed coordination switching strategy is proposed.

At any time, instant, the torque developed by the HEV shown in figure 2 is expressed using equation (4.21):

$$T_{HEV} = T_{m1} + T_{m2} \tag{4.21}$$

According to HEV operation described earlier, equation (4.21) can be rewritten as expressed in equation (4.22):

$$T_{HEV} = c_{m1}T_{m1} + c_{m2}T_{m2} \tag{4.22}$$

c_{m1} and c_{m2} are respectively the torque contribution factors of PMSM1 and PMSM2. Each of these two factors represent the percentage of total load torque handled by each machine. When HEV traction is ensured by PMSM1 only, c_{m1} equals 100% and c_{m2} is null. As soon as HEV switches to dual traction mode, both c_{m1} and c_{m2} are set to 50%. Relation between c_{m1} and c_{m2} and the set of their possible values are given in equation (4.23):

$$\begin{cases} c_{m1} = \{50\%, 100\%\} \\ c_{m2} = \{0\%, 50\%\} \\ c_{m1} + c_{m2} = 100\% \end{cases} \tag{4.23}$$

(a) (b)
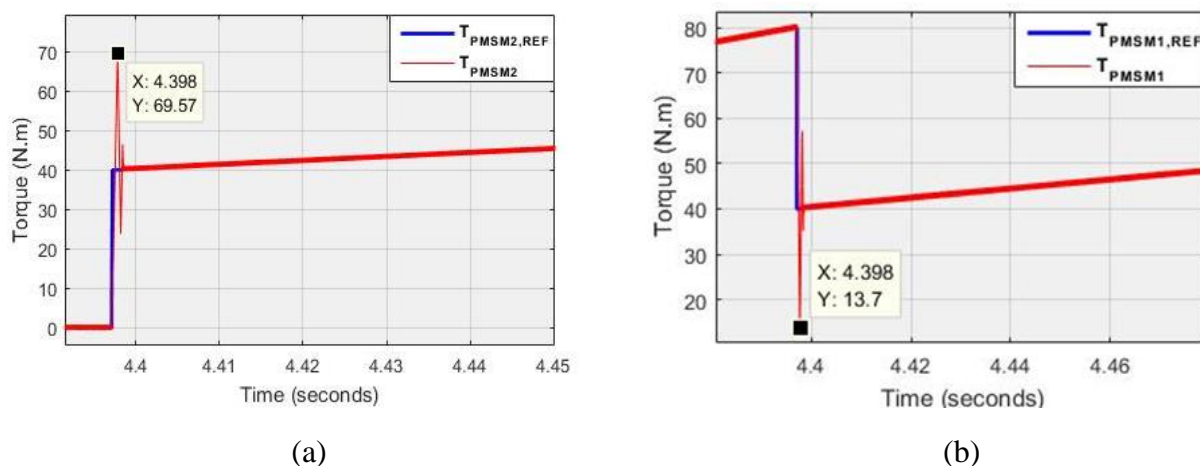
Figure 4.9 Abrupt motor switching, (a) abrupt PMSM2 turn on, (b) abrupt PMSM2 turn off

Instantaneous HEV torque ripples are expressed by taking the time derivative of equation (4.24):

$$\frac{dT_{HEV}}{dt} = \left[T_{m1} \frac{dc_{m1}}{dt} + T_{m2} \frac{dc_{m2}}{dt} \right] + \left[c_{m1} \frac{dT_{m1}}{dt} + c_{m2} \frac{dT_{m2}}{dt} \right] \tag{4.24}$$

Equation (4.25) provides the numerical approximation of each left-hand side term of equation (4.24). T_s in the aforementioned equation represents the calculation step. Derivative of T_{m1} and T_{m2} are equal to zero because the torque developed by PMSM$_1$ and PMSM$_2$ between t and $t+T_s$ is almost the same.

$$
\begin{cases}
\dfrac{dT_{m1}}{dt} \approx \left[\dfrac{T_{m1}\left(t+T_s\right)-T_{m1}\left(t\right)}{T_s} \right] \approx 0 \\[3mm]
\dfrac{dT_{m2}}{dt} \approx \left[\dfrac{T_{m2}\left(t+T_s\right)-T_{m2}\left(t\right)}{T_s} \right] \approx 0 \\[3mm]
\dfrac{dc_{m1}}{dt} \approx \left[\dfrac{c_{m1}\left(t+T_s\right)-c_{m1}\left(t\right)}{T_s} \right] \approx \dfrac{\Delta c_{m1}}{T_s} \\[3mm]
\dfrac{dc_{m2}}{dt} \approx \left[\dfrac{T_{m2}\left(t+T_s\right)-T_{m2}\left(t\right)}{T_s} \right] \approx \dfrac{\Delta c_{m2}}{T_s}
\end{cases}
\tag{4.25}
$$

Using the approximations of equation (4.25), equation (4.24) can be rewritten as follow:

$$
\frac{dT_{HEV}}{dt} \approx T_{m1}\left(\frac{\Delta c_{m1}}{T_s}\right) + T_{m2}\left(\frac{\Delta c_{m2}}{T_s}\right)
\tag{4.26}
$$

Since T_s is in the order of 10^{-6}, the two ratios in the right-hand side of equations (4.26) will result in significant transient torque ripples that lower HEV driving comfort during drive mode switchings and that reduce lifespan of PMSMs and reduce the driving comfort. To avoid these aforementioned drawbacks, a coordinated switching strategy that smoothens drive mode switchings and that coordinates the torque coming from the two traction machines is proposed in this chapter and its basic steps are described by the flowchart of figure 4.10. The old and the new torque contribution factors of PMSM$_1$ denoted respectively by c_{m1}^{old} and c_{m1}^{new} are acquired and stored as given in equation (4.27) where t_{trig} is the instant at which T_L gets beyond or blow T_{TH}.

$$
\begin{cases}
c_{m1}^{old} = c_{m1}\left(t_{trig}-T_s\right) \\[2mm]
c_{m1}^{new} = c_{m1}\left(t_{trig}\right)
\end{cases}
\tag{4.27}
$$

The old and the new torque references of PMSM$_1$ denoted respectively by T_{m1}^{old} and T_{m1}^{new} are calculated as given in equation (30).

$$
\begin{cases}
T_{m1}^{old} = c_{m1}^{old}T_L\left(t_{trig}-T_s\right) \\[2mm]
T_{m1}^{new} = c_{m1}^{new}T_L\left(t_{trig}\right)
\end{cases}
\tag{4.28}
$$

Since T_s is in the order of 10^{-6}, $T_L\left(t_{trig}\right) \approx T_L\left(t_{trig}-T_s\right)$. Hence, equation (4.28) is rewritten as given in equation (4.29).

$$
\begin{cases}
T_{m1}^{old} = c_{m1}^{old}T_L\left(t_{trig}\right) \\[2mm]
T_{m1}^{new} = c_{m1}^{new}T_L\left(t_{trig}\right)
\end{cases}
\tag{4.29}
$$
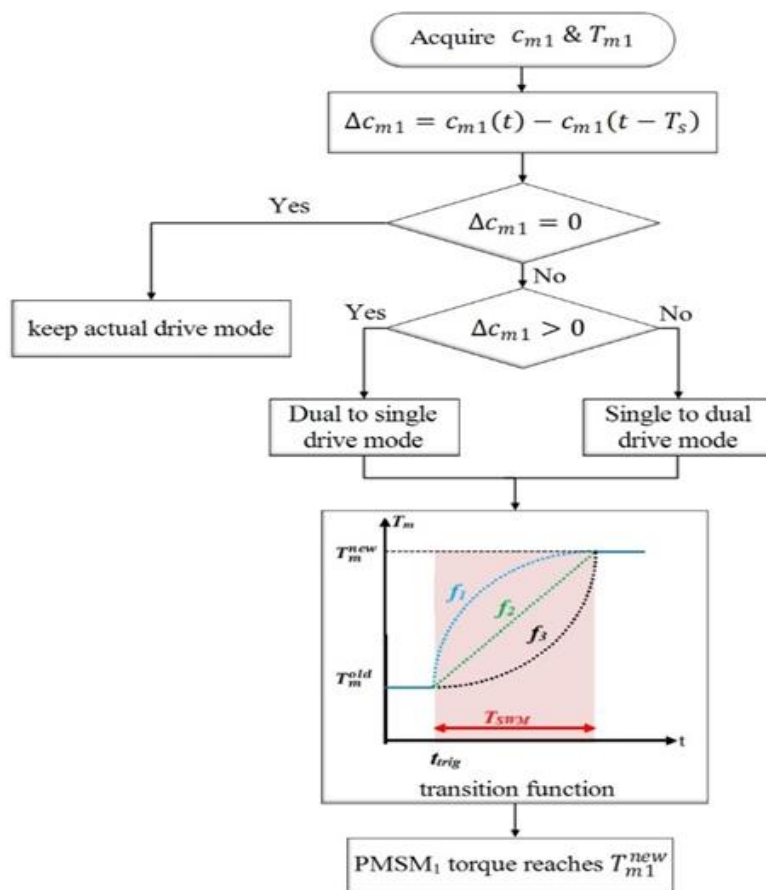
Figure 4.10 Coordinated motor switching flowchart.

    Mathematically, there exist an infinite number of curves that can be used to join the old torque reference of a traction machine, T_{m1}^{old} and its new torque reference T_{m1}^{new}. In this work, the exponential transition function given by equation (4.30) is used to provide smooth and coordinated drive mode switching. Notice that the proposed transition function takes into account PMSM dynamics and control the rate of change of torque reference. τ_{m1} represents $PMSM_1$ time constant which is chosen to be one fifth the duration of the transition period T_{SWM} as stated by equation (4.31).

$$T_{m1}^{ref}(t) = \left(T_{m1}^{old} - T_{m1}^{new}\right)e^{-\frac{\left(t-t_{trig}\right)}{\tau_{m1}}} + T_{m1}^{new} \tag{4.30}$$

$$\tau_{m1} = \frac{T_{SWM}}{5} \tag{4.31}$$

Substituting by equation (31) in (32) yields the coordinated torque reference of $PMSM_1$ in terms of its torque contribution factors as shown below:

$$T_{m1}^{ref}(t) = \left[\left(c_{m1}^{old} - c_{m1}^{new}\right)e^{-\frac{\left(t-t_{trig}\right)}{\tau_{m1}}} + c_{m1}^{new}\right]T_L\left(t_{trig}\right) \tag{4.32}$$

Substituting by equation (34) in equation (23) yields the coordinated torque reference that will be delivered to $PMSM_2$ during drive mode switchings as expressed by the equation (35):

$$T_{m2}^{ref}(t) = 1 - \left[\left(c_{m1}^{old} - c_{m1}^{new} \right) e^{-\frac{\left(t - t_{trig} \right)}{\tau_{m1}}} + c_{m1}^{new} \right] T_L \left(t_{trig} \right) \tag{4.33}$$

Figures 11 shows the evolution of c_{m1} from its old value c_{m1}^{old} to its new c_{m1}^{new} using the proposed exponential transition. This figure shows how PMSM1 achieves smoothly its new torque reference within the defined transition period which is set to 2 seconds in this figure.
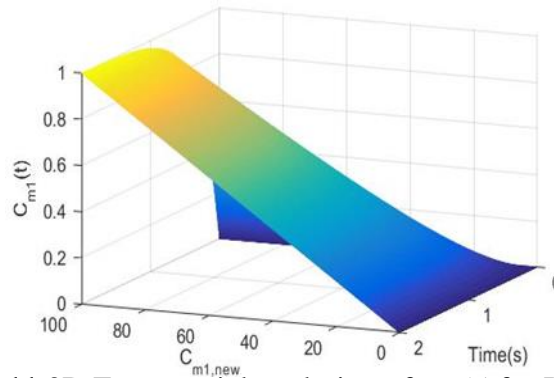
Figure 4.11 3D Exponential evolution of $c_{m1}(t)$ for PMSM1

4.4.2 Coordinated power source switching

Power sources such as batteries, fuel cells and supercapacitors hold a tremendous importance and are being continuously integrated in nowadays energy production and storage systems. This can be easily seen by the large number of works discussing this topic [91-94]. However, the aforementioned power sources are sensitive and have to be used with protection procedures against overcurrent and unwanted transient effects. Undesired transient effects are not only caused exclusively by drive mode switching. They are also noticed during power source switchings as it can be seen in figure 4.9 of [95] and figure 4.15 of [96]. These ripples are due to the transient dynamic difference between HEV power sources. In references [97-98], authors have discussed FC slowness due to the purifier that is responsible of transforming fuel to pure hydrogen. They concluded that the purifier causes a delay of 2.2 seconds the FC no load time constant (τ_{FC}^{NL}) which is given in by equation (4.36) in which R_{act} is the resistance due to activation polarization, R_{con} is the resistance due to conduction polarization and R_{ohm} is the resistance due to ohmic polarization. In references [99-100], purifier's delay is estimated to be $3\tau_{FC}^{NL}$ where τ_{FC}^{NL} is the no load FC time constant.

$$\tau_{FC}^{NL} = \left(R_{act} + R_{con} + R_{ohm} \right) C \tag{4.34}$$

The coordinated switching strategy is proposed in this chapter to compensate for FC poor transient response and to protect sensitive power sources from damages caused by sudden load variations. In this work, FC and SC are used to power the HEV and their usage can be

summarized by the following sentence: *"At any driving instant, FC and SC can deliver any desired fraction of the total power required for traction"*. This last sentence can be expressed mathematically using equations (4.35) shown below where C_{FC} and C_{SC} are respectively the FC and SC power contribution factors that represent the percentage of total required power that FC and SC will deliver. P_{HEV} is the total power required for traction

$$\begin{cases} C_{FC} = \dfrac{P_{FC}}{P_{HEV}} \\ \\ C_{SC} = \dfrac{P_{SC}}{P_{HEV}} \end{cases} \tag{4.35}$$

FC reference power is varied by changing its C_{FC}. In this work we choose to operate FC at five operating points as indicated in equation (4.36).

$$C_{FC} = \{\, 0\%\, , 30\%\, , 50\%\, , 70\%\, , 100\%\, \} \tag{4.36}$$

Following the same approach already presented in subsection 4.1, FC and SC switchings are coordinated using the transition functions given by equations (4.37) and (4.38). P_{FC}^{old} and P_{FC}^{new} represent respectively the old and the new FC reference power. τ_{FC} is the controlled FC time constant which is defined by equation (4.39). T_{FC} is the manufacturer time constant that represents the time required for FC to reach, safely, its full power from off state.

$$P_{FC}^{ref}(t) = \left(P_{FC}^{old} - P_{FC}^{new} \right) e^{-\frac{\left(t - t_{trig} \right)}{\tau_{FC}}} + P_{FC}^{new} \tag{4.37}$$

$$P_{SC}^{ref}(t) = 1 - \left(P_{SC}^{old} - P_{SC}^{new} \right) e^{-\frac{\left(t - t_{trig} \right)}{\tau_{FC}}} - P_{SC}^{new} \tag{4.38}$$

$$\tau_{FC} = \frac{T_{FC}}{5} \tag{4.39}$$

Figure 4.12 shown below highlights how the proposed coordinated strategy is integrated to the energy management strategy. It is worth noticing that the used energy management strategy is not deeply discussed throughout this chapter as it is not the main subject of the study. From figure 4.12, one can notice that the management strategy output is not directly applied to HEV power sources. Instead, it is passed through a coordination switching strategy that compensates the difference between power sources dynamics especially FC slowness and protects them from possible damages caused by sudden load variations.
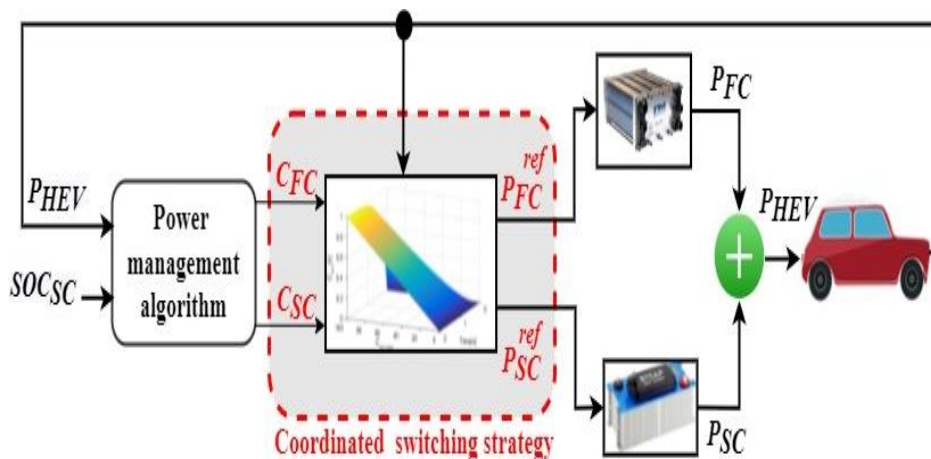
Figure 4.12 Coordinated power management strategy.

4.5 Simulation and results

The effectiveness of all the presented torque distribution strategies and the impact of the coordinated switching technique on vehicle performance are investigated through numerical simulations under MATLAB/Simulink environment using the different simulation parameters shown in table 4.2, 4.3 and 4.4.

Table 4.2 Simulation parameters

Parameter	Value
Tsimulation	94 s
T_S	1e-6 s
T_{TH}	80 N.m
T_{FC}	0.25 s
T_{SWM}	0.25 s
Solver	ode 4

Table 4.3 PSO parameters

Parameter	Value
population	10
iteration	20
w	[0.4; 0.9]
c_1	2
Topology	Full

Table 4.4 PMSM parameters

Symbol	Value
w_n	3000 rpm
Tn	111 N.m
p	4
L_d , L_q	6.35 mH
f	0.002 N.m.s
J	0.011 kg.m2

After the use of benchmark test functions to test the convergence of PSO algorithm alone as discussed earlier, the HEV driving case shown in figure 4.13 is used to test the effectiveness of PSO algorithm when it is integrated with the proposed torque distribution strategy. As it can be seen, the vehicle is assumed to be in a non uniform ground surface. The left side wheels lay in a low friction ground surface compared to right wheels and this is expected to reduce vehicle propulsion torque and power. Notice that a load torque of 50 N.m is applied on the HEV.
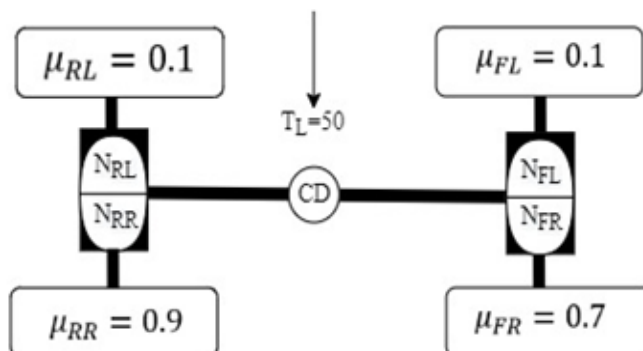
Figure 4.13 HEV driving situation.

Since HEV wheels are in non uniform ground surface, PSO algorithm will be initiated to find the best torque distribution and the best differential arrangements that maximize HEV propulsion torque. Figure 4.14 shows evolution of PSO candidate solutions over iterations for a load torque value of 50 N.m. After 20 iterations, PSO has converged to the optimal torque values to be attributed to each HEV wheel so that to maximize its propulsion. It can be seen that most of the generated torque is sent to HEV right wheels that are on ground surfaces with large friction coefficient and more gripe that maximize HEV propulsion power. Also, the torque value sent to rear right wheel is greater than the one sent to rear front wheel because its corresponding surface friction coefficient is larger. One can remark from figure 4.14 that the sum of torque allocated to HEV wheels is equal to the load torque applied on the vehicle which is 50 N.m. Figure 4.15 shows the differential arrangement that resulted in maximizing the fitness function in equation (4.11). From figure 4.15, $[(N_{RR})_{opt}(N_{RL})_{opt}(N_{FR})_{opt}(N_{FL})_{opt}] = [95\% \ 5\% \ 95\% \ 5\%]$ which means that 95% of rear torque is allocated to the rear right wheel and 95% of front torque is allocated to the front right wheel.

Figure 4.16 shows the evolution of the fitness function given by equation (4.11) over 20 iterations. It could be seen that PSO algorithm has converged to a global best propulsion torque of 42.71 N.m. Using equation (4.8), a TTR of 0.8542 is obtained. This means that 85.42% of the generated torque is converted into propulsion torque thanks to the optimal torque allocation. The driving case of figure 4.13 was simulated using the drivetrain architectures of some recently

published works and the results are shown in table 4.5. Even though [99-100] used, respectively, one and two traction machines, they have obtained the same TTR. The same conclusion can be made on the drivetrain proposed by [87-100] which used 2 and 4 traction machines respectively. One can conclude that over actuating an HEV without an adequate torque distribution doesn't necessary improve HEV propulsion power. Out of table 4.5, it can be seen that PSO-TDS avoids HEV propulsion deterioration in non uniform ground surfaces.
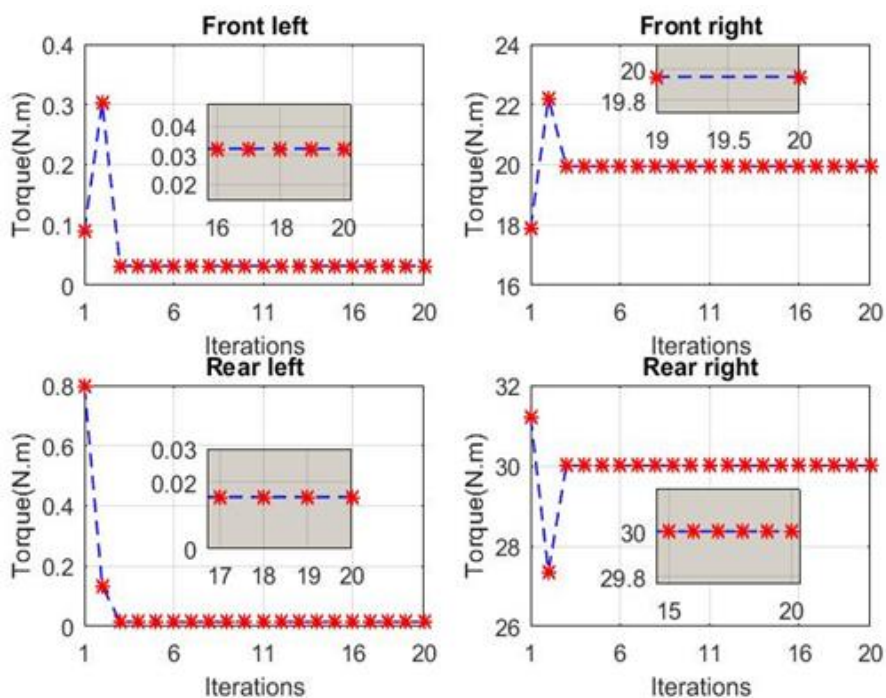
Figure 4.14 Optimum torque distribution vs iterations for T_L=50 N.m.
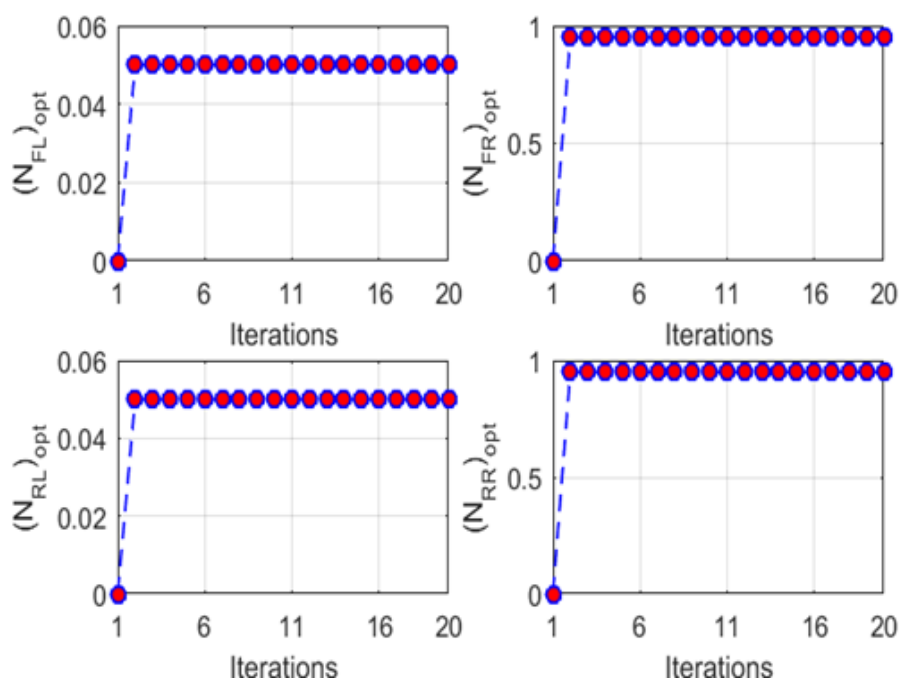
Figure 4.15 Rear and front differential distribution for: T_L=50 N.m

Table 4.5 Comparison to published results

TDS	TTR	Improvement
Proposed PSO-TDS	85.42%	/
[99], [100]	50%	+35.42%
[100], [101]	45%	+40.42%
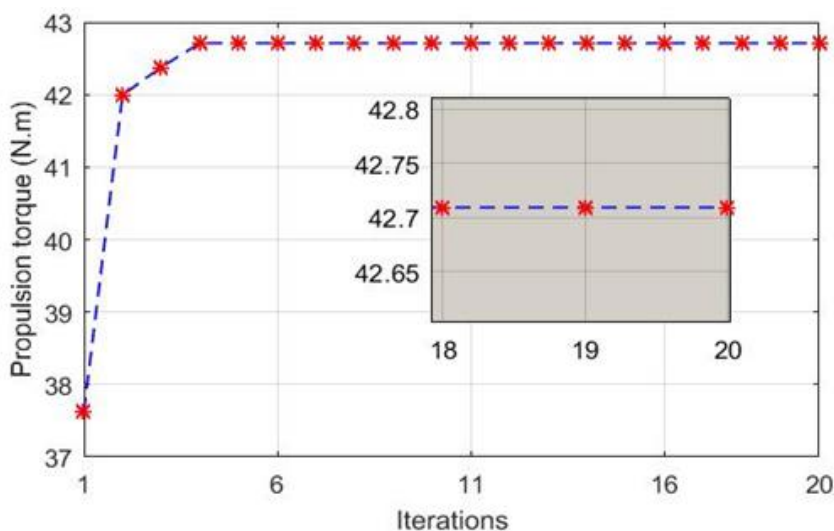
Figure 4.16 HEV best torque propulsion over iterations.

To point out the positive impact of the proposed TDSs and to show the enhancements brought by the proposed coordinated switching strategy on both power sources and traction machines, the driving scenario shown in figure 4.16 is considered. During its ride of 94 seconds, the HEV rolls on a uniform and non uniform ground surfaces. One can notice that in region 2 and 4, respectively, the HEV left and right side wheels lay on a snowy surface and this is expected to reduce HEV propulsion power. Figure 4.17 shows the value of friction coefficient between each HEV tire and the ground surface during the ride.
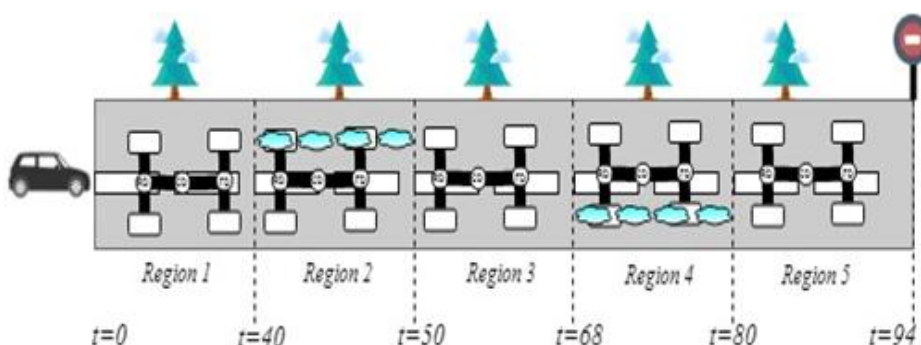
Figure 4.17 HEV ride path.

Figure 4.19 shows the resulting TTR using PSO and FLC. These obtained results are compared to the conventional ETD strategy which assumes that the generated torque will be splitted equally over the four HEV wheels. The first captivating remark is that the two used torque

allocation strategies based on artificial intelligence succeeded to maintain high the HEV torque transfer ratio (TTR) in non uniform ground surfaces (region 2 and 4). However, in uniform ground surfaces (region 1, 3 and 5) both intelligent TDS and ETD strategies resulted in the same TTR. One can see that Fuzzy and PSO torque distribution techniques have kept HEV TTR around 85%. However, ETD strategy resulted in almost 50% TTR drop during the time instants [40 s; 50 s] and [68 s; 80 s] which means that only half of the torque generated by traction machines will be transformed into propulsion torque. From figure 4.19 also, PSO TDS yielded the highest TTR during all vehicle ride in both uniform and non uniform regions. This confirms the effectiveness and the superiority of swarm intelligence.
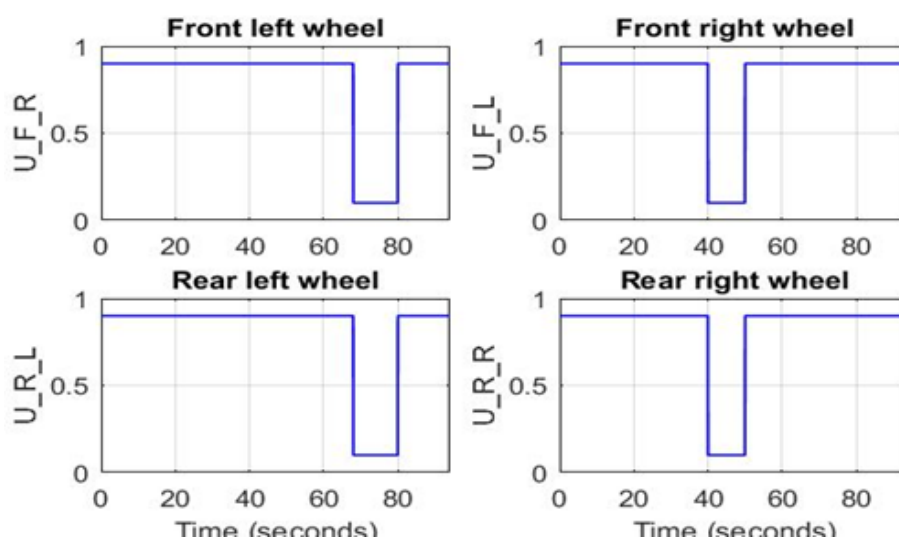
Figure 4.18 Wheels' friction coefficients.
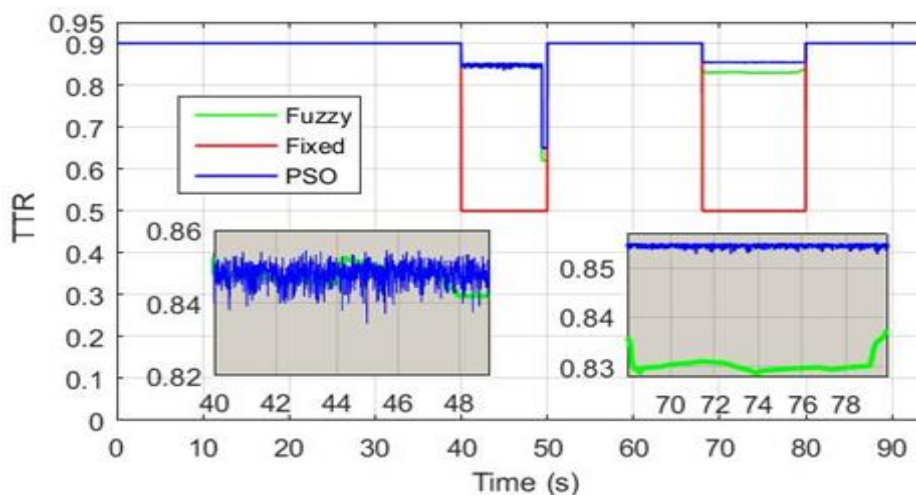
Figure 4.19 Resulting TTR using different allocation strategies.

Figure 4.20 shows the developed HEV propulsion power using different torque distribution strategies. It can be seen that when using Fuzzy and PSO techniques for torque distribution, HEV propulsion power wasn't affected in non uniform ground surfaces. However, vehicle propulsion

power was reduced almost by half when using ETD. The zoom on figure 4.20 confirms that PSO is the distribution technique that maximized the most vehicle propulsion power among other used distribution techniques.
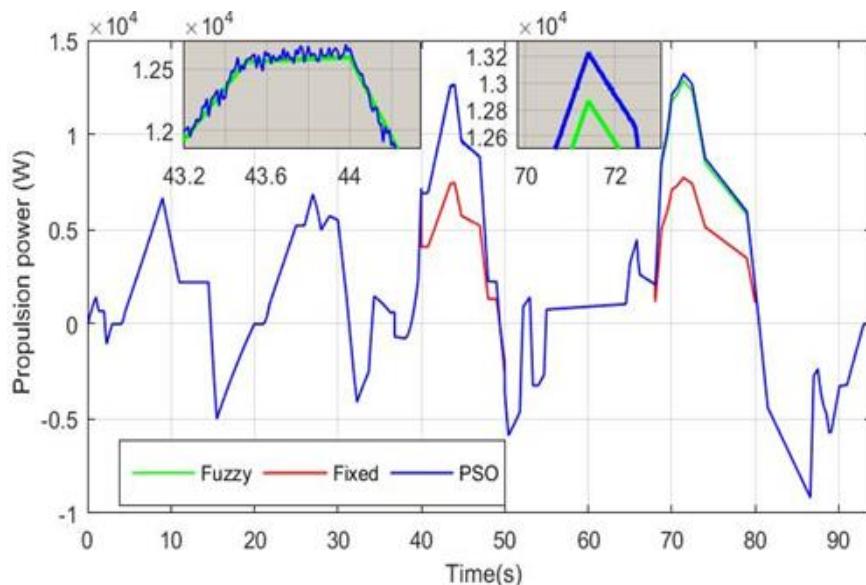
Figure 4.20 HEV propulsion power using different strategies.

Figure 4.21.a and 4.21.b show the torque developed by PMSM$_1$ and PMSM$_2$. It could be noticed that the two traction machines develop a torque that is exactly equal to the load torque exerted on the vehicle. From the two last mentioned figures, one can see that as the load torque applied on PMSM1 reaches 80 N.m, PMSM$_2$ will be switched on to ensure half of the torque applied on the vehicle. One could notice significant torque ripples reaching up to 30 N.m occur each time PMSM$_2$ is switched on or off. These ripples which are due to the application of abrupt and high load torque reference to the traction machines reduce significantly HEV riding comfort and produce unwanted passenger felt jerks. The negative impact of abrupt switching on HEV speed is clearly noticed in figure 4.22 from which one can notice important speed jerks that lower the driving comfort during each motor.

(a)   (b)
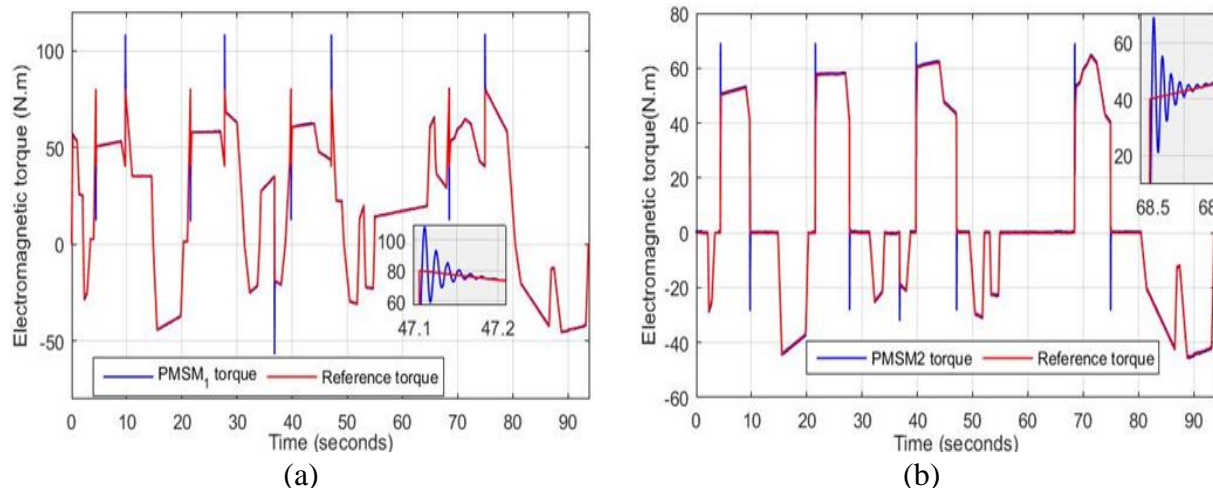
Figure 4.21 Developed electromagnetic torque, (a) PMSM1, (b) PMSM2
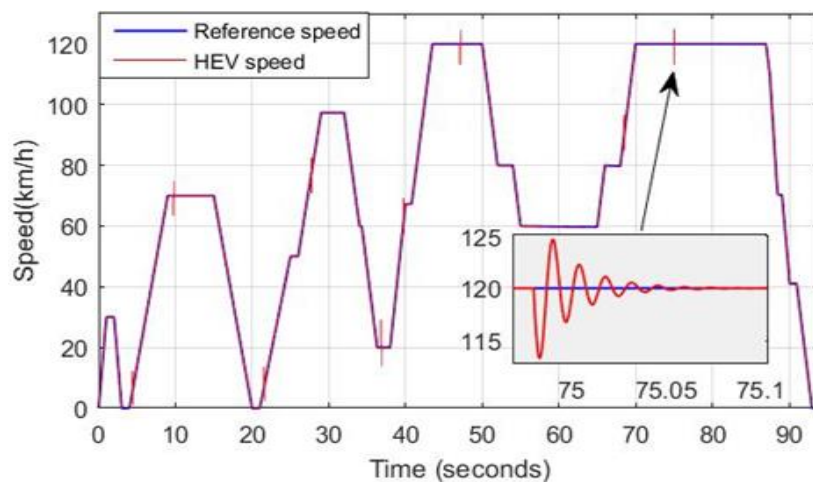
Figure 4.22 HEV speed with non coordinated switching strategy.

Figure 4.23.a and figure 4.23.b show the torque developed by PMSM$_1$ and PMSM$_2$ when they are switched without using the proposed coordinated switching strategy. The proposed coordinated motor switching reduced the transient torque ripples through the use of the transition functions given by equations (4.32-33). This enhances the driving comfort, motors' lifespan and will protect them for possible damages caused by large and abrupt currents.
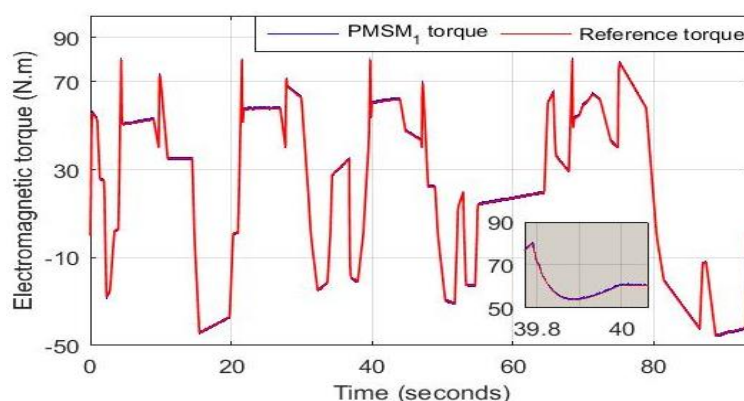
(a)
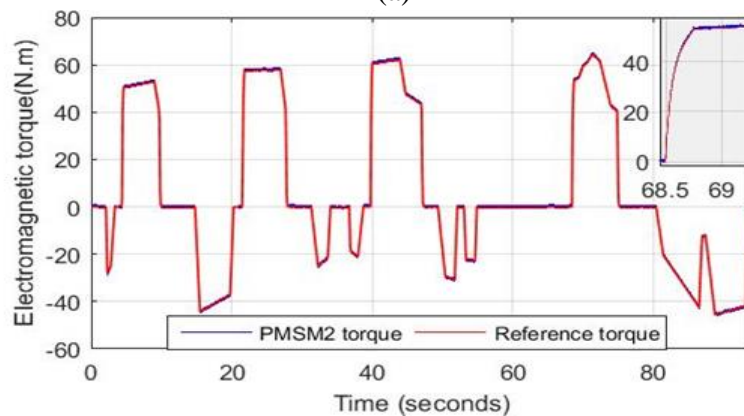
(b)

Figure 4.23 Developed electromagnetic torque, (a) PMSM$_1$, (b) PMSM2.

Figure 24 highlights the obtained HEV speed when the two PMSMs are switched using the proposed coordinated switching strategy. It could be seen that the last-mentioned technique has a positive impact on HEV performance and has almost eliminated the speed jerks noticed during each motor switching and this will enhance the HEV driving comfort.
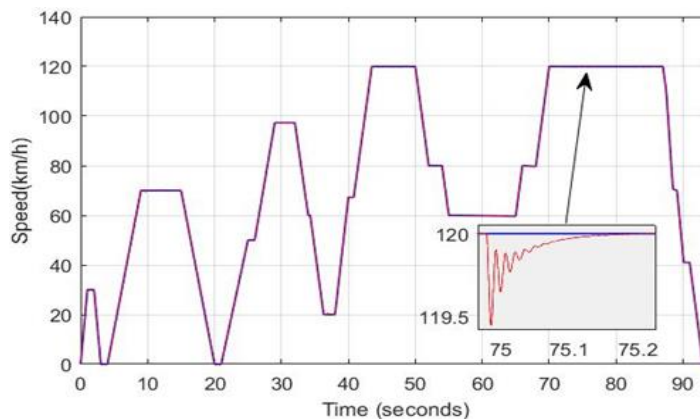
Figure 4.24 HEV speed using coordinated switching.

Figure (25-a) and (25-b) show, respectively, abrupt turn on and extinction of PMSM$_2$. One can notice significant transient ripples on PMSM$_1$ and PMSM$_2$ during transitions from single to dual motor traction mode and vice versa. These unwanted transient phenomena have noteworthy bad effects on traction motors reduces riding comfort.

(a)   (b)
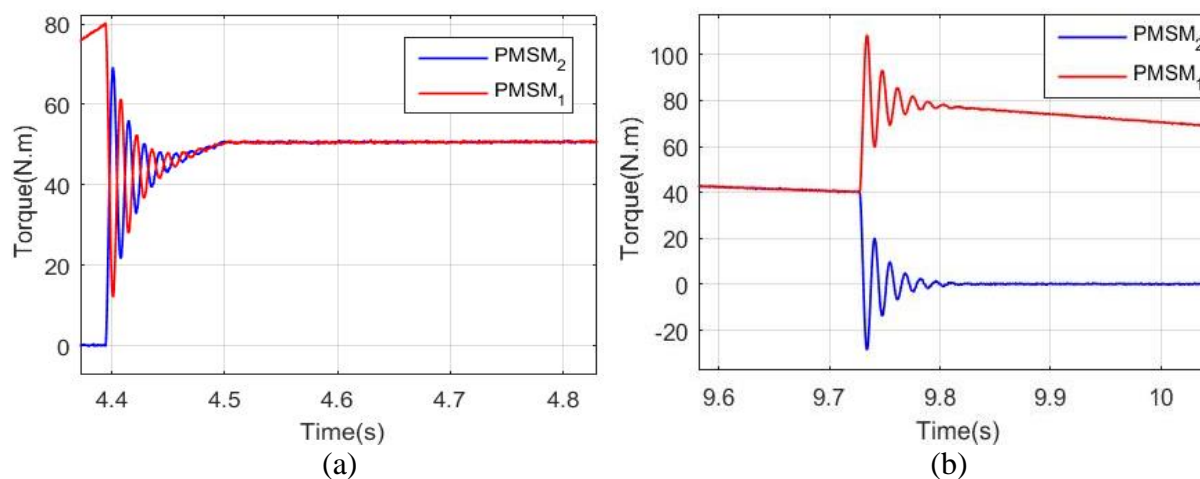
Figure 4.25 Motor switching. (a) Abrupt PMSM1 turn on, (b) Abrupt PMSM2 turn off

In figure 4.26, once the load torque reaches 80N.m, PMSM$_2$ is smoothly turned on using the transition function given by equation (4.34) to ensure half of the load torque applied on the vehicle. Meanwhile, PMSM$_2$ is turned on using the same strategy within a transition period T$_{SWM}$ using the transition function given by equation (4.35) as it is shown in figure 4.27. One can deduce that coordinated motor switchings or coordinated drive mode commutations has suppressed the transient torque ripples that lower vehicle driving comfort.
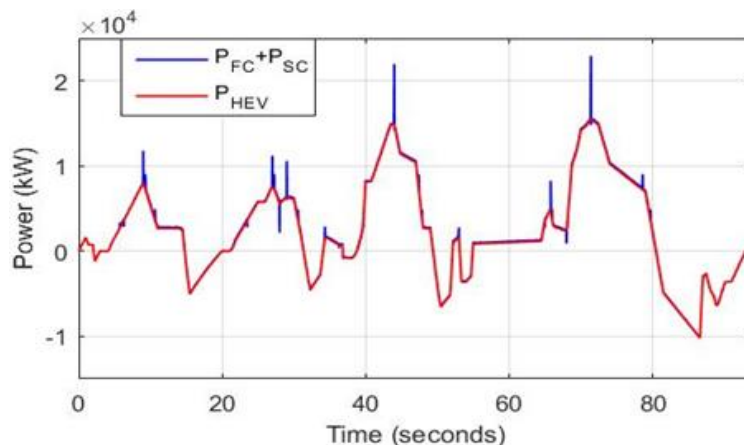
Figure 4.26 Zoom of coordinated PMSM$_1$ turn on
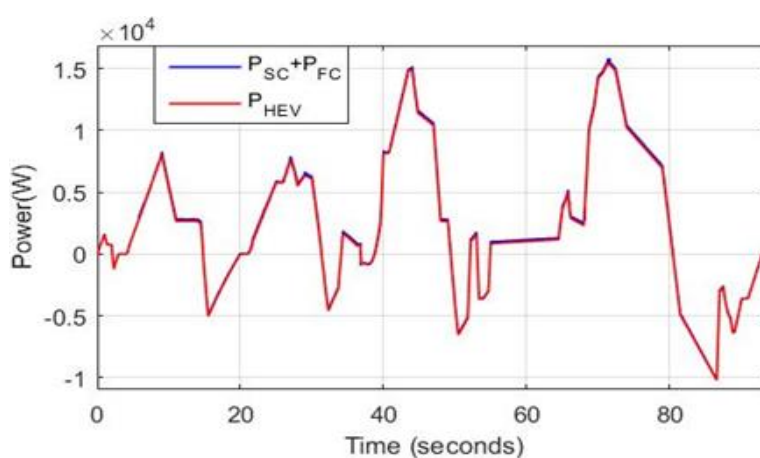
Figure 4.27 Zoom of coordinated PMSM$_2$ turn off

Figure 4.28 shows the evolution of FC and SC powers. From the last mentioned figure, one can notice that FC delivers different percentages of the total required power for traction. For example, during [*29s; 31.34s*], FC delivers 70% of the total required power whereas during [*71.4 s; 78.6 s*] it furnishes only 50%. Figure 4.29 reveals that abrupt switching between FC and SC gives rise to significant and unwanted power peaks. For example at *t=44 s,* a harmful power peaks of *7kW* is observed. These peaks are due to the difference in transient dynamics as it will be demonstrated below. Large transient peaks are harmful for power sources and may cause failures or at least lifespan reduction to sensitive power sources such as FCs. Figure 4.30 shows how the proposed coordinated switching strategy via the transition functions given by equations (4.39- 4.40) have suppressed all the transient power ripples noticed during abrupt switchings between FC and SC. One can notice that the proposed transition functions have compensated the difference in transient power sources dynamics through the control of power coming from them during switching instants. Another advantage of such switching is that power sources are not subjected to high and sudden current which can cause their damage.
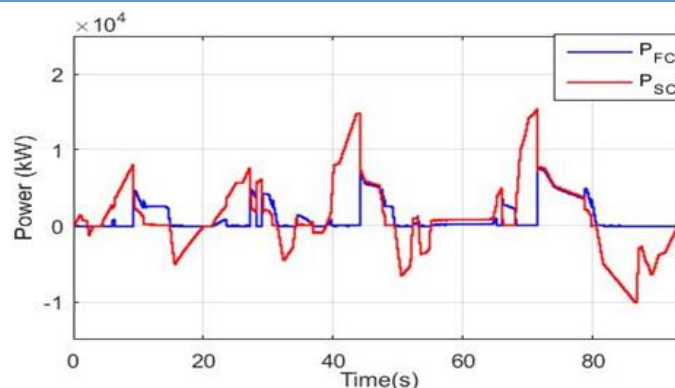
Figure 4.28 FC and SC powers using coordinated switching
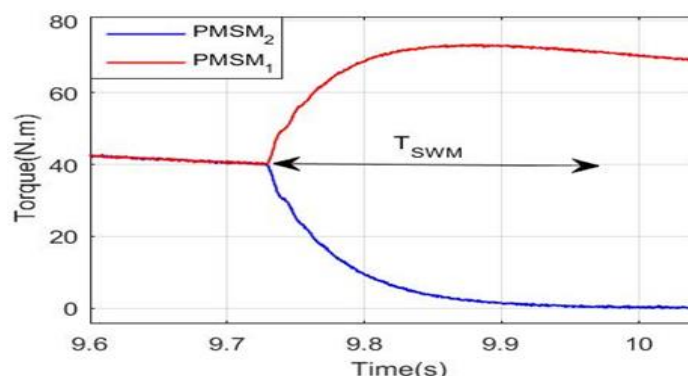
Figure 4.29 Non coordinated FC and SC switching
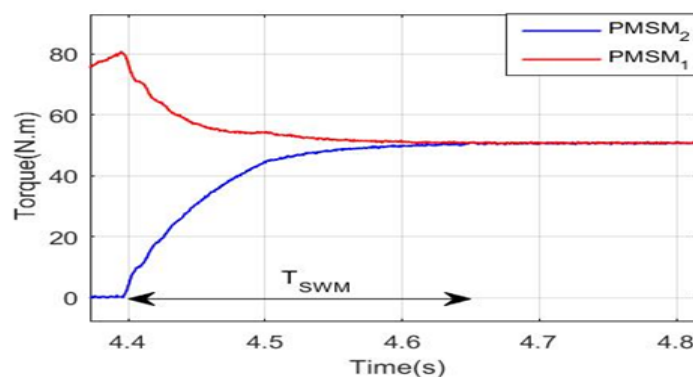
Figure 4.30 Coordinated FC and SC switching

To investigate deeply the reasons that caused the high power ripples during FC and SC switchings, zooms of figures 4.28 and 4.29 are, respectively, shown in figures 4.31 and 4.32. Before the switching instant at $t=69\ s$, both FC and SC were ensuring half of the power required for traction equal to $2.5\ kW$ which means ($C_{FC}=C_{SC}=50\%$). At $t=69\ s$, C_{FC} is set to 100% letting FC ensure all the required power for traction which is 5 kW and SC is turned off by setting C_{SC} to 0. When FC and FC are switched abruptly without the use of the proposed coordinated strategy, the miscoordination is well apparent during the time period delimited by the two dashed lines in figure 4.31. Notice that SC power rapidly went to zero before the FC develops the required power for traction. This creates a transient power lack that causes ripples that impact negatively the performance of the HEV. Note that at any instant between the two dashed lines of figure 4.31, the sum of FC and SC powers is less than the required power for traction. Figure

4.32 depicts a zoom of coordinated FC-SC switching which performed using the proposed exponential transition functions is given by equations 4.38 and 4.39. Notice that at each instant during the transition period delimited by the two dashed lines, the sum of SC and FC powers is almost equal to the required HEV power with a tolerable error. For example, at *t=45.91 s*, the sum of FC and SC powers is equal to 3.98 *kW* and the required power for traction is 4 *kW*. The coordination is performed by forcing FC and SC to follow the reference powers generated by the proposed transition functions. It is worth noticing that this switching strategy protects the power sources from high and abrupt currents which may cause their damage or reduce their lifetime.
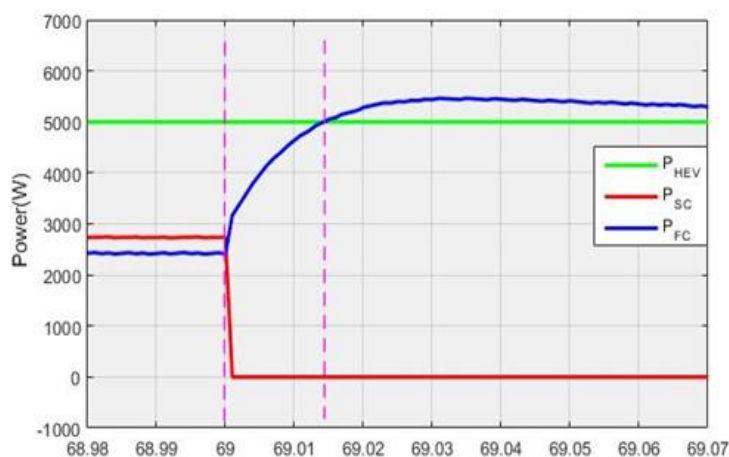
Figure 4.31 Zoom of uncoordinated FC-SC switching
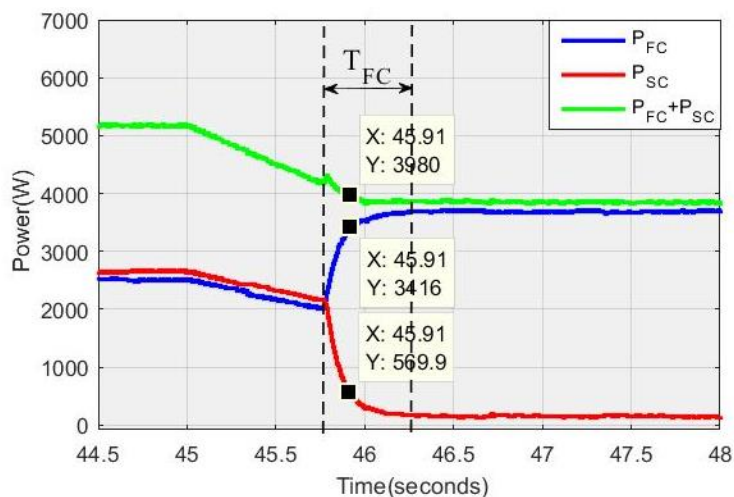
Figure 4.32 Zoom of coordinated FC-SC switching

Figure 4.33 shows DC bus voltage obtained when FC and SC are switched using abrupt switching and the proposed coordinated switching strategy. Abrupt power sources switching resulted in voltage fluctuations within a ripple band of 12 volt. However, the use of coordinated switching strategy for power source switching has minimized DC bus voltage ripples to a narrow band of 3 volts. The proposed coordinated switching strategy minimized up to four times the DC bus ripples compared to classical abrupt switching.
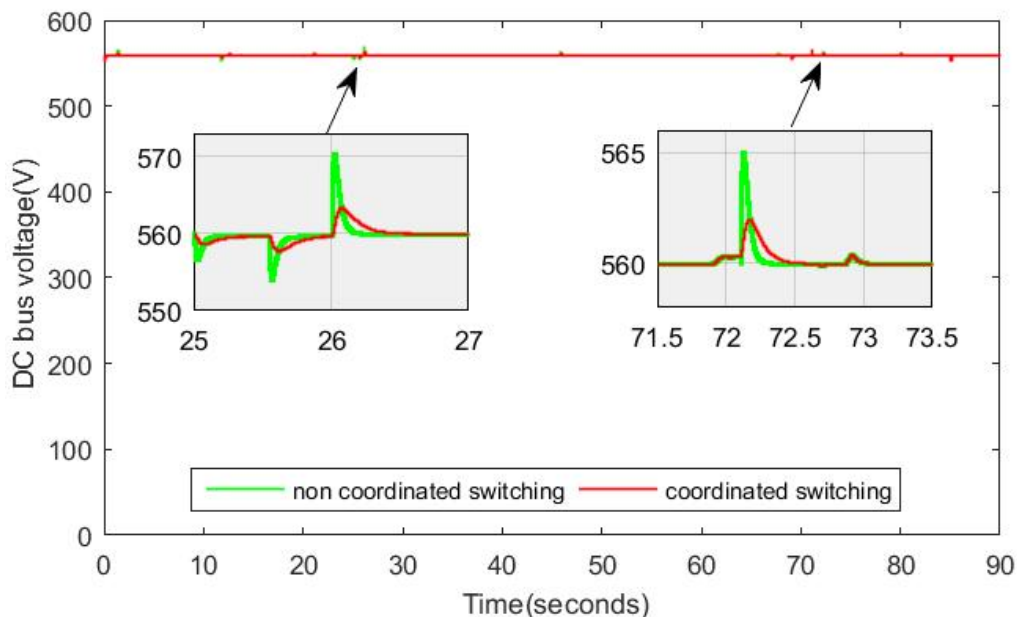
Figure 4.33 DC bus voltage

Table 4.6 summarizes the improvement made by the proposed coordinated switching strategy in comparison to abrupt switching. The comparison is made on basis of DC bus voltage fluctuations and transient torque and power ripples. Notice that the proposed switching strategy have resulted in significant minimization of the previously mentioned quantities and this improves vehicle performance and driving comfort.

Table 4.6 Comparison between transition techniques.

Coordinated switching	Performance	Abrupt switching	Coordinated switching
Power sources	DC bus voltage ripples	20 V	5 V
	power ripples	0.4 kW	8kW
Traction motors	torque ripples	30 N.m	suppressed
	Speed ripples	6.7 km/h	0.55 km/h

Percentage overshoot of DC bus voltage is calculated using equation 4.40. Figure 4.34 compares the PO_V obtained using the proposed coordinated switching strategy to other published works. The proposed coordinated strategy reduced significantly DC bus voltage in comparison to other reference works and resulted in a PO_V of 0.35% and this enhances by much HEV performances.

$$PO_V = \frac{\max\left(V_{DC}\right) - V_{DC,ref}}{V_{DC,ref}} \tag{4.40}$$

Figure 4.35 compares the transient power peaks obtained using the proposed coordinated switching strategy to those obtained in other published works. Notice that large and harmful transient ripples are noticed in many research papers. In [73] 'p. 10', significant transient power

ripples reaching 40 kW are recorded during each SC turn on and extinction. In [74] 'p. 6', power peak of 30 kW is noticed in FC power during the starting and this may cause its damage. The same transient phenomenon is noticed in [96] 'p.68' where a power large peak of 15kW is noticed during FC starting. The proposed coordinated switching strategy has limited the transient power ripples to a narrow hysteresis band of 600 W.
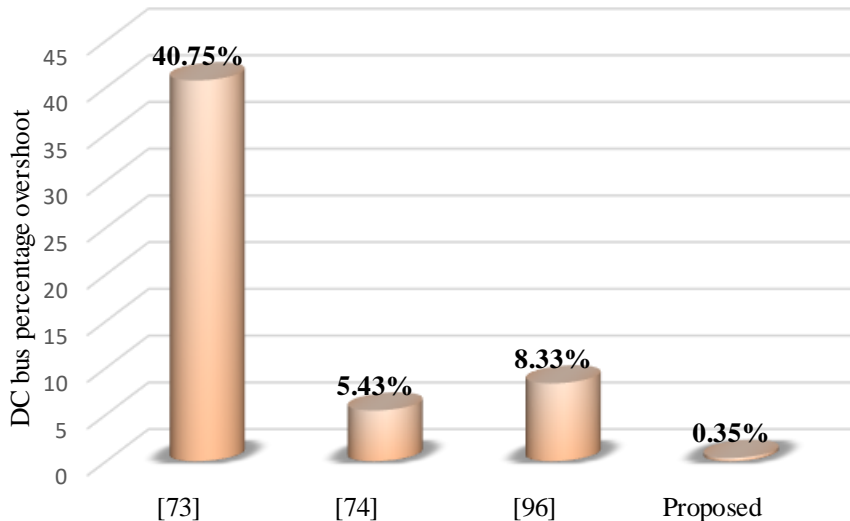
Figure 4.34 Comparison of different maximum transient power peaks.
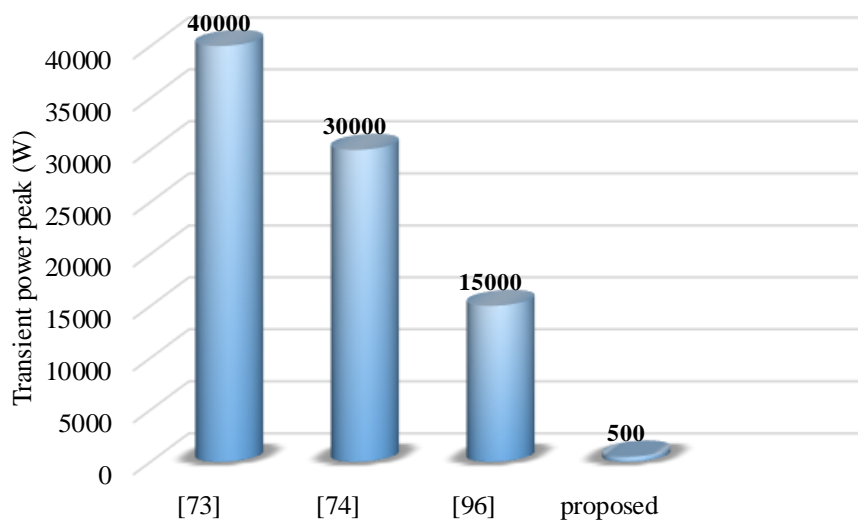
Figure 4.35 Comparison of different voltage percentage overshoots

4.6 Real Time RT LAB simulation

In this section, RT LAB simulator is used to test and validate the real time feasibility of the proposed coordinated switching used for switching from single to dual traction mode. As it is shown in figure 4.36, the first step toward real time simulation is the model separation. HEV system is splitted into computation and console blocs. Blocs that contain computations such as the coordination control strategy, HEV model, FC and SC models are placed on the computation subsystem. Scopes and constants are placed in the console bloc. Each computation subsystem will be executed on one CPU core of the RT simulator. Data between computation subsystem

and console is exchanged asynchronously through the TCP/IP link but data exchange between the two the two computation subsystems is performed synchronously through shared memory. Data from RT simulator are displayed on the digital oscilloscope using BNC to BNC cable.
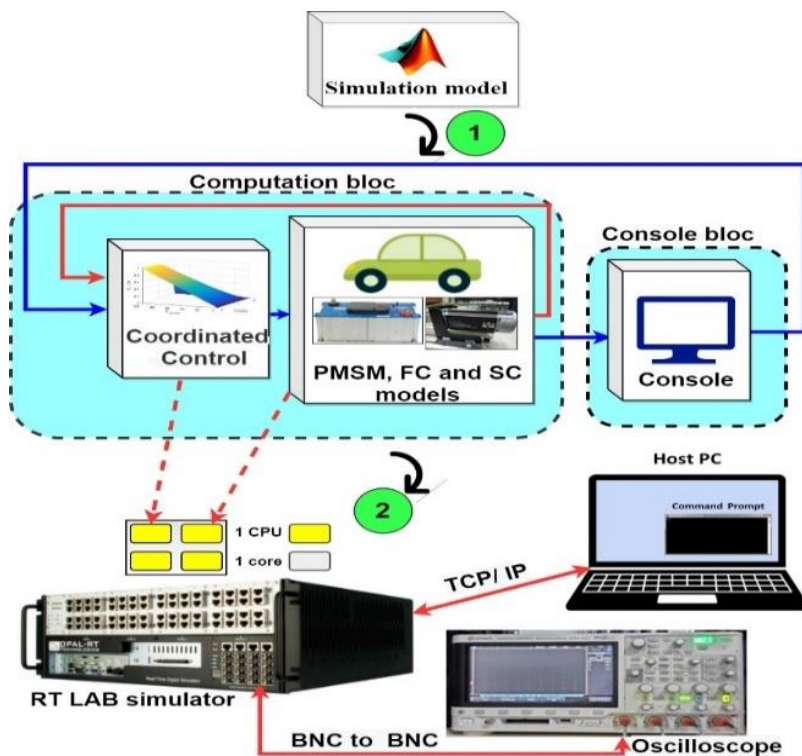
Figure 4.36 Real time based RT LAB simulation scheme.

The real time results of non-coordinated FC-SC switchings obtained using RT LAB are presented in figure 37-a. It can be remarked that large and harmful ripples occur each time FC power toggles from P_{FC}^{old} to P_{FC}^{new}. Figure (37-b) shows the results of FC-SC switchings using the proposed coordinated switching strategy. Notice that coordinated switching strategy has reduced notably the transient power ripples via the exponential based transition function. This switching strategy compensates the difference in dynamics between power sources and protects them from abrupt and high currents which may cause their damage. In subsection 4.2, it is said that FC can deliver any predefined percentage of total traction power. This is can be clearly seen in figure 38 which shows FC delivering different percentages of total required traction power which is set to 7kW. At Q1 the FC delivers all the required traction power whereas at Q2 it is the SC that delivers all the required traction power and FC is off. At Q3, FC delivers 70% of the required power and the SC deliver the remaining 30%. At Q4, FC delivers 30% of the required power and SC delivers the remaining 70%. At Q5, both FC and SC deliver 50% of the required power. Figure 38-a shows PMSM2 phase currents when drive mode is performed without coordinated motor switching. Note that high current ripples occur during motor starting and this produces undesired jerks that reduce vehicle comfort. Figure 38-b shows PMSM2 phase currents when it is

commutated with PMSM1 using the proposed coordinated switching strategy. Note how the phase currents went smoothly from zero to their nominal value without any ripples or jerks which enhances the ride comfort. Figure 39 shows the motor control signals c_{m1} and c_{m2}. It can be seen that as soon as the load torque T_L exceeds the threshold set to 80 *N.m,* c_{m2} will be turned on and will be equal to 0.5 V and c_{m1} will toggle from 1 to 0.5 meaning that both PMSM1 and PMSM2 will ensure 50% of the torque applied on the HEV. Figure 40 and figure 41 show, respectively, motor switching using coordinated switching strategy and abrupt switching. It is worth noting that abrupt motor switching resulted in injurious torque percentage overshoots of 69% for PMSM1 and 72% for PMSM2 during the commutation from single to dual traction mode as it is mentionned in figure 40. On the other hand, the proposed coordinated switching strategy via the use of exponential transition function has provided smooth commutation from single to dual traction mode and vice versa. Figure 41 shows that the torque percentage overshoot for both traction machines is 0%. Furthermore, the rise time of the torque developed by PMSM1 and PMSM2 is 0.09 s, indicating that drive mode switchings are well coordinated.

(a)

(b)
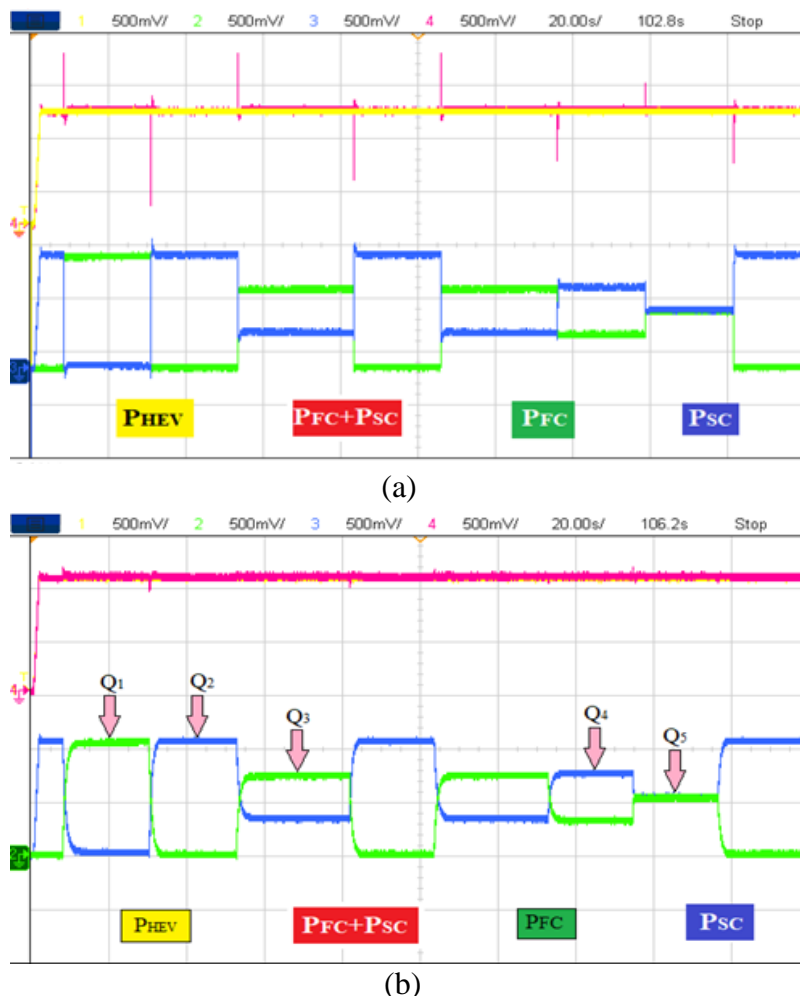
Figure 4.37 FC-SC switching, (a) using non coordinated switching, (b) using coordinated switching.
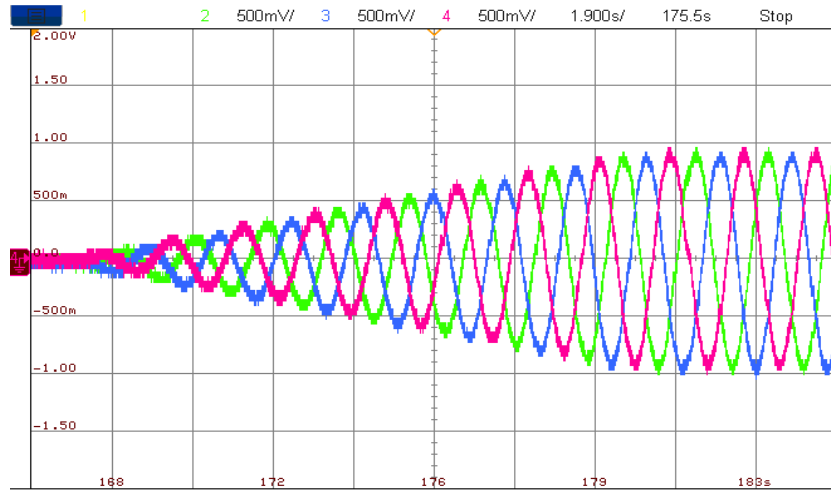
(a)
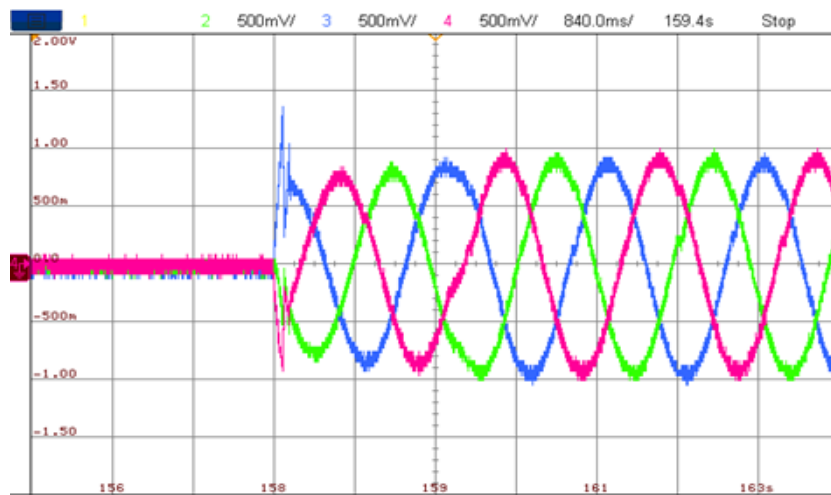
(b)

Figure 4.38 Zoom of PMSM2 phase currents (a) non coordinated switching, (b) coordinated switching.
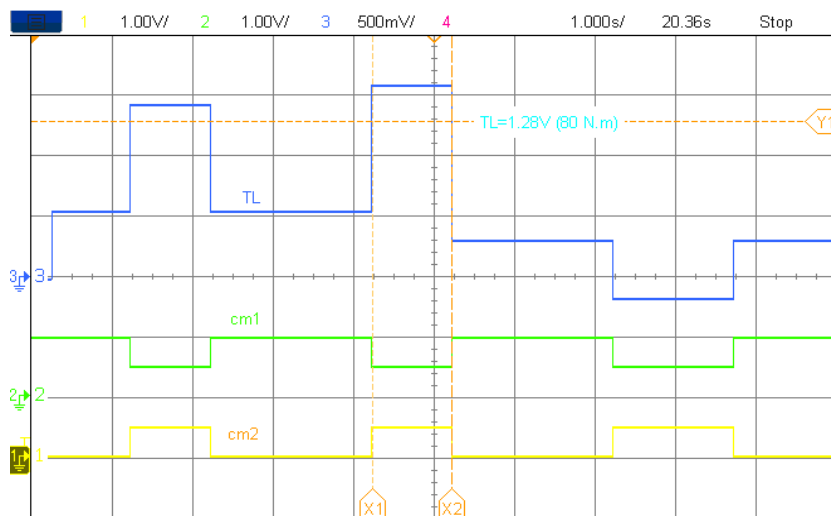
Figure 4.39 Generation of motor control signals c_{m1} and c_{m2}.
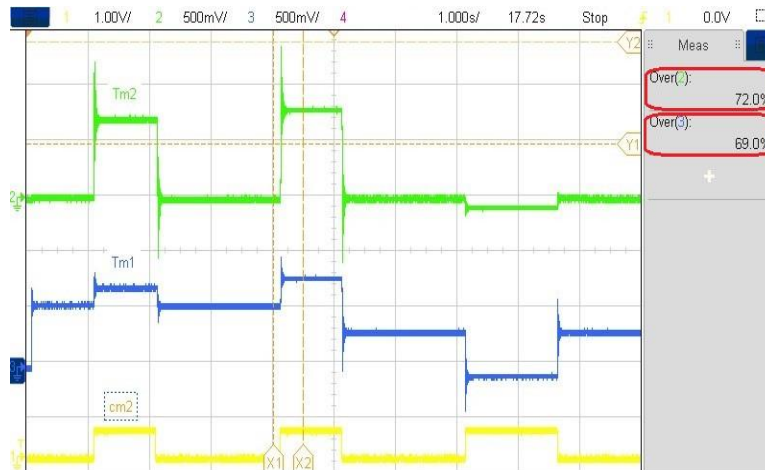
Figure 4.40 Front and rear motor switching abrupt switching.
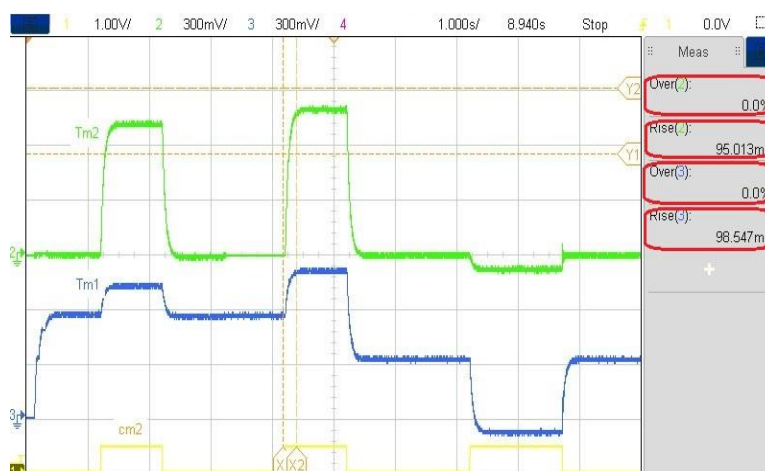
Figure 4.41 Front and rear motor switching abrupt switching.

4.7 Conclusions

The smart torque allocation strategies investigated in this chapter have demonstrated their ability to improve HEV propulsion power while avoiding performance degradation on non-uniform ground surfaces. It was found that PSO and fuzzy torque allocation strategies kept vehicle propulsion power high even on non uniform ground surfaces and have converted 84~86% of the generated torque into propulsion torque. Thanks to the proposed coordinated switching strategy, DC bus voltage percentage overshoot was reduced to 0.35%, the injurious power ripples occurring during power source switchings were reduced to a narrow band of 600 W. Furthermore, the transient torque jerks taking place during drive mode commutations were reduced. As a further work, it is intended to take advantage of PSO intelligence to ensure an optimal torque distribution will minimizing the power drawn from power sources. In addition to that, PSO may also be of great interest if used for maximum energy harvesting during regenerative braking instants.

General conclusion

General conclusion

All the contributions presented throughout this thesis are meant to enhance the performance of electric vehicle and improve its driving comfort. The acheivement of these last mentioned objectives is reached via convinient use of vehicle power sources, efficient motor control strategies and convinient torque allocation over vehicle wheels.

Particle swarm optimization and genetic algorithms used to provide intelligent tuning of electric vehicle controllers have succeeded to find optimal controller gains that resulted in enhancing vehicle transient performance and hence improving driving comfort. Furthermore, the two cost functions proposed for both step and driving cycles speed inputs have proved their effectiveness and their ability to tradeoff between the design objectives.

The proposed fuzzy energy management strategy presented in this work avoided exhausting one source over another by operating both the battery and the fuel cell at safe operating points. Furthermore, the coordinated switching strategy, developed mainly to make up for slow fuel cell transient dynamics, has proven its ability to reduce the undesired transient effects that take place during power sources commutations. All the transition functions presented in this work have resulted in promising results in terms of transient ripple reduction as they have all lowered the stress applied on the fuel cell during abrupt load demands.

Particle swarm optimization and fuzzy logic control have improved vehicle propulsion power while avoiding performance degradation on non-uniform ground surfaces. PSO and fuzzy torque allocation strategies have converted 84~86% of the generated torque into propulsion torque. The proposed coordinated switching strategy resulted in smooth drive mode commutation when it was applied at motor level and it yielded acceptable transient ripples.

Further work

It is true that the set of contributions presented throughout this thesis yielded significant improvements of HEV performance, security and lifespan of its power sources. However, it is worth noticing that there is a lot of work to do in order to meet the high and increasing expectations of customers.

As a further work, it is intended to take advantage of other metaheuristic algorithms to ensure an optimal torque distribution while minimizing the power drawn from power sources. In addition to that, PSO or other optimization algorithms may also be of great interest if used for maximum energy harvesting during regenerative braking instants.

Powertrain architectures are among the characteristics that have been strongly diversified since the invention of HEVs because it is the key factor toward HEV performance enhancement. The number and the location of the used electric machines is used as a scale in HEV classification. It would be interesting to conduct a study to determine the best driveline architecture that results in a better propulsion force, lower cost and maximum effeciency.

References

[1] United States Environmental Protection Agency, Greenhouse Gas Emissions (2017). https://www.epa.gov/ghgemissions/sources-greenhouse-gas-emissions

[2] Katuri R, Gorantla S. (2017). Design and analysis of a control strategy approach for a smooth transition between battery and ultracapacitor. European Journal of Electrical Engineering, Vol. 19, No. 5-6, pp. 313-339. doi: https://doi.org/10.3166/EJEE.19.313-339

[3] Raghavendran, C. R, Sadees, M, Roselyn, J. P, Devaraj, D, (2019). An Intelligent Energy Management System for Grid Connected DFIG based Wind System. In 2019 IEEE International Conference on Intelligent Techniques in Control, Optimization and Signal Processing (INCOS) (pp. 1-5). IEEE. doi: 10.1109/INCOS45849.2019.8951316

[4] Chan CC, Chau KT, (1997), An overview of power electronics in electric vehicles. IEEE transactions on Industrial Electronics. Feb; Vol. 44, No. 5, pp. 3-13. DOI: 10.1109/41.557493

[5] Youssef A.M. (2018). Operations of electric vehicle traction system, Mathematical Modelling of Engineering Problems, Vol. 5, No. 2, pp. 51-57. DOI: https://doi.org/10.18280/mmep.050201

[6] Chan AC, Zhou J, A secure, intelligent electric vehicle ecosystem for safe integration with the smart grid. IEEE Transactions on Intelligent Transportation Systems. 2015 Jul 13;16(6):3367-76. doi: 10.1109/TITS.2015.2449307

[7] Yang, Y. (2020). A vehicle recognition algorithm based on deep convolution neural network. Traitement du Signal, Vol. 37, No. 4, pp. 647-653. doi: https://doi.org/10.18280/ts.370414

[8] Sakhrieh A.H, Al-Hares A.N, Faqes F.A, Al Baqain A.S., Alrafie N.H, (2017). Optimization of oxyhydrogen gas flow rate as a supplementary fuel in compression ignition combustion engines, International Journal of Heat and Technology, Vol. 35, No. 1, pp. 116-122. doi: https://doi.org/ 10.18280/ijht.350116

[9] Ou, K, Yuan, W.W., Choi, M., Yang, S., Jung, S. and Kim, Y.B. (2018), Optimized power management based on adaptive-PMP algorithm for a stationary PEM fuel cell/battery hybrid system, International Journal of Hydrogen Energy, Vol. 43 No. 32, pp. 15433-15444, DOI: 10.1016/j.ijhydene.2018.06.072.

[10] Djerioui, A, Houari, A., Zeghlache, S., Saim, A., Benkhoris, M.F., Mesbahi, T. and Machmoum, M. (2019), Energy management strategy of supercapacitor/fuel cell energy storage devices for vehicle applications", International Journal of Hydrogen Energy, Vol. 44 No. 41, pp. 23416-23428, doi: 10.1016/j.ijhydene.2019.07.060.

[11] Corrêa, J.M., Farret, F.A., Canha, L.N. and Simoes, M.G. (2004), An electrochemical-based fuel-cell model suitable for electrical engineering automation approach", IEEE Transactions on Industrial Electronics, Vol. 51 No. 5, pp. 1103-1112, doi: 10.1109/TIE.2004.834972.

[12] Tremblay, O. and Dessaint, L.A. (2009), A generic fuel cell model for the simulation of fuel cell vehicles, In 2009 IEEE Vehicle Power and Propulsion Conference, IEEE, pp. 1722-1729. DOI:10.1109/VPPC.2009.5289692

[13] Tang, Y., Yuan, W., Pan, M. and Wan, Z. (2011), Experimental investigation on the dynamic performance of a hybrid PEM fuel cell/battery system for lightweight electric vehicle application, Applied Energy, Vol. 88 No. 1, pp. 68-76, doi: DOI:10.1016/j.apenergy.2010.07.033

[14] Garcia-Gabin, W., Dorado, F. and Bordons, C. (2010), Real-time implementation of a sliding mode controller for air supply on a PEM fuel cell, Journal of Process Control, Vol. 20 No. 3, pp. 325-336, doi: 10.1016/j.jprocont.2009.11.006

[15] Rodatz, P., Paganelli, G., Sciarretta, A. Guzzella, L. (2005), Optimal power management of an experimental fuel 910 cell/supercapacitor-powered hybrid vehicle, Control Engineering Practice, Vol. 13 No. 1, pp. 41-53, doi: 10.1016/j.conengprac.2003.12.016.

[16] Yan, W.-M., Soong, C.-Y., Chen, F. and Chu, H.-S. (2005), Transient analysis of reactant gas transport and performance of PEM fuel cells, Journal of Power Sources, Vol. 143 Nos 1/2, pp. 48-56, doi: 10.1016/j.jpowsour.2004.11.058.

[17] Liu, Z., Ciais, P., Deng, Z., Lei, R., Davis, S. J., Feng, S., & Schellnhuber, H. J. (2020). Near-real-time monitoring of global CO2 emissions reveals the effects of the COVID-19 pandemic. Nature communications, Vol.11, No.1, pp.1-12. doi:https://doi.org/10.1038/s41467-020-18922-7

[18] https://www.ev-volumes.com/ Access date: May 16th 2022.

[19] Udaeta, M. E. M., Chaud, C. A., Gimenes, A. L. V., & Galvao, L. C. R. (2015). Electric vehicles analysis inside electric mobility looking for energy efficient and sustainable metropolis. Open Journal of Energy Efficiency, Vol. 4, No.1, doi: 10.4236/ojee.2015.41001

[20] Larminie, J. and Lowry, J. (2003) Electric Vehicle Technology Explained. John Wiley and Sons Ltd., Chichester.

[21] Sun, W., Wang, F., Zhang, B., Zhang, M., Küpers, V., Ji, X., Winter, M. (2021). A rechargeable zinc-air battery based on zinc peroxide chemistry. Science, Vol. 371, No.6524, pp.46-51. doi :10.1126/science.abb9554

[22] Anderson, C.D. and Anderson, J. (2010) Electric and Hybrid Cars: A History. 2nd Edition, McFarland & Company,Inc., Jefferson.

[23] Department of Energy, Energy Efficiency and Renewable Energy. History of Electric Vehicles.http://www.eere.energy.gov/vehiclesandfuels/avta/light_duty/fsev/fsev_history.html

[24] Struben, J., Sterman, J. D. (2008). Transition challenges for alternative fuel vehicle and transportation systems. Environment and Planning B: Planning and Design, Vol. 35. No.6, pp.1070-1097. doi: https://doi.org/10.1068/b33022t

[25] Nash, G. D. (1992). Book Review: The Prize: The Epic Quest for Oil, Money, and Power, by Daniel Yergin. Pennsylvania Magazine of History and Biography, 402-403

[26] Bottura, C.P. and Barreto, G. (1989) Electric Vehicles. UNICAMP, Campinas.

[27] Fagnant, D. J., Kockelman, K. M. (2014). The travel and environmental implications of shared autonomous vehicles, using agent-based model scenarios. Transportation Research Part C: Emerging Technologies, Vol. 40, pp.1-13.doi: https://doi.org/10.1016/j.trc.2013.12.001

[28] Schiffer, M.B. (2010) Taking Charge—The Electric Automobile in America. Smithsonian Institution Press, Washington DC.

[29] Delucchi, M. A., & Lipman, T. E. (2010). Lifetime cost of battery, fuel-cell, and plug-in hybrid electric vehicles. Electric and Hybrid Vehicles: Power Sources, Models, Sustainability, Infrastructure and the Market. Amsterdam, The Netherlands, pp. 19-60.

[30] El Araby, M. (2002). Urban growth and environmental degradation: The case of Cairo, Egypt. Cities, 19(6), 389-400. Doi: https://doi.org/10.1016/S0264-2751(02)00069-0

[31] Habib, S., Khan, M. M., Abbas, F., Sang, L., Shahid, M. U., & Tang, H. (2018). A comprehensive study of implemented international standards, technical challenges, impacts and prospects for electric vehicles. IEEE Access, Vol. 6, pp. 13866-13890. Doi:10.1109/ACCESS.2018.2812303

[32] Faia, S.M.R. (2006) Optimization of Vehicle Propulsion Systems for Fleet. Thesis of M.Sc., Instituto Superior Técnico, Lisboa

[33] Dijk, M., Yarime, M. (2010). The emergence of hybrid-electric cars: Innovation path creation through co-evolution of supply and demand. Technological Forecasting and Social Change, Vol. 77, No. 8, pp. 1371-1390. doi: http://dx.doi.org/10.1016/j.techfore.2010.05.001

[34] Udaeta, M. E. M., Chaud, C. A., Gimenes, A. L. V., Galvao, L. C. R. (2015). Electric vehicles analysis inside electric mobility looking for energy efficient and sustainable metropolis. Open Journal of Energy Efficiency, Vol. 4, No.1, doi:10.4236/ojee.2015.41001

[35] IEA (2011) International Energy Agency, Technology Roadmap: Electric and Plug-In Hybrid Electric Vehicles.

[36] Singh, K. V., Bansal, H. O., & Singh, D. (2019). A comprehensive review on hybrid electric vehicles: architectures and components. Journal of Modern Transportation, Vol. 27, No.2, pp. 77-107. Doi: https://doi.org/10.1007/s40534-019-0184-3

[37] Wu, G., Zhang, X., & Dong, Z. (2015). Powertrain architectures of electrified vehicles: Review, classification and comparison. Journal of the Franklin Institute, Vol.352, No. 2, pp. 425-448. Doi: https://doi.org/10.1016/j.jfranklin.2014.04.018

[38] Buticchi, G., Gerada, D., Alberti, L., Galea, M., Wheeler, P., Bozhko, S., Gerada, C. (2019). Challenges of the optimization of a high-speed induction machine for naval applications. Energies, Vol. 12, No. 12, 2431. doi : https://doi.org/10.3390/en12122431

[39] Electric vehicles and the energy sector - impacts on Europe's future emissions, https://www.eea.europa.eu/publications/electric-vehicles-and-the-energy , accessed: June 25th,2022

[40] Yadav, D.; Verma, A. Performance analysis of permanent magnet synchronous motor drive using particle swarm optimization technique. In Proceedings of the 2016 International Conference on Emerging Trends in Electrical Electronics & Sustainable Energy Systems, pp. 280–285; IEEE: Piscataway, NJ, USA, 2016. Doi: 10.1109/ICETEESES.2016.7581394

[41] Oubelaid, A., Taib, N., & Rekioua, T. (2019, November). Performance Assessment of a Direct Torque Controlled Electric Vehicle considering Driving Cycles and Real Load Conditions. In 2019 International Conference on Advanced Electrical Engineering (ICAEE) (pp. 1-6). IEEE. Doi: 10.1109/ICAEE47123.2019.9014665

[42] Watany, M. (2014). Performance of a road vehicle with hydraulic brake systems using slip control strategy. American Journal of Vehicle Design, Vol. 2, No. 1, pp.7-18. doi:10.12691/ajvd-2-1-2

[43] Kumar, P., Majhi, S. Introduction to Hybrid and Electric Vehicles-Web course.

[44] Kim, D. K., Kim, D. M., Park, J. C., Lee, S. G., Yoo, J., & Lim, M. S. (2022). Torque Ripple Reduction of BLDC Traction Motor of Electric Wheelchair for Ride Comfort Improvement. Journal of Electrical Engineering & Technology, Vol. 17, No. 1, pp. 351-360. Doi:https://doi.org/10.1007/s42835-021-00875-6

[45] Husain, I., Ozpineci, B., Islam, M. S., Gurpinar, E., Su, G. J., Yu, W., Sahu, R. (2021). Electric drive technology trends, challenges, and opportunities for future electric vehicles. Proceedings of the IEEE, Vol. 109, No. 6, pp.1039-1059. Doi:10.1109/JPROC.2020.3046112

[46] Rubino, S., Mandrile, F., Tolosano, L., Armando, E., Bojoi, R. (2021). Direct Flux and Load Angle Vector Control of Permanent Magnet Synchronous Motors. In 2021 IEEE Energy Conversion Congress and Exposition (ECCE) (pp. 4668-4675). IEEE. DOI: 10.1109/ECCE47101.2021.9595616

[47] Agamloh, E., Von Jouanne, A., Yokochi, A. (2020). An overview of electric machine trends in modern electric vehicles. Machines, Vol. 8, No. 2, 20. Doi : https://doi.org/10.3390/machines8020020

[48] Chan, C. C., Cheng, M. (2021). Vehicle traction motors. In Electric, Hybrid, and Fuel Cell Vehicles (pp. 483-513). New York, NY: Springer New York. DOI: https://doi.org/10.1007/978-1-0716-1492-1_800

[49] Elmorshedy, M. F., Xu, W., El-Sousy, F. F., Islam, M. R., & Ahmed, A. A. (2021). Recent achievements in model predictive control techniques for industrial motor: A comprehensive state-of-the-art. IEEE Access, Vol. 9, pp. 58170-58191. DOI: 10.1109/ACCESS.2021.3073020

[50] Niu, F., Wang, B., Babel, A. S., Li, K., & Strangas, E. G. (2015). Comparative evaluation of direct torque control strategies for permanent magnet synchronous machines. IEEE Transactions on Power Electronics, Vol. 1, No. 2, pp. 1408-1424. Doi: 10.1109/TPEL.2015.2421321

[51] Flah, A., Khan, I. A., Agarwal, A., Sbita, L., Simoes, M. G. (2021). Field-oriented control strategy for double-stator single-rotor and double-rotor single-stator permanent magnet machine: Design and operation. Computers & Electrical Engineering, Vol. 90, pp. 106953. doi : https://doi.org/10.1016/j.compeleceng.2020.106953

[52] Takahashi, I., & Noguchi, T. (1986). A new quick-response and high-efficiency control strategy of an induction motor. IEEE Transactions on Industry applications, Vol. 5, pp.820-827. Doi: 10.1109/TIA.1986.4504799

[53] A. Oubelaid, N. Taib, S. Nikolovski, T.E.A. Alharbi, T. Rekioua, A. Flah, S. S. M. Ghoneim, (2022). Intelligent Speed Control and Performance Investigation of a Vector Controlled Electric Vehicle Considering Driving Cycles. Electronics, Vol. 11, No. 13 :1925. Doi: https://doi.org/10.3390/electronics11131925

[54] Mansouri, M., Bey, M., Hassaine, S., Larbi, M., Allaoui, T., Denai, M. (2022). Genetic algorithm optimized robust nonlinear observer for a wind turbine system based on permanent magnet synchronous generator. ISA transactions. Doi : https://doi.org/10.1016/j.isatra.2022.02.004

[55] Godbole, P., Pathak, M. (2022). Particle Swarm Optimization (PSO) Model and Its Application in ANN Controller, doi: https://doi.org/10.46501/IJMTST0801026

[56] Yu Z, Zinger D, Bose A, (2011). An innovative optimal power allocation strategy for fuel cell, battery and supercapacitor hybrid electric vehicle. Journal of Power Sources. Vol. 196, No. 4, pp.2351-2359. doi: https://doi.org/10.1016/j.jpowsour.2010.09.057

[57] Kim BM, Choi YH, Yoo SJ, (2019). Adaptive control of proton exchange membrane fuel cell air supply systems with asymmetric oxygen excess ratio constraints. IEEE Access, Vol. 8, pp.5537-5549. doi: 10.1109/ACCESS.2019.2963334

[58] Hou, J., Yang, M., Ke, C., & Zhang, J. (2020). Control logics and strategies for air supply in PEM fuel cell engines. Applied Energy, Vol. 269, pp. 115059. DOI: https://doi.org/10.1016/j.apenergy.2020.115059

[59] Sun, T., Zhang, X., Chen, B., & Liu, X. (2020). Coordination control strategy for the air management of heavy vehicle fuel cell engine. International Journal of Hydrogen Energy. , Vol. 45, No. 39, pp. 20360-8. DOI: https://doi.org/10.1016/j.ijhydene.2019.10.134

[60] Daud, W. R. W., Rosli, R. E., Majlan, E. H., Hamid, S. A. A., Mohamed, R., & Husaini, T (2017). PEM fuel cell system control: A review. Renewable Energy.Vol.pp.113620-38. doi:https://doi.org/10.1016/j.renene.2017.06.027

[61] Lahyani, A., Abdelhedi, R., Ammari, A. C., Sari, A., & Venet, P.. (2020). Reinforcement learning based adaptive power sharing of battery/supercapacitors hybrid storage in electric vehicles. Energy Sources, Part A: Recovery, Utilization, and Environmental Effects. Vol.29, pp.1-22. doi: https://doi.org/10.1080/15567036.2020.1849456

[62] Kumaravel S, Ashok S. (2015). Optimal power management controller for a stand-alone solar PV/wind/battery hybrid energy system. Energy Sources, Part A: Recovery, Utilization, and Environmental Effects, Vol. 37, No. 4, pp.407-415, DOI: https://doi.org/10.1080/15567036.2011.576414

[63] Ramineni, P., Pandian, A., (2021). Study and investigation of energy management techniques used in electric/hybrid electric vehicles. Journal Européen des Systèmes Automatisés, Vol. 54, No. 4, pp. 599-606. doi : https://doi.org/10.18280/jesa.540409

[64] Fathabadi, H. (2015), Fuel cell/back-up battery hybrid energy conversion systems: dynamic modeling and harmonic considerations. Energy Conversion and Management, Vol.215, No. 103, pp. 573-584. DOI: https://doi.org/10.1016/j.enconman.2015.07.010

[65] Fathabadi, H. (2018). Novel fuel cell/battery/supercapacitor hybrid power source for fuel cell hybrid electric vehicles. Energy, Vol. 143, pp. 467-477. Doi: https://doi.org/10.1016/j.energy.2017.10.107

[66] Tremblay, O., Dessaint, LA. (2009). A generic fuel cell model for the simulation of fuel cell vehicles. IEEE vehicle power and propulsion conference 2009 Sep 7 (pp. 1722-1729). DOI: 10.1109/VPPC.2009.5289692

[67] Corrêa, JM., Farret, FA., Canha, LN., et al. An electrochemical-based fuel-cell model suitable for electrical engineering automation approach. IEEE Transactions on industrial electronics, Vol. 51, No. 5, pp. 1103-12. doi: 10.1109/TIE.2004.834972

[68] Oubelaid, A., Taib, N., Rekioua, T. (2022). Novel coordinated power sources switching strategy for transient performance enhancement of hybrid electric vehicles. COMPEL-The international journal for computation and mathematics in electrical and electronic engineering, (ahead-of-print). doi: https://doi.org/10.1108/COMPEL-10-2021-0399

[69] Zhang, Z., Guan, C., Liu, Z., (2020). Real-time optimization energy management strategy for fuel cell hybrid ships considering power sources degradation. IEEE Access. Vol. 8, pp.87046-87059. doi: 10.1109/ACCESS.2020.2991519

[70] Aouzellag, H., Ghedamsi, K., Aouzellag, D., (2015). Energy management and fault tolerant control strategies for fuel cell/ultra-capacitor hybrid electric vehicles to enhance autonomy, efficiency and life time of the fuel cell system. International journal of hydrogen energy, Vol. 40, No.22, pp. 7204-7213. DOI: https://doi.org/10.1016/j.ijhydene.2015.03.132

[71] Gómez-Peñate, S., López-Estrada, FR., Valencia-Palomo, G., Osornio et al., (2018). Sensor fault diagnosis observer for an electric vehicle modeled as a Takagi-Sugeno system. Journal of Sensors, doi: https://doi.org/10.1155/2018/3291639

[72] Araria R, Berkani A, Negadi K, et al. (2020), Performance analysis of DC-DC converter and DTC based fuzzy logic control for power management in electric vehicle application. Journal Européen des Systèmes Automatisés, vol.53, No. 1, pp.1-9. doi : https://doi.org/10.18280/jesa.530101

[73] Hemi, H., Ghouili, J. and Cheriti, A. (2014). A real time fuzzy logic power management strategy for a fuel cell vehicle. Energy conversion and Management, Vol.80, pp. 63-70. DOI: https://doi.org/10.1016/j.enconman.2013.12.040

[74] Ferahtia S, Djeroui A, Mesbahi T, et al. (2021). Optimal Adaptive Gain LQR-Based Energy Management Strategy for Battery–Supercapacitor Hybrid Power System. Energies, Vol. 14, No.6. pp.1660. doi: https://doi.org/10.3390/en14061660

[75] Das H. S., Tan C. W., Yatim A. H. M., (2017), Fuel cell hybrid electric vehicles: A review on power conditioning units and topologies, Renew. Sustain. Energy Rev., vol. 76, pp. 268–291, doi: https://doi.org/10.1016/j.rser.2017.03.056

[76] F. B. Salem, (2020). Stator winding fault diagnosis of permanent magnet synchronous motor-based DTC-SVM dedicated to electric vehicle applications, in Autonomous Vehicle and Smart Traffic. London, U.K.: IntechOpen, p. 39. doi http://dx.doi.org/10.5772/intechopen.88784

[77] M. H. Iftikhar, B.-G. Park, and J.-W. Kim, (2021), Design and analysis of a five-phase permanent-magnet synchronous motor for fault-tolerant drive, Energies, vol. 14, no. 2, p. 514, doi: https://doi.org/10.3390/en14020514

[78] S.Bouradi, R. Araria, K. Negadi, and F. Marignetti, (2020), Nonlinear control of permanent magnet synchronous motor for high performances electric vehicle, Tecnica Italiana-Italian J. Eng. Sci., vol. 64, nos. 2–4, pp. 317–324, doi: https://doi.org/10.18280/ti-ijes.642-429

[79] M. A. Soumeur, B. Gasbaoui, O. Abdelkhalek, J. Ghouili, T. Toumi, and A. Chakar,(2020). Comparative study of energy management strategies for hybrid proton exchange membrane fuel cell four wheel drive electric vehicle, J. Power Sources, vol. 462, Art. no. 228167. Doi:https://doi.org/10.1016/j.jpowsour.2020.228167

[80] A. Sforza, B. Lenzo, and F. Timpone, (2019). A state-of-the-art review on torque distribution strategies aimed at enhancing energy efficiency for fully electric vehicles with independently actuated drivetrains, Int. J. Mech. Control, vol. 20, no. 2, pp. 3–15 doi: doi: http://shura.shu.ac.uk/id/eprint/25806

[81] S. Singh, A. N. Tiwari, and S. N. Singh, (2020), Performance evaluation of MRAS and SMO based sensorless PMSM drives, World J. Eng., vol. 17, no. 3, pp. 347–355, Mar. 2020. doi:https://doi.org/10.1108/WJE-07-2019-0208

[82] J. J. Zhu, A. Khajepour, J. Spike, S.-K. Chen, and N. Moshchuk, (2016), An integrated vehicle velocity and tyre-road friction estimation based on a half-car model, Int. J. Veh. Auton. Syst., vol. 13, no. 2, pp. 39–114, doi: 10.1504/IJVAS.2016.078763

[83] L. Li, K. Yang, G. Jia, X. Ran, J. Song, and Z. Q. Han, (2015), Comprehensive tire–road friction coefficient estimation based on signal fusion method under complex maneuvering operations, Mech. Syst. Signal Process., vol. 1, no. 56, pp. 76–259, doi: https://doi.org/10.1016/j.ymssp.2014.10.006

[84] De Pinto. S, Camocardi. P, Sorniotti. A, Gruber. P, Perlo. P, Viotto. F, (2016). Torque-fill control and energy management for a four-wheel-drive electric vehicle layout with two-speed transmissions". IEEE Transactions on Industry Applications, Vol. 53, No. 1, pp. 447-458, doi: 10.1109/TIA.2016.2616322

[85] Gasbaoui. B, Nasri. A, Abdelkhalek. O, Ghouili. J, Ghezouani. A, (2017). Behavior PEM fuel cell for 4WD electric vehicle under different scenario consideration. International journal of hydrogen energy, Vol. 42, No. 1, pp. 535- 543. doi: https://doi.org/10.1016/j.ijhydene.2016.08.114

[86] Muduli. U. R, Beig. A. R, Al Jaafari. K, Alsawalhi. J. Y, Behera. R. K, (2020). "Interrupt-Free Operation of Dual Motor Four-Wheel Drive Electric Vehicle Under Inverter Failure", IEEE Transactions on Transportation Electrification, Vol. 7, No. 1, pp. 329-338, doi: 10.1109/TTE.2020.2997354

[87] Soumeur. M. A, Gasbaoui. B, Abdelkhalek. O, Ghouili. J, Toumi. T, Chakar. A, (2020). Comparative study of energy management strategies for hybrid proton exchange membrane fuel cell four wheel drive electric vehicle, Journal of Power Sources, Vol. 462, doi: https://doi.org/10.1016/j.jpowsour.2020.228167

[88] Wang. J, Gao. S, Wang, K. Wang. Y, Wang. Q, (2021). Wheel torque distribution optimization of four-wheel independent-drive electric vehicle for energy efficient driving", Control Engineering Practice, Vol. 110, pp. 104779. doi: https://doi.org/10.1016/j.conengprac.2021.104779

[89] Aouzellag. H., Ghedamsi, K. and Aouzellag, D, (2015), Energy management and fault tolerant control strategies for fuel cell/ultra-capacitor hybrid electric vehicles to enhance autonomy, efficiency and life time of the fuel cell system. International journal of hydrogen energy, Vol. 40 No 22, pp.7204-7213. doi: https://doi.org/10.1016/j.ijhydene.2015.03.132

[90] Fu J, Song S, Fu Z, Ma J, (2019), Design of coordinated control strategy during driving mode switching for parallel hybrid electric vehicles, Trans. Inst. Meas. Control, vol. 41, no. 9, pp. 2507–2520, doi: https://doi.org/10.1177/0142331218803669

[91] Zhou S, Walker P, Tian Y, Zhang N, (2021), Mode switching analysis and control for a parallel hydraulic hybrid vehicle, Vehicle Syst. Dyn., vol. 59, no. 6, pp. 928–948, doi : https://doi.org/10.1080/00423114.2020.1737147

[92] Ghose D., Pradhan S., Shabbiruddin S. (2022), Development of model for assessment of renewable energy sources: A case study on gujarat, India, Int. J. Ambient Energy, vol. 43, no.1,.pp.1157–1166,Doi: https://doi.org/10.1080/01430750.2019.1691650

[93] Inal O. B., Charpentier J.-F., Deniz C. (2022). Hybrid power and propulsion systems for ships: Current status and future challenges, Renew. Sustain. Energy Rev., vol. 156, Art.no.111965. doi: https://doi.org/10.1016/j.rser.2021.111965

[94] Zhang L., Hu X., Wang Z., Ruan J., Ma C., Song Z., Dorrell D. G., Pecht M. G., (2021), Hybrid electrochemical energy storage systems: An overview for smart grid and electrified vehicle applications, Renew. Sustain. Energy Rev., vol. 139, Art. no. 110581. Doi: https://doi.org/10.1016/j.rser.2020.110581

[95] Ferahtia S., Djeroui A., Mesbahi T., Houari A., Zeghlache S., Rezk H., Paul T., (2021), Optimal adaptive gain LQR-based energy management strategy for battery–supercapacitor hybrid power system, Energies, vol. 14, no. 6, pp. 1660, doi: https://doi.org/10.3390/en14061660

[96] Araria R., Berkani A., Negadi K., Marignetti F., Boudiaf M. Performance analysis of DC-DC converter and DTC based fuzzy logic control for power management in electric vehicle application, J. Eur. Syst. Automatisés, vol. 53, no. 1, pp. 1–9, Feb. 2020.

[97] Oubelaid A, Albalawi F, Rekioua T, Ghoneim S. S, Taib, N, Abdelwahab, S. A. M. (2022). Intelligent Torque Allocation Based Coordinated Switching Strategy for Comfort Enhancement of Hybrid Electric Vehicles. IEEE Access. doi: 10.1109/ACCESS.2022.3178956

[98] Bizon N, Raducu M, Oproescu M, (2008). Fuel cell current ripple minimization using a bi-buck power interface. In 2008 13th International Power Electronics and Motion Control Conference, pp. 621-628, DOI: 10.1109/EPEPEMC.2008.4635334

[99] Ruan J, Song Q. A novel dual-motor two-speed direct drive battery electric vehicle drivetrain. (2019), IEEE Access, vol.7, pp. 54330-54342. Doi: 10.1109/ACCESS.2019.2912994

[100] Mokrani Z, Rekioua D, Rekioua T. Modeling, control and power management of hybrid photovoltaic fuel cells with battery bank supplying electric vehicle. (2014). Int. J. Hydrog. Energy. vol. 39, no. 27, pp. 15178-15187. Doi: https://doi.org/10.1016/j.ijhydene.2014.03.215

[101] De Pinto S, Camocardi P, Sorniotti A, Gruber P, Perlo P, Viotto F, (2017), Torque-fill control and energy management for a four-wheel-drive electric vehicle layout with two-speed transmissions. doi: 10.1109/TIA.2016.2616322

Abstract

In this work, several control techniques and energy management strategies that aim to improve vehicle performance are discussed. First, PSO and GA algorithms were used to smartly tune vehicle controllers. This was performed using adequate user defined cost functions. After that, a novel coordinated switching strategy is developed to make up for FC poor transient dynamics and to protect it from possible damages caused mainly by abrupt load variations. The proposed coordinated switching strategy allows the control of the switching period duration. Furthermore, it enables the choice of adequate transition functions that fit the dynamics of power sources undergoing transition. Also, the proposed switching technique is simple and does not require the knowledge of system parameters or the complex control models. Then, a new multi stage fuzzy energy management strategy is developed to improve vehicle autonomy, security and power sources lifespan. Finally, an intelligent torque distribution strategies based on particle swarm optimization and fuzzy logic control to provide convenient torque allocation that maximizes HEV propulsion power.

Keywords: Torque allocation, coordinated switching, Particle swarm optimization, Fuzzy logic, Hybrid Electric Vehicle

Résumé

Dans ce travail, plusieurs techniques de contrôle et stratégies de gestion de l'énergie visant à améliorer les performances des véhicules sont examinées. Tout d'abord, les algorithmes PSO et GA ont été utilisés pour régler intelligemment les contrôleurs du véhicule. Ceci a été réalisé en utilisant des fonctions de coût adéquates définies par l'utilisateur. Ensuite, une nouvelle stratégie de commutation coordonnée est développée pour compenser la faible dynamique transitoire du FC et le protéger des dommages éventuels causés principalement par de brusques variations de charge. La stratégie de commutation coordonnée proposée permet de contrôler la durée de la période de commutation. De plus, elle permet de choisir des fonctions de transition adéquates qui s'adaptent à la dynamique des sources d'énergie en transition. En outre, la technique de commutation proposée est simple et ne nécessite pas la connaissance des paramètres du système ou des modèles de contrôle complexes. Ensuite, une nouvelle stratégie de gestion d'énergie floue à plusieurs niveaux est développée pour améliorer l'autonomie du véhicule, la sécurité et la durée de vie des sources d'énergie. Enfin, une stratégie intelligente de distribution de couple basée sur l'optimisation par essaims de particules et le contrôle par logique floue permet de fournir une allocation de couple pratique qui maximise la puissance de propulsion du véhicule électrique hybride.

Mots clés : Allocation de couple, commutation coordonnée, optimisation de l'essaim de particules, logique floue, véhicule électrique hybride

ملخص:

PSO في هذا العمل، يتم فحص العديد من تقنيات التحكم واستراتيجيات إدارة الطاقة التي تهدف إلى تحسين أداء السيارة. أولاً، تم استخدام خوارزميات لضبط وحدات التحكم في السيارة بذكاء. تم تحقيق ذلك باستخدام وظائف التكلفة المناسبة التي يحددها المستخدم. بعد ذلك، تم تطوير استراتيجية GA و تبديل منسقة جديدة للتعويض عن الديناميكيات العابرة المنخفضة للـ FC وحمايته من التلف المحتمل الناجم بشكل أساسي عن تغيرات الحمل المفاجئة. تتيح استراتيجية التبديل المنسقة المقترحة إمكانية التحكم في مدة فترة التبديل. علاوة على ذلك، فإنه يجعل من الممكن اختيار وظائف الانتقال المناسبة التي تتكيف مع ديناميكيات مصادر الطاقة التي تمر بمرحلة انتقالية. علاوة على ذلك ، فإن تقنية التبديل المقترحة بسيطة ولا تتطلب معرفة معلمات النظام أو نماذج التحكم المعقدة. بعد ذلك، تم تطوير استراتيجية جديدة متعددة المستويات لإدارة الطاقة الغامضة لتحسين استقلالية المركبة، والسلامة، وعمر مصدر الطاقة. أخيرًا، تساعد استراتيجية توزيع عزم الدوران الذكية القائمة على تحسين حشد الجسيمات والتحكم المنطقي الضبابي في توفير تخصيص مناسب لعزم الدوران يزيد من قوة الدفع للمركبة الكهربائية الهجينة.

كلمات مفاتيح :

تخصيص عزم الدوران، والتبديل المنسق، وتحسين سرب الجسيمات، والمنطق الضبابي، والمركبة الكهربائية الهجينة